Broadband cavity-enhanced transient absorption spectroscopy and its application to excited-state intramolecular proton transfer

A Dissertation presented

by

Myles C. Silfies

to

The Graduate School

in Partial Fulfillment of the

Requirements

for the Degree of

Doctor of Philosophy

in

Physics

Stony Brook University

August 2023

Stony Brook University

The Graduate School

Myles C. Silfies

We, the dissertation committee for the above candidate for the

Doctor of Philosophy degree, hereby recommend

acceptance of this dissertation

Thomas K. Allison - Dissertation Advisor
Associate Professor, Department of Physics and Astronomy

Cyrus Dreyer - Chairperson of Defense
Assistant Professor, Department of Physics and Astronomy

Christopher J. Johnson - Committee Member
Associate Professor, Department of Chemistry

Adam J. Fleisher - External Committee Member
Project Leader, National Institute of Standards and Technology

This dissertation is accepted by the Graduate School

Celia Marshik
Dean of the Graduate School

Abstract of the Dissertation

Broadband cavity-enhanced transient absorption spectroscopy and its application to excited-state intramolecular proton transfer

by

Myles C. Silfies

Doctor of Philosophy

in

Physics

Stony Brook University

2023

Ultrafast spectroscopy is widely used to study the dynamics of many different systems following photoexcitation. For studies of molecules, ultrafast optical spectroscopies, such as transient absorption, are very powerful, but typically limited to optically dense samples such as concentrated solutions. The lack of solvent interactions and lowered vibrational temperatures inherent to molecular beams makes gas-phase studies desirable for interpretation and comparison to ab-initio theory, but the low column densities in molecular beams precludes all-optical ultrafast spectroscopy using conventional methods. To address this measurement gap, we developed a new spectrometer using femtosecond enhancement cavities and frequency comb lasers covering almost the entire visible range with a detection limit of $\Delta\text{OD} < 1 \times 10^{-9}$, making transient absorption measurements in molecular beams possible. In this dissertation, I will discuss the development of this spectrometer and the first transient absorption measurements of molecules under variable molecular beam conditions.

To enable these measurements, I developed tunable frequency combs across a wide spectral range with high power, low phase noise, and femtosecond pulse durations at 100 MHz repetition rate. These combs are based on a custom Er- and Yb-doped fiber laser and amplifier systems combined with fiber nonlinear optics and a synchronously-pumped optical parametric oscillator. Additionally, this dissertation will describe the design, characterization, and stabilization of a femtosecond enhancement cavity with an unprecedented tuning range of 450-700 nm.

In this dissertation, I report transient absorption results on several molecules which undergo excited-state intramolecular proton transfer (ESIPT) after photoexcitation with UV light. First, I will discuss the photochromism following ESIPT in salicylideneaniline as well as the dependence of internal conversion rate on both vibrational temperature and cluster environment. These results show that nonradiative relaxation can be turned off by caging the molecule in Ar clusters without affecting the photochromic yield. I will also present results on the excited-state dynamics of 2-nitrophenol which include a competition between ESIPT, fragmentation, and intersystem crossing. Assignment of the complex spectral features is assisted by global analysis and ab-initio theory to isolate individual relaxation signals by their transition dipole moments. Comparisons to more conventional ultrafast techniques as well as theoretical simulations will also be discussed.

Contents

List of Figures vii

List of Tables xviii

Acknowledgements xix

1 Introduction 1
- 1.1 Ultrafast spectroscopy techniques 5
- 1.2 Cavity-enhanced frequency combs 6
  - 1.2.1 Frequency combs 7
  - 1.2.2 Comb-cavity coupling 9
  - 1.2.3 Bandwidth limitations due to group-delay dispersion 9
  - 1.2.4 Cavity-enhanced transient absorption spectroscopy 10

2 Er-doped fiber frequency combs and dispersive wave broadening 12
- 2.1 Introduction and motivation 12
- 2.2 Fiber nonlinear optics background 15
  - 2.2.1 Dispersion 16
  - 2.2.2 Self phase modulation 17
  - 2.2.3 Stimulated Raman scattering 18
  - 2.2.4 Solitons and dispersive waves 19
- 2.3 Experimental realization 22
  - 2.3.1 1060 nm pump branch 22
  - 2.3.2 Tunable seed branches for mid-infrared combs 28
- 2.4 Conclusion and outlook 30

3 Tunable visible frequency comb generation 32
- 3.1 Introduction 32
- 3.2 Experimental setup 34
- 3.3 Results 36
- 3.4 Conclusions 42

4 Widely tunable cavity-enhanced frequency combs 44
- 4.1 Introduction 44
- 4.2 Cavity design 45

4.3 Cavity Finesse 47
4.4 Broadband comb/cavity coupling 48
4.5 Intracavity spectral bandwidth 51
4.6 Intracavity noise 51
4.7 Conclusion 51

5 Broadband cavity-enhanced transient absorption spectrometer 53
5.1 Introduction 53
5.2 Experimental Setup 54
  5.2.1 Light Sources and Enhancement Cavity 54
  5.2.2 Vacuum System and Supersonic Expansion 56
  5.2.3 Procedure for Individual CE-TA Pump/Probe Trace Accumulation 57
  5.2.4 Constructing Transient Absorption Spectra 59
5.3 Results 60
  5.3.1 Individual CE-TA Measurements 60
  5.3.2 Independent instrument response function 62
  5.3.3 Instrument sensitivity 63
  5.3.4 Operation with a Pump Cavity 66
  5.3.5 CE-TAS Spectra 67
  5.3.6 Clusters 69
5.4 Discussion 71

6 Ultrafast internal conversion and photochromism in gas-phase salicylideneaniline 73
6.1 Introduction 73
6.2 Methods 76
  6.2.1 Experimental 76
  6.2.2 Modeling 77
  6.2.3 Theoretical Calculations 78
6.3 Results 80
  6.3.1 The Isolated Molecule 80
  6.3.2 Salicylideneaniline in Argon Clusters 84
  6.3.3 Simulated spectrum 86
6.4 Discussion 88
6.5 Conclusions 90

7 Intersystem crossing, proton transfer, and photolysis in *ortho*-nitrophenol 93
7.1 Introduction 93
7.2 Methods 96
  7.2.1 Experimental 96
  7.2.2 Modeling 96
  7.2.3 Theoretical calculations 98

7.3 Results . . . 99
7.3.1 Isolated Molecule . . . 99
7.3.2 Temperature, and carrier gas dependence . . . 101
7.3.3 Calculated transition dipole moments . . . 106
7.3.4 Calculated fragment absorption . . . 106
7.4 Discussion . . . 107
7.5 Conclusions and Future Directions . . . 110

8 Conclusion 112
8.1 The observables problem . . . 113
8.2 Outlook . . . 114

A Pre-time zero signal and global analysis 116

B Additional fits and computational methods for salicylideneaniline 120
B.1 Goodness of fit . . . 120
B.2 Computational Methods . . . 120
B.2.1 Post-processing of Non-adiabatic Molecular Dynamics Trajectories . . . 120
B.2.2 Simulation of TAS . . . 128
B.2.3 Twisted Enol spectrum . . . 130
B.2.4 Photochrome absorption simulation . . . 130

Bibliography 132

List of Figures

1.1 Schematic diagram of a pump/probe transient absorption measurement. A pump pulse (purple), excites a sample and a probe pulse (orange) records the time dependent absorption from the excited state with variable delay. 2

1.2 Overview of ultrafast spectroscopy methods. The work in this dissertation acts as the halfway point between the established techniques of transient absorption spectroscopy (top left) and time-resolved photoelectron spectroscopy (bottom right) since it shares the observable of the former and the environment of the latter. Reproduced from [1] with permission from the PCCP Owner Societies. 3

1.3 Comparison of signals recorded in, a), transient absorption spectroscopy (TAS) and, b), time-resolved photoelectron spectroscopy (TRPES). In both cases, the pump pulse excites the molecule to the first excited state. In a), the TAS signal is both positive, for excited-state absorption (ESA) and negative, for stimulated emission (SE) or ground-state bleach (GSB), and requires a broadband laser spectrum to probe. In b), the TRPES probe pulse ionizes the molecule with a high energy photon. 4

1.4 Diagram of frequency comb based on a modelocked laser in the, a), time domain and, b), frequency domain. A pulse train from the laser at a repetition rate f_{rep} generates an evenly spaced spectrum of comb "teeth" in the frequency domain separated by f_{rep}. See text for more details. 7

1.5 Diagram of comb/cavity coupling in the, a), time and, b), frequency domain. The free spectral range (FSR) of the cavity must match the frequency comb repetition rate and the f_0 of the comb must be adjusted to center as many comb teeth in cavity resonances which optimizes intracavity bandwidth and reduces noise. The group-delay dispersion of the cavity mirrors leads to changes in the cavity FSR as a function of frequency and causes the cavity resonances to walkoff from the evenly the comb teeth. 8

1.6 Simplified diagram of cavity-enhanced transient absorption spectroscopy. A gas phase sample is injected into the focus of an enhancement cavity that is coupled to the probe frequency comb. A synchronized pump pulse excites the sample and the cavity-enhanced probe signal is recorded as a function of delay. . . . 11

2.1 Overview of the laser system for mid-infrared frequency comb generation. An Er:fiber oscillator seeds two Er-doped fiber amplifiers (EDFAs) followed by nonlinear frequency shifting in fibers. One branch is shifted to 1060 nm and seeds a high-power Yb-doped fiber amplifier (YDFA) which serves as pump while the other tunable arm is the signal for the difference-frequency generation process. The two combs are sent into a nonlinear crystal where the MIR idler light is generated as the frequency difference between pump and signal. 14

2.2 Simulated spectral broadening due to SPM for various input pulse energies, neglecting dispersion. The fiber length is fixed at 2 cm, γ = 5 (W km)$^{-1}$, and the pulse duration is 100 fs FWHM. 18

2.3 Simulated soliton evolution in a nonlinear fiber shown in both the time and frequency domains. a) and b) show an N=1 soliton which remains constant in time and frequency. c) and d) show an N=3 soliton which is periodic in time and frequency. Simulation parameters: center wavelength=1550 nm, β_2 = -7.26 ps^2/km, T$_0$ = 40 fs, γ=10.5 (W km)$^-$1 20

2.4 Simulated pulse evolution of an $N = 3$ soliton in a nonlinear fiber including all dispersive and nonlinear effects discussed. The dispersive wave is generated around 0.1 m and is observable in time as the modulated side feature which trails the main pulse and in the frequency domain as the blue-shifted line near $\Delta\nu T_0 = +3$. Simulation parameters: center wavelength=1550 nm, β_2 = -7.26 ps^2/km, β_3 = 0.056 ps^3/km, T$_0$ = 40 fs, γ = 10.5 (W km)$^{-1}$. 21

2.5 Overview of high power, Yb-fiber amplified pump beam. Starting with an Er:fiber oscillator, the light is first nonlinearly amplified in an Er-doped fiber amplifier (EDFA), shifted to around 1060 nm in a highly nonlinear fiber (HNLF), and then amplified in two Yb-doped fiber amplifier stages. BPF:Band pass filter, LPF:Low pass filter. 22

2.6 Erbium doped fiber amplifier (EDFA) design and performance. a)Schematic layout of the EDFA. The blue fiber is polarization-maintaining passive fiber. Red fiber is Er-doped gain fiber: 1.5 m nLIGHT LIEKKI Er80-4/125-HD-PM. The amplifier is pumped by two 750 mW, 976 nm pump diodes each in both the counter- and co-propagating directions. WDM: wavelength division multiplexer (AFW Technologies WDM-PM-1598-L-5-0-1W). b) EDFA input and output spectra displaying the nonlinearity. Input power is 6 mW. Output power is 350 mW. c) Interferometric autocorrelation trace of optimized output pulse. FWHM duration is 45 fs. 24

2.7 HNLF output spectrum displaying the soliton at ≈2100 nm and dispersive wave at ≈1070 nm. 25

2.8 Yb-doped fiber amplifier (YDFA) design and performance. a) Schematic layout of the YDFA. The blue fiber is polarization-maintaining passive fiber. Red fiber is Yb-doped gain fiber: 2.85 m nLIGHT LIEKKI Yb300-6/125-PM. The amplifier is pumped with 1 copropagating 400 mW 976 nm pump diode via a wavelength division multiplexer (WDM). The additional WDM protects the pump diode from amplified spontaneous emission and back reflections. The photodetector (PD) is used to monitor input power for interlock purposes. b) Input ad output spectrum. The modulation on the input spectrum is due to the low pass filter (shown in Fig. 2.5) mirror coating. Input power is 4 mW. Output power is 130 mW. 26

2.9 Optical heterodyne beat note measurement at 10 kHz resolution bandwidth between amplified dispersive wave and NPRO Nd:YAG laser. 100 MHz tone is comb repetition rate. Beat notes at 30 and 70 MHz represent heterodyne mixing of Nd:YAG with the nearest comb teeth. Beat note starts to collapse at 10 kHz resolution bandwidth. 27

2.10 Yb-doped CPA performance. a) Input and output spectra. Input is measured immediately before PCF amplifier, input power is 25 mW. Output is measured following grating compresor, output power is 11.8 W. b.) Output intensity autocorrelation, demonstrating a pulse duration of 120 fs. 29

2.11 Output spectrum of the tunable EDFA/HNLF signal branch. Dispersive wave shifts to shorter wavelengths for increasing pump power. See text for details. 30

3.1 The optical layout of the synchronously pumped optical parametric oscillator. 34

3.2 Intracavity signal and idler spectra and power at different phase-matching temperatures of LBO in the synchronously pumped optical parametric oscillator. The spectrum centered at 535 nm is the residual pump. Spectra for fundamental and second harmonic are color matched. Optical powers are represented by diamonds for 1 mm BBO and crosses for 2 mm BBO ($2i$ only) and use the right axis. Reported powers for pump, $2i$, and $2s$ are OPO output while signal and idler are intracavity power levels. 36
3.3 Output spatial modes for, a.) the doubled signal and, b.) the doubled idler. Gaussian fits to the vertical and horizontal profiles for each give $1/e^2$ beam radii of $w_x = 0.62$ mm and $w_y = 0.63$ mm for the doubled signal and $w_x = 1.1$ mm and $w_y = 0.96$ mm for doubled idler. 37
3.4 Doubled signal output spectra at a single LBO crystal temperature, T = 138° C as the OPO cavity length and BBO angle are tuned. All spectra normalized to the highest signal observed in the spectrometer. Dashed vertical line indicates the signal wavelength corresponding to the optimum doubled idler center wavelength for the same temperature. 38
3.5 Normalized intensity autocorrelation traces for different visible outputs from SPOPO (solid) and Gaussian fit (black, dashed): a.) residual pump, b.) doubled signal, c.) doubled idler. Quoted pulse durations are FWHM assuming Gaussian pulse shape. 39
3.6 Relative intensity noise (RIN) of OPO pump, doubled signal, and doubled idler. 39
3.7 a.) Setup for measuring pump → $2i$ transfer function or phase noise of pump or $2i$ combs. See text for details as well as changes required for measuring $2s$ comb. SA: summing amplifier, CPL: directional coupler. b.) Pump → $2i/2s$ phase modulation transfer functions. Dashed vertical line indicates OPO cavity half-linewidth. c.) High frequency phase noise power spectral density of pump, doubled signal and doubled idler measured as well as the sum of Eq. (3.6) for comparison to $2i$ noise. 41

4.1 (a) Setup for the CAPS measurement and design of the enhancement cavity. M1 and M4 are partial reflectors (PR) and M2 and M3 are high reflectors (HR). PC: Pockels cell, LIA: lock-in amplifier (b) Theoretical mirror transmission (T) for the 2 mirrors. (c) GDD for the two mirror coatings. Black dashed line is the net cavity GDD assuming the geometry in (a). (d) Measured cavity finesse (circles). Line is theoretical finesse. 46

4.2 Schematics for locking input comb to the enhancement cavity for (a) the doubled idler and (b) the doubled signal. PZT: piezoelectric transducer, EOM: electro-optic modulator, LF: loop filter 48
4.3 (a-c) Intracavity (solid) and input (dashed) spectra for $2s$ (a), pump (b), and $2i$ (c) combs. (d) Optimized intracavity spectral widths compared with the incident width. 49
4.4 Relative intensity noise of the intracavity light. Left axis: RIN power spectral density (solid lines), right axis: integrated RIN up to 100 kHz (dashed lines). 50

5.1 a) Optical layout of the broadband cavity-enhanced transient absorption spectrometer. Tunable frequency combs are derived from a synchronously pumped optical parametric oscillator (OPO) and coupled to a 4-mirror broadband dispersion-managed enhancement cavity. The third harmonic of the Yb:fiber comb at 355 nm is used for molecule excitation in the current experiments. More details regarding the optical components are in the main text and references [2, 3]. b) OPO (dashed) and cavity-enhanced (solid) spectra across the OPO 450-700 nm tuning range. Broadband spectra are assembled from pump/probe traces recorded with different OPO wavelengths. 54
5.2 Molecular beam setup and fluorescence monitor. The fluorescence detection scheme is described in detail in the main text. Inset shows a cutaway of the nozzle assembly. The inner chamber surrounding the heated nozzle contains the sample molecule near the pump/probe overlap region. 57
5.3 a) Pulse sequence at the sample. The reference pulse records any steady-state pump/probe signal $\Delta I(5\text{ns})$ and contains nearly identical noise to the probe for common mode subtraction. b) Noise spectrum of the intracavity light and subtracted signal using 469 nm ($2s$) light. Rejection of common-mode noise using the autobalanced subtraction scheme allows for the ultrafast molecular signal to be detected at the pump modulation frequency of 4 kHz. Also shown is the shot-noise (or quantum noise) limit calculated from the measured photocurrent. 59
5.4 Molecules in the present experiments. HAN = 1'-hydroxy-2'-acetonapthone. SA = salicylideneaniline 61

5.5 Example transient absorption traces for $\lambda_{\text{probe}} = 636$ nm (a) and 494 nm(b) combs recorded from HAN excited at 355 nm. The positive signal in a) corresponds to excited-state absorption and the negative signal in b) to stimulated emission. The parallel and perpendicular polarization data are each the average of three scans with 1s integration time per pump/probe delay. Magic angle data is constructed via $\Delta S_{\text{MA}} = (\Delta S_{\parallel} + 2\Delta S_{\perp})/3$. c) Full 700 ps magic angle data showing the long decay of the transient signal including single-exponential fits (dashed black lines). 62

5.6 Spectrometer FWHM time resolution across the tuning range found by fitting the rising edge of HAN signal to an error function assuming instrument-limited response. Error bars are from fit. Points are color coded according to OPO output for doubled signal (blue), doubled idler (red), and residual pump (green). . 63

5.7 Two-photon absorption coefficient of liquid carbon disulfide measured by z-scan, reproduced from [4, 5]. The individual points correspond to experimental measurements performed by Reichert et al. and the solid line is a theoretical model. The vertical lines indicate the probe range of the spectrometer with deffective degenerate two-photon energy via (E_{pump}+E_{probe})/2. 64

5.8 Comparison of the independent instrument response function and the isolated SA signals at a) 462 nm and b) 616 nm. . . . 64

5.9 a) Allan deviation recorded using repetitive scans at 469 nm 0.5 s of integration per pump/probe delay. Without sample (triangles), the noise averages down with the inverse square root of the measurement time for as long as we have recorded data, following the dashed line with a slope of -1/2. With molecular signal, drift in the molecular column density on the ∼10 minute time scale causes the main limitation to averaging (circles), but this drift can be remedied to some extend using fluorescence normalization (diamonds). b) Two pump/probe traces taken days apart can largely be brought into coincidence using normalization to the fluorescence signal. 65

5.10 Demonstration of the effect of pump cavity operation. The pump/probe signal size recorded from of 2-(2'-hydroxyphenyl) benzothiazole at a probe wavelength of 475 nm increases approximately tenfold due to increased pump power. The single pass pump power is ≈ 500 mW and the cavity power is ≈ 8 W. 67

5.11 a) Magic-angle transient absorption map for jet-cooled HAN excited at 355 nm constructed from 12 probe wavelengths. Stimulated emission is observed on the blue side of the spectrum and excited state absorption on the red. b) Comparison of TA spectra from jet-cooled HAN (magenta) and HAN in cyclohexane (green) from reference [6] at 1 ps (solid), 5 ps (long-dashed), and 50 ps (short-dashed) delays. The solution-phase data has been multiplied by one overall scale factor to make the comparison. c) Noise-levels attained as a function of wavelength for this full TA-map measurement. Points are color coded according to OPO output for doubled signal (blue), doubled idler (red), and residual pump (green). 68
5.12 Parallel and perpendicular polarization CE-TAS data for SA excited at 355 nm in a 0.25 bar He expansion a) and 2.2 bar Ar expansion b). The polarization anisotropy transient decays much more slowly in the Ar data, indicating the formation of large Ar clusters. c) Magic angle data for the Ar expansion and He expansion compared to previous TRPES data recorded in jet-cooled SA from ref. [7]. 70

6.1 General overview of relaxation schemes for SA excited to S_1. After excitation, the excited enol can either (right side) undergo ESIPT and internally convert along the keto pathway through CI1 or (left side) remain in the enol tautomer and relax via CI2 by rotating about the central C-N bond. Bottom left and right insets are alternative ground state minima that are potential photochrome geometries which may be reached via the enol or keto relaxation pathways, repsectively. 74
6.2 CE-TAS of isolated jet-cooled SA molecule. a) Raw signals at 2 representative probe wavelengths. b) TA spectrum constructed from the individual scans. c) DAS from global fit of b) with 2 components, normalized to the maximum of A_1. A_1 and A_2 are associated with time constants of 1.8 ps and >10 ns, respectively. Individual points are at the discrete probe wavelengths which are combined for the full spectrum. The origin and meaning of pre-time-zero signals is discussed in the text. 81
6.3 Lineout comparison between TAS of the jet-cooled SA molecule and in SA in acetonitrile (ACN) for different delay times. One global scaling factor is used between the two datasets at all times. ACN data from [8]. 83

6.4 Comparison of SA dynamics under different molecular beam conditions. “Cold” data are taken with 0.1 bar He stagnation pressure, giving a supersonic expansion and jet-cooled molecules. “Hot” data are recorded from a quasi-effusive beam. The SA:Ar data are taken with 1 bar Ar stagnation pressure, forming large Ar clusters. a) $\lambda_{\mathrm{probe}} = 490$ nm. b) $\lambda_{\mathrm{probe}} = 616$ nm. 83
6.5 Rotational dynamics of isolated SA vs. SA:Ar. CE-TAS signals with pump and probe pulses parallel (red) and perpendicular (blue) for a) isolated jet-cooled SA and b) SA:Ar with 1 bar Ar stagnation pressure. $\lambda_{\mathrm{probe}} = 490$ nm. Formation of large Ar clusters around the SA molecules dramatically slows rotational dephasing. 84
6.6 CE-TAS of SA:Ar from SA seeded in 1 bar of Ar. a) Pump/probe traces at 2 representative probe wavelengths. The time axis shown changes from linear to logarithmic at 10 ps to better show the signal at the negative time delays. b) TA spectrum constructed from the individual scans. c) DAS from global fit of b) with 3 components normalized to the maximum of B_1. $\tau_{B_1} = 24$ ps, $\tau_{B_2} = 850$ ps, and $\tau_{B_3} > 10$ ns. Individual points are at the discrete probe wavelengths which were combined for the spectrum. 85
6.7 Theoretical TAS results from post-processed AIMS calculations containing a) all geometries, b) only keto geometries, and c) only enol geometries. d) DAS from a global fit of the spectrum in a). e) and f) show spectral lineouts using the right axis at 100 fs from the corresponding keto and enol spectra, respectively. See text for details regarding resampling and convolution with experimental resolution. 86
6.8 Proposed relaxation mechanism and photochrome pathway in a) isolated SA and b) SA:Ar. Dashed lines indicate absorption of light and solid lines are emission. Labels indicate DAS features from global analysis. In the isolated molecule, a), the initially excited enol undergoes ESIPT and generates the keto tautomer with a wide range of internal energies. The hottest of which immediately internally convert to CI1 and isomerize to the photochrome. The colder population in the relaxed fluorescent state also decays via CI1, but eventually returns to overall enol ground state. In SA:Ar, b), the the presences of the Ar cage slows down photochrome generation ($\sim 0 \rightarrow 24$ ps) and traps the vibrationally cold keto population such that it can only decay radiatively (1.8 ps $\rightarrow > 1$ ns). 91

7.1 a) *ortho*-nitrophenol b) *aci*-nitrophenol 93

7.2 Dominant relaxation pathways proposed by Xu et al. [9]. Red lines indicate ISC and black lines are internal conversion. ONP photoexcited to S_1 rapidly undergoes ISC followed by internal conversion to T_1 where it either converts back to the ground state, remains trapped, or undergoes ESIPT. 94
7.3 TA of isolated ONP a) Full MA spectrum recorded in 0.3 Bar stagnation pressure of He. b) DAS from global analysis fit with 4 components. Note that the amplitude of A_4 is multiplied by 10. 100
7.4 TA signals with pump/probe relative polarizations parallel, perpendicular, and at the magic angle. Magic angle data is orientation-averaged whereas the polarized signals reveal transition dipole moment information. Recorded at probe wavelengths of, a), 473 nm, b), 509 nm, c), 696 nm. 102
7.5 Comparison of MA TA signals in the gas-phase isolated molecule vs solution-phase measurements in n-hexane from [10]. Comparisons at probe wavelengths of, a), 473 nm, b), 572 nm and, c), 696 nm. Scans are scaled to make the peak positive signals the same. 103
7.6 ONP rotational anisotropy. a) Experimental signal b) Model anisotropy from global analysis of polarized signals. For more details see text. 104
7.7 Dependence of signal on rotational temperature for hot (≈ 365K) and jet-cooled (≈ 80K). Scans recorded at probe wavelength of, a), 472 nm and, b), 626 nm 104
7.8 Comparison of isolated ONP signal with dynamics in the clustered ONP:Ar system. Isolated signals recorded in 0.3 Bar stagnation pressure of He. ONP:Ar signal recorded with 2.6 Bar Ar stagnation pressure. Scans recorded at probe wavelengths of, a), 455 nm and, b), 581 nm. 105
7.9 Parent fragment structures from Vereecken et al. [11] and using their notation in black text, with absorption summarized in Table 7.3. Additionally, similar structures from Guo et al. are labeled in blue with absorption summarized in Table 7.4. . . . 108

A.1 Illustration of origin of negative delay signal. The sample is pumped at $f_{\text{rep}} = 100$ MHz. Each excitation pulse launches a bi-exponential decay molecular response (colored lines) with $\tau_1 = 0.2$ ns and $\tau_2 = 20$ ns $= 2/f_{\text{rep}}$. The CE-TAS signal $\Delta S(\tau)$ is constructed from the difference between the total cumulative steady state change in absorbance signal ΔI sampled at the probe pulses (red dots) and the reference pulses (orange dots) via equation (A.1). For molecules with signals with lifetimes on the order of $1/f_{\text{rep}}$ or longer, this can lead to nonzero signals before time zero, as illustrated in Fig. A.2. 117

A.2 CE-TAS signal ΔS corresponding the scenario of Fig. A.1. A sizable negative signal is seen before time zero. 117
A.3 Single scan fit at 455 nm with isolated time constant contributions using equation A.4. 118

B.1 2 component parallel fit model on isolated SA. a) Experimental spectrum. b) Spectrum returned from fit. c) DAS from b). . . 121
B.2 3 component parallel fit model on isolated SA. a) Experimental spectrum. b) Spectrum returned from fit. c) DAS from b). . . 122
B.3 2 component parallel fit model on SA:Ar. a) Experimental spectrum. b) Spectrum returned from fit. c) DAS from b). 123
B.4 3 component parallel fit model on SA:Ar. a) Experimental spectrum. b) Spectrum returned from fit. c) DAS from b). 124
B.5 4 component parallel fit model on SA:Ar. a) Experimental spectrum. b) Spectrum returned from fit. c) DAS from b). 125
B.6 Isolated SA spectral lineouts including corresponding 2 component fit traces. 126
B.7 SA:Ar spectral lineouts including corresponding 3 component fit traces. 127
B.8 Raw, unconvolved simulated spectrum. a) ESA b) SE c) total signal. 128
B.9 Theoretical TAS from enol geometries with central CN twist angles of $< 140°$, indicative of the CN twist relaxation mechanism via CI2. Note that the maximum amplitude shown here is more than an order of magnitude smaller than the main spectral features on the full spectrum in the main text. 131
B.10 Ground-state absorption from twisted enol and keto photochrome candidates using optimized geometries from [12]. 131

List of Tables

2.1 Comparison of relevant laser parameters between a conventional ultrafast laser and the frequency comb system described in this chapter. 13

7.1 Summary of fit results for global analysis of the MA and polarized signals. 100
7.2 Calculated transition center wavelengths and initial anisotropy, r_0, for potential stimulated emission signals in geometries relevant to the relaxation of ONP. Column 2 indicates the isomer of nitrophenol, either *ortho-* or *aci-* as shown in Fig. 7.1. Geometries are from [9, 13] using their naming conventions. . . . 107
7.3 Summary of transitions found near the experimental probe range for parent aromatic fragments producing HONO, OH, or NO. Geometries are from [11] and are shown in Fig. 7.9. 108
7.4 Summary of transitions found near the experimental probe range for parent aromatic fragments producing HONO, OH. Geometries are from [14] and are shown in Fig. 7.9, labeled in blue. . 109

Acknowledgements

I certainly would not have been able to do all of this alone. I would like to thank my advisor, Tom Allison, for being a constant mentor and motivator. I have always appreciated his intensity and integrity as well as his willingness to get down in the trenches with us to see the work through.

I want to thank Yuning Chen for showing me the ropes and being patient while I slowly dismantled her experiment. I would like to thank Grzegorz Kowzan for forcing me to think with equations and being a constant sounding board for ideas. I also want to thank the rest of the CE-TASers – Neomi Lewis, Ryan Hou, Rudy Popper, Wangshu Wen, and Steven Carnevale – for sticking it out and helping to keep all the plates spinning. I want to thank Alice Kunin, Sergey Chernov, Zach Withers, Yuanchi Qing, Chris Corder, Jin Bakalis, and the rest of the Allison lab members for the many years of good times in the lab and for letting me bounce ideas and frustrations off of all of you.

Outside the group, I want to thank Arshad Mehmood, Ben Levine, Tom Weinacht, and the rest of the observables collaboration for the ideas and support. I also want to acknowledge my fellow basement dwellers – in both chemistry and physics – for being a constant source of support and fun. Lastly, I would like to thank my housemates – Ivan, Matt, and Brian – for keeping me sane all these years.

Chapter 1

Introduction

Ultrafast spectroscopy is used to study the dynamics of photoexcited systems on attosecond to nanosecond time scales and is regularly used across physics, chemistry, biology, and material science. On these ultrashort time scales one can probe the motion of electrons, atoms, molecular vibrations and bond breaking. The broad idea behind ultrafast spectrometers is portrayed in Fig. 1.1, using transient absorption spectroscopy (TAS) as an example. An ultrashort pulse, referred to as the "pump" excites a sample and after some variable time delay, a second optical pulse hits the sample and records snapshots of the time-dependent dynamics initiated by the pump. In the case of TAS, as shown in Fig. 1.1, the optical intensity of the probe pulse itself is measured as a function of time, but other experimental observables are also common as will be discussed below.

In polyatomic molecules, the ultrashort events being studied result in broad spectral features, due to the large number of degrees of freedom typically involved in the dynamics as well as the time-frequency uncertainty principle. Understanding these "blobs" in the frequency domain is difficult. Therefore standard ground-state absorption techniques do not provide a clear picture of the underlying dynamics. This necessitates using ultrafast techniques in an attempt to assign dynamic processes by directly measuring the time-dependent signal and attempting to parse the signal in the time domain.

Despite significant technological advancements, understanding ultrafast spectroscopy signals is still not straightforward and theory and experiment often struggle to agree. One reason for this is limitations intrinsic to the spectroscopic techniques, which can lead to recorded signals not always directly corresponding to a molecular events. Like any measurement, ultrafast spectrometers necessarily project complex dynamics onto more simple observables which are then interpreted to form a "picture" of what really happened. This can result in different experimental techniques arriving at different conclusions for the same system. Put another way, the decay of a measured ultrafast signal, and its time constant from an exponential fit, does not always correspond to the lifetime of some molecular state and may, instead, be dependent on the measurement technique used to probe the dynamics.

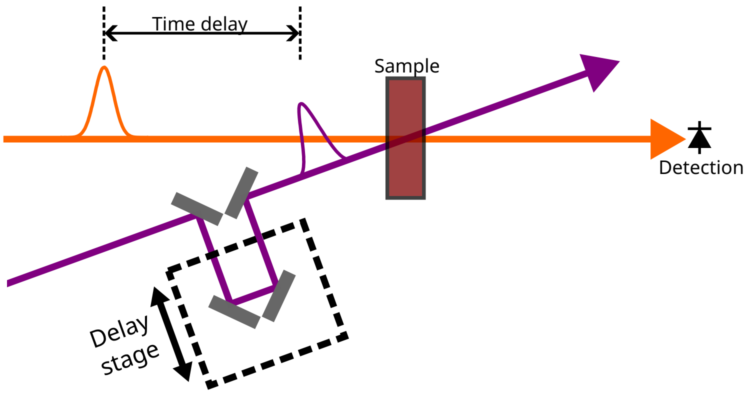

Figure 1.1: Schematic diagram of a pump/probe transient absorption measurement. A pump pulse (purple), excites a sample and a probe pulse (orange) records the time dependent absorption from the excited state with variable delay.

In a pump/probe measurement, the time-dependent excited state $\Psi(t)$ is measured by projecting it onto a final state,Ψ_f, with a probe pulse:

$$S_f(t) \propto |\langle\Psi_f|\hat{\mu}|\Psi(t)\rangle|^2 \tag{1.1}$$

where $\hat{\mu}$ is the dipole operator. In order to piece together a more accurate picture of the underlying ultrafast dynamics, the same system must be projected onto different final states and a consistent picture must be formed. Unfortunately, this is not often done due to the large differences between the common ultrafast spectroscopic techniques.

A summary and comparison of two of the current tools available in the ultrafast toolbox is shown in Fig. 1.2. In the solution phase, optical measurements such as transient absorption spectroscopy (TAS) [15] or two-dimensional spectroscopy measure excited-state dynamics via direct absorption or emission of the probe light from the excited state. In this case, the final state, Ψ_f, is a state of the neutral molecule. Alternatively, to study dynamics in the gas phase, time-resolved photoelectron spectroscopy (TRPES) is typically used [16,17]. In TRPES, the probe pulse ionizes the sample, and the ejected photoelectron or photoion yield and/or energy distribution is measured as a function of delay. The final state in a TRPES measurement is a cation + electron state. Comparing between the results of these two measurements is very difficult as they have both a different sample environment – solution vs. gas phase – and a different probe signal – optical absorption vs. photoionization.

Theoretical simulations can assist with understanding recorded ultrafast spectroscopic signals but often these approaches calculate the excited state without including the measurement conditions [18]. Recent trends in the ultrafast community have shown that performing the same projection in theoretical sumulations as the measurement technique as in Eqn. (1.1) is important for direct comparison with experimental signals [19–25]. In the case of TRPES measurements, simulating the ionization process typically requires

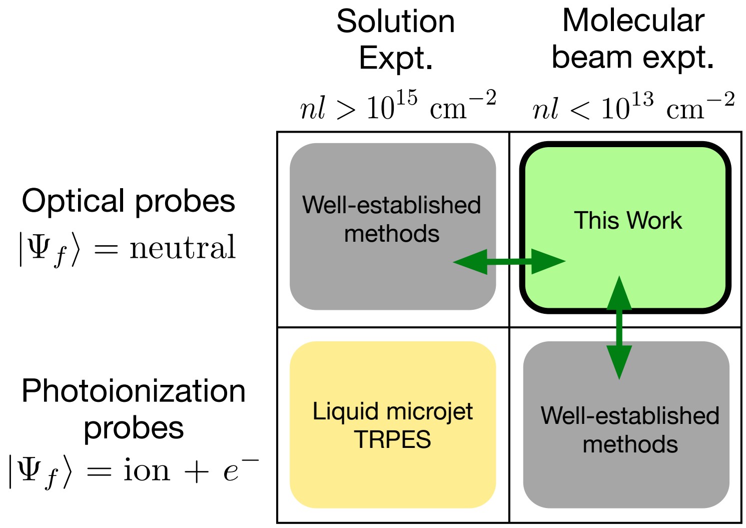

Figure 1.2: Overview of ultrafast spectroscopy methods. The work in this dissertation acts as the halfway point between the established techniques of transient absorption spectroscopy (top left) and time-resolved photoelectron spectroscopy (bottom right) since it shares the observable of the former and the environment of the latter. Reproduced from [1] with permission from the PCCP Owner Societies.

calculating Dyson orbitals to approximate the ionic states and electron in the continuum [26,27]. The simulation of TAS measurements does not require any Dyson orbital projections since the final state being probed is still the neutral molecule, but simulating solution-phase TAS measurements also presents difficulties, due to the complications involved simulating the solvent interactions properly [28, 29]. Fortuitously, these solvent effects are clearly not required when simulating gas-phase TRPES measurements.

Previously, our group demonstrated optical pump/probe measurements operating in dilute molecular beams using frequency comb lasers and femtosecond enhancement cavities [30]. These cavity-enhanced transient absorption (CE-TA) measurements had a detection limit of $\Delta\text{OD} = 2 \times 10^{-10}$ and a 120 fs time resolution. This new technique shares the environment with TRPES and the optical probe of TAS, i.e. the top right square of Fig. 1.2. Additionally, this method bypasses some of the theoretical challenges described above since it does not require the simulation of either solvent effects or Dyson orbitals.

The initial CE-TA demonstration experiment was at a single, degenerate pump/probe wavelength. To be able to parse the nonlinear signal from complex ultrafast molecular dynamics, a broadband spectrometer is required. In this dissertation I will describe the development and application of this new instrument which operates in the near ultraviolet (UV) and visible spectral ranges.

To accomplish this goal, significant technological advancements were required which will be described in detail in this dissertation. Specifically, Chap-

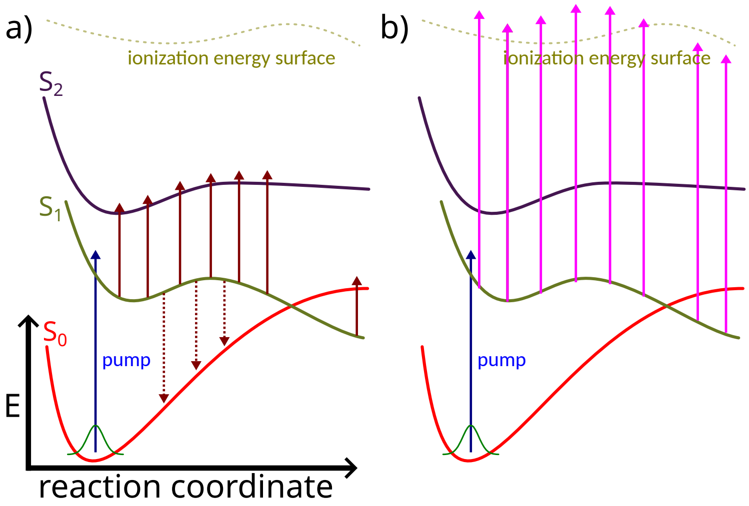

Figure 1.3: Comparison of signals recorded in, a), transient absorption spectroscopy (TAS) and, b), time-resolved photoelectron spectroscopy (TRPES). In both cases, the pump pulse excites the molecule to the first excited state. In a), the TAS signal is both positive, for excited-state absorption (ESA) and negative, for stimulated emission (SE) or ground-state bleach (GSB), and requires a broadband laser spectrum to probe. In b), the TRPES probe pulse ionizes the molecule with a high energy photon.

ter 2 will discuss the development of a high power frequency comb based on Er:fiber laser technology and fiber-based nonlinear optics. This comb serves as the backbone for further nonlinear optics for the experiments described in this dissertation and for future spectroscopy goals. Chapter 3 describes a scheme for the generation of tunable visible frequency combs which serve as the probe for the broadband CE-TA spectrometer. To enhance the nonlinear signal in the pump/probe measurement, Chapter 4, introduces a tunable femtosecond enhancement cavity and broadband comb/cavity stabilization schemes which operates from 450 to 700 nm.

Chapter 5 describes the broadband spectrometer in its entirety including overall performance and first measurements on gas-phase molecular dynamics. Additionally, Chapters 6 and 7 present molecular dynamics results in two excited-state intramolecular proton transfer (ESIPT) systems studied using the new spectrometer. Chapter 6 investigates photochromism after ESIPT in salicylideneaniline and its dependence on sample environment and temperature along with detailed comparisons to simulated TAS spectra. In Chapter 7, the complex competition between ESIPT, internal conversion, and intersystem crossing in *ortho*-nitrophenol is discussed.

1.1 Ultrafast spectroscopy techniques

As discussed above, the two main approaches for measuring ultrafast dynamics are with optical absorption or action-based methods like photoionization. Here, I focus more specifically on the two most common techniques, one from each approach, for measuring electronic excited-state dynamics in molecules – TAS and TRPES. To better illustrate the recorded signals and limitations of each measurement, a diagram comparing the signals recorded in each case is shown in Fig. 1.3. The vertically displaced curves indicate different singlet electronic potential energy surfaces, labeled S_0-S_2, of the neutral molecule along an effective molecular reaction coordinate

For the work covered in this dissertation, all ultrafast dynamics are being probed after electronic excitation, depicted by the pump pulse in Fig. 1.3 which excites the molecule from the ground state. In the Franck-Condon approximation, this excitation vertically translates a nuclear wavefunction made up of eigenstates of the S_0 potential energy surface to the first excited, S_1, potential energy surface [31]. Since this vertically translated wavefunction is not an eigenstate of the new potential energy surface, dynamics occur on the excited state which can lead to changes in the molecular geometry along the simplified reaction coordinate. These changes, represented by the distribution of the wavefunction on the excited state, $\Psi(t)$, are being measured by the probe pulse in the pump/probe measurement, as in Eqn. (1.1). The crossing point between S_0 and S_1 represents a conical intersection, a degeneracy point between two states which can facilitate rapid depopulation of the upper state nonradiatively via internal conversion.

In transient absorption spectroscopy, shown in Fig. 1.3a), the probe is a second optical excitation to another state of the neutral molecule [15, 32]. These excitations, shown as maroon arrows in Fig. 1.3a), are either excited-state absorption (ESA) from S_1 to S_2, shown via solid arrows, or stimulated emission (SE) from S_1 back down to S_0, shown as dashed arrows. In the latter case, the TAS signal is an increase of probe light, which is presented as a negative signal in this work by our convention of plotting absorption via:

$$\Delta\mathrm{OD} = \log_{10}\left(\frac{I_0}{I_T}\right) \approx -\log_{10}(e)\left(\frac{\Delta I}{I_0}\right) \tag{1.2}$$

where I_0 is the incident probe intensity, I_T is the transmitted intensity, and $\Delta I = I_T - I_0$ is the change in intensity. The approximation in Eqn. (1.2) is only valid for small changes in intensity. In addition to ESA and SE, TAS can also record a decrease in absorption from the ground state caused by the pump called a ground-state bleach (GSB) which is also negative.

Understanding the signal recorded from TAS can be quite complicated [33]. First, in order to see a signal, there must be an electronic state at a nearby energy which satisfies the necessary selection rules for ESA or SE, i.e. the maroon arrows in Fig. 1.3 need to be able to reach another potential energy surface and the transition must be allowed. As the dynamics continue, signals can disappear because the two states diverge and not because the excited-state population has decreased by some other means. To overcome this drawback, broadband probe pulses must be used which span the ultraviolet to near infrared [24, 34]. In TAS, both positive and negative signals can be recorded, resulting in potentially overlapping features which can obscure the underlying dynamics. Typically, fitting techniques like global analysis [35–37] must be used to parse out these features.

In time-resolved photoelectron spectroscopy, the probe pulse ionizes the molecule and the ejected electron and/or remaining cation is recorded as the signal [38,39]. The pump/probe scheme for a TRPES measurement is shown in Fig. 1.3b). After the pump pulse, a high-energy probe pulse excites an electron to the continuum, as shown by the long fuchsia arrows from S_1 to above the ionization potential surface. The probe pulse in TRPES does not need to be tunable or broadband like in TAS; just the photon energy needs to be sufficiently high to ionize the sample for all relevant geometries. Additionally, the selection rules in TRPES are relaxed for the ionization step, i.e. dark states can be probed. If the probe energy is too low, "energy windowing" effects can artificially reduce time constants recorded in TRPES experiments [19, 20, 23, 40]. This effect is demonstrated in Fig. 1.3b). As the reaction coordinate increases, probe excitation arrows no longer reach the ionization surface and the signal disappears. Often, the probe step in TRPES is actually a multiphoton process driven by a laser with lower photon energy, which can also affect the measured time constants [41].

1.2 Cavity-enhanced frequency combs

Cavity enhancement is commonly used to increase the sensitivity of linear spectroscopic signals, where the sample only interacts with a single electric field, such as in the techniques of cavity ringdown spectroscopy [42–44] and direct cavity-enhanced direct frequency comb spectroscopy [45–48], to perform gas-phase absorption measurements or trace-gas detection. For light circulating in an enhancement cavity, the absorption enhancement for any spectroscopic signal in the cavity is proportional to the cavity finesse, $\mathcal{F}$, defined as:

$$\mathcal{F} = \frac{\pi\sqrt{r_1 r_m}}{1 - r_1 r_m} \approx \frac{2\pi}{[\text{cavity loss}]}, \tag{1.3}$$

where r_1 and r_m are the field reflection coefficients for the input coupler mirror and the effective reflection for the rest of the cavity, respectively and the approximation assumes high-reflectivity mirrors. For a two-mirror cavity with identical mirrors or an impedance-matched ring cavity, $r_m = r_1$ and the absorption enhancement is $\mathcal{F}/\pi$. For a more detailed discussion of optical cavity energy relations and signal enhancement, see [49, 50].

In order to perform ultrafast spectroscopy, optical pulses must be used which are short in the time domain and, by Fourier transform and the time-

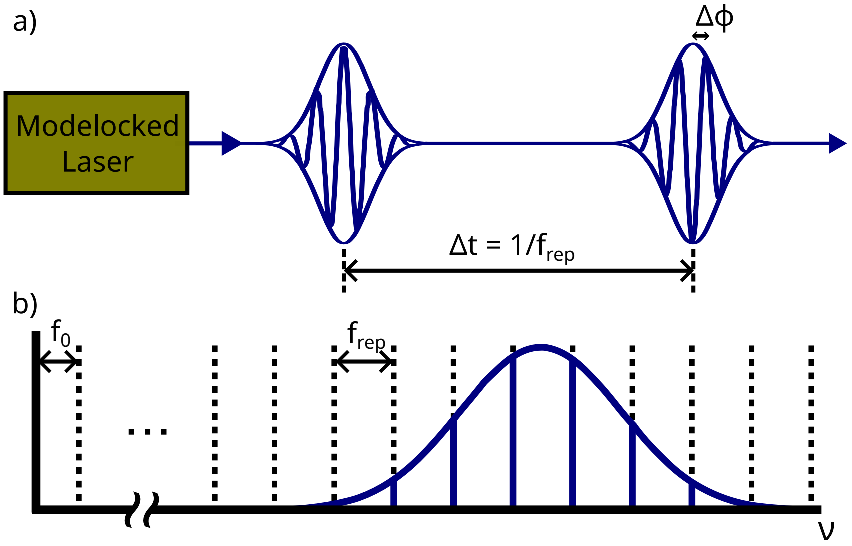

Figure 1.4: Diagram of frequency comb based on a modelocked laser in the, a), time domain and, b), frequency domain. A pulse train from the laser at a repetition rate f_{rep} generates an evenly spaced spectrum of comb "teeth" in the frequency domain separated by f_{rep}. See text for more details.

frequency uncertainty principle, inherently broad in the frequency domain [51]. For reasons which will become clear in section 1.2.2 below, in order to enhance an ultrafast pulse train in a cavity, the pulse train must be derived from a low-noise frequency comb laser. Although this ultrafast measurement is a nonlinear spectroscopy, where the sample interacts with multiple electric fields, the same absorption enhancement of $\mathcal{F}/\pi$ applies. This is because the probe measurement can be thought of as a linear absorption measurement recorded from an excited sample.

1.2.1 Frequency combs

Since their advent, frequency combs have become useful across spectroscopy, metrology, and sensing [52–54]. Most often, a frequency comb is generated from a stabilized pulse train from a mode-locked laser, as shown in Fig. 1.4. In the time domain, as in Fig. 1.4a), the oscillator operating at a repetition rate of f_{rep} emits pulses separated in time by $1/f_{\text{rep}}$. The carrier envelope offset (CEO) phase of the pulse advances with respect to the previous pulse by $\Delta\Phi$. In the frequency domain, Fourier transforming the pulse train results in a spectrum of evenly-spaced, narrow linewidth comb "teeth" as shown in Fig. 1.4b). The teeth are separated by f_{rep} and shifted from DC by an offset frequency, f_0. In this way, the optical frequency, ν_n, of the n$^{\text{th}}$ tooth can each be defined by the simple relation,

$$\nu_n = n f_{\text{rep}} + f_0, \tag{1.4}$$

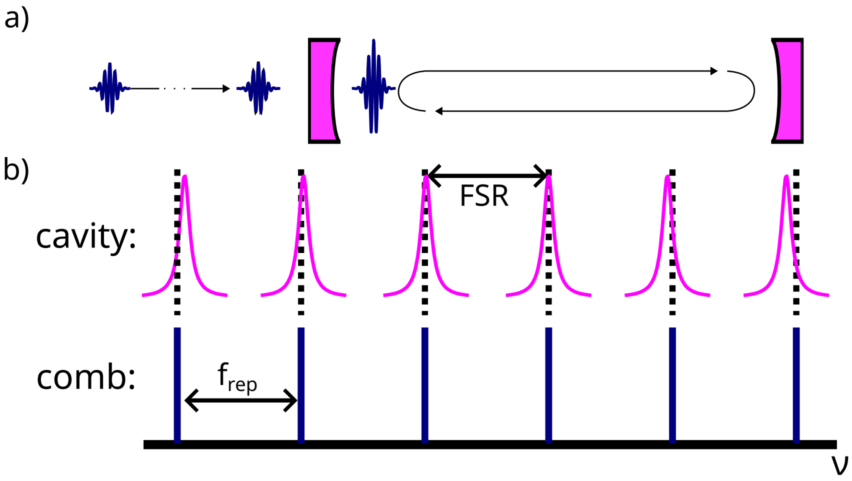

Figure 1.5: Diagram of comb/cavity coupling in the, a), time and, b), frequency domain. The free spectral range (FSR) of the cavity must match the frequency comb repetition rate and the f_0 of the comb must be adjusted to center as many comb teeth in cavity resonances which optimizes intracavity bandwidth and reduces noise. The group-delay dispersion of the cavity mirrors leads to changes in the cavity FSR as a function of frequency and causes the cavity resonances to walkoff from the evenly the comb teeth.

where f_0 is related to the CEO phase advance via

$$f_0 = \frac{\Delta\Phi}{2\pi} f_{\text{rep}}. \tag{1.5}$$

The width of the comb teeth is dominated by optical phase and frequency noise of the original laser [55, 56]. Although the work in this dissertation only involves modelocked laser frequency combs, these same relations hold for combs generated from quantum cascade lasers [57,58], microresonators [59,60], and electro-optic combs [61, 62].

The utility of the frequency comb is in controlling and/or stabilizing f_{rep} and f_0, which are typically electronically countable radio frequencies, and getting a “free” multiplication of $n \approx 10^5 - 10^7$ to an optical frequency. This control is achieved via actuators in the modelocked oscillator to provide feedback on the two degrees of freedom. Typically, these values are stabilized to atomic references or clocks to use the comb as a “standard ruler” for precision measurement [63,64]. Alternatively, two frequency combs can be referenced to each other to perform dual comb spectroscopy [65], which can be thought of as Fourier transform spectroscopy without the use of mechanical delay stages. Here, we require a frequency comb laser to couple to an enhancement cavity and match the cavity resonance frequencies.

1.2.2 Comb-cavity coupling

A simple schematic of coupling a frequency comb to an enhancement cavity is shown in Fig. 1.5. To coherently build up a pulse in the time domain, as in Fig. 1.5a), the total round-trip time for a pulse circling the cavity must equal the time spacing between input pulses. To match subsequent pulses from an input comb at repetition rate f_{rep}, the total round-trip cavity length must be $\ell = c/f_{\text{rep}}$. In the frequency domain, shown in Fig. 1.5b), an enhancement cavity has resonances with a free spectral range (FSR) of c/ℓ, with c, the speed of light [49]. To couple a frequency comb to the cavity, the cavity FSR must match the repetition rate of the incoming comb, as shown in Fig. 1.5b). In most cases, this must be done via active feedback to the comb f_{rep} and/or cavity length. In addition to f_{rep}, the frequency comb f_0 must also be controlled to match the round trip phase offset of the cavity in order to couple as much of the frequency comb spectrum into the cavity as possible [50,66,67]. This round trip phase is not zero due to cavity mirror coatings and the Guoy phase at the cavity focus [49,68].

The cavity places restrictions on the incoming frequency comb performance. For low-noise comb-cavity coupling, the comb tooth linewidth should be less than the enhancement cavity mode width, as is the case in Fig. 1.5b). The cavity mode linewidth FWHM, $\Delta\nu_{1/2}$, is related to the cavity finesse and FSR via

$$\Delta\nu_{1/2} = \frac{\text{FSR}}{\mathcal{F}}, \tag{1.6}$$

which means that for a fixed FSR, higher finesse cavities require quieter input combs.

1.2.3 Bandwidth limitations due to group-delay dispersion

The group-delay dispersion (GDD) of the enhancement cavity mirrors limits the simultaneous optical bandwidth which can be in the cavity. This effect is demonstrated in Fig. 1.5b), where the comb teeth and cavity resonances are not all perfectly lined up. The frequency comb teeth are perfectly spaced by f_{rep} but the cavity FSR only applies locally. The mirror coating GDD causes the FSR to change as a function of the optical frequency, leading to walkoffs in comb-cavity mode overlap. The sensitivity to the mirror GDD increases with increasing cavity finesse, meaning that higher finesse cavities require lower total GDD to enhance the same simultaneous bandwidth.

The effect of GDD also influences the design of the tunable spectrometer in this dissertation. Typically, in modern transient absorption spectrometers, a broadband probe pulse covering the entire visible spectral region is generated via supercontinuum generation. The whole spectrum is then measured simultaneously with a frequency resolving detector, such as a grating spectrometer, as a function of delay [24,34]. To cavity enhance such a broadband spectrum, the GDD of the cavity mirror coatings would need to be impossibly small. When coupling a comb to the cavity, the two degrees of freedom of the comb can be used to compensate for zeroth and first-order dispersion, therefore the total round-trip phase shift, δ is dominated by group-delay dispersion which takes the form [51]:

$$\delta = \frac{1}{2}\psi_2(\omega-\omega_0)^2 = 2\pi^2\psi_2(\Delta\nu)^2 \tag{1.7}$$

where $\psi_2 = \frac{\partial^2\psi}{\partial\omega^2}$ is the total GDD of the mirror coatings evaluated at the central frequency and $\Delta\nu$ is the spectral bandwidth. For light in an enhancement cavity, ignoring any wavelength-dependent reflectivity, the circulating intensity, I_c, relative to the input intensity, I_0, is proportional to the round-trip phase shift via [49, 69]:

$$\frac{I_c}{I_0} \propto \frac{1}{1+4(\mathcal{F}/\pi)^2\sin^2(\delta/2)} \approx \frac{1}{1+4\pi^2\mathcal{F}^2\psi_2^2\Delta\nu^4}. \tag{1.8}$$

where the approximation assumes only small phase variation entirely due to GDD. The maximum tolerable GDD to support a half width at half maximum intracavity spectrum can be found by setting the right hand side to 1/2 and solving for the required GDD:

$$\psi_2 = (2\pi\mathcal{F}\Delta\nu^2)^{-1}. \tag{1.9}$$

Assuming a frequency comb with a bandwidth of 240 Thz, and a cavity with a finesse of 1000, the cavity mirrors would need to have a total GDD of less than .01 fs^2 which is not possible to manufacture with current technology [70]. This forces the instrument to be tunable rather than simultaneously broadband. For a more reasonable bandwidth of 2.2 THz, corresponding to an approximately 200 fs transform-limited pulse, the cavity mirrors would require a net GDD of less than 130 fs^2 which is achievable with current mirror coating technology. Therefore, we must record our transient absorption spectra using sequential scans from narrowband probe pulses and combine the signals between wavelengths. In this way, we record a spectrum with the same total bandwidth of 240 THz, but constructed from many spectra each with ≈2.2 THz bandwidth.

Additionally, the walkoff in comb and cavity mode overlap leads to increased amplitude noise on the intracavity light. For comb teeth that are not centered on cavity modes, any frequency noise is turned into amplitude noise by the slope of the cavity resonance. The effect of GDD is discussed more in Chapter 4 and also in [69].

1.2.4 Cavity-enhanced transient absorption spectroscopy

Typically, the cavity enhancement of frequency combs is done to allow for simultaneous broadband spectroscopy of gases [47, 54]. Here, we take advantage of the fact that the stabilized comb in the enhancement cavity is still a

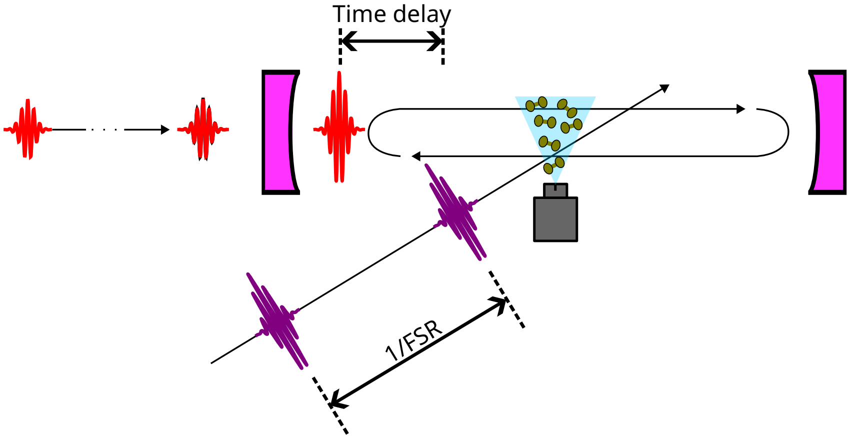

Figure 1.6: Simplified diagram of cavity-enhanced transient absorption spectroscopy. A gas phase sample is injected into the focus of an enhancement cavity that is coupled to the probe frequency comb. A synchronized pump pulse excites the sample and the cavity-enhanced probe signal is recorded as a function of delay.

circling pulse train and can be used for ultrafast measurements. The overall concept is shown in Fig. 1.6 in a simplified diagram. A gas-phase sample is injected into the middle of an enhancement cavity via a molecular beam. A frequency comb laser is coupled to the enhancement cavity which serves as the probe in the transient absorption measurement. A time-synchronized pulse is crossed through the molecular beam which excites a small fraction of the molecules which the cavity-enhanced probe measures. In this way, the same absorption enhancement factor of $\mathcal{F}/\pi$ applies the nonlinear pump/probe signal [30]. The signal enhancement can also be understood in terms of four-wave mixing of frequency combs [71] More details on the actual spectrometer and its performance are included in Chapter 5.

Chapter 2

Er-doped fiber frequency combs and dispersive wave broadening

2.1 Introduction and motivation

To perform spectroscopy, a light source is needed that matches a corresponding electronic, vibrational, or rotational transition in the sample, i.e. you need to tune the laser wavelength to be on resonance. Although the bulk of the work discussed in this dissertation focuses on electronic excitations in the near-to-mid UV(200 - 400 nm) and visible (400-700 nm) spectral ranges, a major motivation for the cavity-enhanced ultrafast spectrometer is in the mid-infrared (MIR). A scientific goal has been to perform two-dimensional infrared (2DIR) spectroscopy of water clusters and other hydrogen bonded systems [30, 71]. The linear absorption spectra of both $(H_2O)_n$ and $(D_2O)_n$ clusters for n=2-6 was measured previously in a molecular beam using cavity ring-down spectroscopy [72, 73]. The optical transitions of interest are in the range of 3.1 to 4.2 μm. Generating light in this spectral region is nontrivial even for conventional laser systems.

Due to the low sample density in molecular beams, the 2DIR measurement must be cavity enhanced. As discussed in Chapter 1, cavity-enhanced ultrafast spectroscopy uses frequency combs. Frequency comb technology is mature in the near-infrared based on mode-locked fiber lasers with Yb- and Er-doped gain media which operate around 1030 and 1550 nm, respectively [74, 75]. These wavelengths are far from the MIR spectroscopy goal, so we must use nonlinear optics to generate light in more relevant spectral ranges. Additionally, tunable frequency comb sources are generally useful both in spectroscopy and time frequency transfer. Since an enhancement cavity converts optical phase and frequency noise to amplitude noise [49], care must be taken to ensure not only that the initially generated comb is low noise but also that any nonlinear frequency conversion does not add significant noise.

The enhancement cavity also places limits on the repetition rate of the frequency comb. As discussed in Chapter 1, the cavity free spectral range is

	“Typical” Ti:saph laser	Allison group fiber frequency comb
Repetition rate	1-10 kHz	100 MHz
Average power	1-10 W	10 W
Energy per pulse	1 mJ	100 nJ
Pulse duration	30 fs	100 fs
Peak power	33 GW	1 MW

Table 2.1: Comparison of relevant laser parameters between a conventional ultrafast laser and the frequency comb system described in this chapter.

c/ℓ, which must match the laser repetition rate. For a cavity with a reasonable length of .5 to 5 meters, which will easily fit in vacuum chambers, the corresponding laser repetition rate must be 600 to 60 MHz. Lower repetition rates reduce the duty cycle of the experiment and require long cavities which are more difficult to stabilize for a given finesse due to the decreased cavity linewidth described in Chapter 1. Higher repetition rates reduce the attainable laser peak intensity, which makes driving nonlinear optical processes more difficult. Here, we choose a 100 MHz repetition rate which is a middle ground between the two extremes – with both reasonable peak intensities and attainable noise constraints.

An electric field, $\mathbf{E}$, in a medium induces a polarization density, $\mathbf{P}$, proportional to the incident field via:

$$\mathbf{P} = \epsilon_0 \left[\chi^{(1)}\mathbf{E} + \chi^{(2)}\mathbf{EE} + \chi^{(3)}\mathbf{EEE}\right] \tag{2.1}$$

Where $\chi^{(n)}$ is the n^{th}-order susceptibility tensors which are intrinsic to the material. At low powers, $\mathbf{P}$ is linear with the input field which results in, for a linear isotropic medium, the index of refraction, $n = \sqrt{(1+\chi^{(1)})}$. For increasing electric field strengths, the higher-order terms must be included which lead to mixing of frequencies and the generation of new frequency components. These nonlinear effects scale strongly with powers of the input electric field strength, as can be seen in Eqn. (2.1). Second order effects, proportional to $\chi^{(2)}$ are responsible for the more commonly encountered nonlinear processes such as second harmonic generation (SHG) and sum or difference frequency generation (SFG, DFG). $\chi^{(2)}$ is only present in materials which lack inversion symmetry like BBO, LBO, and other common nonlinear crystals. $\chi^{(3)}$, however, is present in all materials, including optical fibers, and is responsible for several nonlinear effects such as self-focusing and self-phase modulation [76,77]. More details of the third order nonlinearities encountered in optical fibers will be discussed below in section 2.2.

For most ultrafast spectroscopy labs, tuning the wavelength via nonlinear optics is relatively easy due to high peak intensities of most conventional ultrafast lasers. A “typical” approach is to use a titanium-sapphire (Ti:saph) laser and amplifier system generating mJ-level pulses at a repetition rate of 1-10 kHz resulting in GW peak powers [78]. For the work discussed in this

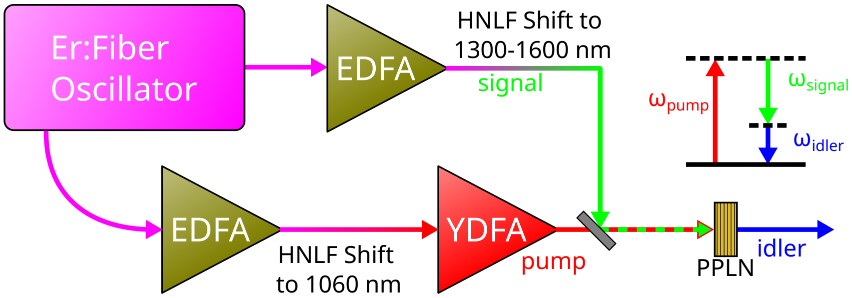

Figure 2.1: Overview of the laser system for mid-infrared frequency comb generation. An Er:fiber oscillator seeds two Er-doped fiber amplifiers (EDFAs) followed by nonlinear frequency shifting in fibers. One branch is shifted to 1060 nm and seeds a high-power Yb-doped fiber amplifier (YDFA) which serves as pump while the other tunable arm is the signal for the difference-frequency generation process. The two combs are sent into a nonlinear crystal where the MIR idler light is generated as the frequency difference between pump and signal.

dissertation, we use a 100 MHz repetition rate frequency comb laser, to be described below, with a maximum of 100 nJ pulse energies and $\sim$ 1 MW peak powers. For most of the fiber nonlinearities described below, this peak power is significantly lower still. A summary of relevant laser parameters comparing our system to a more typical laser used for ultrafast spectroscopy in physical chemistry experiments is shown in Table 2.1.

Due to reduced peak intensities achievable with the 100 MHz comb, we need to enhance nonlinear interactions to efficiently generate new frequencies. The two main approaches to accomplish this are to multipass the nonlinear medium with a resonant cavity or increase the interaction length via fiber optics. This dissertation describes examples of both of these approaches, with cavity-enhancement discussed in Chapter 3 in the form of an optical parametric oscillator and fiber nonlinearities discussed below.

In addition to the previous constraints placed on the laser design, performing ultrafast spectroscopy measurements requires short, isolated pulses. For the measurement goals in both the UV-vis and 2DIR cavity-enhanced spectroscopies, 100 fs pulse durations are sufficient. While fiber broadening optical spectra is commonplace in frequency combs [79], the nonlinear broadening of the original laser does not require a clean pulse in the time domain and often the supercontinua generated are made up of several pulses generated via cascaded nonlinear processes [80]. However in our case, care must be taken to ensure that isolated pulses are generated, which will be discussed in section 2.3.

As discussed above, a major goal of the laser system described in the subsequent sections in this chapter is to generate mid-infrared frequency (MIR) combs in the range of (at least) 3-5 μm. Our plan to accomplish MIR comb generation with sufficient power is shown in Fig. 2.1. Starting from an Er:fiber oscillator, one branch is shifted to around 1060 nm with highly nonlinear fibers and amplified in a Yb:fiber amplifier system to serve as a high power pump in difference frequency (DFG) stage. A second output from the same laser is shifted using similar highly nonlinear fibers to serve as a tunable NIR signal laser. Then MIR light is generated using difference frequency generation (DFG) between the NIR beams in a bulk crystal. In the DFG process, the pump laser at ω_{pump} amplifies the input signal beam at ω_{signal} and generates an idler field at $\omega_{\text{idler}} = \omega_{\text{pump}} - \omega_{\text{signal}}$. Due to power scaling limitations in Er [81, 82], the pump light is ideally from an amplified Yb-fiber source near 1060 nm. For a pump wavelength near 1060 nm, the signal branch must be tunable from $\approx 1300 - 1650$ nm to generate the required MIR idler range.

We initially considered two possible approaches for pump and tunable signal generation from the same starting laser oscillator. The first is to start with a Yb-fiber oscillator and broaden to longer wavelengths. This approach requires photonic crystal fibers (PCFs) with engineered dispersion. This approach has been explored before by several groups, who have reported large phase noise on the Raman-shifted light [75,83–85]. Furthermore, the small-core PCFs have lower optical damage threshold than step-index fibers, and we have observed damage occuring in small-core PCFs pumped at 1 micron in other applications. The second approach utilizes an Er:fiber oscillator followed by dispersive-wave broadening in step-index highly nonlinear fiber [86, 87]. This technique is unique to Er lasers due to the group velocity dispersion in optical fibers being anomalous at 1550 nm, enabling soliton formation which will be discussed below. Additionally, this wavelength band overlaps with the telecom industry, enabling cheaper, more available, and better performing optical fiber components and more robust infrastructure. We've selected this latter approach, as illustrated in Fig. 2.1, and below I will briefly describe the nonlinear optical physics of the broadening mechanism followed by the experimental realization. While the total MIR comb system has not yet been realized, the DFG pump laser and progress towards the tunable signal comb will be discussed.

2.2 Fiber nonlinear optics background

Optical fibers enhance nonlinear optical effects by guiding high-intensity light with a constant, small spot size. In this section I will provide a background on the nonlinear effects which occur predominantly in optical fibers and lead to dispersive-wave broadening. This discussion follows the framework of Agrawal's [76] and Weiner's [51] textbooks, and builds off of work from the groups of Scott Diddams and Alfred Leitenstorfer, among others. For more background on the development, refer to the dissertations of Gabriel Ycas [88] and Daniel Maser [89].

For an optical pulse in an optical fiber, the electric field can be written, under the slowly varying envelope approximation, as

$$\mathbf{E}(\mathbf{r}, t) = \frac{1}{2}\hat{\epsilon}\left[F(x, y)A(z, t)\exp(i(\beta_0 z - \omega_0 t)) + \text{c.c}\right] \tag{2.2}$$

where $\hat{\epsilon}$ is the polarization vector, $F(x, y)$ governs spatial mode profile of the beam, $A(z, t)$ is the pulse envelope in the time domain at a distance z along the fiber, and the exponential term carries information about the oscillatory field at frequency, ω_0, with $\beta = n(\omega_0)\omega_0/c$ and c.c is the complex conjugate. For most of the effects discussed in this section, working with just the slowly varying envelope, $A(z, t)$, is sufficient. In general, while propagating down a fiber, $A(z, t)$ is governed by the general pulse propagation equation:

$$\frac{\partial A(z, t)}{\partial z} = \left[\hat{D} + \hat{N}\right] A(z, t), \tag{2.3}$$

where $\hat{D}$ represents all dispersion terms and $\hat{N}$, all nonlinear terms. The actual forms of each term will be introduced below for specific dispersive and nonlinear interactions. The interplay of dispersion and nonlinearities sets the limits on spectral broadening, shifting, and supercontinuum generation. Although dispersion and nonlinearities both occur in the time domain as the pulse propagates, numerical approaches to solving Eqn. (2.3) apply the dispersion terms in the frequency domain via a split-step approach [90]. All simulated figures of nonlinear interactions included in this chapter were generated using the PYNLO software package [91].

2.2.1 Dispersion

For light propagating through a material, the input accumulates a frequency-dependent phase due to material dispersion of the form:

$$A_{\text{out}}(\omega - \omega_0) = A_{\text{in}}(\omega - \omega_0)e^{i(\beta(\omega) - \beta_0)L} \tag{2.4}$$

where $\beta = n(\omega)\omega/c + \Delta\beta\omega$, with $n(\omega)$ the index of refraction and $\Delta\beta$ the waveguide dispersion caused by the tight confinement of the field in the optical fiber. L is the length of the nonlinear medium which, in this case, is the fiber length. Typically, β is Taylor expanded around a central carrier frequency, ω_0,

$$\beta(\omega) = \beta_0 + \beta_1(\omega - \omega_0) + \frac{1}{2}\beta_2(\omega - \omega_0)^2 + \frac{1}{6}\beta_3(\omega - \omega_0)^3 + ..., \tag{2.5}$$

where $\beta_n = \frac{\partial^n \beta}{\partial \omega^n}|_{\omega_0}$ is the n^{th}-order dispersion term. β_0 is responsible for phase velocity and β_1 the group velocity [92]. By Fourier transforming to the time domain the effect of dispersion can also be rewritten as

$$\hat{D} = -\sum_{n=1} \beta_n \frac{i^{n+1}}{n!}\frac{\partial^n}{\partial t^n}. \tag{2.6}$$

which can be inserted into Eqn. (2.3).

For optical pulses, dispersion terms beyond the first order ($n \geq 2$) contribute to temporal broadening or compression. The second order term is typically the dominant effect and is called group velocity dispersion (GVD). Positive GVD is more common in materials in the visible and near infrared spectral ranges and is called "normal dispersion." This corresponds to lower frequencies having a higher group velocity than higher frequencies in the material ("red faster than blue"). Negative GVD is called "anomalous dispersion" which results in higher frequencies having higher group velocities ("blue faster than red"). Fused silica, the dominant material of optical fibers, has anomalous dispersion for near-infrared wavelengths longer than approximately 1310 nm. The effects of GVD, and higher orders, are linear and therefore additive. This means a pulse broadened by dispersion can be compressed again with the opposite sign of dispersion.

2.2.2 Self phase modulation

As discussed in the introduction above, there are no second-order nonlinear optical interactions in materials with inversion symmetry. Therefore, the lowest-order nonlinearities in optical fibers are third-order and proportional to $\chi^{(3)}$. One of the most important third-order interactions is self phase modulation (SPM) [93], where the refractive index is dependent on the intensity, I, via:

$$\tilde{n}(I) = n + n_2 I. \tag{2.7}$$

where n_2 is a the second-order nonlinear index, a material property proportional to $\chi^{(3)}$.

For a pulse, the time-dependent intensity leads to a time-dependent $\tilde{n}$ and, therefore, a time-dependent phase shift across the pulse:

$$\phi(t) = \tilde{n}(I) k_0 L - \omega t \tag{2.8}$$

Since frequency is the derivative of phase, the instantaneous frequency varies across the envelope of the pulse:

$$\omega(t) = -\frac{\partial \phi}{\partial t} = \omega_0 - \frac{d\tilde{n}(I)}{dt} k_0 L = \omega_0 - n_2 \frac{dI}{dt} k_0 L. \tag{2.9}$$

where the negative sign comes from the phase convention defined in Eqn. (2.2). For an optical pulse, $\frac{dI}{dt}$ is asymmetric – positive on the rising edge and negative on the falling edge. This results in the generation of new, lower frequency (red) components being generated at the beginning of the pulse and new higher frequency (blue) components being generated at the back of the pulse. As this process continues, the derivative nature of the broadening causes spectral "wings" to form on the edges of the pulse with no broadening occurring in the middle of the pulse, where $\frac{dI}{dt} = 0$. In the high power or long

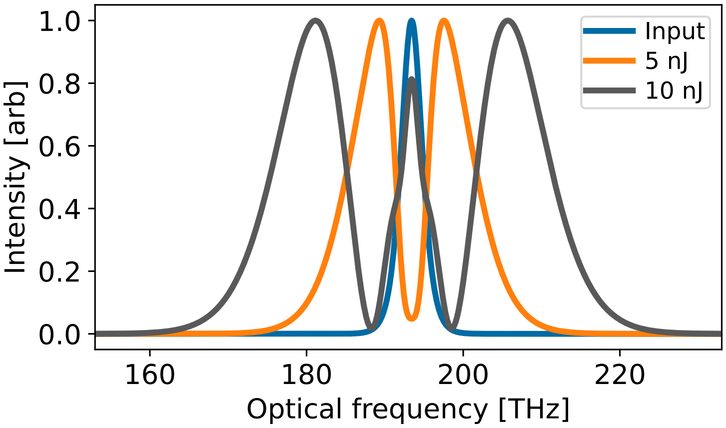

Figure 2.2: Simulated spectral broadening due to SPM for various input pulse energies, neglecting dispersion. The fiber length is fixed at 2 cm, $\gamma = 5$ (W km)$^{-1}$, and the pulse duration is 100 fs FWHM.

interaction length limit, this process can cascade and form a broad, modulated spectrum as shown in Fig. 2.2 simulated for a variety of input pulse powers.

Typically for fibers and other waveguides, rather than use n_2 and I, the nonlinear parameter, γ is used:

$$\gamma = \frac{k_0 n_2}{A_{eff}} \tag{2.10}$$

where $A_{\text{eff}} = \pi w^2$, the effective mode area of the light in the fiber, with w the 1/e^2 radius in the Gaussian approximation to the TEM$_{00}$ fiber mode [76]. For a typical telecom-style optical fiber, $\gamma \approx 1(\text{w km})^{-1}$. Using this convention, SPM can be written in the form of

$$\hat{N}_{\text{SPM}} = i\gamma |A|^2, \tag{2.11}$$

to be inserted in Eqn. (2.3).

2.2.3 Stimulated Raman scattering

Most nonlinear optical interactions are parametric meaning no energy is lost to the material. This is not the case for Raman scattering, where light propagating in a material excites low-frequency molecular vibrations [94]. The vibrational energy is subtracted from the input light which results in a lower frequency red-shifted field. The input "pump" beam generates the lower frequency, labeled as "stokes" beam which can be continuously and coherently amplified by the pump beam [95]. For a femtosecond pulse of light with a broadband spectrum, the bluer edge of the spectrum can act as a pump which amplifies the red edge of the spectrum and can lead to an overall redshift of the pulse. This technique has been used widely in Raman lasers [96,97] as well as a spectroscopic probe for vibrational spectra [98, 99].

At the fundamental level, Raman scattering is quite complicated and beyond the scope of the current discussion. In general terms, the absorption of the Raman pump occurs over the duration of the pulse and the emission of the stokes light can be delayed [100]. To include the delayed nature of Raman scattering, a nonlinear response function $R(t)$, of the form

$$R(t) = (1 - f_R)\delta(t) + f_R h_R(t), \tag{2.12}$$

must be used with f_R a constant less than 1 which determines the fractional contribution of the Raman response and $h_R(t)$ the material's Raman response function. The prompt term proportional to $\delta(t)$ is the electronic contribution with negligible delay which is responsible for instantaneous nonlinearities like SPM. The nuclear contribution $h_R(t)$ includes the effect of vibrations persisting for 100s of femtoseconds after Raman excitation. To include the delayed response, the response function must be convolved with the pulse envelope. The total nonlinear contribution, $\hat{N}$ which still includes the effects of SPM above, is now [101]

$$\hat{N} = i\gamma \left(1 + i\frac{1}{\omega_0}\frac{\partial}{\partial t}\right)\left(\int_0^\infty R(t')|A(z, t - t')|^2 dt'\right) \tag{2.13}$$

The derivative term in Eqn. (2.13) is the result of including higher-order terms in the overall third-order nonlinear polarization shown in Eqn. 2.1 which is necessary for capturing the time delayed Raman response. One side effect of the new derivative term in Eqn. (2.13) is the inclusion of self-steepening, a higher-order correction to SPM which leads to an intensity-dependent group velocity. For more information on this derivation or any of the other discussions in this section, see [76] and all the references therein.

2.2.4 Solitons and dispersive waves

The lowest order dispersive and nonlinear effects most strongly affecting pulses in optical fibers are GVD and SPM, respectively, as described above. Eqn. (2.3) including only these effects becomes the nonlinear Schrödinger equation:

$$\frac{\partial A(z,t)}{\partial z} = -i\beta_2 \frac{\partial^2 A}{\partial t^2} + i\gamma|A|^2 A \tag{2.14}$$

For negative β_2, meaning the material has anomalous dispersion, the effects of SPM and GVD can cancel out for certain pulse shapes and powers. This is because, as described above, SPM generates new red components on the front of the pulse and new blue frequencies on the back which broadens the pulse in frequency and time. For negative GVD, blue components have higher group velocity than red, which can effectively cancel out any temporal changes due to SPM and negate the spectral broadening.

These stable pulses are called solitons, and are solutions to Eqn. (2.14) which take the form of hyperbolic secants:

$$A(0,t) = \sqrt{P_0}\text{sech}(t/T_0), \tag{2.15}$$

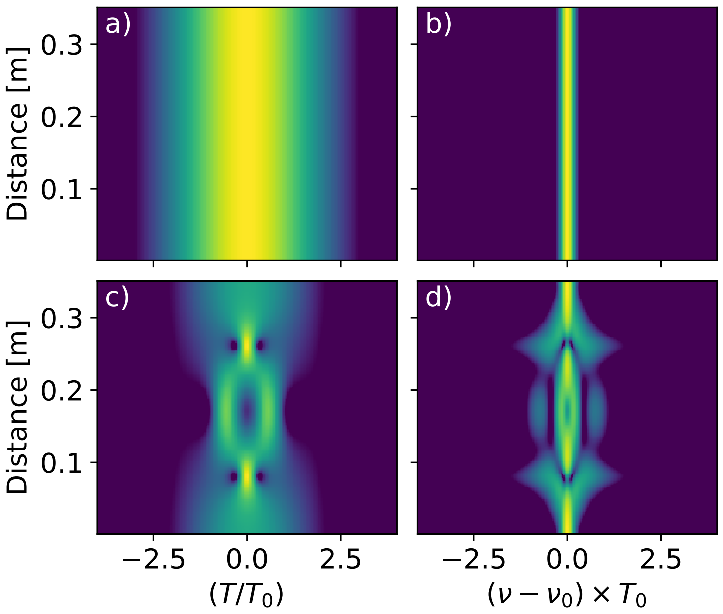

Figure 2.3: Simulated soliton evolution in a nonlinear fiber shown in both the time and frequency domains. a) and b) show an N=1 soliton which remains constant in time and frequency. c) and d) show an N=3 soliton which is periodic in time and frequency. Simulation parameters: center wavelength=1550 nm, β_2 = -7.26 ps^2/km, T$_0$ = 40 fs, γ=10.5 (W km)$^-$1

where T_0 is the pulse width (FWHM = $1.76T_0$) and P_0 is the required power for a soliton of order N to form:

$$P_0 = N^2 \frac{|\beta_2|}{\gamma T_0^2}, [] \tag{2.16}$$

with gamma defined in Eqn. (2.10).

The fundamental (N=1) soliton, simulated in Fig. 2.3a) and b), is constant in time and frequency down the length of the fiber. For higher-order (N >1) solitons, SPM and GVD are in competition which leads to periodic evolution of the pulse in time and frequency. Figures 2.3c) and d) show a simulated N = 3 soliton in the same fiber as Fig. 2.3a) and b). The pulse expands and contracts rapidly and symmetrically in both time and frequency as the pulse propagates along the fiber such that the pulse at the z = 0.35 m matches the input at z = 0. This pattern continues down the entire length of the fiber. If a pulse does not meet the power requirements of an exact integer soliton order, it will behave like the nearest integer N, found by rearranging Eqn. (2.16) to:

$$N = \left(\frac{\gamma P_0 T_0^2}{|\beta_2|} \right)^{1/2} \tag{2.17}$$

The preceding discussion assumed only lowest-order dispersive and nonlinear interactions. In realistic optical fibers, both higher-order dispersion

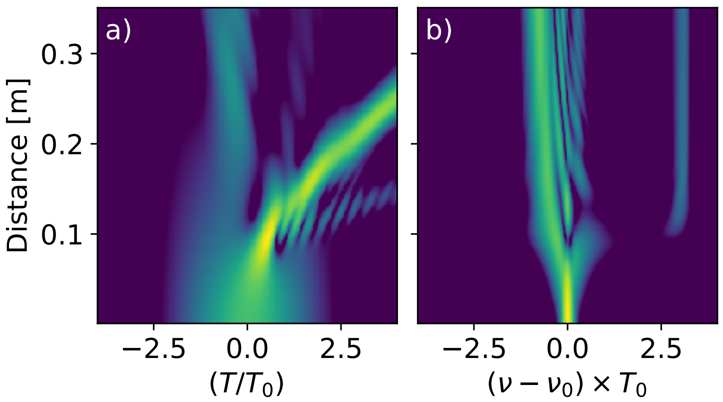

Figure 2.4: Simulated pulse evolution of an $N = 3$ soliton in a nonlinear fiber including all dispersive and nonlinear effects discussed. The dispersive wave is generated around 0.1 m and is observable in time as the modulated side feature which trails the main pulse and in the frequency domain as the blue-shifted line near $\Delta\nu T_0 = +3$. Simulation parameters: center wavelength=1550 nm, β_2 = -7.26 ps^2/km, β_3 = 0.056 ps^3/km, T$_0$ = 40 fs, γ = 10.5 (W km)$^{-1}$.

terms and nonlinear effects like self steepening and Raman scattering must be included. These effects perturb the “perfect” soliton and can cause it to undergo additional nonlinear processes. For higher-order solitons, these effects can cause the soliton to break up into the lower-order solitons. Raman scattering can also take place within the solition as described above and cause it to red shift while still retaining its solitonic nature.

Additionally, a soliton perturbed by higher order dispersion or nonlinear effects can “shed” some energy in the form of a dispersive wave. This dispersive wave is a phase-matched pulse that occurs in the normal dispersion regime of the optical fiber, typically at higher frequency. Phase matching occurs for a frequency with an identical phase velocity to the soliton. Energy is transferred from the soliton to the dispersive wave via cascaded four-wave mixing with the intermediate mixing steps not necessarily phase matched [102].

A more realistic picture of an approximately N=3 soliton pulse propagating in a nonlinear fiber is shown as a simulation in Fig. 2.4. The breakup in the time domain and modulation in the frequency domain after the first 0.1 m of fiber is indicative of soliton fission. The dispersive wave is the weaker, modulated pulse which breaks off from the main pulse at around 0.1 m in Fig. 2.4. The dispersive wave lags behind the soliton because it typically has lower group velocity. In the frequency domain, the dispersive wave is observable around $\delta\nu T_0 = +3$ in Fig. 2.4b). As the pulse continues to propagate, the fissioned solitons will shift to longer wavelengths due to Raman scattering. For dispersion profiles in silica fibers, the red shifting soliton will phase match to a blue shifting dispersive wave. More information on the complex and fascinating physics of solitons and dispersive waves can be found in [76]. By tuning the pulse duration and/or input power, the center wavelength of the

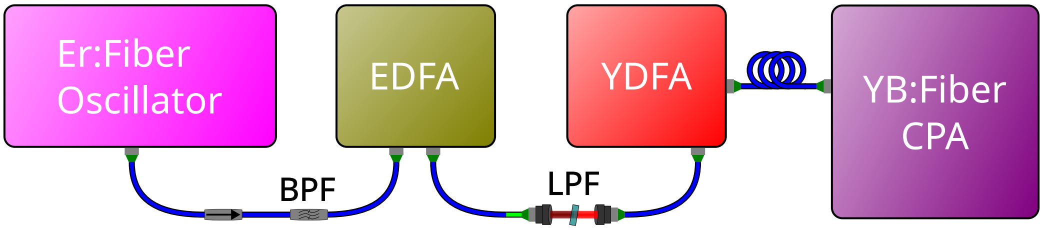

Figure 2.5: Overview of high power, Yb-fiber amplified pump beam. Starting with an Er:fiber oscillator, the light is first nonlinearly amplified in an Er-doped fiber amplifier (EDFA), shifted to around 1060 nm in a highly nonlinear fiber (HNLF), and then amplified in two Yb-doped fiber amplifier stages. BPF:Band pass filter, LPF:Low pass filter.

soliton and dispersive wave can be controlled. Here, we exploit this effect for the generation of tunable NIR frequency combs starting at 1550 nm.

2.3 Experimental realization

As discussed in the introduction above, a goal of the laser platform is to generate tunable and broadband MIR frequency combs. In order to perform cavity-enhanced ultrafast spectroscopies, these combs require low phase noise and must have isolated ≈ 100 fs pulse durations at a 100 MHz repetition rate. To accomplish this goal, we developed a tunable NIR system based on an Er-doped fiber laser frequency comb operating near 1550 nm. In the future, MIR combs will be generated via DFG between a dispersive-wave-shifted, high-power pump comb at 1060 nm and a tunable NIR signal laser, both generated from the same oscillator, as shown in Fig. 2.1.

2.3.1 1060 nm pump branch

The overall scheme for the generation of the high-power 1060 nm pump comb is shown in Fig. 2.5. The reason for centering this laser at 1060 nm rather than the Yb gain maximum of 1030 nm is because Yb-based lasers and amplifiers support wider bandwidths and, therefore, shorter pulse durations when operating at 1060 nm [103, 104].

The initial comb is generated in a commercial Er-doped fiber oscillator from Menlo Systems with an all polarization-maintaining (PM), “Figure 9” design [105–108]. Most of the laser system is made with PM fiber to reduce polarization noise and be less sensitive to environmental fluctuations [108,109]. At 1550 nm, most standard telecom optical fiber has anomalous GVD meaning that solitons can form if the conditions described in Eqns. 2.15 and 2.16 are met.

The oscillator is followed by an optical isolator to protect against stray back reflections and a fiber-based band pass filter (BPF) with a width of ≈ 12 nm at a center wavelength of 1550 nm. The BPF “cleans up” the spectrum of the initial laser, leading to a more symmetric pulse in time and frequency which undergoes nonlinear broadening in a more controlled manner and is less sensitive to fiber lengths before amplification [89, 110]. The filtered spectrum is shown in Fig. 2.6b) labeled "input" and the power is 6 mW.

After filtering, the pulse is amplified in a home-built nonlinear Er-doped fiber amplifier (EDFA) as shown in Fig. 2.5, and schematically in Fig. 2.6a). The nonlinear nature of the EDFA is easily observable by the dramatic spectrum changes between the input and output shown in Fig. 2.6b). The gain medium is 2.5 m of nLIGHT LIEKKI Er80-4/125-HD-PM which has normal dispersion at 1550 nm due to the reduced core size of the fiber. The EDFA is core-pumped by 4 grating-stabilized 976 nm pump diodes with linearly polarized outputs and PM fiber pigtails, each with $\approx$ 750 mW of power at 1200 mA of drive current. The diodes are combined in pairs via fused fiber polarization beam combiners ("PM combiners" shown in Fig. 2.6) (Gooch and Housego FFP-5M3180G10) with one diode on each polarization axis of the output fiber. These diode pairs are then coupled to the gain fiber in both directions – counter- and co-propagating with the input comb light via wavelength division multiplexers (WDMs) which act as fiber-based dichroic beam splitters.

The goal of the EDFA is both to increase the power and decrease the pulse duration of the input pulse. The main experimental "knob" to optimize the pulse duration is the output fiber length. Since the gain fiber in the EDFA is normal GVD, the pulse undergoes SPM spectral broadening and increases in pulse duration while being amplified. The signature of SPM can be seen in the modulated central portion of the output spectrum shown in Fig. 2.6b). The standard PM-1550 fiber after the gain fiber has anomalous dispersion, which will compensate both for the positive GVD of the gain fiber and the positively chirped SPM-generated new frequency components. As the pulse gets shorter in the output fiber, additional SPM broadening occurs as well as soliton formation. Too much compression fiber on the output can lead to pulse breakup and soliton fission.

From a practical standpoint, the output pulse from the EDFA is optimized by measuring pulse durations as a function of output fiber length until the shortest pulse width is found. Fiber mating adapters (FC/APC) are used for all connections to the EDFA to facilitate quick length adjustments. The pulse duration is measured using a home-built, all-reflective, split-mirror autocorrelator [111, 112]. The all-reflective design, including reflective focusing, was chosen to avoid chromatic effects in transmission optics operating across the broad bandwidth of the output spectrum shown in Fig. 2.6b). The nonlinear autocorrelation signal is recorded in a home-built 2-photon photodetector using an amplified, reverse-biased GaAs LED. This photodetector has a nonlinear response in the range of 1200 to 1700 nm. The optimized output pulse interferometric autocorrelation is shown in Fig. 2.6c). The autocorrelation trace shown is Fourier filtered to only the oscillatory portion of the output of the split-mirror autocorrelator to be less sensitive to alignment [112].

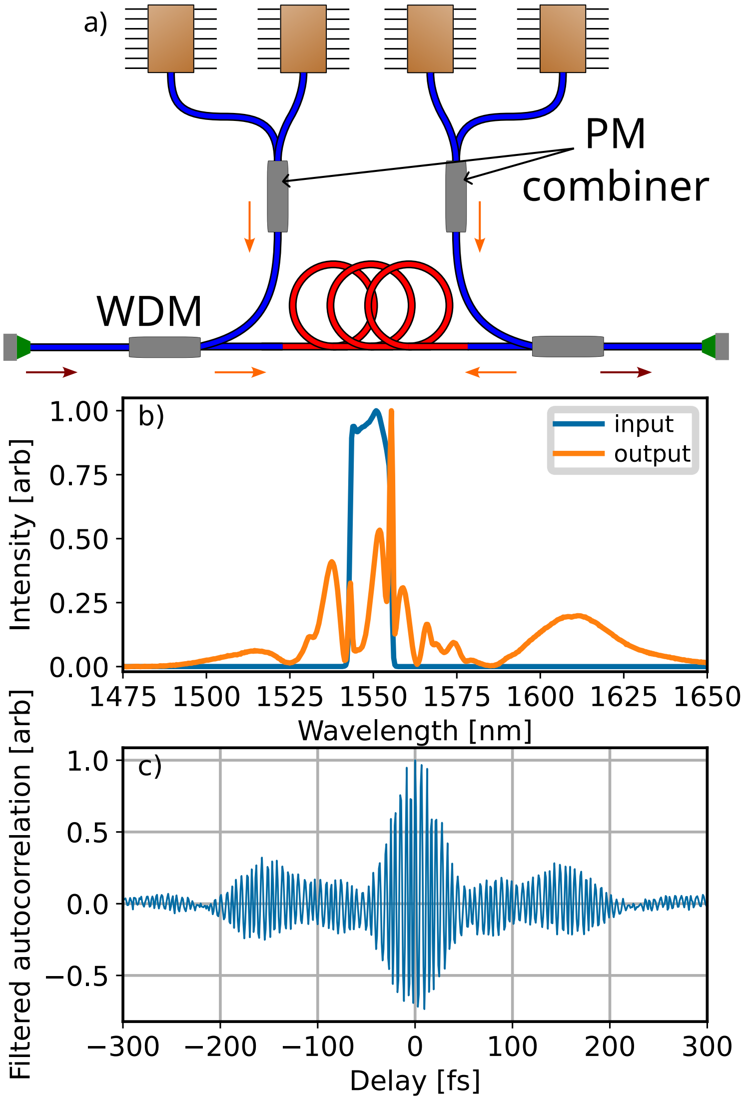

Figure 2.6: Erbium doped fiber amplifier (EDFA) design and performance. a)Schematic layout of the EDFA. The blue fiber is polarization-maintaining passive fiber. Red fiber is Er-doped gain fiber: 1.5 m nLIGHT LIEKKI Er80-4/125-HD-PM. The amplifier is pumped by two 750 mW, 976 nm pump diodes each in both the counter- and co-propagating directions. WDM: wavelength division multiplexer (AFW Technologies WDM-PM-1598-L-5-0-1W). b) EDFA input and output spectra displaying the nonlinearity. Input power is 6 mW. Output power is 350 mW. c) Interferometric autocorrelation trace of optimized output pulse. FWHM duration is 45 fs.

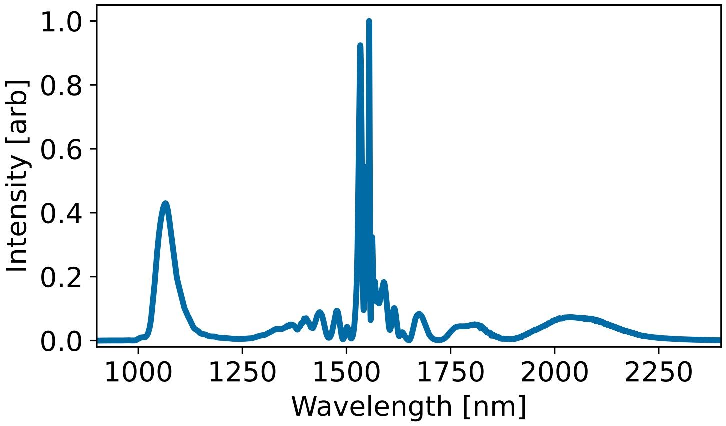

Figure 2.7: HNLF output spectrum displaying the soliton at ≈2100 nm and dispersive wave at ≈1070 nm.

The shortest pulse attained from the EDFA, shown in Fig. 2.6b) and c), is approximately 45 fs in duration (FWHM) with an average power of 350 mW. The broader "pedestal" around the central pulse is sufficiently low in intensity to not participate substantially in further nonlinear broadening. This pulse required approximately 80 cm of PM-1550 fiber to compress after the gain fiber, with 45 cm included inside the boxed EDFA components and the other 35 cm connected to the outside. The output pulse duration is largely insensitive to the input fiber length prior to the EDFA, which is 1.5 m for the current case. Typically, the ideal pulse from this EDFA design has a spectrum similar to the output Fig. 2.6b). The reddest portion near 1610 nm is indicative of soliton formation, which can be confirmed by increasing the fiber length after the EDFA. With more fiber after the EDFA, this portion will redshift in frequency and the pulse in the time domain will develop side pulses with the central pulse remaining roughly constant in width [88].

After amplification, a small piece of highly-nonlinear fiber (HNLF) is spliced to the EDFA output to shift the light to 1060 nm for seeding Yb-doped fiber amplifiers, as shown in Fig. 2.5. The HNLF is PM and has a reduced core size of $\sim 4\mu$m in diameter vs. the standard PM-1550 fiber's $\sim 12\mu$m core. This increases the nonlinear parameter, γ, defined by Eqn. (2.10), to approximately 10.5 (W km)$^{-1}$. Through dispersion engineering and doping, the GVD of the HNLF remains anomalous with $\beta_2 = -7.26$ ps^2/km (D = 5.7 ps/nm/km) at 1550 nm, allowing for soliton formation and dispersive wave generation. To reduce losses, the HNLF is spliced directly to the optimized length of output fiber after the EDFA and connectorized for free space collimation. The pulse entering the HNLF has a soliton number of 11.2. The HNLF length is kept short at 4 cm to avoid soliton fission and the generation of multiple dispersive waves. This length was selected with the assistance of simulations using the optimized EDFA pulse as input.

An example measured HNLF ouput spectrum is shown in Fig. 2.7. This spectrum was recorded with a different Er:fiber oscillator than the rest of

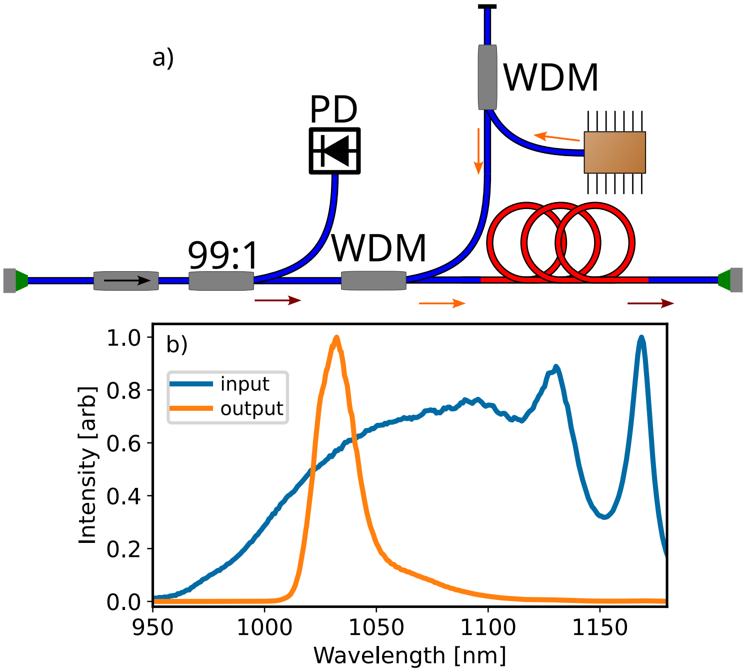

Figure 2.8: Yb-doped fiber amplifier (YDFA) design and performance. a) Schematic layout of the YDFA. The blue fiber is polarization-maintaining passive fiber. Red fiber is Yb-doped gain fiber: 2.85 m nLIGHT LIEKKI Yb300-6/125-PM. The amplifier is pumped with 1 copropagating 400 mW 976 nm pump diode via a wavelength division multiplexer (WDM). The additional WDM protects the pump diode from amplified spontaneous emission and back reflections. The photodetector (PD) is used to monitor input power for interlock purposes. b) Input ad output spectrum. The modulation on the input spectrum is due to the low pass filter (shown in Fig. 2.5) mirror coating. Input power is 4 mW. Output power is 130 mW.

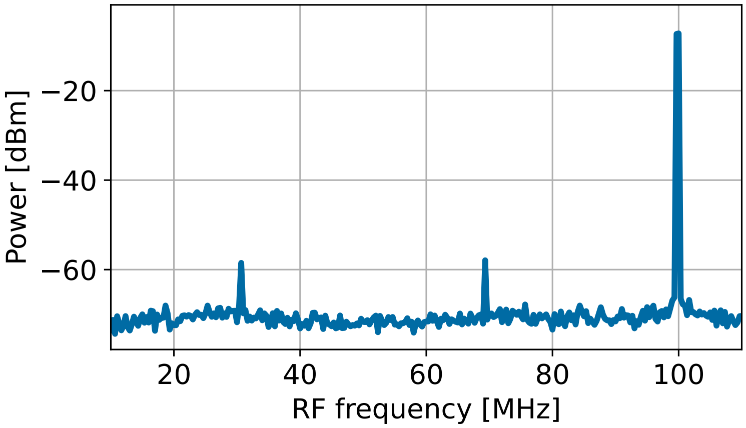

Figure 2.9: Optical heterodyne beat note measurement at 10 kHz resolution bandwidth between amplified dispersive wave and NPRO Nd:YAG laser. 100 MHz tone is comb repetition rate. Beat notes at 30 and 70 MHz represent heterodyne mixing of Nd:YAG with the nearest comb teeth. Beat note starts to collapse at 10 kHz resolution bandwidth.

the data shown here and the optimized output pulse from the EDFA was slightly shorter (≈ 35 fs FWHM), resulting in highly efficient dispersive wave generation. This ideal HNLF performance was never fully recreated with later systems. The portion centered around 2100 nm is the red shifted soliton which initially formed closer to 1700 nm as in Fig. 2.6b). The soliton is phase matched to the dispersive wave on the blue edge of the spectrum, centered around 1070 nm. The spectrum achieved for daily operation seeding the YDFAs, after filtering is shown in Fig. 2.8b).

To drive nonlinear processes, the power of 1060 nm pump laser is increased via a two-stage Yb:fiber amplifier as shown in Fig. 2.5. First a core-pumped Yb-doped fiber amplifier (YDFA) which acts as a preamplifier for a high-power, cladding-pumped chirped pulse amplifier (CPA) previously described in [113].

Prior to amplification, the HNLF spectrum is sent through a dichroic low-pass filter (LPF) as shown in Fig. 2.5. The transmitted light below 1100 nm is shown in Fig. 2.8b) labeled “input”. The modulation on the long wavelength side of the spectrum is due to the transmission coating curve of the dichroic filter and does not affect laser performance since it is not within the Yb gain bandwidth [114]. Filtering in free-space avoids further nonlinear effects in fibers before the YDFA. Before coupling back into the fiber, the total power in this spectral region is approximately 20 mW. An isolator and fiber-based polarizer are placed before the YDFA. After coupling and insertion losses, the total power at the YDFA input is approximately 4 mW measured at the 1% tap indicated on Fig. 2.8.

The design of the YDFA is shown in Fig. 2.8a). The gain fiber is 2.85 m of nLIGHT LIEKKI Yb300-6/125-PM. This fiber was selected due to its resistance to failure via photodarkening [115, 116], which affected the performance of several previous amplifier designs. The amplifier is pumped with one grating-stabilized 976 nm diode in the forward, copropogating direction via a fused WDM. An additional WDM is placed upstream in the pump line to further isolate the 1060 nm light from the amplifier pump light in order to protect the diode from backreflections. All fiber connections are fusion spliced to avoid connector damage which occurs more often in Yb lasers and can lead to YDFA failure. The output power of the amplifier is 130 mW for ≈400 mW of pump power (630 mA) and the output spectrum is shown in Fig. 2.8b). Due to gain narrowing effects in the amplifier [117], the output spectrum is drastically changed compared to the input.

To verify the phase noise properties of the dispersive wave, we performed a beat note measurement between the YDFA output and an ultralow noise cw NPRO Nd:YAG laser at 1064 nm, shown in Fig. 2.9 at a resolution bandwidth of 10 kHz. The lasers are combined in a fiber beamsplitter and the output sent to a fast photodiode and read out with an RF spectrum analyzer. The spike at 100 MHz is the repetition rate of the frequency comb. The other tones at ≈ 30 and ≈ 70 MHz are the free-running heterodyne beat frequencies between the YAG and the two nearest comb teeth. By measuring the height of these peaks as a function of spectrum analyzer resolution bandwidth, the comb tooth linewidth can be estimated relative to the Nd:YAG which has a linewidth of ≈ 3 kHz. The beat note amplitude decreases at the resolution bandwidth of 10 kHz, giving a rough estimate of the comb tooth linewidth of about 10 kHz. For a 100 MHz cavity with a finesse of 1000, the cavity linewidth is 100 kHz, therefore the frequency comb teeth are sufficiently narrow for comb-cavity coupling.

The Yb-fiber CPA, described in [113], is designed for operation around 1060 nm. A filtering mirror between amplifier stages selects only the long wavelength tail of the YDFA preamp output spectrum shown in Fig. 2.8b) to seed the Yb-fiber CPA. The filtered input spectrum is shown in Fig. 2.10a). The total input power is 25 mW. The amplifier stage consists of a Yb-doped large mode area photonic crystal fiber pumped with 30 W of 915 nm pump diode [113]. The free-space compression gratings after amplification reshape the spectrum a small amount due to grating efficiency, resulting in the output spectrum shown in Fig. 2.10a). The total power after compression is 11.8 W. The output pulse, measured with an inensity autocorrelator, is shown in Fig. 2.10b). The FWHM pulse duration retrieved from the autocorrelation is 120 fs.

2.3.2 Tunable seed branches for mid-infrared combs

To generate the tunable NIR signal combs to seed the MIR DFG process as shown in Fig. 2.1, a second EDFA and HNLF setup is built similar to the one described above. For this branch, the HNLF has a dispersion of $\beta_2 = -2.93$ ps^2/km (2.3 ps/nm/km) at 1550 nm which moves the zero dispersion wavelength closer to 1500 nm. This facilitates the formation of redder dispersive waves, due to the phase matching condition for dispersive wave gen-

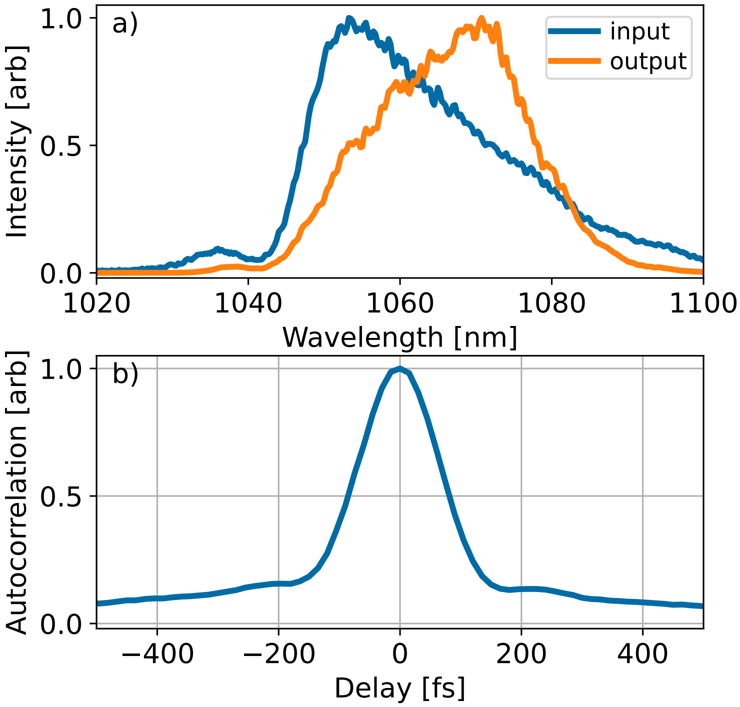

Figure 2.10: Yb-doped CPA performance. a) Input and output spectra. Input is measured immediately before PCF amplifier, input power is 25 mW. Output is measured following grating compresor, output power is 11.8 W. b.) Output intensity autocorrelation, demonstrating a pulse duration of 120 fs.

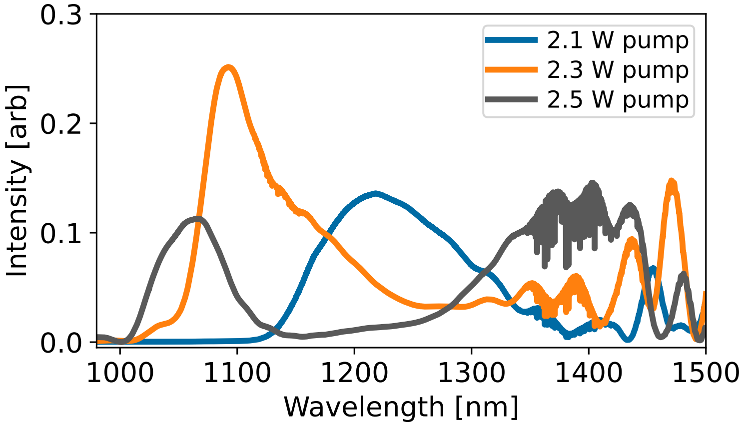

Figure 2.11: Output spectrum of the tunable EDFA/HNLF signal branch. Dispersive wave shifts to shorter wavelengths for increasing pump power. See text for details.

eration which requires normal dispersion at the wavelength of the dispersive wave [118].

The output spectrum of the tunable NIR EDFA/HNLF branch is shown in Fig. 2.11 as a function of total EDFA pump power. For optimized EDFA conditions, increasing the EDFA pump power increases the amount of SPM broadening which occurs in the amplifier which, decreases the attainable output pulse duration. For a shorter input pulse, soliton formation happens earlier in the HNLF which leads to larger accumulated Raman shift and a more blue-shifted dispersive wave, as discussed above. Tuning this way has also been accomplished by applying a frequency chirp to the input pulse [119].

2.4 Conclusion and outlook

In this chapter I described a scheme for tunable frequency comb generation including the challenges imposed by high repetition rate nonlinear optics, an overview of the nonlinear processes involved, and a detailed description of the experimental implementation. The tunable platform is enabled by Er:fiber technology and dispersive wave generation and produces frequency combs with low phase noise and isolated pulses at a 100 MHz repetition rate which satisfies the requirements of cavity-enhanced ultrafast spectroscopy.

In addition to the setup described above, care also was taken to ensure stability and repeatability of the whole laser system. A home-built, FPGA-enabled safety interlock system protects both the laser and amplifiers from seed failures. Also, a custom laser control software makes the complex system essentially turnkey and the 1060 nm pump laser has been in continuous daily operation for nearly 5 years.

The original motivation for the tunable comb scheme was for gas-phase 2DIR of hydrogen-bond networks. For more progress in this direction, see

[120]. This application is not be realized in this dissertation, but there are numerous other uses for this comb platform in linear and nonlinear spectroscopy as well as time and frequency transfer. The 1060 nm comb described above has sufficient power and pulse duration to drive further nonlinear frequency generation other than DFG. The second harmonic of this comb is used as the pump for generation of tunable visible frequency combs to be described in Chapter 3 and the third and fourth harmonics of this comb serve as the pump laser in the broadband UV/Vis cavity-enhanced transient absorption spectrometer described in Chapter 5. Additionally, the nonlinear EDFA described above has been used with a normal dispersion HNLF to generate broadband NIR frequency combs with ultrashort $\approx$ 10 fs compressed pulse durations [121, 122]. These high intensity pulses were then used for low-power broadband MIR generation via intrapulse DFG in the range of 3-12 μm and broadband linear spectroscopy experiments [121, 122]

Chapter 3

Tunable visible frequency comb generation

This chapter contains a reproduction of our publication *Tunable visible frequency combs from a yb-fiber-laser-pumped optical parametric oscillator,* Yuning Chen and Myles C. Silfies, Grzegorz Kowzan, Jose Miguel Bautista, and Thomas K. Allison, *Applied Physics B,* **125**(5):81, (2019) [3], with the permission of Springer Nature.

3.1 Introduction

Frequency comb lasers have achieved tremendous success in many applications, at many different wavelengths [53, 121, 123–125]. In metrology applications where a frequency comb is used to measure the frequency of a continuous wave laser or calibrate a spectrograph, supercontinuum generation in highly nonlinear fibers (HNLF) usually provides sufficient power at the wavelength to be measured. For applications in which the frequency comb is used to interact with atoms and molecules directly, i.e. "Direct-frequency comb spectroscopy" (DFCS) [46, 54, 65], higher spectral brightness than is available from fiber supercontinua is desired. Thus, the generation of tunable or broadband high-power frequency combs has recently been a subject of intense study, particularly in the mid- and long-wave infrared [121, 126–133].

In this chapter, we address the problem of tunable visible frequency comb generation, which has received somewhat less attention. Our target application is widely tunable cavity-enhanced ultrafast transient absorption spectroscopy (CE-TAS), recently demonstrated at one wavelength by our research group [30]. A tunable CE-TAS system operating in the visible can record the ultrafast dynamics of electronically excited jet-cooled molecules [134], clusters [135], and radicals [136] in the same way that conventional ultrafast spectrometers routinely exploit this spectral region to study the dynamics of condensed-phase samples [32]. This is a demanding application, requiring high powers ($>$ 10 mW), short pulses, control over the comb's carrier-envelope offset frequency

(f_0), low optical phase noise, and a wide tuning range due to the broad spectral features inherent to molecules undergoing ultrafast dynamics. A robust fiber-based backbone, requiring minimal maintenance, is also desired due to the complexity of the downstream experiment.

Previous work has reported the achievement of subsets of this list. Doubling the tunable dispersive waves from an Er:fiber laser pumped HNLF in a periodically-poled lithium niobate crystal (PPLN), Moutzouris et al. [137] demonstrated multi-millliwatt tunable comb generation at 108 MHz repetition rate. However, the pulse durations were long (300-1000 fs) and the tuning range only extended down to 520 nm. In another example, using a series of HNLFs pumped with 1020 nm laser pulses, Tu et al. [138] demonstrated dispersive wave generation in the spectral range of 347 - 680 nm. This covered nearly the entire visible with average powers of 1-9 mW, but to cover the whole tuning range, 7 different HNLFs were required, necessitating replacing the fiber and realigning the system to change wavelength. Using fiber-laser-pumped synchronously pumped optical parametric oscillators (SPOPO), widely tunable combs with larger average powers [139, 140] and shorter pulses [141] have been achieved. Some work has explored intracavity doubling and sum frequency generation for tunable visible and UV comb generation [142–145]. However, these previous fiber-laser-pumped SPOPOs have only demonstrated coverage of small portions of the visible spectrum. SPOPOs pumped by the second harmonic of Ti:Sapphire lasers have achieved impressive tuning ranges [146] covering nearly the entire visible with the signal beam alone. Such combs can in principle be well stabilized [147], but still require managing the drawbacks of the Ti:Sapphire pump comb compared to fiber lasers, namely greater expense, higher maintenance, and faster f_0 drifts when not actively stabilized.

In this chapter, we report the development of a Yb-fiber-laser-pumped singly-resonant SPOPO delivering short pulses, high-power, and low optical phase noise throughout the visible spectral range. The OPO cavity is designed to intracavity double both the signal and idler beams using a single BBO crystal, and also utilize the collinear and co-polarized pump comb. In this way, nearly continuous tuning over the range of 420-700 nm (> 9000 cm^{-1}) is achieved with only small gaps near OPO degeneracy, where signal and idler wavelengths are equal. Frequency locking of all three collinearly outcoupled combs (pump, doubled signal, and doubled idler) to a $\sim$100 kHz linewidth femtosecond enhancement cavity [148] facilitates direct comparison of their optical phase noise and phase modulation transfer functions. We find that the phase relations established for singly resonant OPOs [149, 150] cause phase modulation to be transferred nearly completely from the pump to the non-resonant idler. More precisely, the phase modulation of the pump acts on the resonant signal comb with a fixed point [75, 151] near the signal comb optical carrier frequency. This has important consequences for the noise and stabilization of the combs.

While our target application has been widely tunable CE-TAS, this work can also be useful to researchers working on more conventional ultrafast spec-

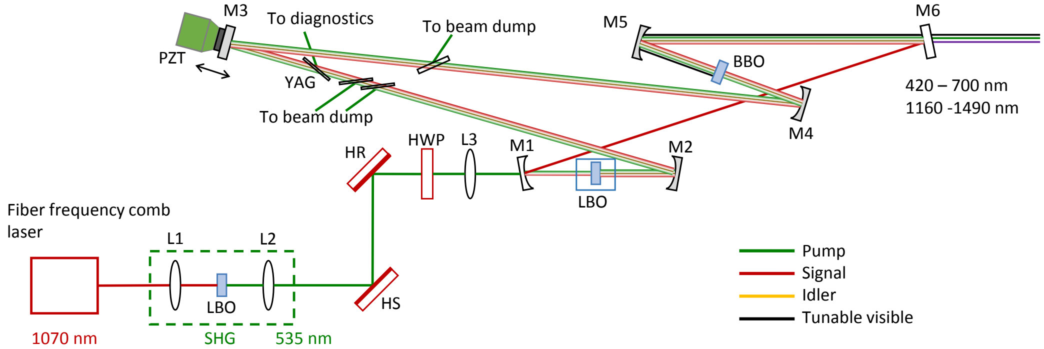

Figure 3.1: Schematic of the synchronously pumped optical parametric oscillator. A frequency comb laser centered at 1070 nm is frequency doubled in an LBO crystal to 535 nm, providing the pump for the OPO. The tunable visible light is generated by frequency doubling both the signal and idler. Mirror M5 collimates the visible light and M6 couples the light out of the cavity. L1, L2: focal length = 10 cm; HS: harmonic separator; HR: high reflector; HWP: half waveplate; L3: focal length = 15 cm; M: mirror. More details in the main text.

troscopy, high-resolution multidimensional spectroscopy [152], visible dual-comb spectroscopy [153], ultrafast nonlinear microscopy [154, 155], and researchers working on the stabilization of OPOs in general [149].

3.2 Experimental setup

The optical layout of the OPO is shown in Fig. 3.1. In our laser, the pump comb is initially derived from an Er:fiber oscillator (Menlo Systems Ultra Low Noise variant), shifted to 1.07 μm using a short highly nonlinear fiber as described in Chapter 2 [87]. However this detail is not a critical to the results reported here. The pump can be derived from any low-noise comb operating around 1 μm suitable for amplification in Yb:fiber, for example the oscillators described in [113]. In the current setup, the shifted Er:fiber comb is amplified in the large-mode area Yb-doped photonic crystal fiber amplifier previously described in [113]. After the compressor, the pulses are 120 fs long with a pulse energy of 115 nJ at a repetition rate of 100 MHz. This laser is frequency doubled in a 2 mm thick LBO crystal cut for type I second harmonic generation (SHG) at 1064 nm with a conversion efficiency of 40%. The resulting 4.5 watts at 535 nm is the pump of the OPO.

The OPO cavity contains two nonlinear crystals, a lithium triborate (LBO) crystal for parametric gain and a beta barium borate (BBO) crystal for intracavity doubling the signal and idler. The LBO crystal is 3 mm long and cut for type I noncritical phase-matching. The crystal has angles of θ=90° and ϕ=0° [156]. Both sides have anti-reflection coatings at 535 nm and 850 - 1060 nm for the pump and signal respectively. The crystal is housed in a compact home-built oven for controlling the crystal temperature between 25° C and 200° C [140]. The compact oven design allows small (~ 90 mrad angle of incidence) angles on the curved mirrors M1 and M2 for reducing astigmatism and the OPO's spatial footprint. The pump beam $1/e^2$ radius before L3 is 2.1 mm. Using the ABCD matrix formalism [92] for the OPO cavity, at $\lambda = 900$ nm we estimate signal beam radii at the LBO and BBO crystals to be 30 μm and 70 μm, respectively.

Intracavity second harmonic generation of both signal and idler is phase matched by rotating the BBO crystal about its horizontal axis (θ). We select BBO for the broad phase-matching tunability and moderately high nonlinear coefficient. Using SNLO [157], we calculate the phase-matching angle for type I SHG of 850 nm is $\theta = 27.6°$ and SHG of 1400 nm is $\theta = 20.0°$. The BBO crystal has a cut angle of $\theta = 19.8°$ for type I SHG of 1500 nm and is protective coated. BBO crystals of both 1 and 2 mm length were used, with some results for both shown in Sect. 3.3. The doubled output is optimized by tuning θ while adjusting the OPO cavity length to maintain resonance.

The OPO cavity is designed to be resonant for the signal from 850 nm to 1060 nm, focus both the signal and idler at the BBO crystal, and collimate and outcouple the doubled idler ($2i$), doubled signal ($2s$), and residual pump in a collinear and co-polarized fashion. This is achieved by using protected silver mirrors for M2-M5 and dichroic mirrors ($R > 99.9\%$ at 850 - 1060 nm and $R < 5\%$ reflectivity for 450 - 700 nm). All four curved mirrors have a radius of curvature of 20 cm. The two dichroic mirrors M1 and M6 are lossy for the idler, so that resonance is only attained for the signal. The round trip loss of the signal power caused by the optics is estimated to be 16%, resulting in a finesse of ≈ 35. The pump is vertically (s) polarized, and thus the signal and idler are generated at the LBO crystal with horizontal (p) polarization. The doubled signal and doubled idler are then generated with vertical s-polarization in the BBO crystal, such that the pump, $2s$, and $2i$ beams emerge collimated, collinear, and co-polarized from M6.

Four YAG plates at Brewster's angle are placed in the cavity to attenuate the residual s-polarized pump light at the BBO crystal and the output coupler (M6) to 200 mW. YAG was chosen for it's high index of refraction and corresponding shallow Brewster's angle. The YAG plates also provide intracavity dispersion enabling stable operation closer to degeneracy. One of the YAG plates is mounted on a rotation stage so it can be rotated from the Brewster condition by a known angle, allowing us to outcouple a fraction of the signal and idler to diagnostics, the fraction calculated from the Fresnel equations. The outcoupled light is analyzed using calibrated germanium photodetectors and an optical spectrum analyzer.

We control the OPO cavity length by moving mirror M3 with a micrometer and two piezoelectric transducers (PZT). The micrometer is used for coarsely finding the resonance condition of OPO free spectral range = pump f_{rep}. A long travel (~ 10 micron) PZT stage allows further coarse tuning of the OPO cavity length and long-term in-loop correction for drift. A faster "copper

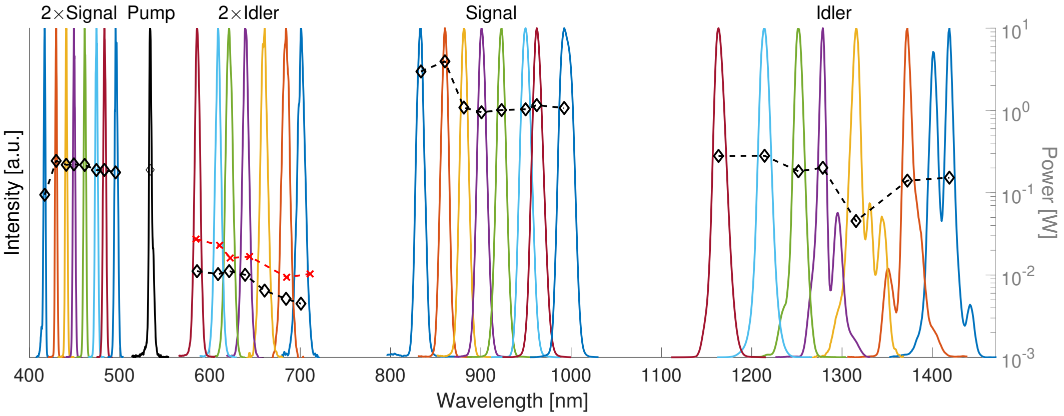

Figure 3.2: Intracavity signal and idler spectra and power at different phase-matching temperatures of LBO in the synchronously pumped optical parametric oscillator. The spectrum centered at 535 nm is the residual pump. Spectra for fundamental and second harmonic are color matched. Optical powers are represented by diamonds for 1 mm BBO and crosses for 2 mm BBO ($2i$ only) and use the right axis. Reported powers for pump, $2i$, and $2s$ are OPO output while signal and idler are intracavity power levels.

bullet" style PZT [158] is used for frequency stabilization of the OPO when using the doubled signal beam. The incident angle on M3 is set to be $\sim 1.5°$, so that the cavity misalignment is negligible when changing the cavity length on the sub-mm scale.

3.3 Results

The threshold pump power required to see parametric oscillation was measured to be around 1.7 W, and was not strongly affected by the insertion of the doubling crystal. The spectrum and power of signal and idler with 4.5 watts pump power are shown on the right side of Fig. 3.2. The signal and idler intracavity powers are reported with the diamond symbols using the right axis of the figure. By varying the LBO temperature from 122° C to 145° C and adjusting the OPO cavity length as in [140], the signal is tuned between 835 nm to 990 nm and the corresponding idler ranges from 1490 nm to 1160 nm. Tuning towards shorter signal wavelengths is limited by the coating of M1 and M6. As we get closer to degeneracy, where signal and idler wavelengths are equal, the signal and idler spectra become broader and unstable due to the low intracavity dispersion and the broad phase matching bandwidth in LBO. The signal and idler spectra displayed in Fig. 3.2 were taken when their respective second harmonics were optimized. Removing the BBO typically resulted in roughly a factor of 2 increase in intracavity power for both signal and idler.

The spectra and output power of the tunable visible combs provided by the combination of $2s$, $2i$, and pump are also shown in Fig. 3.2, along with

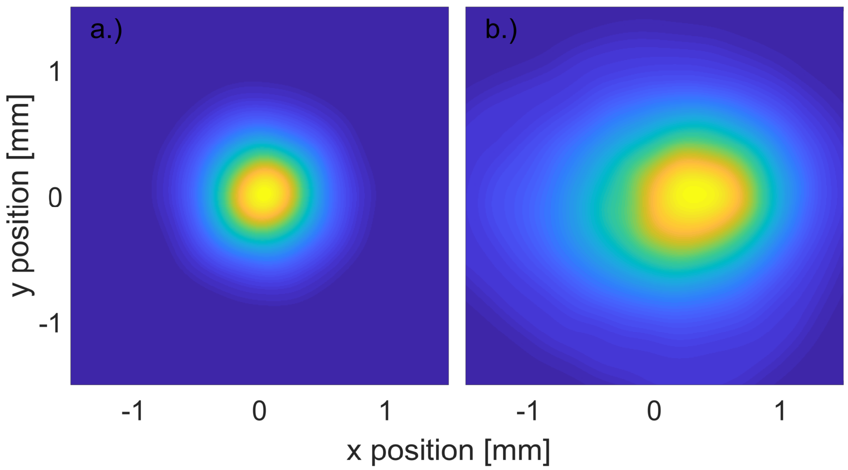

Figure 3.3: Output spatial modes for, a.) the doubled signal and, b.) the doubled idler. Gaussian fits to the vertical and horizontal profiles for each give $1/e^2$ beam radii of $w_x = 0.62$ mm and $w_y = 0.63$ mm for the doubled signal and $w_x = 1.1$ mm and $w_y = 0.96$ mm for doubled idler.

outcoupled power using the right axis. The displayed spectra were taken with the 1 mm BBO in the cavity. With the 1 mm thick BBO crystal the outcoupled $2s$ power is 100-200 mW and the outcoupled $2i$ power is 5-10 mW across the tuning range. Figure 3.3 shows the spatial profiles of the outcoupled $2s$ and $2i$ beams using the 1 mm BBO crystal for doubling, measured 45 cm from the output coupler M6. With the 2 mm thick BBO crystal, higher doubled powers are attained but the spatial profile of the $2s$ beam degrades significantly, while beam quality of the $2i$ beam was retained. Power with the longer crystal is also plotted for the doubled idler in Fig. 3.2, indicated by cross marks and using the right axis.

When doubling the idler, the idler wavelength found by optimizing the $2i$ power agree with both calculations for the LBO phase matching for the given crystal temperature as well as the idler wavelength found by optimizing the intracavity idler power without the BBO crystal. However, the oscillating signal wavelength found by optimizing $2s$ power is shifted, as illustrated in Fig. 3.4. The LBO parametric gain is phase matched over a large bandwidth due to the low group-velocity walkoff in the LBO crystal [157], and the OPO can thus oscillate far away from optimum parametric gain. Doubling the resonant signal influences the OPO oscillation and causes the optimum $2s$ power to be found blueshifted from the wavelength expected from both the LBO phase matching calculation and the optimum idler/$2i$ wavelengths found when not doubling the signal. Additional parasitic or cascaded nonlinear processes are not observed, and the idler wavelength shifts accordingly when the doubled signal was optimized.

We measured the visible pulse durations with a home-built two-photon autocorrelator. The interferometric autocorrelator uses an all-reflective design

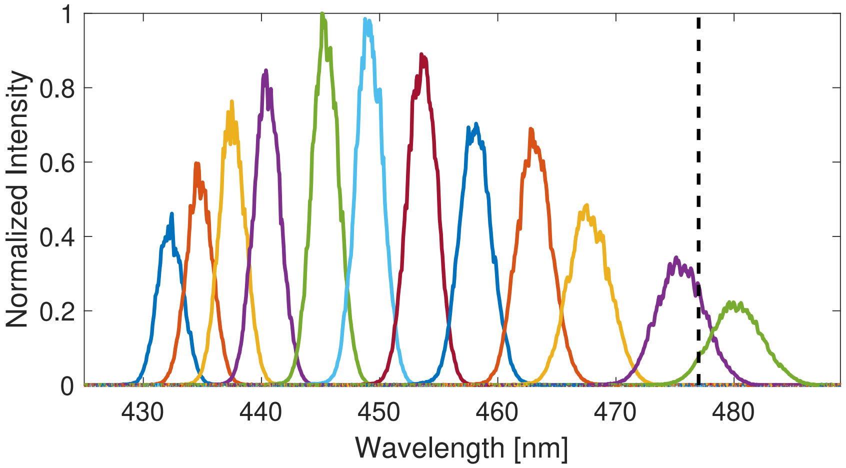

Figure 3.4: Doubled signal output spectra at a single LBO crystal temperature, T = 138° C as the OPO cavity length and BBO angle are tuned. All spectra normalized to the highest signal observed in the spectrometer. Dashed vertical line indicates the signal wavelength corresponding to the optimum doubled idler center wavelength for the same temperature.

similar to the one reported in [111] and uses a SiC two-photon photodiode (IFW Optronics) for the detector. The data is low-pass filtered to show only the intensity autocorrelation signal. Autocorrelations for the pump, $2s$, and $2i$ wavelengths are shown in Fig. 3.5 as well as Gaussian fits to the data. Assuming Gaussian pulses, all pulse durations are less than 150 fs.

For our target application of cavity-enhanced ultrafast spectroscopy [30], both low optical phase noise and low amplitude noise (RIN) are critical. In Figs. 3.6 and 3.7 we report both. For the RIN plot, the signal is recorded with a home-built low-noise amplified Si detector. At high frequencies, the RIN of the $2s$ and $2i$ beams is comparable to the low-RIN fiber laser used as the pump and competitive with high-performance fiber laser combs [159]. At frequencies below 1 kHz, the greater susceptibility of the free-space OPO cavity to acoustic and mechanical perturbations is seen in both the $2s$ and $2i$ RIN spectra.

For phase noise, the situation is more interesting. In steady state, the three frequency combs must share the same repetition rate and the optical pulses must obey the phase relationship [149, 150, 160]

$$\theta_p = \theta_s + \theta_i + \pi/2, \tag{3.1}$$

where θ_s, θ_i, and θ_p correspond to the optical carrier phases (i.e. carrier-envelope offset phase) of the signal, idler, and pump pulses, respectively. This relationship was explicitly verified by Kobayashi and Torizuka [150] for a singly-resonant OPO by observing heterodyne beats between the doubled signal and pump + idler. The beat notes were found to shift as the OPO

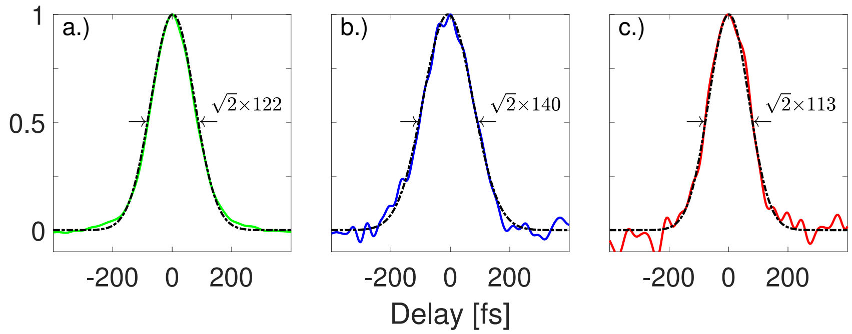

Figure 3.5: Normalized intensity autocorrelation traces for different visible outputs from SPOPO (solid) and Gaussian fit (black, dashed): a.) residual pump, b.) doubled signal, c.) doubled idler. Quoted pulse durations are FWHM assuming Gaussian pulse shape.

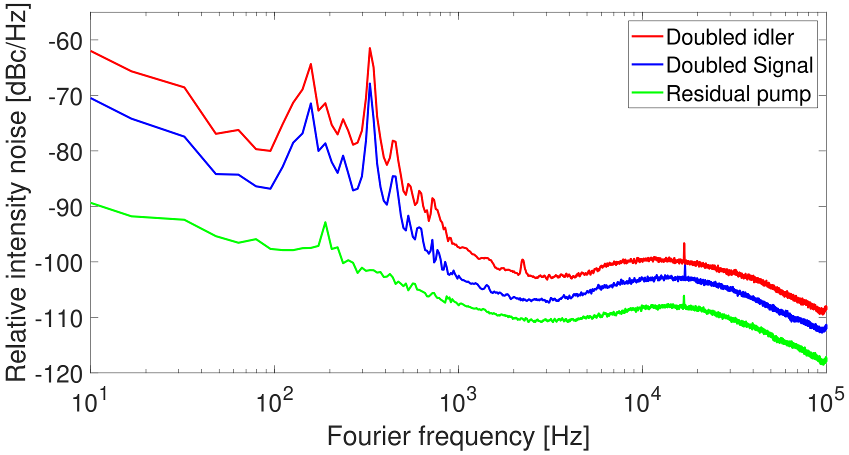

Figure 3.6: Relative intensity noise (RIN) of OPO pump, doubled signal, and doubled idler.

cavity length was changed, determining the relation

$$\left(\frac{\partial\theta_i}{\partial\theta_s}\right)_p = -1, \tag{3.2}$$

The notation $()_p$ is used to indicate that no actuation is done on the pump comb. The pump comb's f_0 is fixed and the relation shows direct phase transfer from signal to idler.

If instead the optical phase of the pump comb is perturbed, either via f_{rep} or f_0, in principle the signal and idler can share this phase change via Eq. (3.1) in a non-trivial way. To study how pump phase is shared between signal and idler, we measure the pump $\rightarrow 2i, 2s$ phase modulation transfer function and phase noise using the setup shown in Fig. 3.7a. The combs are stabilized to a 4-mirror femtosecond enhancement cavity (fsEC) with a finesse of ~ 1000 and net intracavity GDD < 100 fs^2 using a two-point Pound-Drever-Hall (PDH) technique [148, 161]. For locking the pump and doubled idler, 8 MHz PDH sidebands and fast feedback are applied to the combs via an electro-optic modulator, EOM1, in the Er:fiber oscillator, as shown in Fig. 3.7a. For the doubled signal, since the phase modulation transfer from the pump to the doubled signal is near zero (shown below), PDH sidebands are applied using a second EOM2 placed between the SPOPO and the fsEC, and fast feedback is applied to the copper bullet PZT on M3 of the OPO cavity. More technical details of the two-point locking feedback loops, broadband comb/cavity coupling, and the attainable performance will be discussed in Chapter 4. In the present discussion, we use the cavity as an optical phase discriminator. At high frequencies well above both the fsEC linewidth and the frequency-lock servo bandwidth, the PDH error signal acts as a phase discriminator [49, 56] and is insensitive to the details of the fsEC linewidth or the servo-loop. Essentially, the light reflected from the cavity is heterodyned with the intracavity light. A grating is used to disperse the spectrum reflected from the fsEC [148], so only a small fraction of the frequency comb bandwidth contributes to the PDH error signal used to record phase modulation.

To measure the pump → $2i, 2s$ phase modulation transfer functions, we apply sinusoidal phase modulation to the pump via EOM1 and record the modulation strength transferred to the $2s$ and $2i$ combs via the modulation sideband strength observed in the PDH error signal, similarly to [162]. The doubled signal and idler data is then divided by the the pump phase modulation strength measured the same way. The resulting pump → $2i, 2s$ transfer function is shown in Fig. 3.7b. The mean of the doubled idler transfer data (red) is 1.96 and the standard deviation is 0.13. The signal transfer coefficient (blue) is more than 20 times smaller than pump → $2i$ at all modulation frequencies. Since $\theta_{2i} = 2\theta_i$, the data in Fig. 3.7b imply

$$\left(\frac{\partial\theta_i}{\partial\theta_p}\right)_\ell = \frac{1}{2}\left(\frac{\partial\theta_{2i}}{\partial\theta_p}\right)_\ell = 1 \tag{3.3}$$

$$\left(\frac{\partial\theta_s}{\partial\theta_p}\right)_\ell \approx 0 \tag{3.4}$$

The notation $()_\ell$ is used to indicate that no actuation is done on the SPOPO cavity length. To our knowledge this is the first explicit verification of relations (3.3) and (3.4) and direct measurement of the transfer functions in Fig. 3.7b for a singly resonant OPO. This un-equal sharing result is quite different than the degenerate case measured by Wan et al. [163], where phase modulation on the pump is shown to be shared equally between the degenerate subharmonic signal and idler combs. The transfer function in Fig. 3.7b also shows that the OPO cavity linewidth is irrelevant for the transfer of optical phase from the pump to the non-resonant comb since there is no observable roll-off at the SPOPO cavity half-linewidth of 1.35 MHz.

Since all three combs must share the same f_{rep} (at least for modulation frequencies below the SPOPO cavity linewidth), Eq. (3.4) implies that for fixed SPOPO cavity length small repetition rate changes of the pump comb Δf_{rep}

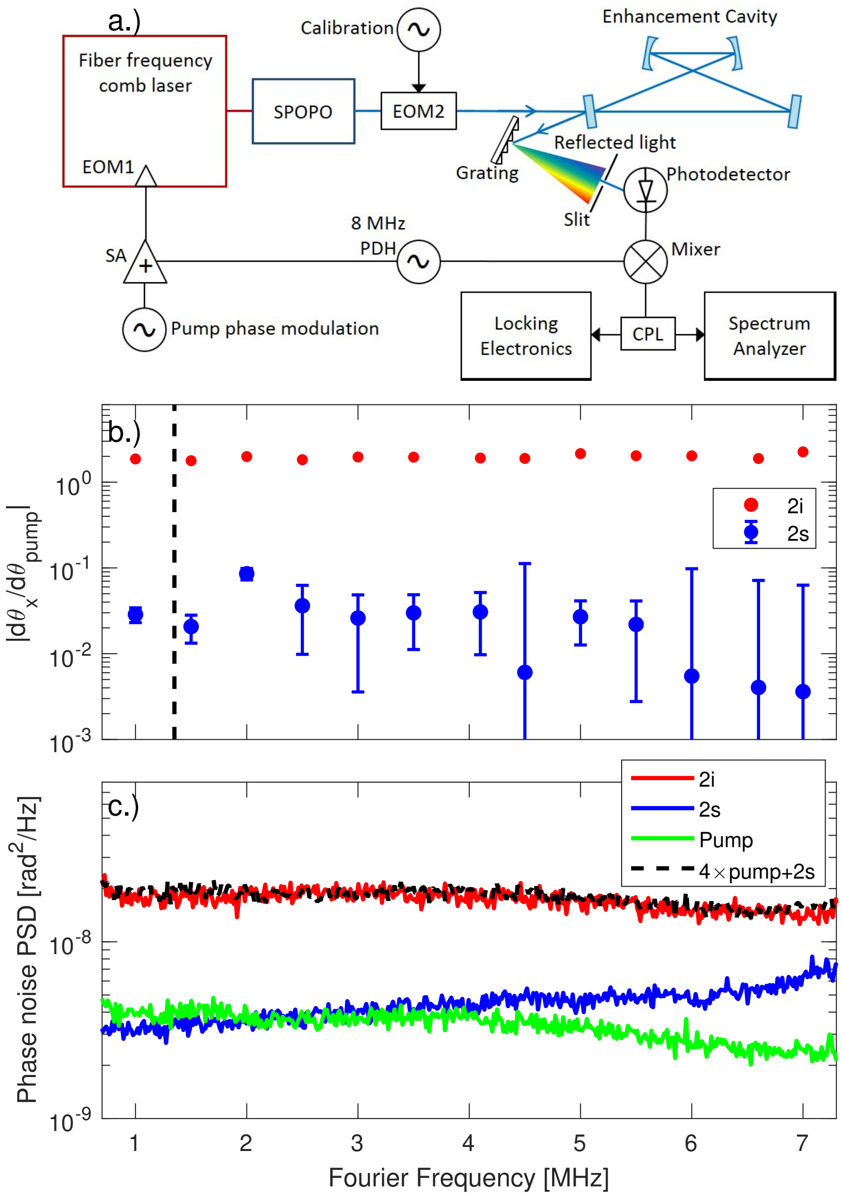

Figure 3.7: a.) Setup for measuring pump → $2i$ transfer function or phase noise of pump or $2i$ combs. See text for details as well as changes required for measuring $2s$ comb. SA: summing amplifier, CPL: directional coupler. b.) Pump → $2i/2s$ phase modulation transfer functions. Dashed vertical line indicates OPO cavity half-linewidth. c.) High frequency phase noise power spectral density of pump, doubled signal and doubled idler measured as well as the sum of Eq. (3.6) for comparison to $2i$ noise.

are counterbalanced by f_0 changes of the signal comb order $\Delta f_{0,s} = -\Delta f_{\text{rep}} \frac{\nu_s}{f_{\text{rep}}}$, where ν_s is the signal's optical carrier frequency. In this way, the fixed point [75] of the signal comb under pump actuation is the signal's optical carrier frequency. More precisely, the data of Fig. 3.7b constrain the location of this fixed point to be within 15 THz of the signal's optical carrier frequency.

We also used the setup of Fig. 3.7a to measure the optical phase noise of the $2s$, $2i$, and pump combs. Figure 3.7c shows the measured optical phase noise power spectral densities for Fourier frequencies 1MHz $< f <$ 7MHz in rad^2/Hz. The y-axis of the figure is calibrated by applying a known phase modulation to all three combs in identical fashion using EOM2. The pump and doubled signal are at similar levels while the doubled idler is about 4 times (6 dB) higher. This can be understood using the phase transfer relations (3.2), (3.3), (3.4). Equations (3.3) and (3.4) imply that optical phase fluctuations of the pump are transferred with unit efficiency to the idler, and any intrinsic OPO noise on the signal comb is uncorrelated. This implies that the two noise sources contribute to the idler phase noise in quadrature, viz.

$$(\Delta\theta_i)^2 = \left(\frac{\partial\theta_i}{\partial\theta_p}\right)_\ell^2 (\Delta\theta_p)^2 + \left(\frac{\partial\theta_i}{\partial\theta_s}\right)_p^2 (\Delta\theta_s)^2 \tag{3.5}$$

or in terms of the $2i$, $2i$ and pump combs

$$(\Delta\theta_{2i})^2 = 4\left(\frac{\partial\theta_i}{d\theta_p}\right)_\ell^2 (\Delta\theta_p)^2 + \left(\frac{\partial\theta_i}{\partial\theta_s}\right)_p^2 (\Delta\theta_{2s})^2 \tag{3.6}$$

The sum on the right-hand side of Eq. (3.6) is also plotted on Fig. 3.7c as a dashed, black line, for comparison with the the measured $2i$ phase noise power spectral density. Excellent agreement is found over the entire measured frequency range.

3.4 Conclusions

In this chapter, we have provided a detailed description of the design and performance of a fiber-laser-pumped OPO delivering high-power tunable frequency combs across the visible region. The high output power and broad tuning range make the combs particularly suitable for performing ultrafast nonlinear spectroscopy with combs, where frequency comb methods have recently allowed large improvements in resolution [152, 164] and sensitivity [30]. The tunable combs can also be used in other comb applications such as high-resolution cavity-enhanced (linear) comb spectroscopy [46, 165], or in myriad less specialized applications where tunable high-repetition rate femtosecond sources are needed [154, 155].

Using an external cavity as a phase discriminator, we directly compared the phase noise of all three combs and the pump → signal and pump → idler phase modulation transfer functions. We find that phase perturbations on the pump are transferred to the (non-resonant) idler comb via the optical phase relations (3.3) and (3.4). These relations have two important consequences for the use of the SPOPO's signal and idler beams for comb applications. First is that the phase noise of the resonant signal is uncorrelated to that of the pump. This further helps explain the extremely low noise performance obtainable with (resonant) OPO combs, in addition to the technical reasons discussed in [149]. The second is that actuation on the non-resonant SPOPO-generated comb via the phase of the pump does not suffer a low-pass filter due to the SPOPO cavity. This enables the use of high-bandwidth transducers, such as EOMs, in the pump comb's mode-locked laser cavity [113, 166] to be used to control the phase of the non-resonant comb (in our case the idler) of the OPO without needing to consider the SPOPO cavity linewidth in the design. For our SPOPO, with ~ 2.7 MHz linewidth, the SPOPO cavity would not impose a significant low-pass filter in any event, but this point is important for SPOPOs that use higher cavity finesses to achieve low pump-power thresholds for oscillation [167].

Chapter 4

Widely tunable cavity-enhanced frequency combs

This chapter contains a reproduction of our publication *Widely tunable cavity-enhanced frequency combs*, Myles C. Silfies, Grzegorz Kowzan, Yuning Chen, Neomi Lewis, Ryan Hou, Robin Baehre, Tobias Gross, and Thomas K. Allison, *Optics Letters* **45**:2123, (2020) [2], with permission from Optica publishing. The original manuscript was modified slightly for clarity and formatting.

4.1 Introduction

The cavity enhancement of stabilized ultrafast pulse trains, or frequency combs, first demonstrated around the turn of the century [148, 168], has since been used in many applications. In this technique, successive pulses from the frequency comb are constructively interfered with a circulating intracavity pulse by tuning both the comb's repetition rate (f_{rep}) and carrier-envelope offset frequency (f_0) such that the frequency comb's "teeth" are matched with the enhancement cavity resonance frequencies over a large spectral bandwith. In some applications, this method is used to enhance the intracavity power to drive nonlinear processes at high repetition rate. For example, with kilowatts of circulating average power, one can generate high-order harmonics at high repetition rate [169], and this is now being used for precision spectroscopy [123] and high-repetition rate photoelectron spectroscopy experiments [170–172]. Other ultrafast nonlinear processes have also used the high intracavity power, such as molecular alignment [173] and spontaneous parametric down conversion [174]. In another class of applications, it is the enhancement of sensitivity that is sought, such as in cavity-enhanced direct frequency comb spectroscopy, reviewed by Adler et al. in 2010 [46] and continuing to make rapid progress since then [48, 175, 176]. A new application of cavity-enhanced frequency combs developed by our group uses the enhancement of both laser power and sensitivity to obtain a large improvement in the detection-limits of ultrafast nonlinear spectroscopy [30, 71].

In all of this previous work, the cavities have been carefully designed to enhance frequency combs with a certain center wavelength for a specifically targeted intracavity experiment, with limited bandwidth and little or no tuning range. In contrast, frequency comb experiments without cavities are increasingly using combs covering very wide spectral ranges, and the development of widely tunable and broadband frequency combs has recently been the subject of intense research [121, 126–133].

The cavity-enhancement of frequency combs over a wide spectral range poses a number of technical challenges. First, one must have a tunable frequency comb with transducers to control both the f_{rep} and f_0 of the comb, with at least one high-bandwidth transducer to tightly lock the comb to the cavity or vice/versa. This makes it difficult to use the recently popular offset-free "DFG combs" [87, 177], for example. Second, the combs should have low optical phase noise. For typical repetition rates of ~ 100 MHz, even modest cavity finesses of ~ 1000 have small optical linewidths of ~ 100 kHz. The linewidths of the comb's "teeth" should then be substantially narrower than this in order to avoid increased intensity noise on the intracavity light or a reduction in effective input power, and accomplishing this requires special care [113]. Third, in order to couple a large comb bandwidth, and thus short pulses, into the cavity, very good control of the cavity's intracavity group-delay dispersion (GDD) must be achieved. The intracavity spectral width (HWHM) that a cavity with finesse $\mathcal{F}$ is approximately $\Delta\omega = \sqrt{2\pi/(\mathcal{F}\Phi_{GDD})}$. Maintaining sub-200 fs pulses in a cavity with finesse of ~ 1000 therefore requires GDD control at the level of ~ 100 fs^2. Achieving intracavity GDD this low at one design wavelength is straightforward, but managing dispersion at this level over a wide tuning range, while also satisfying the constraints imposed by high cavity finesse and high average powers requires careful design of the cavity mirror coatings and precise control of the coating process.

4.2 Cavity design

In this chapter, we address the challenges introduced above, focusing on the visible spectral range, using a recently developed widely tunable frequency comb source [3] and a novel cavity coating design. The design of our femtosecond enhancement cavity (fsEC) is shown in Fig. 4.1(a). The fsEC is a 4-mirror bow-tie configuration with 2 plane partial reflectors, M1 and M4, of nominally 0.3% transmission and 2 high reflectors (transmission $< 0.1\%$), M2 and M3, with 50 cm radius of curvature. The theoretical mirror transmission is shown in Fig. 4.1(b) for the design range of 450 to 700 nm. In order to minimize net cavity GDD, the two mirror coatings have opposite chirp i.e., the high reflector is constructed such that longer wavelengths reflect from deeper in the coating whereas in the partial reflector this relation is reversed [178]. The GDD, measured by white light interferometry, is shown in Fig. 4.1(c) for both

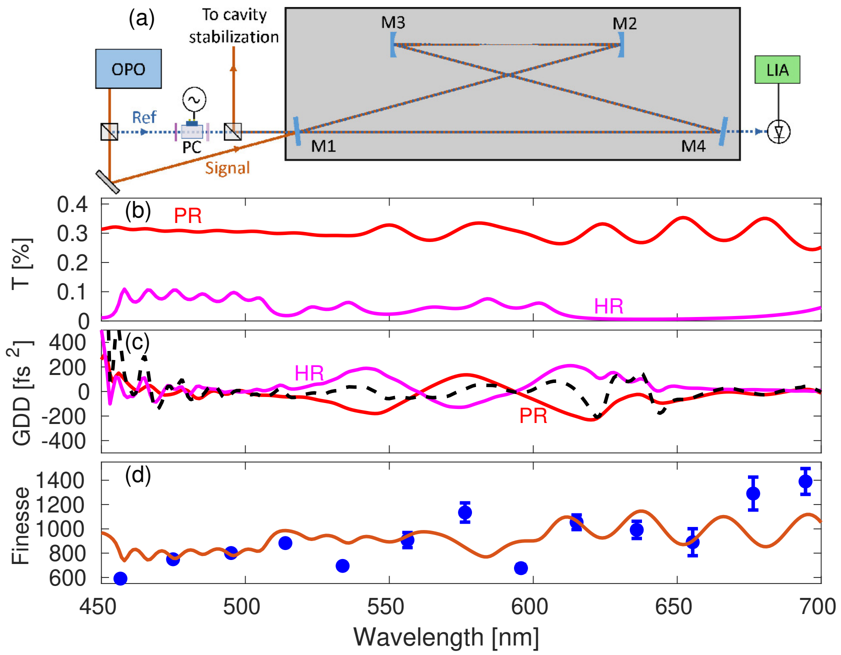

Figure 4.1: (a) Setup for the CAPS measurement and design of the enhancement cavity. M1 and M4 are partial reflectors (PR) and M2 and M3 are high reflectors (HR). PC: Pockels cell, LIA: lock-in amplifier (b) Theoretical mirror transmission (T) for the 2 mirrors. (c) GDD for the two mirror coatings. Black dashed line is the net cavity GDD assuming the geometry in (a). (d) Measured cavity finesse (circles). Line is theoretical finesse.

mirrors as well as the expected net cavity GDD assuming two of each mirror (black, dashed). Both the net GDD and reflectivity are varying and structured which is expected for such a large operating range, and this results in an overall cavity performance that varies with wavelength. The mirrors were coated using ion beam sputtering with alternating layers of Ta_2O_5 and SiO_2. The total coating structures have thickness of 6.45 μm and 4.86 μm for the HR and PR respectively and the coatings were annealed first at 200°C for 5 hours and then at 300°C for an additional 4 hours to reduce loss. The spot size at the smaller waist is calculated using the ABCD matrix formalism to have a $1/e^2$ radius of 65 µm at 530 nm. The spot size scales with wavelength only weakly as $\sqrt{\lambda}$ [92]. The entire cavity is contained in a vacuum chamber which is held at a pressure below 100 mTorr to minimize GDD from air and avoid air currents.

The input combs are derived from a home-built synchronously pumped optical parametric oscillator (OPO) operating at 100 MHz repetition rate, previously described in Chapter 3 [3]. This OPO is pumped by the second harmonic of a home-built high-power frequency comb laser consisting of a dispersive-wave shifted Er:fiber comb [87] with high-bandwidth transducers, amplified in a Yb-doped photonic crystal fiber amplifier [113]. To cover the entire tuning range, we use all three of the frequency doubled signal ($2s$, 450-

515 nm), residual pump (535 nm), and doubled idler ($2i$, 555-700 nm) from the OPO.

4.3 Cavity Finesse

To characterize the fsEC performance, we first measure the cavity finesse, $\mathcal{F}$, across the design wavelength range. To measure the finesse, we use the cavity attenuated phase shift (CAPS) method [179, 180]. In this method, the input laser to the cavity is amplitude modulated at an angular frequency Ω and the relative phase shift of the cavity transmitted light is measured. The phase shift, ϕ, is due to the cavity acting as a low pass filter and is related to the cavity storage time, τ, by:

$$\tan(\phi) = -\Omega\tau \tag{4.1}$$

Which, in turn, is related to finesse via:

$$\mathcal{F} = 2\pi\tau f_{\text{rep}} \tag{4.2}$$

To measure finesse via the CAPS method while remaining frequency-locked to the cavity, we send two identical beams into the cavity in counterpropogating directions as shown in Fig. 4.1(a) and described in [30]. The forward beam, labeled signal, is used for locking while the second, labeled reference, is used for the measurement. For our CAPS implementation, the reference beam is sent through a Pockels cell between two polarizers. The Pockels cell is driven with sine wave with a peak value $\approx 3\%$ of the half-wave voltage. The first polarizer is detuned from the second, which optically biases the cell to get a cleaner sinusoidal output at the drive frequency. The reference beam at the cavity output is sent to a photodiode and lock-in amplifier measuring the phase shift relative to a leakage reference beam which bypasses the cavity.

The measured cavity finesse across the design range is shown in Fig. 4.1(d) along with the theoretical finesse, calculated assuming the reflectivity is one minus the transmission shown in Fig. 4.1(b). The mean measured value is 927. The data shown is an average of 2 CAPS phase measurements taken at 70 and 90 kHz modulation frequency. At each frequency, the lock-in phase is recorded for 10 seconds and then the average and standard deviation is calculated which is used to find the error in each measurement. The error is higher on the long wavelength side due to both lower output intensity and higher intensity noise, which will be discussed below. In general, the measured data agrees well with theory, following the general trend of increasing finesse at longer wavelengths. The discrepancies on the blue side we suspect are due to absorption in the coatings and on the red side we believe are due to changes in the coating during annealing and geometrical differences such as not perfectly matching the angle of incidence to the design. The cavity loss is dominated by the two PR mirrors and the cavity is nearly impedance matched [49]. In this case the absorption sensitivity enhancement factor remains approximately $\mathcal{F}/\pi$ and is greater than 190 across the tuning range [50].

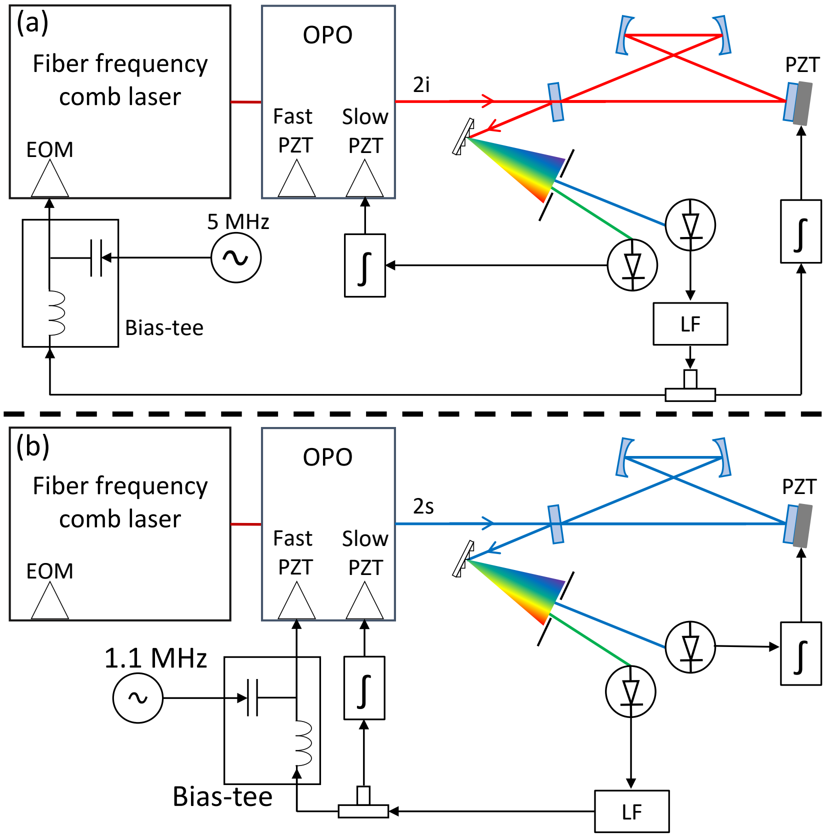

Figure 4.2: Schematics for locking input comb to the enhancement cavity for (a) the doubled idler and (b) the doubled signal. PZT: piezoelectric transducer, EOM: electro-optic modulator, LF: loop filter

4.4 Broadband comb/cavity coupling

The finesse measurements are relatively simple and independent of the details of the comb/cavity coupling. For measuring the performance of the setup for cavity-enhancing frequency combs with maximum bandwidth, more discussion of the frequency comb and stabilization schemes is required. For all these measurements, we use a two-point Pound-Drever-Hall (PDH) locking scheme [161], with a fast servo loop tightly locking one portion of the frequency comb to the cavity, and a second slower loop bringing another part of the comb onto resonance with a linearly independent actuator. This basic scheme has been used previously in many contexts [30,47,148,181]. However, accomplishing comb/cavity coupling over such a large and unprecedented tuning range presents technical challenges. In particular, the phase transfer properties of the OPO, studied in detail in [3], necessitate different comb/cavity stabilization schemes for each of the three combs from the OPO (pump,2i,2s), as discussed below.

For coupling the $2i$ comb to the cavity, since phase modulation on the pump is transferred directly to the $2i$ comb with no bandwidth penalty imposed by

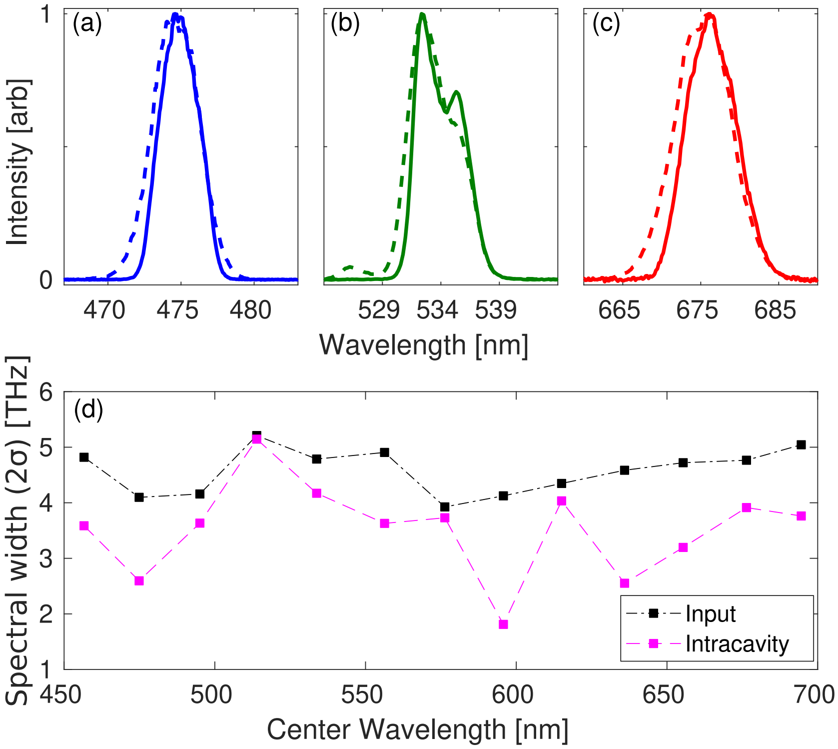

Figure 4.3: (a-c) Intracavity (solid) and input (dashed) spectra for $2s$ (a), pump (b), and $2i$ (c) combs. (d) Optimized intracavity spectral widths compared with the incident width.

the OPO cavity [3], we use an electro-optic modulator (EOM) in the mode-locked fiber laser to apply both 5 MHz PDH sidebands and for feedback in the fast PDH loop, as shown in Fig. 4.2(a). This acts on the pump and $2i$ combs with a fixed point [75] near DC, mainly acting on the f_{rep} degree of freedom of the combs. The cavity's free spectral range is kept within the EOM's f_{rep} tuning range with an additional slow servo acting on the enhancement cavity length. For controlling the second comb degree of freedom in the slow PDH loop, we actuate on the OPO cavity length, which acts only on the comb's f_0 degree of freedom. When coupling the pump light to the enhancement cavity, the fast loop is identical to the $2i$ case shown in Fig. 4.2(a) and the slow loop actuates on a the temperature of the EOM in the mode-locked fiber laser to control f_0.

For coupling the $2s$ comb to the cavity, the high-speed actuators of the pump laser are of no use since phase modulation on the pump comb is not transferred to the $2s$ comb, as discussed in detail in [3]. Thus, comb/cavity coupling is accomplished with the pump comb free-running, and feedback signals are instead applied to the OPO cavity and fsEC, as shown in Fig. 4.2)(b) The fast servo PDH loop drives a copper-bullet-style piezoelectric transducer (PZT) [158] to actuate on OPO cavity length and the f_0 of the $2s$ comb. PDH sidebands at 1.1 MHz are also generated by this PZT at a mechanical resonance. The slow loop controls the fsEC cavity length with a long travel PZT. When locking either the $2i$ or $2s$ combs, care must be taken when selecting the locking points in the spectrum since small changes in OPO cavity length can change the output spectrum dramatically which can result in complicated, multi-peaked intracavity spectra or significantly decreased power. Monitoring of the input and intracavity spectra simultaneously while locking helps avoid

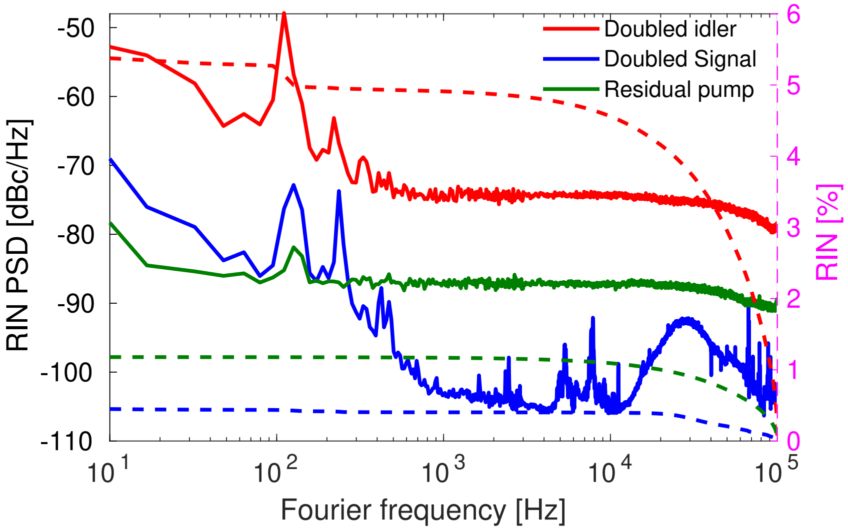

Figure 4.4: Relative intensity noise of the intracavity light. Left axis: RIN power spectral density (solid lines), right axis: integrated RIN up to 100 kHz (dashed lines).

this problem.

4.5 Intracavity spectral bandwidth

The fundamental limit to the attainable intracavity pulse duration is given by the attainable intracavity spectral width, which is in turn related to the input spectrum and the intracavity dispersion. We have measured both the incident OPO input spectrum and intracavity spectra across the tuning range. Example intracavity spectra of the $2s$, $2i$, and pump combs are shown in Figs. 4.3(a)-(c), along with the corresponding input spectra. Figure 4.3(d) shows the input and intracavity spectral widths (2σ) measured at 13 wavelengths across the tuning range. The attainable intracavity bandwidth is less than the input OPO bandwidth due to residual mirror dispersion. Due to GDD, the intracavity spectra are more square-shaped than the input so standard Gaussian transform limit relations do not apply. Still, even the smallest bandwidths measured support sub-200 fs FWHM pulses across the tuning range when Fourier transformed.

4.6 Intracavity noise

In order to use the cavity-enhanced combs for our target application of ultrasensitive ultrafast optical spectroscopy [30, 71], low noise on the intracavity light is required. We have previously measured the amplitude noise of the input combs and found it to be sufficient [3]. However, since an optical cavity is a phase discriminator [49, 56], residual phase noise present on the input comb is converted to amplitude noise on the intracavity light. The relative intensity noise (RIN) data is shown in Fig. 4.4 for the $2s$, $2i$, and pump combs. The OPO idler inherits the phase noise from the pump and signal such that the $2i$ comb has the highest phase noise [3] of the three combs and thus the largest high-frequency RIN. Conversely, the $2s$ comb has the lowest optical phase noise and thus the lowest high-frequency RIN, despite far inferior servo bandwidth for the PZT locking scheme of Fig. 4.2(b).

4.7 Conclusion

In conclusion, we have for the first time demonstrated the cavity-enhancement of frequency combs with a widely tunable platform. The wide tuning range of > 7900 cm^{-1} covers nearly the entire visible spectrum. Despite the technical challenges wavelength tuning imposes on the frequency comb generation, cavity mirrors, and comb/cavity coupling, we have demonstrated performance that is comparable to that used in previous experiments using cavity-enhanced combs [30, 170, 182]. For example, comparing to the previous one-wavelength demonstration of cavity-enhanced transient absorption spectroscopy [30], we report here the achievement of comparable or better intracavity RIN across the tuning range, with higher cavity finesse, while maintaining similar intracavity optical bandwidth. We expect further refinements in cavity-mirror coating technology and frequency combs to further improve the attainable performance.

Chapter 5

Broadband cavity-enhanced transient absorption spectrometer

This chapter contains a reproduction of our publication *Broadband cavity-enhanced ultrafast spectroscopy,* Myles C. Silfies, Grzegorz Kowzan, Neomi Lewis and Thomas K. Allison, *Phys. Chem. Chem. Phys.* , **23**:9743, (2021) from Ref. [1] with permission from the PCCP Owner Societies. The text has been edited for continuity, the introduction is modified from the original manuscript, and sections 5.3.2 and 5.3.4 are original.

5.1 Introduction

In this chapter, I report the development of a broadband cavity-enhanced ultrafast transient absorption spectrometer (CE-TAS) operating across the wavelength band of 450-700 nm—a bandwidth greater than 7900 cm^{-1} (240 THz) covering almost the entire visible spectral range. To go from the previously demonstrated single wavelength CE-TA [30] to broadband CE-TA**S** has involved considerable innovation, since many of the necessary components did not exist prior to our work. Previous chapters reported results regarding aspects of the optical technology critical to CE-TAS, namely the development of widely tunable, low noise, high-power frequency combs [3] and the enhancement of these widely-tunable combs in a femtosecond enhancement cavity with custom mirror coatings [2]. Achieving reliable and reproducible transient absorption spectroscopy data with Δ OD $< 10^{-9}$ using this optical technology has also required significant innovation which we detail in this chapter, where we present the first spectroscopy results from this system. To our knowledge, this also the first cavity-enhanced comb spectroscopy of any kind (ultrafast or otherwise) using a widely tunable platform.

This work establishes CE-TA**S** as a new broadly applicable technique for gas-phase chemical physics, and creates a missing link between gas-phase and

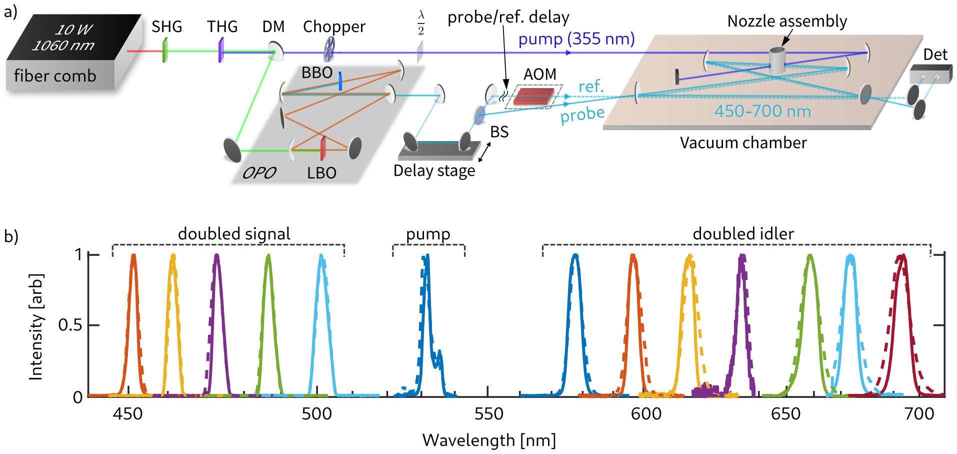

Figure 5.1: a) Optical layout of the broadband cavity-enhanced transient absorption spectrometer. Tunable frequency combs are derived from a synchronously pumped optical parametric oscillator (OPO) and coupled to a 4-mirror broadband dispersion-managed enhancement cavity. The third harmonic of the Yb:fiber comb at 355 nm is used for molecule excitation in the current experiments. More details regarding the optical components are in the main text and references [2,3]. b) OPO (dashed) and cavity-enhanced (solid) spectra across the OPO 450-700 nm tuning range. Broadband spectra are assembled from pump/probe traces recorded with different OPO wavelengths.

solution-phase studies as discussed in Chapter 1. For gas-phase molecules, UV-visible CE-TAS provides another projection of the dynamics complimentary to gas-phase TRPES, with a dataset that is directly comparable to solution-phase work via the common observable. Cluster studies enabled by CE-TAS also allow probing intermediate levels of solvation.

These broadband CE-TAS methods can also be adapted for work on solids, ultra-dilute solutions, or sparsely covered surfaces that would benefit from improved sensitivity. In the sections below I will describe the many unique aspects of the spectrometer and a detailed analysis of its performance.

5.2 Experimental Setup

5.2.1 Light Sources and Enhancement Cavity

The optical setup is illustrated in Fig. 5.1a). As described in Chapter 2, the initial frequency comb at 1064 nm is derived from a 1550 nm Er:fiber oscillator (Menlo Systems Ultra-Low-Noise variant), shifted to 1064 nm using dispersive-wave generation in a short highly nonlinear fiber [87]. We then amplify the shifted Er:fiber comb to 10 W average power in a home-built large-mode-area Yb-doped photonic crystal fiber amplifier previously described [113]. The 100 MHz repetition-rate (f_{rep}) amplified pulse train from this laser is frequency doubled and tripled (2+1) in critically phase-matched lithium triborate (LBO) and beta barium borate (BBO) crystals, respectively. We use the third harmonic at 355 nm from this setup, with approximately 500 mW of average power, for the pump in the CE-TAS measurements presented here. For most of the present measurements, working with molecules with relatively large excitation cross sections, we obtain sufficient signal to noise without employing an enhancement cavity for the pump to boost the pump power, as was done in Reber et al. [30]. Operation with a UV pump cavity will be briefly described in section 5.3.4 below for samples with lower vapor pressure. We use the residual second harmonic (4.5 W) to pump a home-built tunable synchronously-pumped optical parametric oscillator (OPO) with subsequent intracavity doubling for both the signal and idler [3]. Using the 532 nm pump as well to cover the gap near OPO degeneracy, this provides tunable combs over the range of 420-720 nm, as described in Chapter 3 [3].

We couple the tunable combs from the OPO to a broadband enhancement cavity with custom mirror coatings optimized to manage group-delay dispersion (GDD) over a wide tuning range, as described in detail in Chapter 4 [2]. Fig. 5.1b) shows representative OPO and enhanced intracavity spectra across the tuning range. The intracavity spectra are narrower that the OPO spectra due to residual GDD of the enhancement cavity. As has been discussed in previous works [66, 67, 169], GDD sets the limit to the simultaneous intracavity bandwidth, and thus intracavity pulse duration, that can be attained irrespective of the incident comb bandwidth. The cavity is in a bow-tie configuration with two plane mirrors for the input and output couplers (nominal 0.3% transmission), and two high reflectors with 50 cm radius of curvature. With most of the cavity loss coming from the input and output couplers, the cavity is close to the impedance-matched condition [49]. We calculate the beam size ($1/e^2$ radius) to be $w_{\text{probe}} = 65\ \mu$m at 532 nm using the ABCD matrix formalism, and this only scales weakly with probe wavelength as $w_{\text{probe}} \propto \sqrt{\lambda}$ [92]. The cavity has a nominal finesse ($\mathcal{F}$) varying from 600 to 1400 across the range of 450-700 nm. OPO output wavelengths outside this range are not used due to the limits of the cavity mirror high-reflectance band. We focus the 355 nm pump beam to a waist size of approximately $w_{\text{pump}} = 150\ \mu$m and overlap the pump focus with the enhancement cavity focus above the molecular beam source, as illustrated in Fig. 5.1. The pump beam is chopped at a frequency between 3 and 4 kHz, well inside the enhancement cavity's minimum linewidth of 70 kHz (above which the cavity would low-pass filter the CE-TA signal unless higher-order modes are used [49, 71]), but above the lab's $1/f$ noise.

Although the residual OPO pump (532 nm), doubled signal ($2s$), and doubled idler ($2i$) combs follow the same optical path, there are substantial differences to the setup for using each of these three combs. First of all, the OPO optical-phase transfer relations discussed in Chapter 3 [3] necessitate that the three different combs are frequency-locked to the enhancement cavity using three different schemes with different actuators, as discussed in Chapter 4 [2].

Furthermore, there are substantial differences in the relative intensity noise (RIN) spectra of the intracavity light before the common-mode noise rejection scheme described below is applied [2]. Also, we change the mode-matching optics between the OPO and the enhancement cavity when changing between output combs to account for different spatial modes and divergence from the OPO. Despite all these differences, comparable CE-TAS performance can be obtained using all three combs as we show in section 5.3.

5.2.2 Vacuum System and Supersonic Expansion

The enhancement cavity is mounted on a 60 cm × 120 cm breadboard inside a rectangular vacuum chamber. The breadboard is supported via legs that protrude through the bottom of the chamber via bellows down to the optical table. In this way the breadboard is isolated from vibrations of the vacuum chamber or flexure of the vacuum chamber upon pump out.

Molecules are introduced at the common focus of the probe cavity and the pump beam using a continuously-operating slit nozzle. A planar expansion, as opposed to an axisymmetric expansion from a pinhole, is used to attain a higher column density of molecules and also facilitate cluster studies [183]. The gas load of the continuous planar expansion is handled by a three-stage pumping system consisting of two Roots pumps (5000 m^3/hr and 1400 m^3/hr) in series backed by a two-stage 100 m^3/hr oil-sealed rotary vane pump.

To prevent cavity mirror contamination, the supersonic expansion takes place in a small inner chamber inside the main vacuum chamber, as shown in Fig. 5.2. The inner chamber is maintained at $\sim$100 mTorr via the Roots pumping system. The inner chamber is connected to the main chamber via two 3 mm holes that allow the laser beams to pass through. We then flow Argon gas into main chamber which creates a flow of Ar into the inner chamber via these 3 mm holes. This steady purging flow prevents sample molecules from exiting the inner chamber. Argon is used instead of nitrogen to avoid possible artifacts due to non-resonantly excited rotational coherences [184]. Typical argon pressures in the main chamber are $\sim$10 mbar, which is sufficient to prevent mirror contamination, but small enough that it does not produce enough group delay dispersion to narrow the enhanced comb bandwidth [185]. A small flow of oxygen is also directed at each cavity mirror to further help mitigate hydrocarbon contamination.

For introducing non-volatile molecules to the experiment, molecules are sublimed at temperatures up to 150° C in a cell external to the vacuum chamber and then entrained in a flow of noble carrier gas. The supersonic nozzle assembly and associated gas feedline are also heated to prevent molecule condensation. Typical sample consumption rates are 0.5-3 g/hr.

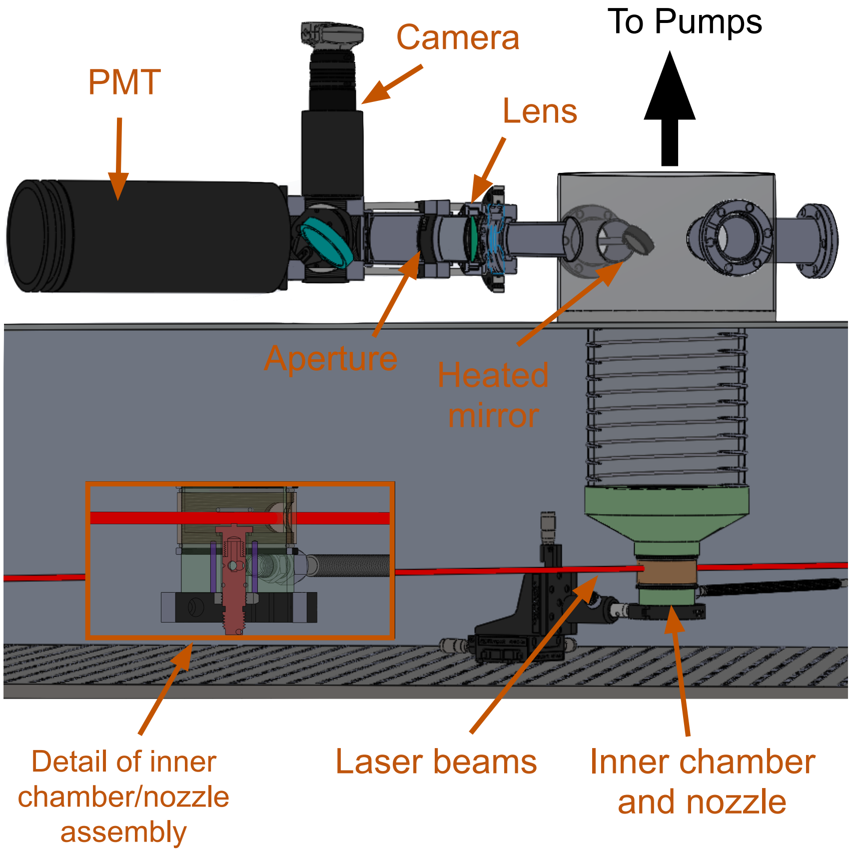

Figure 5.2: Molecular beam setup and fluorescence monitor. The fluorescence detection scheme is described in detail in the main text. Inset shows a cutaway of the nozzle assembly. The inner chamber surrounding the heated nozzle contains the sample molecule near the pump/probe overlap region.

5.2.3 Procedure for Individual CE-TA Pump/Probe Trace Accumulation

When recording transient absorption measurements using any of the three combs, we couple a delayed reference pulse train to the cavity in a counter-propagating direction as shown in Fig. 5.1a). The resulting pulse sequence at the molecular beam is shown in Fig. 5.3a). The reference beam pulses arrive ∼5 ns later than the probe and pump. The normalized pump/probe CE-TA signal (ΔS) at each OPO wavelength is recovered via autobalanced subtraction (probe−reference) [186] and lock-in detection at the pump modulation frequency, such that the CE-TAS signal is given by

$$\Delta S(\tau) = \frac{\pi}{\mathcal{F}} \frac{\Delta I(\tau) - \Delta I(\tau + 5\text{ ns})}{I_{\text{probe}}} \equiv \beta \left[\Delta I(\tau) - \Delta I(\tau + 5\text{ ns})\right] \qquad (5.1)$$

where τ is the pump/probe delay, I_{probe} is the intracavity light intensity for the probe beam, the ΔI are pump-induced changes in the intracavity light intensity, and the factor $\pi/\mathcal{F}$ is the inverse of the cavity enhancement cavity for impedance-matched cavity and our experimental geometry [50]. The subtraction accomplishes two critical tasks. First and most important is common-mode noise subtraction. The probe ($\Delta I(\tau)$) and reference ($\Delta I(\tau + 5 \text{ ns}) \approx \Delta I(5 \text{ ns})$) share mostly the same noise, but have different pump/probe delay-dependent signals due to their timing with respect to the pump pulse train. Since at $\tau + 5$ ns all fast dynamics have subsided, the subtraction retrieves the femtosecond-delay dependent signal from the noise. Fig. 5.3b) shows the effect of this common-mode noise rejection scheme on the relative intensity noise (RIN) of the intracavity light. With autobalanced subtraction, the noise floor of the measurement is within one order of magnitude (20 dB in RIN) of the quantum noise limit.

Second is that the $\Delta I(\tau+5 \text{ ns})$ reference signal also contains any signal due to repetitive pumping of the sample or molecular excitation that lives longer than $1/f_{\text{rep}} = 10$ ns. Another way to think of this is that due to the 100 MHz repetition rate, in steady state $\Delta I(\tau = 5 \text{ ns}) = \Delta I(\tau = -5 \text{ ns})$ such that the subtraction of the reference signal removes any signal due to preceding pump/probe pulse sequences. This is relevant since for a molecular beam speed of 500 m/s (e.g. for an Ar supersonic expansion), each molecule sees approximately $f_{\text{rep}} \times (300\ \mu\text{m}/500\text{m/s}) = 60$ pump pulses. The problem can be exacerbated via velocity slip between the sample molecule and the carrier gas, and even for molecules with short-lived excited states, a ground-state bleach signal may persist. Subtraction of any persistent signal enables CE-TAS to work even with these complications. For most purposes $\Delta S(\tau)$ can be regarded as the femtosecond to picosecond component of the true TAS signal induced by a single pump pulse, simply with a DC offset subtracted. However, one must be aware of subtleties. For example, since the absolute signal size is reduced via subtraction of $\Delta I(5 \text{ ns})$, care must be taken in considering signal ratios as discussed in section 5.3.

The polarization of the probe light is horizontal (p). The pump polarization is controlled to be either p or s (vertical) with a zero-order half wave plate to give pump/probe signals for both parallel ($\Delta S_{\parallel}$) and perpendicular ($\Delta S_{\perp}$) polarization conditions, respectively. We construct magic-angle signals, insensitive to molecular orientation or rotational coherences, via $\Delta S_{MA} = (\Delta S_{\parallel} + 2\Delta S_{\perp})/3$ [51, 187]. Another interesting subtlety of CE-TAS is that magic-angle data cannot be recorded simply by orienting the pump polarization 54.7° to the probe, as is usually done in transient absorption spectroscopy. This is due to the fact that the non-zero angles of incidence on the enhancement cavity mirrors causes the p and s eigenmodes of the cavity to be non-degenerate. Thus light scattered into an s mode of the cavity by a magic angle pump would not be exactly on resonance, leading to increased noise and also a different signal enhancement. Using only s and p pump polarizations ensures that the intracavity probe light remains p-polarized by symmetry.

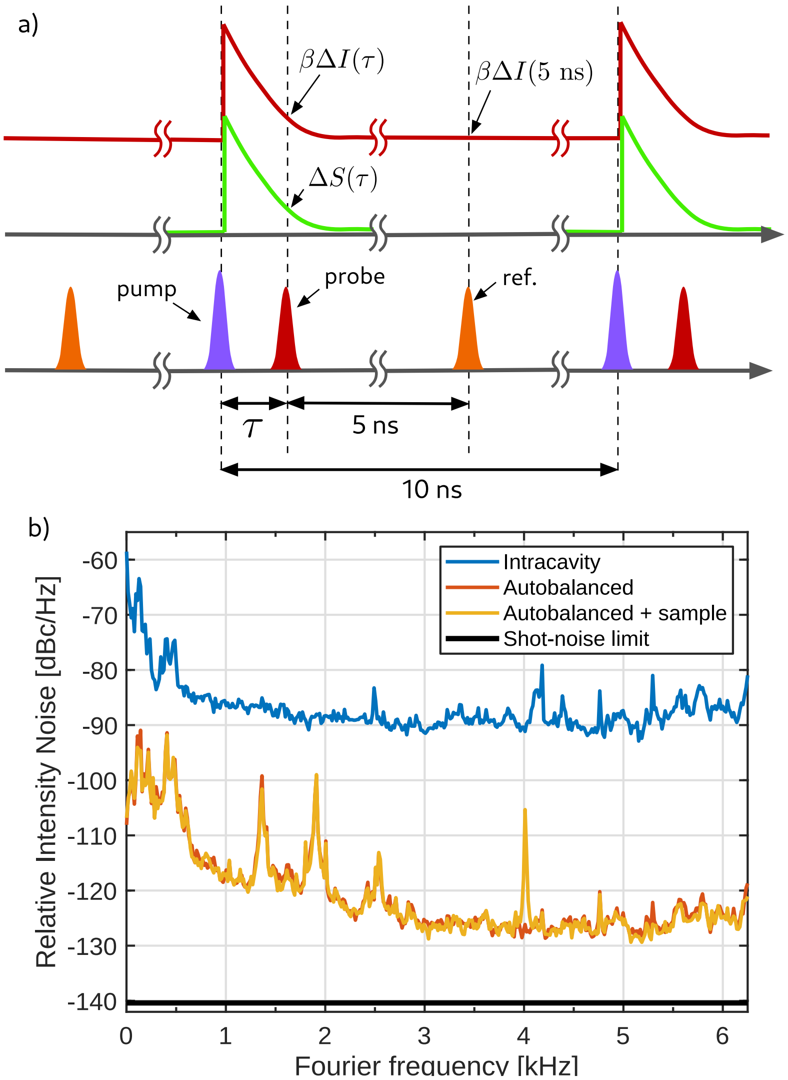

Figure 5.3: a) Pulse sequence at the sample. The reference pulse records any steady-state pump/probe signal ΔI(5ns) and contains nearly identical noise to the probe for common mode subtraction. b) Noise spectrum of the intracavity light and subtracted signal using 469 nm ($2s$) light. Rejection of common-mode noise using the autobalanced subtraction scheme allows for the ultrafast molecular signal to be detected at the pump modulation frequency of 4 kHz. Also shown is the shot-noise (or quantum noise) limit calculated from the measured photocurrent.

5.2.4 Constructing Transient Absorption Spectra

The probe bandwidth of each individual CE-TA measurement describe above, with the OPO output tuned to a particular wavelength, is less than 10 THz (Fig. 5.1b). We thus assemble broadband transient absorption spectra by combining a collection of measurements taken at different wavelengths. Changing wavelengths typically takes 10-20 minutes and accumulating the data for an entire broadband CE-TAS spectrum takes approximately one full workday. With this long, non-parallel data acquisition scheme, controlling systematics is then of the utmost importance to assemble reliable and reproducible spectra, as several parameters affecting the signal size vary intrinsically with wavelength and can also vary with time over the course of an experimental run.

To control for cavity finesse variation, we periodically perform in-situ cavity ring-down measurements at each wavelength in between pump/probe delay scans. We do this by inserting an acousto-optic modulator (AOM) in the reference beam to quickly ($\sim$ 20 ns) turn off the reference beam while the Pound-Drever-Hall lock between the comb and cavity is maintained using the probe beam. To achieve 100% turn-off of the reference beam for clean ring-down signals, we use the first-order diffracted beam from the AOM. The AOM is driven by a $2f_{\mathrm{rep}}$ radio-frequency signal derived from the Er:fiber comb. Using an integer multiple of f_{rep} to drive the AOM ensures that the frequency-shifted diffracted comb is still resonant with the enhancement cavity.

To control for potential variations in pump power and sample molecule density at the focus, we record fluorescence from the pump/probe interaction region using the scheme shown in Fig. 5.2. A mirror in the supersonic expansion path reflects fluorescence out of the chamber. The mirror is heated to prevent sample molecule condensation. To eliminate scattered light background, we then use an f = 10 cm lens to image the pump/probe overlap region to an adjustable aperture which rejects light from elsewhere. The remaining light from the pump/probe overlap region is recorded with a photomultiplier tube (PMT) using lock-in detection at the pump modulation (chopper) frequency. This scheme produces a background-free fluorescence signal that is proportional to the column density of excited molecules in the focal region, and this fluorescence signal can then used to normalize and combine pump/probe data accumulated over extended periods of time.

5.3 Results

5.3.1 Individual CE-TA Measurements

For the present demonstration of the instrument, we present results on 1'-hydroxy-2'-acetonaphthone (HAN), and Salicylideneaniline (SA), two archetypal systems for excited-state intramolecular proton transfer (ESIPT) shown in Fig. 5.4. These molecules have previously been studied using both solution-phase TAS [6,8] and gas-phase TRPES [7,188], so they serve as good systems to benchmark the instrument.

Fig. 5.5a) and b) show typical pump/probe data recorded in HAN using the $2i$ and $2s$ combs respectively. Each trace is the average of three scans. Near time zero, a large polarization anisotropy is seen, but this rapidly decays as the many rotational coherences excited by the pump pulse dephase from each other [187] in this asymmetric top molecule. Thinking about the problem classically (which is also appropriate here given the large number of rotational states involved) one can think that the pump pulse preferentially excites molecules with their transition dipole oriented along the pump polarization, but then these molecules freely rotate in random directions leading to an isotropic distribution. We note that if one attempts to use the CE-TAS signal (Eqn. 5.1) to calculate a normalized anisotropy parameter $r'(\tau) = (\Delta S_{\|} - \Delta S_{\perp})/(\Delta S_{\|} + 2\Delta S_{\perp}) = (\Delta S_{\|} - \Delta S_{\perp})/(3\Delta S_{\mathrm{MA}})$, this parameter need not be bounded in the usual range of $(-0.2, 0.4)$ due to the subtraction of the long-lived TAS signal sampled by the reference beam. The numerator (a simple difference) gives no artifact, but even if the anisotropy decays to zero at long delays, the denominator of the expression for $r'(t)$ is still reduced by $3\beta\Delta I_{\mathrm{MA}}$, throwing off the ratio. This is particularly acute for a molecule like HAN, with a fluorescence yield of approximately 1% and a radiative decay rate of 1/(10 ns) [189], for which the steady-state excited state population in the focal volume can build up over multiple pump pulses. Indeed, $r'(\tau = 0)$ for the data shown in Fig. 5.5b) is 0.6, suggesting a steady-state magic angle background signal of $\Delta I_{\mathrm{MA}}(5\mathrm{ns}) = 0.3\Delta I_{\mathrm{MA}}(\tau = 0)$, which is reasonable under our experimental conditions.

Fig. 5.5c) shows magic-angle pump/probe traces for HAN over the full 700 ps delay range accessible with our delay stage. Fitting these data with a single exponential + offset gives a time constant of 70 ps for internal conversion in HAN, in agreement with previous TAS measurements in cyclohexane [6] and fluorescence measurements in the gas phase [189, 190]. However, we note that the observed time constant is quite different than the previous gas-phase ultrafast spectroscopy measurement based on TRPES [188], which reported 30 ps decay time constants even when using longer excitation wavelengths closer to the origin of the $S_0 \rightarrow S_1$ transition. This shows the impact of the observable on the measurement of the kinetic time constants discussed in Chapter 1.

With the assumption that the enol-keto tautomerization and the corresponding appearance of excited-state absorption and redshifted stimulated emission in HAN happen much faster than our time resolution [6], for this first set of measurements in HAN we estimate the time resolution of the instrument by fitting the rising edge of the CE-TA traces with an error func-

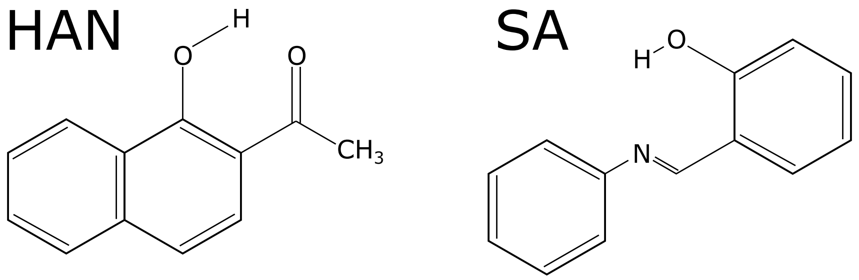

Figure 5.4: Molecules in the present experiments. HAN = 1'-hydroxy-2'-acetonapthone. SA = salicylideneaniline

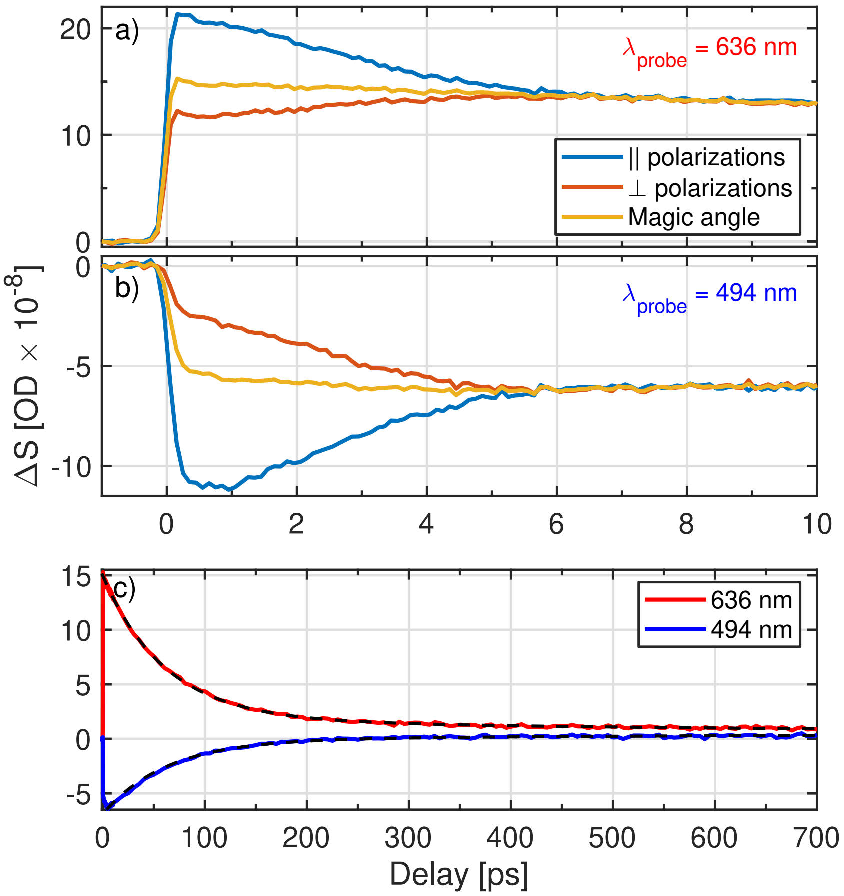

Figure 5.5: Example transient absorption traces for $\lambda_{\text{probe}} = 636$ nm (a) and 494 nm(b) combs recorded from HAN excited at 355 nm. The positive signal in a) corresponds to excited-state absorption and the negative signal in b) to stimulated emission. The parallel and perpendicular polarization data are each the average of three scans with 1s integration time per pump/probe delay. Magic angle data is constructed via $\Delta S_{\text{MA}} = (\Delta S_{\parallel} + 2\Delta S_{\perp})/3$. c) Full 700 ps magic angle data showing the long decay of the transient signal including single-exponential fits (dashed black lines).

tion. Fig. 5.6a) shows the resulting extracted instrument response FWHM as a function of wavelength. Impulse response widths less than 275 fs are attained across the tuning range, with somewhat better time-resolution observed using the $2i$ comb.

5.3.2 Independent instrument response function

To independently verify the instrument response function (IRF) of the spectrometer, we measure the two-photon absorption of carbon disulfide. Carbon disulfide was selected after an extensive search due to its use as a calibration sample in z-scan measurements [4,191]. The two-photon absorption coefficient,

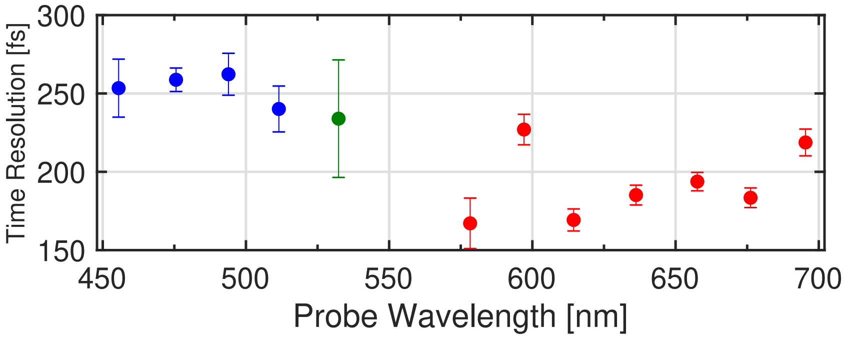

Figure 5.6: Spectrometer FWHM time resolution across the tuning range found by fitting the rising edge of HAN signal to an error function assuming instrument-limited response. Error bars are from fit. Points are color coded according to OPO output for doubled signal (blue), doubled idler (red), and residual pump (green).

measured by Reichert et al. [4] is shown in Fig. 5.7. The vertical dashed lines indicate the effective degenerate two-photon energy of the probe range of the spectometer calculated via (E_{pump}+E_{probe})/2 where E_{pump} and E_{probe} are the pump and probe photon energies, respectively.

Example pump/probe scans of gas-phase carbon disulfide are shown in Fig. 5.8a) and b) compared to measurements of SA at probe wavelengths of 462 nm and 616 nm, respectively. Also shown is the cumulative integral of the carbon disulfide data to better compare to the error function response of SA. These measurements were performed with identical intracavity spectra by changing samples under one continuous comb/cavity lock. We do not observe a meaningful delay in time SA signal onset, any apparent shift is within the experimental and/or fit error.

5.3.3 Instrument sensitivity

We now discuss the sensitivity of the instrument. There are two main sources of uncertainty (i.e. noise) to consider. The first is the optical noise floor of the system (Fig. 5.3b) due to residual un-subtracted noise on the intracavity light and uncorrelated quantum noise in probe/reference detection. The second is drifts of the instrument over longer time scales required to assemble a full data set. Both can be quantified using an Allan deviation analysis [49, 192]. Fig. 5.9a) shows the Allan deviation calculated from data sets where the same signals are scanned repeatedly.

The intrinsic noise performance of the optical setup is captured by data taken without any sample (triangles on Fig. 5.9a). Without sample, the Allan deviation comes down with a slope of $-1/2$ on the log-log plot which indicates white-noise-limited performance (i.e. no drift). We observe this behavior for as long as we have averaged for and have seen noise down to ΔOD$= 2.6\times10^{-11}$ (off the chart) after 90 minutes of integration without sample, with a corresponding

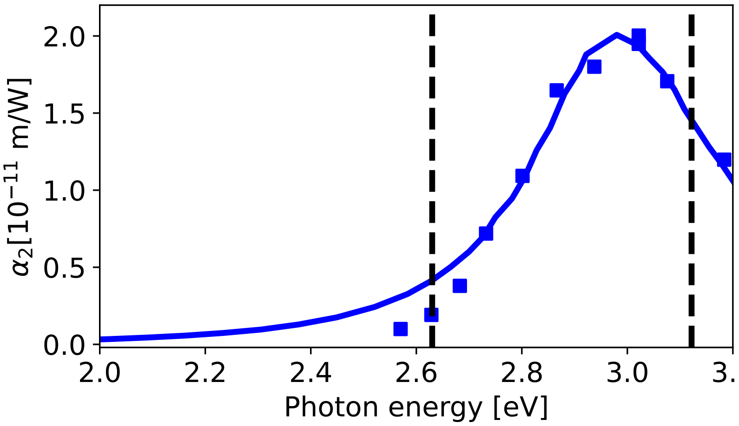

Figure 5.7: Two-photon absorption coefficient of liquid carbon disulfide measured by z-scan, reproduced from [4, 5]. The individual points correspond to experimental measurements performed by Reichert et al. and the solid line is a theoretical model. The vertical lines indicate the probe range of the spectrometer with deffective degenerate two-photon energy via $(E_{pump}+E_{probe})/2$.

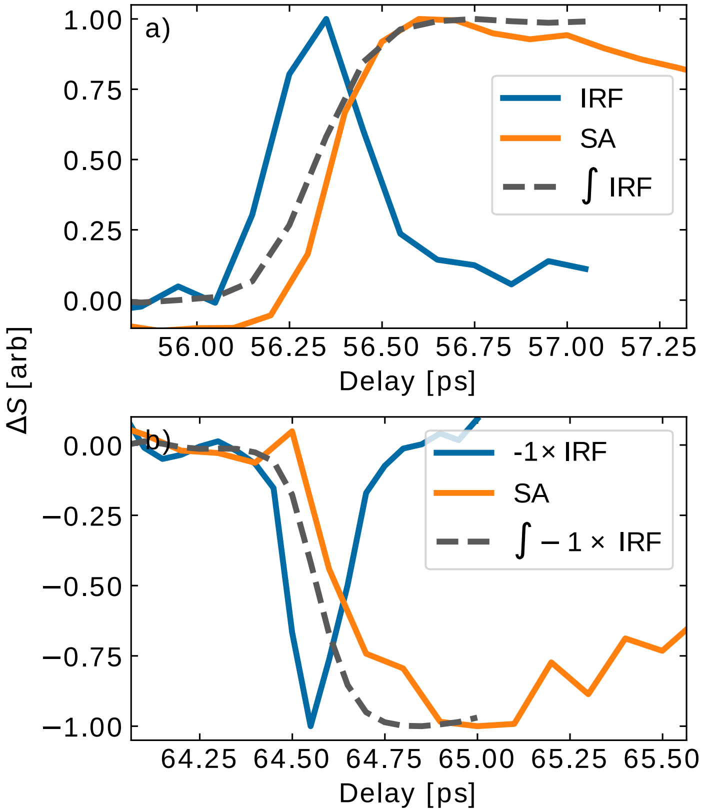

Figure 5.8: Comparison of the independent instrument response function and the isolated SA signals at a) 462 nm and b) 616 nm.

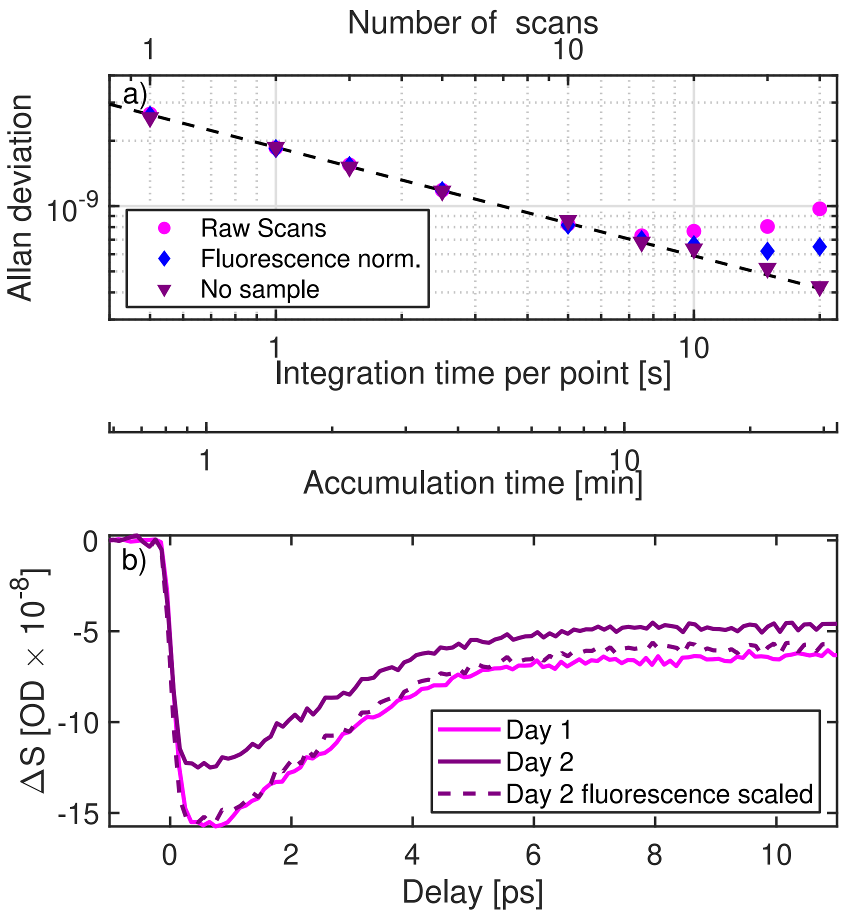

Figure 5.9: a) Allan deviation recorded using repetitive scans at 469 nm 0.5 s of integration per pump/probe delay. Without sample (triangles), the noise averages down with the inverse square root of the measurement time for as long as we have recorded data, following the dashed line with a slope of -1/2. With molecular signal, drift in the molecular column density on the ~10 minute time scale causes the main limitation to averaging (circles), but this drift can be remedied to some extend using fluorescence normalization (diamonds). b) Two pump/probe traces taken days apart can largely be brought into coincidence using normalization to the fluorescence signal.

normalized sensitivity of $\Delta\mathrm{OD} = 2 \times 10^{-9}/\sqrt{\mathrm{Hz}}$. Similar results with the 2i comb (not shown) give a sensitivity of $\Delta\mathrm{OD} = 3 \times 10^{-9}/\sqrt{\mathrm{Hz}}$. These results are consistent with the optical noise floor of the subtracted signal observed in Fig. 5.3 and comparable to the single-color result of Reber et al. [30] of $\Delta\mathrm{OD} = 1 \times 10^{-9}/\sqrt{\mathrm{Hz}}$ [30], despite the significant additional complexity of the current setup, showing the intrinsic robustness of CE-TAS method.

When accumulating an actual molecular signal, the uncertainty in ΔS (circles on Fig. 5.9a)) becomes dominated by drift for long accumulation times. These data are accumulated by repeated scanning of a pump/probe signal (parallel polarizations, 469 nm, 88 points, 0.5 s/point) such that the same pump/probe delay is re-encountered every 44 seconds. In this case, the Allan deviation differs (circles in 5.9a) from white-noise performance [49] and actually increases with averaging time for real accumulation times longer than 10 minutes. The main source of drift is variation in the sample molecular column density, which can be mitigated using the fluorescence monitor as we describe below.

Fig. 5.9b) demonstrates fluorescence normalization for an extreme case. The two scans, both at a probe wavelength of 455 nm and at equivalent sample backing pressures, were recorded several days apart. On the second day, there was less HAN remaining in the sample cell which resulted in reduced fluorescence and CE-TA signal. Scaling the day 2 data by the ratio of fluorescence signals brings the two TA signals back into coincidence. The Allan deviation of CE-TA data normalized using the fluorescence monitor is shown as diamonds on Fig. 5.9a)). With normalization, individual CE-TA pump/probe traces can be accumulated with a noise level of $\Delta\mathrm{OD} = 6 \times 10^{-10}$ with repetitive scans over a real accumulation time of 22 minutes. This corresponds to a S/N of 167 for this particular data set.

5.3.4 Operation with a Pump Cavity

For molecules with reduced absorption cross sections or low vapor pressures, sample excitation fraction can be increased thorugh the use of a pump enhancement cavity. The overall experiment looks nearly the same as Fig. 5.1 but with a second bowtie cavity constructed around the reflective pump focusing mirror. The input coupler has a transmission of 3% and the rest of the mirrors are high reflectivity (>99.8%) for an expected finesse of 172 [69]. The curved mirrors have a radius of curvature of 75 cm and are separated by a distance of 103 cm. The pump beam has a beam waist of $w_{\mathrm{pump}} = 110$ μm from ABCD matrix calculations.

To stabilize the pump comb to the cavity, the cavity transmitted light is sent to a grating which spatially disperses the spectrum onto two photodetectors used for error signal generation. The first lock point stabilizes f_{rep} with a fast piezoelectric transducer [158] using the side-of-line discriminator, as described in [30]. To "chop" the intracavity light for signal lock-in, the lock-point is sinusoidally modulated. To stabilize the pump comb f_0, the second photodetector is sent to a lock-in amplifier to monitor chopped intracavity power which is sent to an integrator with input offset control. The integrator output goes to a line driver which actuates on a the temperature of the EOM inside the oscillator via a peltier element.

Stable operation of the pump cavity with up to 15W of intracavity power has been achieved. To demonstrate the utility of increased pump power, Fig. 5.10 shows pump/probe scans both with and without the pump cavity recorded from 2-(2'-hydroxyphenyl)benzothiazole (HBT) in the gas phase. HBT has a similar absorption cross section to both SA and HAN but a reduced vapor pressure at similar temperature [193,194]. The single pass pump measurements

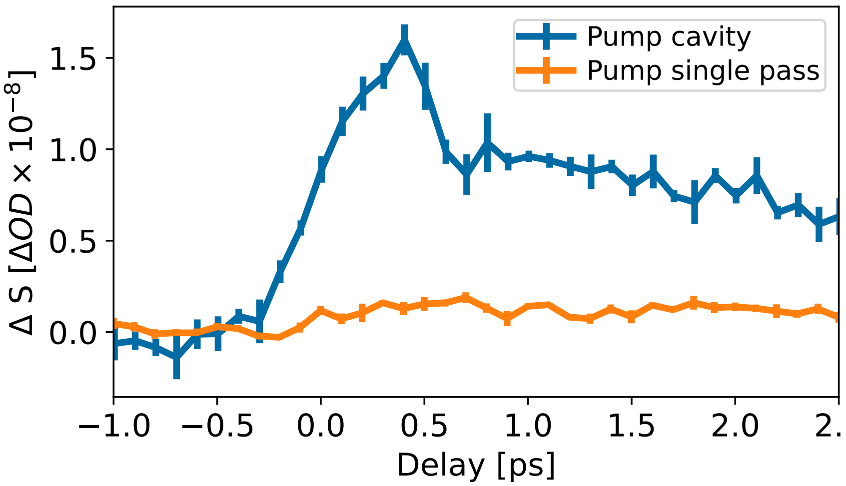

Figure 5.10: Demonstration of the effect of pump cavity operation. The pump/probe signal size recorded from of 2-(2'-hydroxyphenyl) benzothiazole at a probe wavelength of 475 nm increases approximately tenfold due to increased pump power. The single pass pump power is ≈ 500 mW and the cavity power is ≈ 8 W.

were recorded with ≈500 mW, similar to the other measurements presented in SA and HAN, while the pump cavity data was recorded with ≈8 W intracavity power. The 10 times increase in signal size due to the pump cavity increases the signal-to-noise ratio substantially. This reduces necessary averaging times for the instrument enabling more rapid spectrum acquisition.

5.3.5 CE-TAS Spectra

In Fig. 5.11a), we show a constructed magic angle transient absorption map for HAN in a He-seeded supersonic expansion (0.25 Bar stagnation pressure) working 3 mm from the nozzle. This spectrum is sampled at the same 12 discrete probe wavelengths as in Fig. 5.6 and the same delay axis as Fig. 5.5c). For each wavelength, we take three scans for parallel and three scans for perpendicular pump/probe polarizations with an integration time of 1 s/delay. With 260 points/scan distributed over pump/probe delays out to 700 ps, each scan then takes 260 s = 4.3 minutes. Thus, we are accumulating data for a total of 26 minutes per wavelength. The entire spectrum comprising 12 wavelengths is collected over the course of a day. Fig. 5.11c) shows the noise level for the magic angle signals, using fluorescence normalization, obtained under these practical conditions as a function of wavelength.

In Fig. 5.11b), we extract TA spectra of the molecule at 1, 5, and 50 ps delay and compare them to the TAS data reported by Lochbrunner et al. for HAN in cyclohexane [6]. The most obvious difference between our results from the jet-cooled molecule and the cyclohexane data is a solvatochromic blueshift of the TA data by ∼25 nm going from cyclohexane to gas-phase, similar (but not

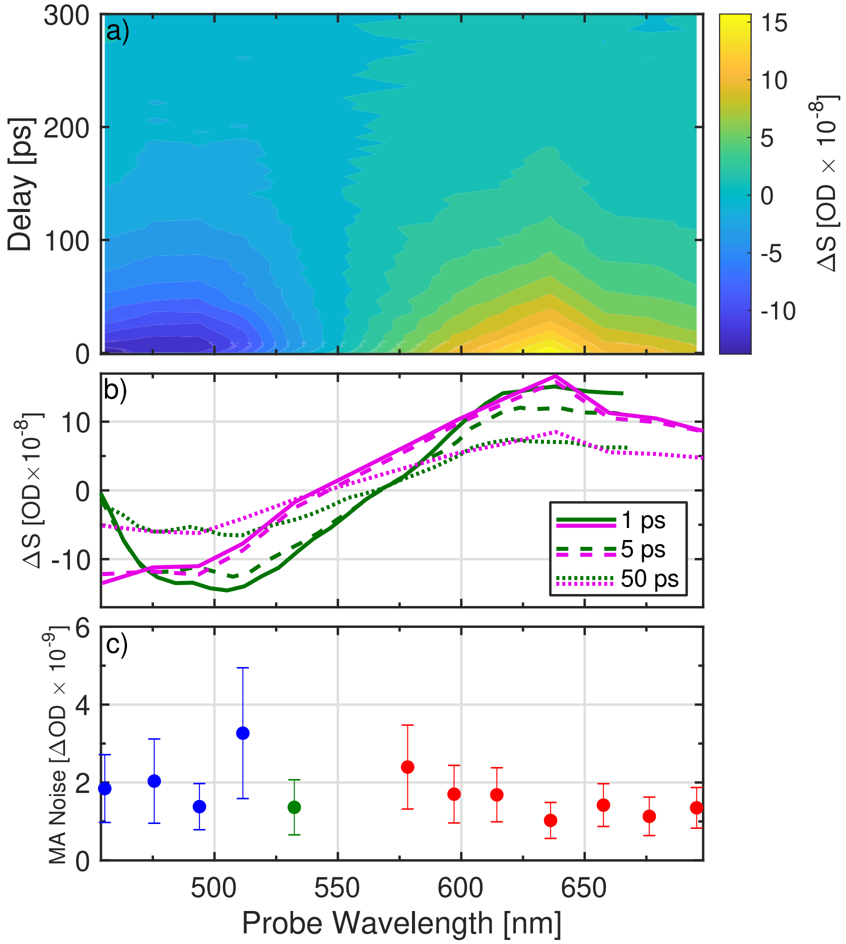

Figure 5.11: a) Magic-angle transient absorption map for jet-cooled HAN excited at 355 nm constructed from 12 probe wavelengths. Stimulated emission is observed on the blue side of the spectrum and excited state absorption on the red. b) Comparison of TA spectra from jet-cooled HAN (magenta) and HAN in cyclohexane (green) from reference [6] at 1 ps (solid), 5 ps (long-dashed), and 50 ps (short-dashed) delays. The solution-phase data has been multiplied by one overall scale factor to make the comparison. c) Noise-levels attained as a function of wavelength for this full TA-map measurement. Points are color coded according to OPO output for doubled signal (blue), doubled idler (red), and residual pump (green).

identical) to the 15 nm shift for fluorescence reported by Catalan et al. [189]. Furthermore, the differences in the TA spectra are not fully explained only by a solvatochromic shift. A more comprehensive analysis of the full HAN data is beyond the scope of this paper but will be the subject of a future publication including global analysis and comparison to *ab initio* theory [195].

5.3.6 Clusters

Working 3 mm from the 200 μm slit nozzle, we can easily generate clusters with sufficient column density for CE-TAS studies and we demonstrate this here. Figures 5.12a) and b) shows an example of this for SA recorded at λ_{probe} = 455 nm expanded in helium and argon, respectively. Using He carrier gas, we observe the rotational anisotropy to decay in ∼10 ps, whereas for Ar carrier gas, the parallel and perpendicular polarizations data do not converge to the same signal until ∼50 ps. In the optimized ground state geometry calculated by Pijeau et al. [196], the rotational constants of SA are $A = 0.066$ cm^{-1}, $B = 0.0091$ cm^{-1}, and $C = 0.0082$ cm^{-1}, making the molecule nearly a symmetric top. For a symmetric top, the width of the rotational anisotropy transient scales as $1/\sqrt{BT}$ [197], indicating a large change in the rotational constant is required to explain the 5x increase in the width of the rotational anisotropy transient. It is important to note that for the case of SA, with much faster internal conversion than HAN and much smaller fluorescence yield of $\sim 10^{-4}$ [8], the rotational anisotropy parameter $r'(t)$ constructed from the CE-TAS signals ΔS is free from the aforementioned complications due to reference subtraction and is bounded by $(-0.2, 0.4)$. Assuming the temperature is similar in the two expansions, from the increased width of the rotational anisotropy, we estimate that the SA molecules have gained on average 24 Ar atoms, although actually this number should be taken as a lower bound since excitation of the molecule may promptly evaporate many Ar atoms, as commonly exploited in tag-loss spectroscopy [198].

The effect of Ar clustering on the internal dynamics of the molecule can be seen in the magic angle data shown in Fig. 5.12c). For He expansions, where no clustering is expected, we observe fast decays of the TA signal in agreement with previous solution-phase TAS [8] and gas-phase TRPES [7]. However when forming large Ar clusters, the internal conversion is shut off and the excitation is long-lived, as shown in Fig. 5.12. A corresponding large increase in the fluorescence signal is also observed, further supporting a suppression of internal conversion pathways in the Ar cluster. Also shown for direct comparison is TRPES data from Sekikawa et al. [7], which shows a much faster decay of the observable than TAS, similar to what we have also observed in HAN.

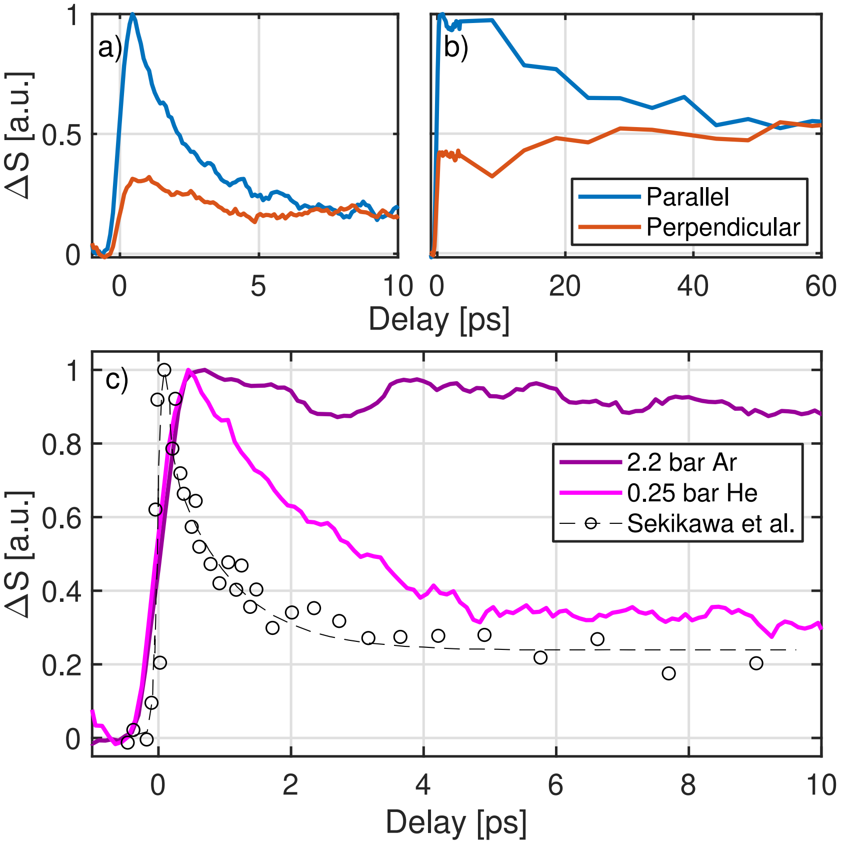

Figure 5.12: Parallel and perpendicular polarization CE-TAS data for SA excited at 355 nm in a 0.25 bar He expansion a) and 2.2 bar Ar expansion b). The polarization anisotropy transient decays much more slowly in the Ar data, indicating the formation of large Ar clusters. c) Magic angle data for the Ar expansion and He expansion compared to previous TRPES data recorded in jet-cooled SA from ref. [7].

5.4 Discussion

In this chapter, we have described the performance of a broadband ultrasensitive spectrometer for recording transient absorption spectra with ultrafast time resolution. The overall performance of the spectrometer is comparable to a previous 1-color demonstration of the main concept in molecular I_2 [30], despite the significant additional complexity of both the optical setup and molecular beam system necessary to go past demonstrations and record data on chemically relevant systems. We have also demonstrated the linkages between different measurement techniques discussed in Chapter 1 by directly comparing cavity-enhanced transient absorption data to solution-phase TA measurements and gas-phase TRPES for two example systems. We expect a wealth of information can be extracted from such comparisons going forward, given the large body of high-quality data existing from these well-established techniques. Furthermore, performing CE-TAS measurement on clusters can enable a detailed microscopic understanding of the effect of the solvent on molecular dynamics, as has been done for linear spectroscopy.

For electronically excited molecules, UV-VIS CE-TAS offers a complimentary ultrafast observable to those provided by well-established TRPES methods, with the idea that via comparison to theory more information can be extracted from the combination than can be had from either observable alone. This multi-observable approach has recently been promoted by others for the combination of diffraction and spectroscopy data [23]. We note that for the work presented here on 2 molecules, our observed time constants agree more closely with the solution-phase TAS work and are a factor of ∼2 longer than the gas-phase TRPES measurements. We suspect that for the current comparisons this difference is due 'energy windowing', or reduction in the TRPES signal when the molecule moves to regions on the excited-state potential energy surface where the probe photon energy is insufficient to ionize the molecule, due to the low-energy probe photons used in the previous SA and HAN experiments. This artifact can be more pronounced for multi-photon ionization experiments [41] such as the SA measurements by Sekikawa et al. [7], but also present in experiments using single-photon ionization for the probe [19, 20]. However, more data is required to understand if the trend observed here for two molecules is more general and also if it may be due to additional factors beyond energy windowing such that it may also appear in the comparison of TRPES measurements using higher probe photon energies with TAS.

The methods described here can also be implemented in the mid-infrared to study purely vibrational dynamics on the electronic ground state, and we are actively working on developing cavity-enhanced two-dimensional infrared spectroscopy (CE-2DIR) [71]. It is important to note that in contrast to the current work, which provides a complimentary view of the dynamics of gas-phase molecules after electronic excitation, for which other action-based spectroscopy methods exist, an action-based analog of 2DIR with ultrafast time resolution does not currently exist. In many ways, we expect CE-2DIR spectroscopy to be less technically challenging than the current demonstration due to the reduced bandwidth requirements of 2DIR and also less difficulties with mirror contamination due to the absence of UV light cracking residual hydrocarbons in the vacuum system.

Finally, we note that the methods demonstrated here can be adapted to liquids and sparsely covered surfaces, as has been done for cavity-enhanced linear spectroscopy [199]. For example, inclusion of a reflection off a glass/liquid interface into the cavity could be used to perform cavity-enhanced ultrafast attenuated total reflectance spectroscopy on molecules at the interface. Translating the current sensitivity to a molecular film indicates that coverages below 10^{-4} monolayer could be investigated. The challenges in adapting CE-TAS to condensed-phase contexts are 1) managing the dispersion and loss of additional intracavity elements and 2) managing sample excitation and refresh rate. While it is likely that compromises regarding 1) and 2) would reduce performance, CE-TAS methods could still find applicability for small-signal condensed phase measurements inaccessible with other techniques.

Chapter 6

Ultrafast internal conversion and photochromism in gas-phase salicylideneaniline

This chapter contains a reproduction of our publication *Ultrafast internal conversion and photochromism in gas-phase salicylideneaniline,* Myles C. Silfies, Arshad Mehmood, Grzegorz Kowzan, Edward Hohenstein, Benjamin Levine, and Thomas K. Allison, *Journal of Chemical Physics*, accepted (2023) [200] with permission of AIP Publishing.

6.1 Introduction

Tracking and understanding the redistribution of internal energy has been one of the main goals of ultrafast spectroscopy since its inception. In photochromic molecules, the absorption of light causes large electronic reorganization leading to a reversible change in absorption and a corresponding material color change [201]. Often, these changes are driven by excited state intramolecular proton transfer (ESIPT) reactions and/or rapid isomerization on sub-picosecond timescales, requiring ultrafast techniques to follow the dynamics. Additionally in the case of ESIPT, the redistribution of energy results in a large (~ 1 eV) Stokes shifted fluorescence [202,203]. Recently, there has been a significant amount of work to use photochromic and/or ESIPT molecules in applications such as textiles [204], optical memories [205,206], and sensors [207–209].

Even as the absorption and emission shifts found in ESIPT/photochromic materials are now being exploited for consumer and industrial applications, many foundational spectroscopy studies continue on increasingly larger systems as well as in the closely related field of proton-coupled electron transfer (PCET) [210,211]. As the complexity of the molecule increases, so does the difficulty in understanding the relaxation dynamics and potential photochromism mediated by proton or hydrogen transfer as opposed to internal conversion me-

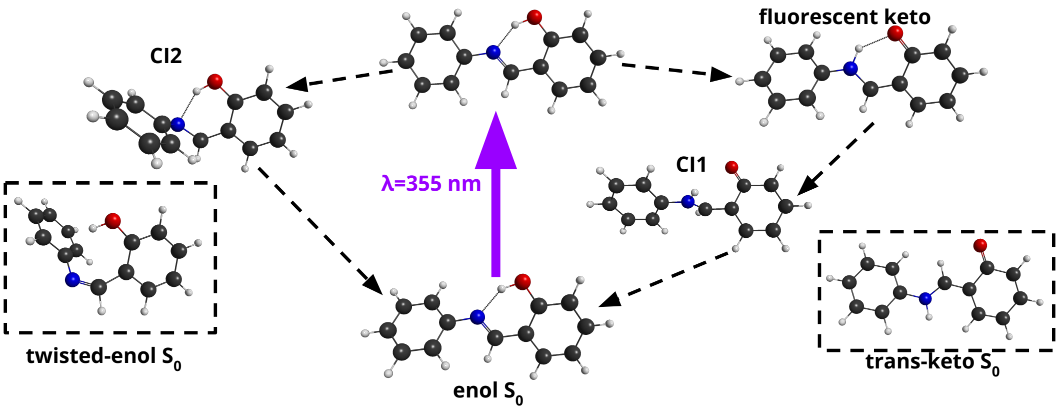

Figure 6.1: General overview of relaxation schemes for SA excited to S_1. After excitation, the excited enol can either (right side) undergo ESIPT and internally convert along the keto pathway through CI1 or (left side) remain in the enol tautomer and relax via CI2 by rotating about the central C-N bond. Bottom left and right insets are alternative ground state minima that are potential photochrome geometries which may be reached via the enol or keto relaxation pathways, repsectively.

diated by other degrees of freedom. One of the most studied photochromic systems exhibiting competing dynamic pathways is the archetypal Schiff base salicylideneaniline (SA) depicted in Fig. 6.1. In solution and solid phases, SA becomes red after irradiation with UV light and remains trapped in this metastable state that can be reversed via irradiation by blue light. [212–215]. Spectroscopically, this "photochrome state" is observable as a photoinduced, long-lived absorption feature most likely due to a trapped population of an isomerized ground state geometry.

Although still under debate, the general photoinduced relaxation scheme was recently summarized and improved by Pijeau et al. with high-level dynamics simulations [196] which built off of earlier work [12, 216, 217]. This scheme, shown in Fig. 6.1 is described as follows. In the ground state, SA is in the enol form and nonplanar with a $\approx 35° - 50°$ twist around the anilino C-N bond depending on the level of theory or experimental data [12, 196, 216, 218]. Theory indicates that the barrier to proton transfer is lower with decreasing twist angles and ESIPT is more likely to occur from planar geometries [7, 12, 196, 216]. Therefore, upon UV excitation to the $S_1(\pi, \pi*)$ state ($\lambda_{\text{max}} \approx$ 350nm), SA must first planarize before undergoing ESIPT to form the excited keto form. However, the ground state potential energy depends only weakly on the anilino C-N twist angle so even at low temperatures there is a nonzero probability of planar geometries [7].

The keto form populated after ESIPT can relax via a number of channels, with sequencing and branching ratios not well understood or agreed upon. Spectroscopic signals indicate that a portion of molecules decay radiatively from a fluorescent keto form or become trapped in a long-lived photochromic state which absorbs blue light as described above. Additionally, some population of excited molecules can undergo internal conversion back to the ground state via a conical intersection (CI) followed by ground-state back proton transfer. The keto CI, labeled “CI1” on Fig. 6.1, was found theoretically and requires a rotation of nearly 90° around the phenolic C-C bond. [196]. Using DFT calculations, Ortiz-Sánchez et al. found the ground state keto minimum structure shown on the bottom right of Fig. 6.1, which has a full 180° rotation about the same phenolic bond, and this is widely accepted as the photochrome geometry [12, 219–221].

Additionally, due to the nonplanar structure, a competing relaxation channel involving the excited enol without ESIPT has been proposed [12, 196, 216]. This pathway, shown on the left side of Fig. 6.1, requires a large internal twist of 90° around the central C-N bond to reach CI2 and relax to the ground state. A secondary enol ground state minimum was found along this trajectory and is shown in the bottom left of Fig. 6.1. This twisted enol geometry is also a candidate for the photochromic state, especially if excited with higher energy light [12, 220, 222]. Pijeau et al. investigated the branching ratios and internal conversion rates of the 2 main channels and found that 80% of the excited-state population relaxes via CI1 after ESIPT within 800 fs and 20% via the enol CN twist channel in ≈ 250 fs [196].

SA has been studied using a variety of ultrafast techniques to observe the competing reaction dynamics and determine the nature of the various decay channels. Mitra and Tamai recorded the first femtosecond transient absorption spectra (TAS) in various solvents and found an instrument-limited proton transfer time and a monoexponential decay of both excited-state absorption (ESA) and stimulated emission (SE) with 4 ps time constant in cyclohexane, as well as a long-lived signal assigned to the photochrome [223, 224]. They proposed, like many of the early studies [215, 225], that the initially hot keto state relaxes into either a relaxed fluorescing keto or the photochrome within the first several hundred fs and then the fluorescent state undergoes internal conversion on the picosecond time scale, with the lifetime depending on solvent environment. TAS measurements by Ziółek et al. further refined the proton transfer time to < 50 fs and an excited state relaxation time constant of 7 ps in acetonitrile [8]. Their interpretation finds a sequential model along the keto channel with the photochrome evolving from the relaxed keto state in competition with back-proton transfer on the ground state, disagreeing with previous work. Fluorescence upconversion measurements in acetonitrile also agree with this model. [226].

In the gas phase, Sekikawa et al. performed time-resolved photoelectron spectroscopy (TRPES) in a helium seeded molecular beam [7]. Their results agreed with the solution TAS work on the ESIPT timescale being $\lesssim 50$ fs but found the intermediate decay time constant was 1.2 ps which was assigned to a combination of the ESIPT and CN twist channels. They also observed a long-lived feature which they assigned as the trans keto photochrome but suggested that the isomerization occurs in the excited state. To further understand the dynamics, the authors performed tunable pump measurements which will be discussed in section 6.4 in comparison to our results. In general, it is difficult to determine if the lack of agreement between TAS and TRPES is due to the observable (optical absorption vs. photoionization) or the environment (solution vs. gas phase), and this is particularly true for a molecule with many competing relaxation channels, such as SA.

In this chapter we address the dynamics of salicylideneaniline after excitation to S_1 with $\lambda = 355$ nm using a combination of cavity-enhanced transient absorption spectroscopy (CE-TAS) and quantum chemistry/molecular dynamics calculations that directly simulate the observable. CE-TAS [1, 30] uses a combination of high-power fibers lasers [113] and tunable cavity-enhanced frequency combs [2,3] for broadband transient absorption measurements in dilute molecular beams. CE-TAS acts as a halfway point between TAS and TRPES – sharing the observable of the former and the environment(s) of the latter. By varying the molecular beam conditions, we record dynamics of vibrationally hot SA (420 K), jet-cooled SA, and SA embedded in Ar clusters. We directly compare the CE-TAS measurements to calculations of the transient absorption spectra using a newly-developed real time time-dependent complete active space configuration interaction (TD-CASCI) technique [195, 227].

Overall, we find stronger agreement with the results of previous solution-phase TAS studies than the conclusions of gas-phase studies based on photoionization. We find prompt ESIPT after photoexcitation and relaxation dynamics in accordance with the previously proposed keto channels under all our studied conditions. We do not observe any evidence of the CN twist channel within our detection window, but cannot rule it out completely as we calculate that the TAS signal for this channel should lie to the blue of our shortest 450 nm wavelength. Most strikingly, we find that for SA in Ar clusters, internal conversion of the fluorescent state is shut off while the photochrome yield remains unchanged. This supports a parallel mechanism for fluorescence and the photochrome state. Comparing all the measurements and theory, we present a comprehensive picture of the keto relaxation channels of salicylideneaniline in section 6.4.

6.2 Methods

6.2.1 Experimental

SA was purchased from TCI chemicals (97%) and used as received. For all experiments, the sample is placed in a stainless steel cell and heated to 125° C to increase the vapor pressure. Either He or Ar is used as carrier gas for a planar supersonic expansion from a 5 mm × 0.2 mm slit nozzle, as described previously. [1]. Unless otherwise specified, the He stagnation pressure is 0.1 bar and the Ar stagnation pressure is 1 bar. For all measurements shown, the interaction region is 3 mm above the nozzle, well within the expansion's "zone of silence." [183].

The cavity-enhanced transient absorption spectrometer operating at 100 MHz repetition rate used for all experiments is described in detail in Chapter 5 [1]. The pump wavelength is 355 nm and the cavity-enhanced probe wavelength is tunable from 450 to 700 nm [2, 3]. The CE-TAS signal ΔS is constructed from subtraction of two signals from counter-propagating cavity-enhanced frequency combs delayed by $T_{\mathrm{pr}} \approx 5$ ns, as described previously [1, 30]. For pump/probe signals with much shorter lifetime than $1/f_{\mathrm{rep}} = 10$ ns, the CE-TAS signal ΔS is the same as one would normally record in conventional transient absorption spectroscopy setups. However, for longer-lived signals there are additional subtleties which must be accounted for, and we discuss these in subsequent sections and the Appendix A.

Unless otherwise stated, all data shown are magic angle signals constructed from signals recorded with pump and probe polarizations parallel ($\Delta S_{\parallel}$) and perpendicular ($\Delta S_{\perp}$) via $\Delta S_{MA} = (\Delta S_{\parallel} + 2\Delta S_{\perp})/3$. All broadband spectra (e.g. Fig. 6.2) shown are built up piecewise from pump/probe scans at 10–12 discrete probe wavelengths, taking into account the wavelength-dependent cavity finesse. To generate contour plots from the individual scans, a marching squares algorithm is used for interpolation. In the case of data taken with large amounts of Ar carrier gas, producing Ar clusters around the SA molecules that suppresses internal conversion, signal amplitudes are scaled by fluorescence signals recorded independently during the pump/probe measurements [1]. For data taken with He carrier gas, the fluorescence signal was too weak for the current instrument sensitivity, so the data are unnormalized. However, when using He the molecule pickup is more stable than in the Ar case, most likely due to the lower stagnation pressures and the lack of clustering, and we find good reproducibility across multiple data sets even without fluorescence normalization.

Since the previously-measured ESIPT occurs below our instrument response of ≈ 200 fs [7,8], fitting the rising edge of the signal to an error function is used for aligning time zero for each scan in the spectrum. We verified that the rising edge of the signal is indeed instrument-response-limited by separately measuring the instrument response function at several probe wavelengths using 2-photon absorption in gas-phase carbon disulfide immediately following an SA measurement as described in Chapter 5.

6.2.2 Modeling

A standard tool for analyzing transient absorption spectra is global analysis (GA) [35], in which the transient absorption signal is modeled as a sum of decay associated spectral (DAS) components $\mathrm{X}_n(\lambda)$ each with its own exponential decay with characteristic time constant, τ_n, viz.

$$G(\lambda, t) = \mathrm{IRF}(t) \otimes \sum_n \mathrm{X}_n(\lambda) \exp(-t/\tau_n) \tag{6.1}$$

In equation (6.1) the GA model is convolved with a Gaussian instrument response function IRF(t). For many CE-TAS experiments on molecules with short-lived signals with $\tau \ll 1/f_{\text{rep}}$ this standard GA model is sufficient since the CE-TAS signal ΔS is essentially the same as TA signals recorded by conventional transient absorption spectrometers. However, for data with long-lived components, with $\tau_n \gtrsim 1/f_{\text{rep}}$, it is more appropriate to use a modified model which accounts for multiple excitation of the sample and reference-pulse subtraction in the following manner

$$\Delta S_{\text{model}}(\lambda, t) = \sum_{m=0}^{N} G(\lambda, t + m/f_{\text{rep}}) - G(\lambda, t + m/f_{\text{rep}} + T_{\text{pr}}) \ . \qquad (6.2)$$

In equations (6.1) and (6.2), $G(\lambda, t)$ represents the intrinsic molecular dynamics and $\Delta S_{\text{model}}(\lambda, t)$ is the modeled CE-TAS signal. The time offset in the subtracted signal is due to the reference pulse reaching the sample T_{pr} before the probe. N is the approximate number of pump pulses that molecules see as they fly through the focus. For the modeling shown here, we use $N = 20$, but the DAS are not sensitive to this choice as long as it is much larger than 1. Note that although the *sample* is excited by $\sim N$ pulses, as discussed in Chapter 5 [1], the excitation density is sufficiently low that multiple excitation of the same *molecule* is negligible. All experimental data is modeled using equation (6.2), although for the isolated molecule with only one long-lived component similar results are obtained using either (6.1) or (6.2). Also note that for modeling CE-TAS data we use a wavelength dependent IRF. The fit parameters are optimized by minimizing the reduced χ^2 using a Levenberg-Marquardt global fitting algorithm. A parallel model is used because the proposed relaxation channels occur in parallel following the initial excitation and not in sequence. Additionally, any photochrome signature in the fit is sufficiently slow such that the DAS for the photochrome does not depend on whether a parallel or sequential model is used.

6.2.3 Theoretical Calculations

All the theoretical calculations presented in this study utilize the excited state trajectories derived from the previously published [196] molecular dynamics simulations conducted by one of the authors (EGH). Those calculations used the *ab-initio* multiple spawning (AIMS) method [228, 229] for modelling nonadiabatic molecular dynamics. The potential energy surfaces (PES) were computed on-the-fly via complete active space configuration interaction (CASCI) method, which employs a set of pre-determined orbitals to minimize computational costs and ensure the generation of well-behaved PES [230]. The orbitals were determined utilizing the Floating Occupation Molecular Orbitals (FOMO) method [231–234], based on the Gaussian broadening of each orbital's energy level at an electronic temperature parameter β=0.35 a.u. The FOMO temperature serves as a crucial empirical parameter, capable of precise calibration to attain the desired orbital characteristics and accuracy. When the temperature is excessively low, the FOMO orbitals regress to Hartree-Fock canonical orbitals, which inadequately describe electronic excited states. The dynamic electron correlation effects which are neglected by the CASCI method were incorporated by using the density functional theory embedding correction [235] with ωPBEh functional [236]. An active space of two electrons in two orbitals was employed which is adequately flexible to accurately describe the specific regions of interest on the S_1 potential energy surface. We will abbreviate this method ωPBEh-FOMO(0.35)-CAS(2,2)CI/6-31g**, going forward.

The direct calculation of the spectroscopic observables from *ab-initio* molecular dynamics simulations enables more definitive assignments of spectral features than is possible by the indirect comparison of experimentally observed lifetimes to simulations [19,24,237–239]. The TAS signal is computed theoretically from the AIMS simulations. The simulated spectra shown in this chapter were generated by Arshad Mehmood from Ben Levine's group at Stony Brook University. A detailed description of the method for calculation of the TAS spectrum is included in Appendix B, so here we provide only a short overview. Representative geometries are systematically drawn from the AIMS simulations via a clustering algorithm. Specifically, 80 distinct conformations are sampled from each $\approx$ 24 fs window of the dynamics simulations, for a total of 6720 structures. The ESA and SE are computed via three time-dependent (TD-) CASCI method [227, 240] simulations at each geometry, with light polarized in the x, y, and z directions, respectively. In doing, we take advantage of the fact that time-dependent electronic structure methods are a robust and efficient method to compute molecular absorption spectra [241–245]. Previous studies [227] conducted by one of the authors (BGL) have established that TD-CASCI presents numerous advantages in comparison to the commonly employed real-time time-dependent density functional theory and its implementations for the modern computational hardware allow us to use thousands of geometries to simulate TAS at an affordable cost. To adequately account for the excitations to the higher excited states, a larger (8,8) active space is used to calculate the TAS spectrum and, to avoid possible convergence failure with employed active space, the FOMO temperature was reduced to 0.25 a.u, with the other parameters of the electronic structure method as described above for the dynamics (ωPBEh-FOMO(0.25)-TD-CAS(8,8)CI/6-31g**). The electronic wavefunctions at each geometry are excited by a δ function pulse and then propagated for 45 fs with a 0.003 fs steps. Fourier transforms of the resulting correlation functions provide spectra with a spectral resolution of 0.11 eV ($\Delta\lambda$ = 28 nm at λ = 450 nm; $\Delta\lambda$ = 74 nm at λ = 700 nm). The ESA and SE signals are separately shifted by +0.944 and -1.595 eV respectively to better agree with more trustworthy complete active space second order perturbation theory calculations of ESA and the experimental absorption maximum [224], respectively. In total, the spectra presented required the simulation of 0.9 ns of electron dynamics, which was enabled by our previously-reported GPU-accelerated direct TD-CASCI algorithm [227]. All electronic structure calculations were carried out using the TeraChem software package [246–248]. Additional methodological details can be found in Appendix B, and a separate paper focused on the theoretical method for computing TAS is forthcoming [195].

To facilitate comparison with the experiment, we process the theoretical TAS results in a manner analogous to how the experiment is performed and analyzed. First, the theoretical TAS data from the AIMS/TD-CASCI are sampled at points with 15 nm spacing with a 3 THz FWHM instrument response, which approximately corresponds to the intracavity bandwidth with which each experimental TA trace is recorded. The sampled dataset is then further convolved with a 200 fs FWHM Gaussian in time.

Several sources of error are present in these calculations: statistical error arising from trajectory sampling, as well as error inherent to the electronic structure and dynamics simulation methods. We estimate that the majority of the error is associated with physical approximation, not sampling. However, quantifying statistical error is not practical, because the application of a clustering algorithm prior to computing the probe prevents us from seperating the computed signal into contributions from individual trajectories without performing a large number of additional electronic structure calculations.

6.3 Results

6.3.1 The Isolated Molecule

The TA of SA cooled in He carrier gas is shown in Fig. 6.2. Representative pump/probe scans are shown in Fig. 6.2a) and the full TA spectrum in Fig. 6.2b). Note that the negative ΔS at negative time delays is due to long-lived excited-state absorption in the signal on the blue side of the spectrum. The origin of this pre time-zero signal is illustrated with examples in Appendix A. This negative delay ΔS signal provides information on long-lived components of the true TA signals, and these long-lived DAS are extracted via modeling the full signal (i.e. both negative and positive delays) as discussed in section 6.2.2.

The SA ground-state minimum does not absorb in the visible range, therefore no bleach signal is considered [224], i.e. all negative signals are from stimulated emission. From modeling of the decay of the polarization anisotropy (i.e. the weighted difference between signals recorded with parallel and perpendicular relative polarizations) using the procedure of Felker et al. [187], we estimate the rotational temperature in the expansion to be 80 K, well above the condensation temperature of He, such that no clustering in the helium expansion is expected or observed.

We fit the data using equations (6.1) and (6.2) with $\mathrm{X}_n \equiv \mathrm{A}_n$. The DAS for the isolated SA are shown in Fig. 6.2c) for GA with two time constants

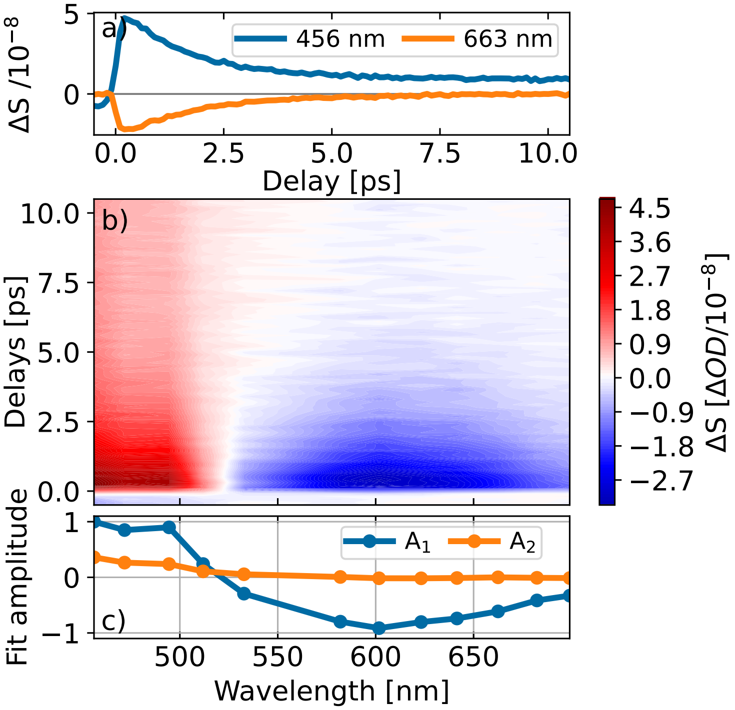

Figure 6.2: CE-TAS of isolated jet-cooled SA molecule. a) Raw signals at 2 representative probe wavelengths. b) TA spectrum constructed from the individual scans. c) DAS from global fit of b) with 2 components, normalized to the maximum of A_1. A_1 and A_2 are associated with time constants of 1.8 ps and >10 ns, respectively. Individual points are at the discrete probe wavelengths which are combined for the full spectrum. The origin and meaning of pre-time-zero signals is discussed in the text.

(reduced $\chi^2 = 1.9$). The associated time constants are $\tau_{\mathrm{A}_1} = 1.8$ ps and τ_{A_2} >10 ns. The points shown on the DAS are the discrete probe wavelengths that make up the spectrum. The same fit procedure was also tested for 1 (reduced $\chi^2 = 51.5$) and 3 (reduced χ^2=2.7) components.

The short-lived A_1 is composed of both negative and positive features in the spectrum indicating excited state absorption (ESA) and stimulated emission (SE) from the same state, and is the typical type of TAS signature seen for excited-state proton transfer in many molecules [6, 249–251]. The 1.8 ps time constant lies between those reported for gas-phase TRPES [7] and solution-phase TAS [8, 223, 224]. The long-lived A_2 extends out from blue edge of the spectrum, is only positive, and remains nearly constant out to the maximum delay of the instrument (700 ps). In the raw pump-probe traces, A_2 also appears as a negative signal for wavelengths less than 530 nm which is accounted for in the model as described in section 6.2.2. This feature is most likely ground-state absorption from the long-lived photochromic state observed in numerous previous experiments. The assignment and origin of this state is further discussed in section 6.4.

In Fig. 6.3, we compare our TA spectra to those reported by Ziółek et al [8] for SA excited at $\lambda = 390$ nm in acetonitrile. The data shown has only a single global scaling to overlap the bluest probe value at 0.5 ps and this scale factor is applied to all of the gas-phase data. The spectra show remarkable similarity, without even a solvatochromic shift. Additionally, Mitra and Tamai also measured solution-phase fs TAS of SA in several solvents and there are only minor spectral shifts between their data and our gas-phase measurements [223, 224].

While we do not vary the excitation energy in our experiments, we do vary the initial vibrational energy via coarse control of the temperature. The nozzle is held at 155° C, and for an effusive beam (i.e. no carrier gas) or very low carrier gas stagnation pressures (quasi-effusive beam) such that there is no supersonic expansion, we expect the molecular temperature in the beam to be approximately the same as the nozzle. In practice, we find the SA density in the beam to be more stable for quasi-effusive beam, and record "hot SA" data with 0.02 bar stagnation pressure of He. We have verified that identical dynamics are obtained with quasi-effusive beam and with no carrier gas and analyzing the rotational anisotropy, we find a rotational temperature for "hot SA" of 420 ± 20 K for the quasi-effusive beam, consistent with the nozzle temperature.

Fig. 6.4 compares pump/probe traces for "hot SA" with the quasi-effusive beam and "cold SA" recorded with a He stagnation pressure of 0.1 bar. Higher He stagnation pressures do not alter the signal significantly. The vibrationally hot molecule decays slightly faster and shows a slightly larger amplitude for the long-lived signal.

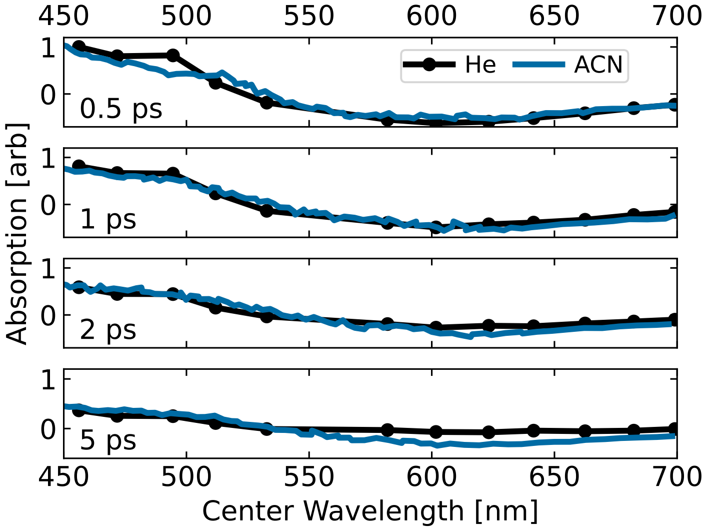

Figure 6.3: Lineout comparison between TAS of the jet-cooled SA molecule and in SA in acetonitrile (ACN) for different delay times. One global scaling factor is used between the two datasets at all times. ACN data from [8].

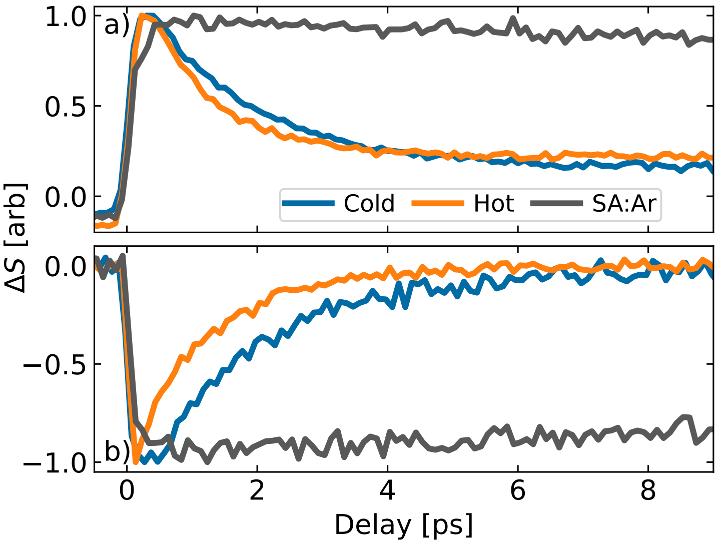

Figure 6.4: Comparison of SA dynamics under different molecular beam conditions. “Cold” data are taken with 0.1 bar He stagnation pressure, giving a supersonic expansion and jet-cooled molecules. “Hot” data are recorded from a quasi-effusive beam. The SA:Ar data are taken with 1 bar Ar stagnation pressure, forming large Ar clusters. a) $\lambda_{\text{probe}} = 490$ nm. b) $\lambda_{\text{probe}} = 616$ nm.

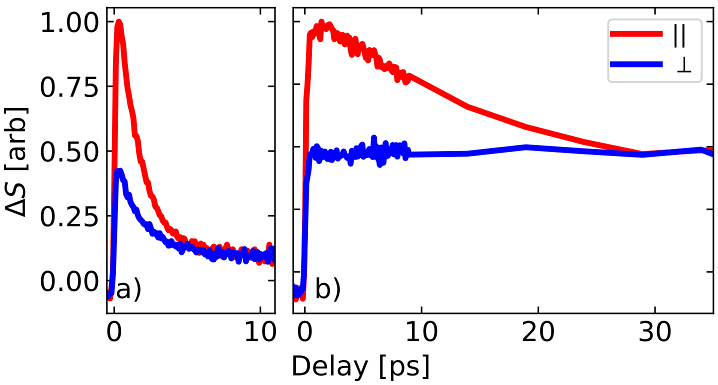

Figure 6.5: Rotational dynamics of isolated SA vs. SA:Ar. CE-TAS signals with pump and probe pulses parallel (red) and perpendicular (blue) for a) isolated jet-cooled SA and b) SA:Ar with 1 bar Ar stagnation pressure. $\lambda_{\text{probe}} = 490$ nm. Formation of large Ar clusters around the SA molecules dramatically slows rotational dephasing.

6.3.2 Salicylideneaniline in Argon Clusters

To further understand the different parallel relaxation channels of SA, we perform experiments on SA in Ar clusters which we denote SA:Ar. Similar to a rare-gas matrix environment, Ar clustering can affect the dynamics in two ways: (1) by providing a channel for the dissipation of vibrational energy and (2) by providing steric hindrance to large amplitude motions, such as the isomerizations shown in Fig. 6.1. Figure 6.4 compares the CE-TAS signals for the SA:Ar system to the isolated molecule. The SA:Ar signal decays much slower in the clustered sample than in the hot or cold SA case. From our fluorescence measurements, we can place a lower bound on the enhancement of the total fluorescence yield of SA:Ar vs. isolated SA of 100x. Fluorescence enhancement in SA has also been previously reported in matrix isolation studies [225]. The data in Fig. 6.4 were recorded at 1 bar since this provided a workable, stable signal for recording a full spectrum. Increasing the Ar pressure continues to enhance this effect until the pump/probe signal is nearly constant out to 700 ps at a stagnation pressure of 2.5 bar.

We estimate the average cluster size by analyzing the rotational anisotropy. Fig. 6.5 compares $\Delta S_{\parallel}$, $\Delta S_{\perp}$ data taken in a He expansion to an Ar expansion with 1 bar stagnation pressure. The rotational anisotropy persists roughly 5 times longer due to the increased moment of inertia of the SA:Ar system. Considering that the rotational dephasing time scales as $1/\sqrt{B}$ [187], where B is the rotational constant, we estimate an average number of 15 Ar atoms clustered to the SA molecules [252].

A full CE-TAS dataset for the SA:Ar system is shown in Fig. 6.6 with representative scans shown in Fig. 6.6a) and the full spectrum in Fig. 6.6b). Just as in the case of the individual lineouts discussed above, the entire spectrum decays with a significantly longer time constant than in the cold SA case above.

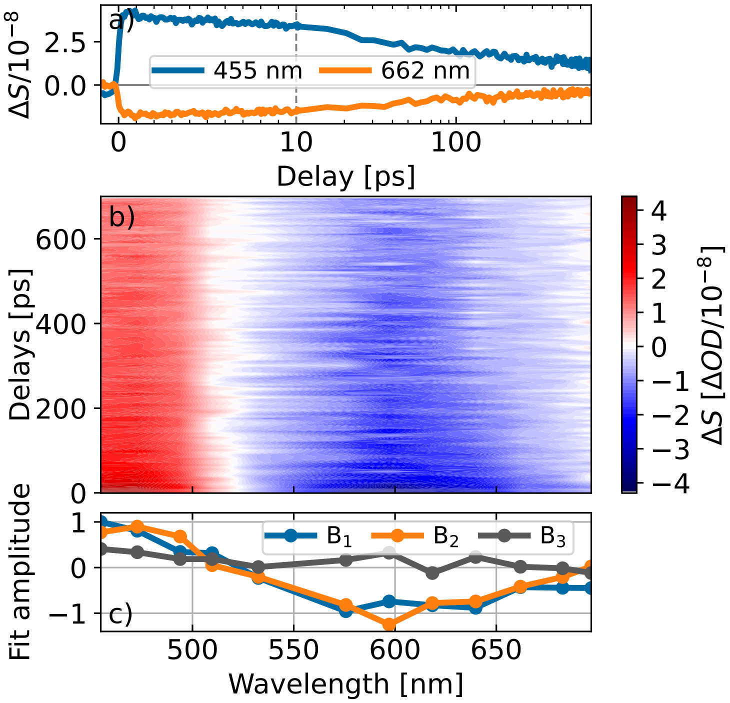

Figure 6.6: CE-TAS of SA:Ar from SA seeded in 1 bar of Ar. a) Pump/probe traces at 2 representative probe wavelengths. The time axis shown changes from linear to logarithmic at 10 ps to better show the signal at the negative time delays. b) TA spectrum constructed from the individual scans. c) DAS from global fit of b) with 3 components normalized to the maximum of B_1. $\tau_{B_1} = 24$ ps, $\tau_{B_2} = 850$ ps, and $\tau_{B_3} > 10$ ns. Individual points are at the discrete probe wavelengths which were combined for the spectrum.

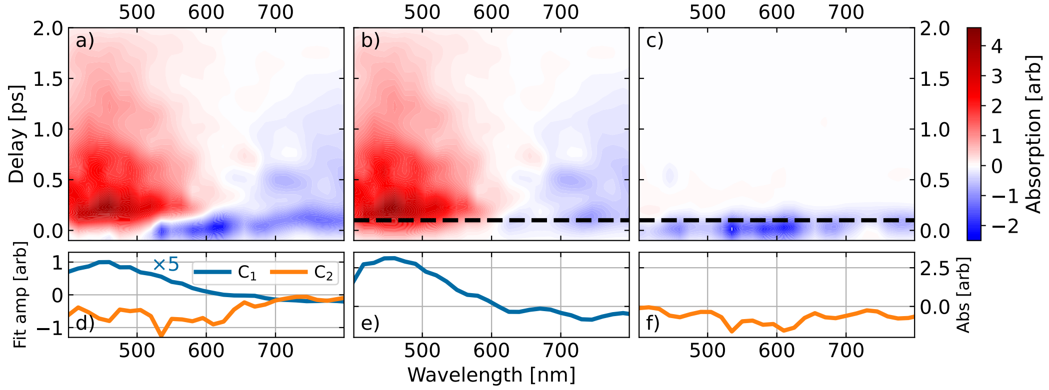

Figure 6.7: Theoretical TAS results from post-processed AIMS calculations containing a) all geometries, b) only keto geometries, and c) only enol geometries. d) DAS from a global fit of the spectrum in a). e) and f) show spectral lineouts using the right axis at 100 fs from the corresponding keto and enol spectra, respectively. See text for details regarding resampling and convolution with experimental resolution.

Despite the slower decay, the initial rise time remains instrument response limited, indicating rapid ESIPT rates unaffected by the cluster environment.

We fit the data using equations 6.1 and 6.2 with $X_n \equiv B_n$. The DAS from the fit are shown in Fig. 6.6c) for 3 components (reduced χ^2=4.2). The associated time constants are $\tau_{B_1} = 32$ ps, $\tau_{B_2} = 1030$ ps, and $\tau_{B_3} >$10 ns. The same fit procedure was also tested for 2 (reduced $\chi^2 = 5.0$) and 4 (reduced χ^2=4.1) time constants. The 4-component fit is shown in Appendix B(Fig. B.5). The additional DAS for the 4-component fit has only a small amplitude at all wavelengths and a long decay time not apparent in the raw data, and thus was determined to be not significant. In general, the fits on the SA:Ar data are worse than the He case due to increased noise from turbulence from the higher pressure gas and scatter from bare Ar clusters.

The overall shapes of the DAS are nearly identical to the He case in Fig. 6.2b), indicating that the clustering is not modifying the electronic energies significantly. The only major change in the fit results is the additional component B_1. B_1 and B_2 are nearly identical to each other and to A_1 which most likely indicates that the monoexponential A_1 feature in cold SA becomes a biexponential $B_1 \rightarrow B_2$ decay in SA:Ar. Previous fluorescence measurements in matrix isolation also observed biexponential decay in the fluorescence [225].

6.3.3 Simulated spectrum

The simulated TAS spectrum is presented in Fig. 6.7a). The raw theoretical data is presented in Appendix B Fig. B.8. Just as for the experimental data, a global fit was applied to the theoretical data, with $X_n \equiv C_n$ in equation (6.1). Fig. 6.7d) shows the DAS from a global fit to the data with 2 components. The associated time constants are $\tau_{C_1} = 0.62$ ps and $\tau_{C_2} = 20$ fs. Removing or adding components resulted in either a poor or non-physical (i.e. two nearly identical time constants) fit. The trajectories in the AIMS simulations performed by Pijeau et al. were ended once the initial S_1 wavepacket population decayed below 0.01, so there is no contribution of trajectories on the ground-state surface to the spectrum [196]. Importantly, this means that the photochrome signal is not present in the simulated TAS dataset, but we address this drawback with static calculations discussed below.

A major benefit of directly computing experimental observables from theoretical trajectory data is that it is possible to analyze the spectrum by decomposing it into contributions that correspond to different molecular structures. To analyze the signature of proton transfer, we separate the spectrum into contributions from only keto or enol geometries by comparing O-H and N-H distances along the proton transfer coordinate. When $d_{\text{O-H}} - d_{\text{N-H}}$ is positive (negative), these geometries are labeled enol (keto). The spectral contributions from the keto and enol tautomers are shown in figures 6.7b) and 7c), respectively. For comparison with the DAS of Fig. 6.7d), we plot lineouts of the spectra at 100 fs in Fig. 6.7e) and 6.7f). From this comparison, it is clear that the C_1 DAS corresponds to the keto spectrum after ESIPT.

C_2 on figures 6.7d) and 6.7f) is entirely negative across most of the spectrum representing prompt, broadband stimulated emission from enol tautomers during only the first ≈ 100 fs. The C_2 component corresponds well with the prompt enol geometry signal seen in Fig. 6.7f), corresponding to near-planar enol geometries before and during ESIPT.

To further understand the spectral contribution from the CN twist relaxation mechanism, we filter the enol-only spectrum by CN twist angle, shown in Appendix B Fig. B.9 for signals from geometries with angles less than 140°. In the ground state, this angle is 180° for a planar orientation and ≈ 90° near CI2 [12, 196] so any features on Appendix B Fig. B.9 should be signatures of the internal conversion towards CI2. Within the experimental observation window of 450-700 nm, all absorption or emission features from twisted enol geometries are more than an order of magnitude smaller than the main spectral components in Fig. 6.7a). Thus, the CN twist channel may be present, but it is unlikely discernible in the TAS signal.

Separate from the AIMS/TD-CASCI calculations we perform several TD-CASCI calculations at fixed geometries for the ground state local minima found by Ortiz-Sánchez et al [12]. The calculated absorption spectra for both prospective photochrome conformers are included in Appendix B Fig. B.10. Our calculated trans keto photochrome (shown in the bottom right box of Fig. 6.1) spectrum has an absorption peak centered near 480 nm. We also calculate the absorption spectrum of the Ortiz-Sánchez's twisted enol minimum (shown in the bottom left box of Fig. 6.1), and found absorbance at ≈ 300 nm which is beyond the range probed in this experiment.

6.4 Discussion

Our overall proposed scheme for dynamics in both the isolated molecule and SA:Ar is shown in Fig. 6.8. Much of the dynamics is born out in the global analysis of the TA spectrum, which we describe step by step below.

In the isolated molecule, the initially excited enol quickly undergoes ESIPT, giving rise to the classic ESA/SE signature seen in the GA component A_1. We assign A_1 to the fluorescent keto state, and this assignment is consistent with the theory component C_1 and the keto-filtered theory data of figure 6.7b). This assignment is also in accord with previous work on SA and other ESIPT molecules. At longer delays, after the fluorescent state has decayed, we assign the remaining long-lived signal, captured by A_2 to the keto photochrome. This assignment is supported by the correspondence between A_2 and other reported spectra of the metastable photochrome state [8, 213–215, 222, 224] and also our calculated absorption spectrum for the trans keto minimum. We do not observe any signatures of the initially excited enol (C_2 and Fig. 6.7c) in the experimental data, most likely due to our time resolution and excess pump energy, but we do note that it was observed in solution by fluorescence upconversion. [226].

The 1.8 ps decay time of the excited keto state we observe is significantly slower than those observed in gas-phase TRPES by Sekikawa et al [7]. This highlights the role of the observable on the measured dynamics, since nominally these two measurements are taken under the same molecule and excitation conditions. The shorter lifetime measured by TRPES could be due to energy windowing effects, [19, 20, 253] especially since the TRPES study was done using 1+2 photoionization [7].

Comparing to solution phase work, the gas-phase TA spectra very closely correspond to those measured in solution, as shown in the raw data in figure 6.3. This is not unexpected since the TA spectrum shape has been previously shown to be relatively insensitive to the choice of solvent. [223,224]. Regarding the dynamics, our 1.8 ps time constant is slightly shorter than the shortest S_1 keto lifetimes reported in solution phase work. A range of solution-phase lifetimes measured via TAS between 3.5 and 50 ps have been previously reported, with a strong solvent dependence [8, 223, 224]. The faster internal conversion in the absence of solvent supports the mechanism of internal conversion occurring at geometries very twisted compared to the ground state, as solvent can impede or slow down this large-amplitude motion.

Previous gas-phase experiments on SA varied the internal energy by changing the excitation wavelength. Sekikawa et al. observed a larger long-lived photochrome signal as the excitation energy was increased and assigned this feature to enhanced ESIPT with larger excitation energy due to barriers to ESIPT at twisted geometries [7]. In our experiment, we vary the internal energy of the molecule via large changes in temperature. Notably, we find that the appearance of the fluorescent keto signal (A_1) is equally prompt for both the hot SA and cold SA as shown in Fig. 6.4, and thus find no evidence for a delay in the ESIPT at lower internal energies. However, we do find that the photochrome yield is higher for the vibrationally excited molecule, in accord with Sekikawa et al. We attribute this latter effect to the photochrome being formed from vibrationally excited keto molecules as illustrated in Fig. 6.8a). This was previously proposed by Rosenfeld et al [214] and others [215,216,224,225], but has since been disputed [7,8,222]. This conclusion is further supported by the impact of Ar clustering on the dynamics as discussed below.

While the clustering of SA with Ar has dramatic changes on the observed *dynamics* of the fluorescent state, captured by GA components B_1 and B_2, the *spectrum* of the fluorescent keto state is essentially unchanged. This is not unexpected given the weak solvent dependence observed in previous TA work. [223,224]. Our justifications for assigning B_1 and B_2 to the excited keto are the same as discussed in the isolated molecule, namely correspondence with theory and previous work. The keto lifetime increases from 1.8 ps to a biexponential decay with $\tau_{B_1} = 32$ ps and $\tau_{B_2} = 1030$ ps when measured with 1 bar Ar stagnation pressure. These lifetimes continue to increase with increasing Ar carrier pressure, which we attribute to increasing the fraction of SA molecules in the beam clustered with Ar.

As mentioned before, Ar clustering can affect the dynamics in two ways: (1) dissipation of vibrational energy and (2) steric hindrance of large amplitude motions. From the hot/cold comparison in the isolated molecule, where we observe only a small effect of vibrational energy of the dynamics, we conclude that the dominant effect is steric hindrance. Ar atoms clustered around the central bonds can inhibit the large rotation necessary to reach CI1. Similar overall trends were observed in SA in different environments using ps time-resolved fluorescence, with only minor changes (factors of 2-5) in lifetimes across a wide range of solvents and a few hundredfold increase in matrices and glasses [225].

While the excited keto population giving rise to fluorescence is stabilized upon clustering with Ar, the photochrome yield we observe (captured by B_3), as judged by the ratio of the photochrome signal compared to the initial TAS signal amplitudes, is the same in SA:Ar as the isolated molecule. This strongly supports a parallel channel for the production of the photochrome, separate from the relaxed fluorescent keto state. After ESIPT, keto geometries are formed with a wide range of internal energies. The B_1 and B_2 DAS components are very similar, indicating a similar electronic state and geometry, and we assign B_1 to the hotter portion of the keto population. The absence of a spectral shift between B_1 and B_2, i.e. B_2 is not a shifted IVR product of B_1, further supports a parallel model. In the proposed dynamic scheme of Fig 6.8b), the vibrationally more energetic population of keto geometries is formed promptly and reaches CI1 more easily. This “hotter” population can then continue to isomerize on the ground state to the trans keto photochrome state. Note that the initial internal energy is similar in the cold isolated and SA:Ar cases, and thus the hot keto population fraction and photochrome yields are the same, whereas the photochrome yield for the hot isolated molecule is larger than both jet-cooled SA and SA:Ar.

The vibrationally cooler population, to which we assign to B_2, like A_1, represents the state responsible for fluorescence. Instead of forming the photochrome, this population returns to the ground state cis keto and, eventually, undergoes back proton transfer to the S_0 enol minimum. In this model, the initially excited enol is the common precursor to both channels that produce the photochrome and fluorescent state, as proposed by Zgierski and Grabowska [216]. Note that biexponential nature and hot keto population is not observed in the isolated molecule case because the hot population can go through CI1 and form the photochrome much more quickly, and this is not resolvable with our time resolution. The major difference between the isolated and SA:Ar cases, highlighted in Fig. 6.8 is the relaxation mechanism from the relaxed fluorescent state. In the isolated molecule, this decay to the ground state keto takes 1.8 ps and occurs predominantly via internal conversion to CI1 due to the short excited state lifetime and reduced fluorescence yield. In SA:Ar, the clustering shuts off the internal conversion pathway and forces radiative decay to be the dominant pathway which we observe as an increase in fluorescence and excited state lifetime.

6.5 Conclusions

In this chapter we have combined cavity-enhanced transient absorption spectroscopy with AIMS/TD-CASCI calculations to study the dynamics of salicylideneaniline after excitation to S_1. This study introduces several new paradigms in ultrafast spectroscopy. For one example, our experiments on SA in Ar clusters are analogous to matrix isolation, where ultrafast spectroscopy has previously been very difficult and limited mostly to "action"-based methods based on fluorescence detection [254–256]. Using the CE-TAS method we have shown how one can effectively record conventional ultrafast transient absorption (i.e. direct absorption) measurements in rare-gas matrix environments with rapid sample refreshment. For another example, we have shown how long-lived TA signals with lifetime $\tau \gtrsim 1/f_{\mathrm{rep}}$ can be recovered via careful analysis of data at negative pump/probe delays and the modified GA model of equation (6.2). These new techniques can be applicable for both future CE-TAS studies and other ultrafast spectroscopy contexts.

The TD-CASCI technique presented here allows for quickly simulating TAS spectra from AIMS calculations which, when compared to experimental spectra, facilitate spectral assignment. Additionally, processing the simulated and experimentally measured data in an identical way further helped assign dynamics. With gas phase TAS measurements, we are measuring the free molecular dynamics which makes direct simulation easier without the need for solvent models.

By combining these new experimental and theoretical techniques, we provide insight into the relaxation dynamics of SA, summarized in Fig. 6.8. In

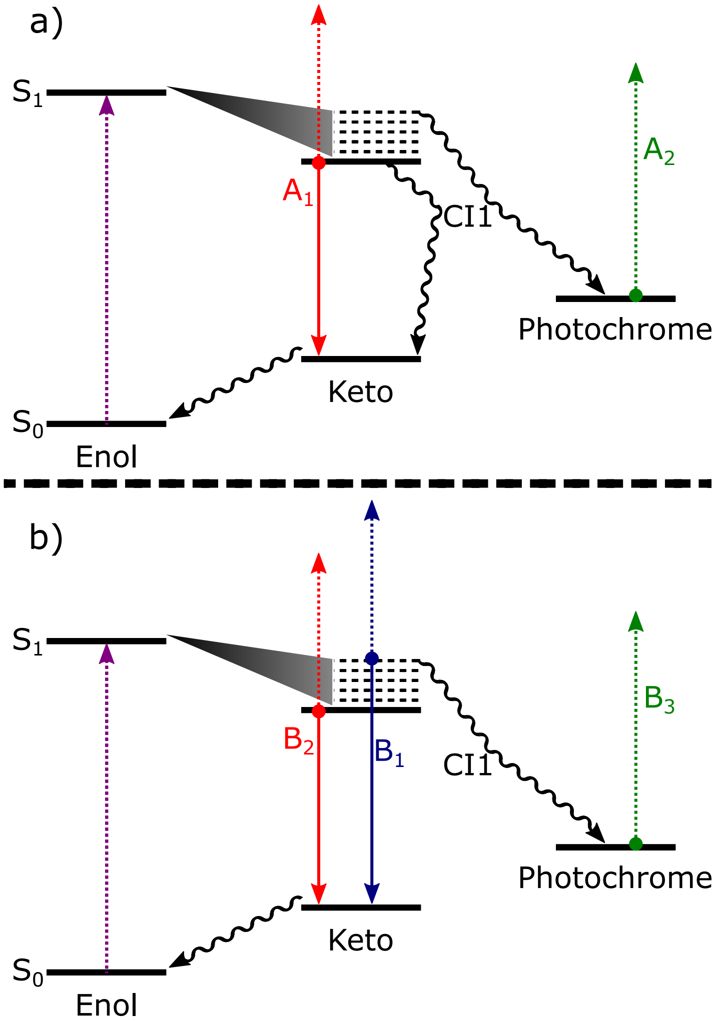

Figure 6.8: Proposed relaxation mechanism and photochrome pathway in a) isolated SA and b) SA:Ar. Dashed lines indicate absorption of light and solid lines are emission. Labels indicate DAS features from global analysis. In the isolated molecule, a), the initially excited enol undergoes ESIPT and generates the keto tautomer with a wide range of internal energies. The hottest of which immediately internally convert to CI1 and isomerize to the photochrome. The colder population in the relaxed fluorescent state also decays via CI1, but eventually returns to overall enol ground state. In SA:Ar, b), the the presences of the Ar cage slows down photochrome generation ($\sim 0 \rightarrow 24$ ps) and traps the vibrationally cold keto population such that it can only decay radiatively (1.8 ps $\rightarrow > 1$ ns).

general, we find stronger agreement with the time constants and interpretations from previous solution-phase TAS work although we do agree with the trends found in TRPES. By comparing and contrasting with previous work and reinterpreting within the scope of our analysis we hope to provide a more universal model. After prompt ESIPT, keto geometries are formed with a broad energy distribution, the hottest of which rapidly internally convert through CI1 and isomerize to the trans-keto photochromic state. The colder keto population relaxes more slowly through CI1 to reach the cis-keto ground state in 1.8 ps for the isolated molecule and eventually return to the enol S_0 minimum. Increasing the internal energy by lowering the gas pressure results in more hot keto population and more yield of the long-lived photochrome. Embedding the SA molecule in Ar clusters sterically hinders isomerization such that only the hot keto population can undergo internal conversion to the photochrome state, with a dramatic increase in the S_1 lifetime recorded in TAS and also the fluorescence yield. We find no experimental evidence for the proposed secondary enol twist relaxation channel, but our calculations indicate that it likely lies outside our detection window.

Chapter 7

Intersystem crossing, proton transfer, and photolysis in *ortho*-nitrophenol

7.1 Introduction

Ortho-nitrophenol (ONP), shown in Fig. 7.1a), has attracted significant interest in the past 20 years as a potential source of nitrous acid (HONO) and the hydroxyl radical (OH) in the atmosphere [257–261]. ONP is produced from combustion in automobiles and other industrial processes including biomass burning [262–264]. In the atmosphere, ONP can absorb sunlight and photolyse to produce OH or HONO which contribute to smog and ozone formation as well as facilitate secondary organic aerosol formation [265]. Because of its role as a pollutant, understanding the mechanisms driving the photolysis processes in ONP is a complex and important problem in atmospheric chemistry. Also, from a fundamental chemistry perspective, there has been significant interest in understanding the photoreactivity and charge-transfer properties found in many nitroaromatic compounds, including ONP [266, 267].

As shown in Fig. 7.1a), ONP is planar in the ground state with a stabilizing internal hydrogen bond between the hydroxyl and nitro groups [268]. ONP

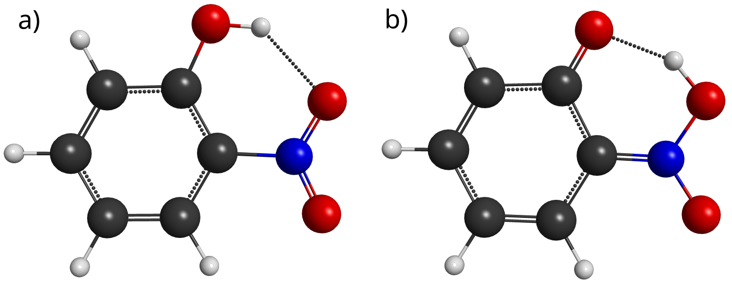

Figure 7.1: a) *ortho*-nitrophenol b) *aci*-nitrophenol

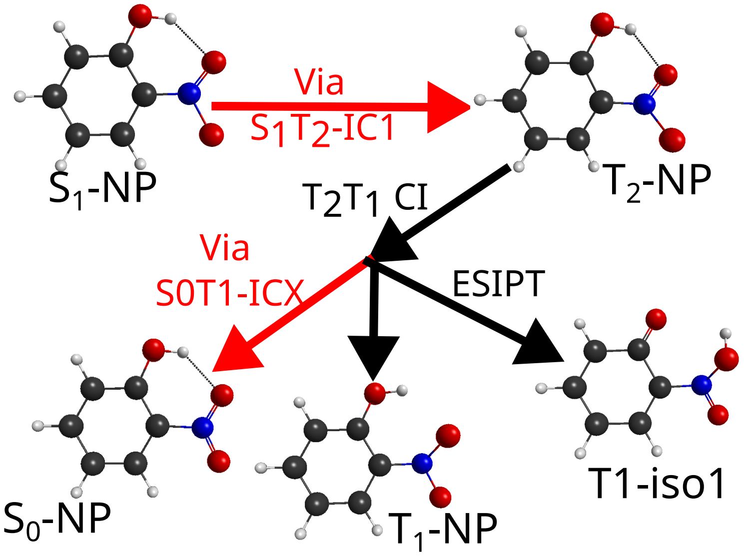

Figure 7.2: Dominant relaxation pathways proposed by Xu et al. [9]. Red lines indicate ISC and black lines are internal conversion. ONP photoexcited to S_1 rapidly undergoes ISC followed by internal conversion to T_1 where it either converts back to the ground state, remains trapped, or undergoes ESIPT.

absorbs in a broad range in the UV with two main bands corresponding to excitation to $S_1 \leftarrow S_0$ with a maximum near 355 nm or $S_4 \leftarrow S_0$ with a maximum near 260 nm [10, 259]. After photoexcitation, there are several proposed competing decay channels in ONP involving internal conversion, intersystem crossing, and fragmentation.

When excited to the S_1 state, excited-state intramolecular proton transfer (ESIPT) can occur rapidly along the internal hydrogen bond, moving the proton from the hydroxyl group and forming a HONO side chain. This structure, called *aci*-nitrophenol (*aci*-NP), is shown Fig. 7.1b) and has been confirmed by infrared spectroscopy following UV irradiation [269]. After ESIPT, the *aci*-NP side chain can fragment either at the C-N bond, producing HONO, or at the upper O-N bond, producing OH. Additionally, photolysis channels involving the production of NO have been proposed [11] and recently confirmed when excited at 266 nm [270, 271].

Due to the strong spin-orbit coupling present in many nitroaromatic compounds [272, 273], ONP is thought to undergo rapid intersystem crossing (ISC) to the triplet manifold where internal conversion and fragmentation can occur. No fluorescence has been recorded from ONP, indicating rapid depopulation from the singlet manifold. Studies by Vereecken et al. and Guo et al., using quantum chemistry methods and RRKM calculations both found OH and HONO production to be more favorable from the lowest triplet state than the singlet states [11, 14]. Additionally, rotationally-resolved laser-induced fluorescence studies of the photolysed OH produced from ONP appeared to come from a triplet parent [260].

Tracking and understanding the complex and rapid relaxation dynamics in photoexcited ONP is a challenge ideal for ultrafast spectroscopy. Several studies have been performed, both experimentally and using theoretical dynamics simulations. In the gas phase, Ernst et al. recorded the dynamics excited to S_1 with time-resolved photoelectron spectroscopy [10]. They found evidence of prompt ESIPT within 14 fs, a long-lived signal which the authors assigned to a trapped population in the triplet T_1 state, and a 130 fs time constant assigned to the S_1 lifetime before reaching a conical intersection (CI) to the ground state. This CI, identified theoretically by the authors, involves a 90° out-of-plane twist of the HONO group after ESIPT [10]. Also in the gas phase, Nitta et al. [258] performed similar TRPES measurements on S_1 with an XUV photoionization probe. The authors interpreted a delayed photoelectron signal as a signature of HONO formation proposed to occur from the triplet manifold. Otherwise, they generally agreed with the dynamics interpretation from Ernst et al. [10].

In the solution phase, Ernst et al. also performed transient absorption (TA) spectroscopy on S_1 [10]. They found prompt stimulated emission (SE) in the range of 500-1100 nm lasting only 200 fs and overlapping excited-state absorption (ESA) features from 480 to 600 nm decaying biexponentially with 400 fs and 9 ps time constants in n-hexane. They assign the SE and fastest ESA components to the same S_1 internal conversion via CI as their TRPES work and the longer-lived ESA component to internal conversion in the triplet manifold. Additionally, in some solvents they observe a long-lived component assigned to the trapped T_1 population.

To understand the competing ultrafast processes in ONP, Xu et al. performed static CASSCF calculations to find CI and ISC points followed by trajectory surface hopping dynamics simulations [9, 13]. They found several possible relaxation mechanisms, summarized in Fig. 7.2 using the labeling schemes from the original works. After excitation, Xu et al. propose rapid ISC to T_2 followed by internal conversion to T_1. A portion of the molecules remain trapped in the T_1 minimum while the rest either undergo ESIPT or undergo ISC again back to the S_0 minimum without proton transfer occurring. The dynamics simulations do not include any fragmentation channels.

The competition between different decay channels clearly makes interpreting experimental signals difficult and theory complex. The disagreement between gas and solution phase work also complicates the assignment of features. To help bridge the gap between solvent environments, here we perform gas-phase transient absorption measurements on ONP excited to $S_1(\pi, \pi*)$. We also investigate the affect of temperature and cluster environment on the dynamics. Additionally, we build off previously published theoretical work with additional calculations to help assign the stimulated emission signatures and fragmentation pathways.

In general, our measurements agree more with the solution-phase TA work but disagree with the dynamics model of Ernst . [10]. We find fast ISC in ONP as well as possible fragmentation signatures and rapid internal conversion, consistent with some of the decay channels proposed by Xu et al. [9].

7.2 Methods

7.2.1 Experimental

ONP was purchased from Sigma-Aldrich (98%) and used as received. The solid sample is placed in a stainless steel sample cell and was heated to 70° C to increase vapor pressure. The spectrometer is described in detail in Chapter 5 and [1]. For all measurements discussed, the interaction region is 3 mm above the nozzle. The 355 nm pump pulse is not cavity-enhanced and the average pump power is 400 mW. Since there is no measurable fluorescence or phosphorescence signal from ONP, there is no point-by-point scaling to compensate sample drift. However, there is no discernible signal drift over sequential scans and no large changes between scans taken on different days, so sample drift normalization is not necessary. Separate probe wavelength scans are scaled by pump power as well as cavity finesse as discussed in Chapter 5. Unless otherwise specified, He is used as carrier gas at a stagnation pressure of 0.3 Bar. An independent instrument response function (IRF) recorded from 2-photon absorption in gas-phase carbon disulfide, as discussed in Chapter 5, is recorded at every probe wavelength immediately following ONP scans except at 658 and 678 nm where the data is fit with an error-function for the IRF.

7.2.2 Modeling

We fit the spectrum using global analysis [35] and include the long-lived signal "artifact", similarly to Chapter 6:

$$\Delta S_{\mathrm{model}}(\lambda, t) = \sum_{m=0}^{N} G(\lambda, t + m/f_{\mathrm{rep}}) - G(\lambda, t + m/f_{\mathrm{rep}} + T_{\mathrm{pr}}) \tag{7.1}$$

where ΔS represents the background-subtracted signal recorded in the experiment. T_{pr} is the probe/reference delay time equal to 5 ns, and $G(\lambda, t)$ is a traditional global analysis model. We sum over $N = 20$ previous experiments to model the background absorption feature. For the MA spectrum, we assume a model consisting of n parallel exponential decays with time constants, τ_n, and decay associated spectra (DAS), A_n convolved with a wavelength-dependent IRF, i.e,

$$G_{\mathrm{MA}}(\lambda, t) = \mathrm{IRF}(t) \otimes \sum_{n} \left[\mathrm{A}_n(\lambda) \exp(-t/\tau_n) \times H(t - t_n^{\mathrm{shift}})\right] \tag{7.2}$$

where $H(t_n^{\mathrm{shift}})$ is the Heaviside function and a t_n^{shift} is a free time zero shift parameter on each decay component. During the fitting procedure, t_n^{shift} is only allowed to be positive to ensure that the relaxation channels can only begin after the independently-measured time zero. Using time zero as a fit parameter was used in previous studies, due to ESIPT, ISC, or non-exponential dynamics [10,258]. We assume a parallel model because several of the proposed relaxation pathways are thought to occur simultaneously [9, 13] and there is no experimental consensus for a particular sequential dynamic model. The difference between the fit and experimental/simulated data is minimized using a Levenberg–Marquardt fit algorithm.

Additionally, to help disentangle overlapping dynamics and more definitively assign spectral signatures, we apply global analysis to the signals taken with parallel and perpendicular pump/probe polarizations separately as described in [274, 275]. These signals include a rotational component relative to the orientation-averaged MA signal due to the relative alignment of the transition dipole moment (TDM) for the pump and probe excitations. The pump excitation preferentially excites the molecules with TDMs more aligned with the laser polarization which the polarized probe pulse then samples using the excited-state TDMs. This distribution leads to an initial rotational anisotropy, r_0, which is bounded from -0.2 for pump/probe TDMs perpendicular to 0.4 for parallel [51, 276]. The pump-induced anisotropy decays in time from the initial value either due to rotational dephasing or transition dipole moment reorganization [187, 277, 278]. The parallel and perpendicular TA signals,$\Delta I_{||}$ and $\Delta I_{\perp}$, can be constructed from the purely electronic magic angle signal, ΔI_{MA}, and the time-dependent anisotropy R in the following way [274]

$$\Delta I_{||} = \frac{1}{3} I_{\mathrm{MA}} \left[1 + 2R\right] \tag{7.3}$$

$$\Delta I_{\perp} = \frac{1}{3} I_{\mathrm{MA}} \left[1 - R\right] \tag{7.4}$$

To model the parallel and perpendicular polarization signals, a modified global analysis model including orientational effects is used. The parallel and perpendicular signals are constructed via combinations of the MA signal from Eqn. (7.2) and the anisotropy, $R_n^{\mathrm{model}}(t)$, analogous to Eqn. (7.3) and (7.4):

$$G_{||}(\lambda, t) = \frac{1}{3}\mathrm{IRF}(t) \otimes \sum_n \mathrm{A}_n(\lambda) \exp(-t/\tau_n) \left[1 + 2R_n^{\mathrm{model}}(t - t_n^{\mathrm{shift}})\right] H(t - t_n^{\mathrm{shift}}) \tag{7.5}$$

$$G_{\perp}(\lambda, t) = \frac{1}{3}\mathrm{IRF}(t) \otimes \sum_n \mathrm{A}_n(\lambda) \exp(-t/\tau_n) \left[1 - R_n^{\mathrm{model}}(t - t_n^{\mathrm{shift}})\right] H(t - t_n^{\mathrm{shift}}) \tag{7.6}$$

The time zero free parameter from Eqn. (7.2) also applies to the rotational component due to the Heaviside function.

Rotational anisotropy is assumed to decay exponentially from the initial anisotropy:

$$R_n^{\mathrm{model}}(t) = B_n \exp(-t/\Phi_n) \tag{7.7}$$

In this associative model [274, 275], each MA component has an independent rotational component with an initial amplitude corresponding to the TDM of spectral feature i.e., $B_n = r_0$ for each transition. During the fit, B_n is bounded to [-0.2,0.4]. For ONP, the electronic dynamics are completed within the first ≈ 1 ps, while the expected rotational time constant is several times longer, so Φ_n does not contain much actual information and the value returned from fits is large with a significant error. This results in the fit optimization essentially ignoring the time dependence of R^{model} and just varying each component's B_n, and therefore r_0.

Long-lived "artifacts" from reference subtraction are included via the full fit to the data obtained by inserting Eqns. (7.5) and (7.6) into Eqn. (7.1). To optimize the orientational parameters with global analysis, the output time constants from the MA fit are used as initial conditions for a combined fit which minimizes the error between the model and experiment for MA, parallel, and perpendicular signals simultaneously. The DAS and MA time constants do not change appreciably when fitting the orientational components.

7.2.3 Theoretical calculations

To help assign spectral features, ab-initio calculations are performed using geometries from previous work. Based on the dynamics work of Xu et al. in refs [9, 13], we calculate TDMs at several geometries of interest in both the singlet and triplet manifolds and adopt the naming conventions from the original work. For the current study, we focus on the geometries which contribute an SE signal to help assign the experimental component discussed in Section 7.3. The same level of theory as the original work is used, 6 state averaged complete active space self-consistent field with an active space of 10 electrons in 10 orbitals (SA-6-CASSCF(10,10)) and the 6-31G(d, p) basis. These calculations were done using Molpro 2020.2 [279] with the assistance of Arshad Mehmood from Ben Levine's group at Stony Brook University.

To compare to the retrieved anisotropy parameter from global analysis discussed above, we calculate a theoretical r_0 from the returned simulated TDMs as in [280–282]:

$$r_0 = \frac{1}{5}(3\cos^2\Delta\theta - 1) \tag{7.8}$$

where $\Delta\theta$ is the angled between the pump TDM and the excited state TDM.

As discussed in the introduction, several theoretical studies and experiments have indicated that ONP can be photolysed to form different possible fragments. Two theoretical studies have investigated the different possible fragmentation pathways possible. The first, from Vereecken et al. [11] using quantum chemistry methods combined with RRKM calculations, found several channels possible occurring in both the triplet and singlet manifolds, producing OH or NO radicals as well as HONO. These small fragments are known experimentally to not absorb in the visible range [283, 284], but the aromatic parent fragment may have absorption within our probe range. To determine if there is any spectral contribution from these structures following fragmentation, we calculate transition energies for several geometries provided by the authors using time-dependent density functional theory (TDDFT) with the CAMB3LYP functional and 6-31G(d, p) basis set. Nearly all the fragments are open-shell radical molecules so an unrestricted Hartree Fock reference is used. Additionally, Guo et al. [14], performed a similar study on the fragmentation channels leading towards OH and HONO production, and we perform TDDFT simulations on the parent fragment geometries provided by the authors as well. All fragment calculations are performed in GAMESS-US 2021 (R1) [285]. Naming conventions from the original works will be used with the first author name for clarity.

7.3 Results

7.3.1 Isolated Molecule

The magic angle (MA) TAS of the jet-cooled, isolated ONP molecule in He carrier gas is shown in Fig. 7.3a). Individual lineouts at selected probe wavelengths and for different pump/probe relative polarizations are shown in Fig. 7.4. Due to the short-lived electronic dynamics and complex orientational reorganization which will be discussed below, rotational temperatures in the molecular beam cannot be estimated simply using the methods described in previous chapters. The molecule in the ground state does not absorb in the probe range, so all negative signals are due to spontaneous emission [10].

Figure 7.5 shows comparisons at 473, 572, and 696 nm to the TA recorded in n-hexane from Ernst et al. at similar probe wavelengths [10]. These scans are scaled to the make the peak positive signal the same at each probe wavelength. The more rapid decay of stimulated emission in the solution phase measurement is most likely due to the time resolution, which the authors report as being less than 200 fs, being shorter than our current instrument [10]. Overall we find close agreement between the two experiments, a surprising trend observed in the gas-phase TA experiments we have performed so far.

The MA spectra in Fig. 7.3 is satisfactorily modeled with 3 or 4 time constants using Eqns 7.1 and 7.2. In order to capture the orientational dynamics, which will be discussed below, 4 components are necessary. The DAS for a 4 component fit are shown in Fig. 7.3b) and the associated time constants are summarized in Table 7.1. This fit includes a time shifts on all components as shown in Eqn. (7.2). The inclusion of these shifts improved the fit residuals, particularly in the middle of the spectrum where the SE and ESA from multiple components overlap, but it had little effect on the time constants or DAS.

The two DAS components with short time constants, A_1 and A_2, have very similar fit parameters except they are opposite signs. A_1 is negative across the whole spectrum representing broadband SE. A_2 is positive for all

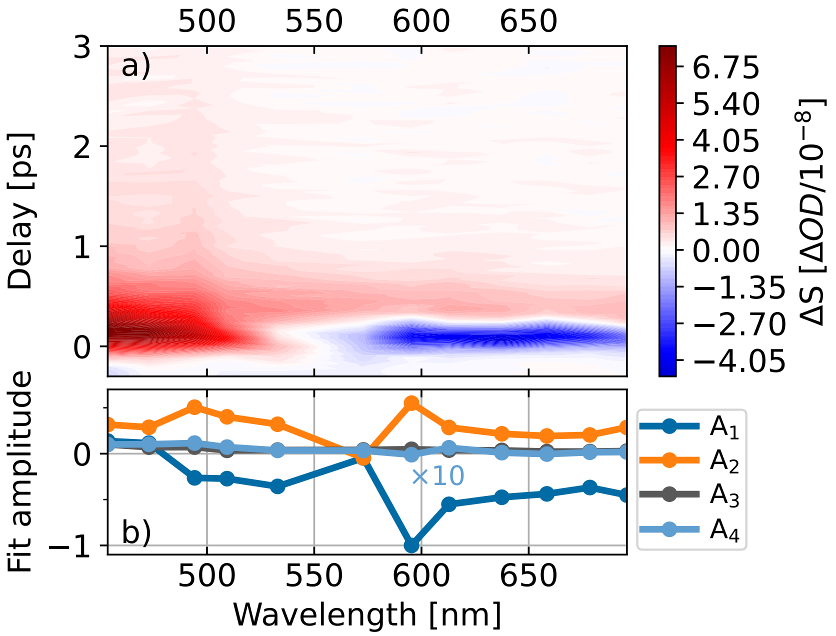

Figure 7.3: TA of isolated ONP a) Full MA spectrum recorded in 0.3 Bar stagnation pressure of He. b) DAS from global analysis fit with 4 components. Note that the amplitude of A_4 is multiplied by 10.

n	τ_n	t_n^{shift}	r_0	Φ_n
1	90 fs	20 fs	0.38	7 ns
2	120 fs	20 fs	0.24	5 ns
3	420 fs	190 fs	0.35	> 10 ns
4	>10 ns	430 fs	0.08	> 10 ns

Table 7.1: Summary of fit results for global analysis of the MA and polarized signals.

wavelengths, indicating broadband ESA. Since the two components have very similar time constants and shifts, both features are most likely emission and absorption from the same initially excited state. The two transitions have different TDMs, which is why they require separate fit components. The ESA and SE overlap in across the whole probe range but, as can be seen in the data, SE is dominant for redder wavelengths. For a 3 component MA fit, these two features are combined into one DAS with both positive and negative features.

A_4 is a small contribution on the blue edge of the spectrum and is observable out to the maximum scan range of the current instrument (700 ps) without change and is also responsible for the pre-time zero signal. This feature is most likely long-lived absorption from a trapped triplet state or a fragment left after photoinduced dissociation as discussed above. The time-zero shift on A_4 appears to be an artifact of the fitting process, as several fits optimized to different values with similar goodness-of-fit. The intermediate DAS component, A_3, is a relatively flat, broadband ESA feature which begins at a delayed time. It is not clear from the fits if this warrants a kinetic model or if the generation of this state occurs in parallel via a dark precursor. The assignment of these features is discussed in more detail in section 7.4.

To further understand the dynamics of the isolated molecule, we model the parallel and perpendicular signals using Eqns. 7.1, 7.5, and 7.6. The results of the fit are shown in Fig. 7.6, comparing the, a), experimentally measured to, b), modeled anisotropy calculated from $R(t) = (\Delta S_{||} - \Delta S_{\perp})/\Delta S_{\mathrm{MA}}$. The artifacts shown on both the experiment and model plots observable as large positive or negative features are due to division-by-zero errors when calculating R(t).

As indicated in Chapters 5 and 6, measured rotational anisotropies typically decay on the few ps timescale for similarly-sized molecules under similar molecular beam conditions. Most of the electronic dynamics of isolated ONP are completed within the first 1 ps after excitation, therefore the fit was largely insensitive to the orientational time constants, Φ_n. The initial anisotropy, r_0 for each MA component is summarized in Table 7.1. The dependence on r_0 indicates that each MA component is recorded from a transition with a different excited-state TDM, as discussed in section 7.2.2. The orientational dynamics show clear evidence for the necessity of including t_n^{shift} in the fit. The line of 0 values across the anisotropy around 250 fs in both the experiment and fit in Fig. 7.6 are a signature of a rapid change in transition dipole moments. This feature is captured by t_3^{shift} on A_3. This unexpected feature will be discussed below in section 7.4. Additional fits were also performed with more orientational components as well as with wavelength-dependent r_0 but the fit was not improved.

7.3.2 Temperature, and carrier gas dependence

To assist with the assignment of the dynamics in the isolated molecule, scans are performed with higher internal energy using an effusive beam source.

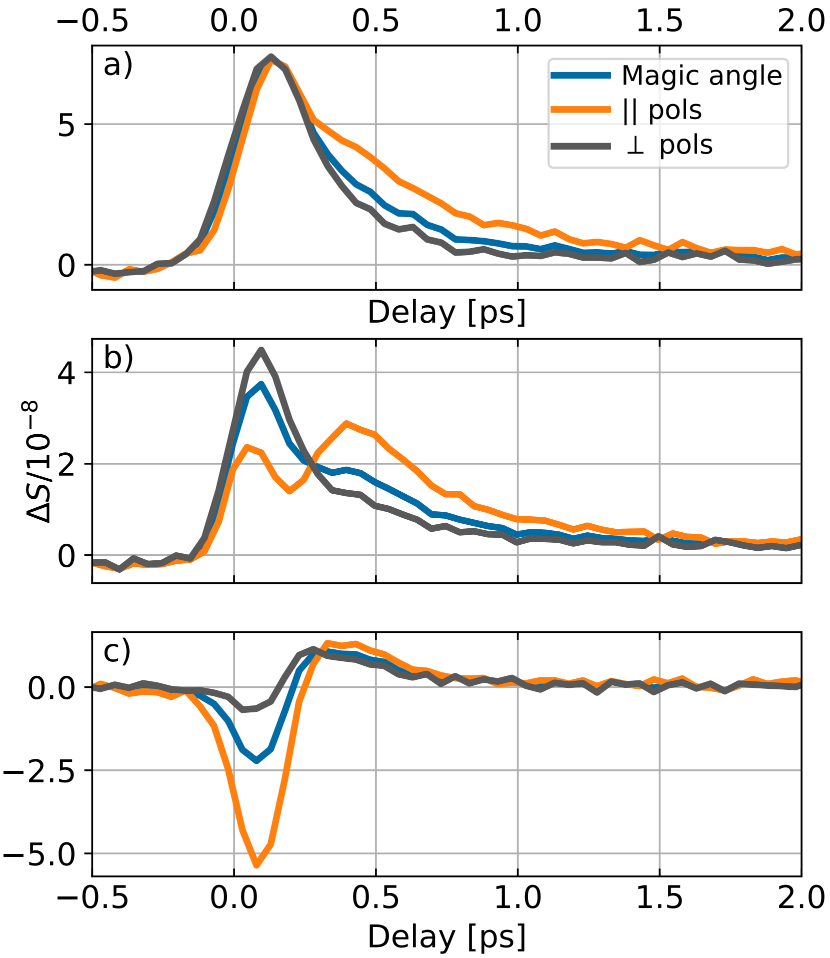

Figure 7.4: TA signals with pump/probe relative polarizations parallel, perpendicular, and at the magic angle. Magic angle data is orientation-averaged whereas the polarized signals reveal transition dipole moment information. Recorded at probe wavelengths of, a), 473 nm, b), 509 nm, c), 696 nm.

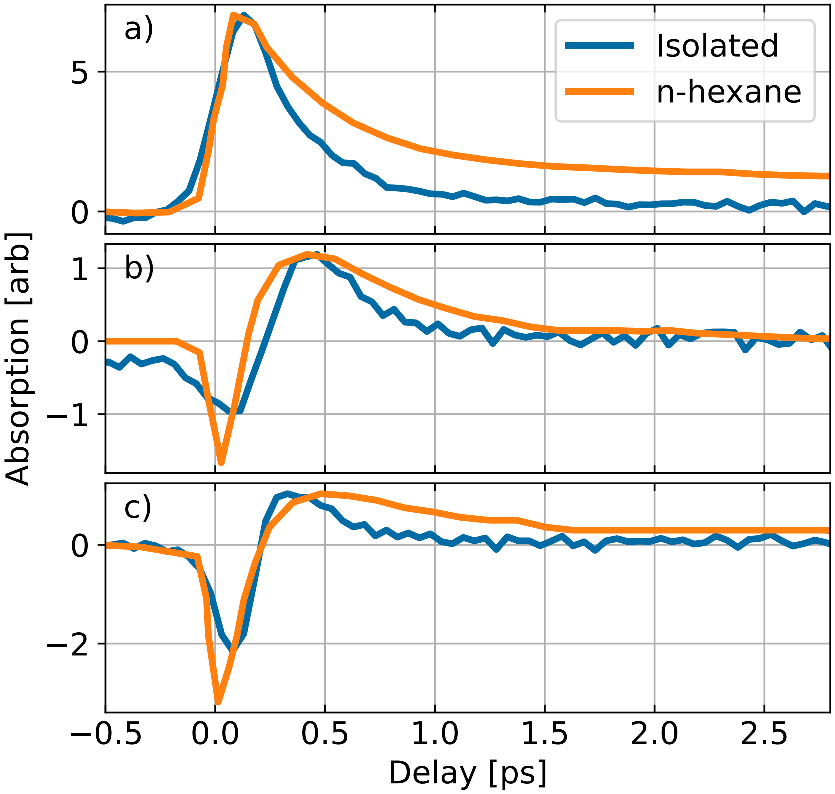

Figure 7.5: Comparison of MA TA signals in the gas-phase isolated molecule vs solution-phase measurements in n-hexane from [10]. Comparisons at probe wavelengths of, a), 473 nm, b), 572 nm and, c), 696 nm. Scans are scaled to make the peak positive signals the same.

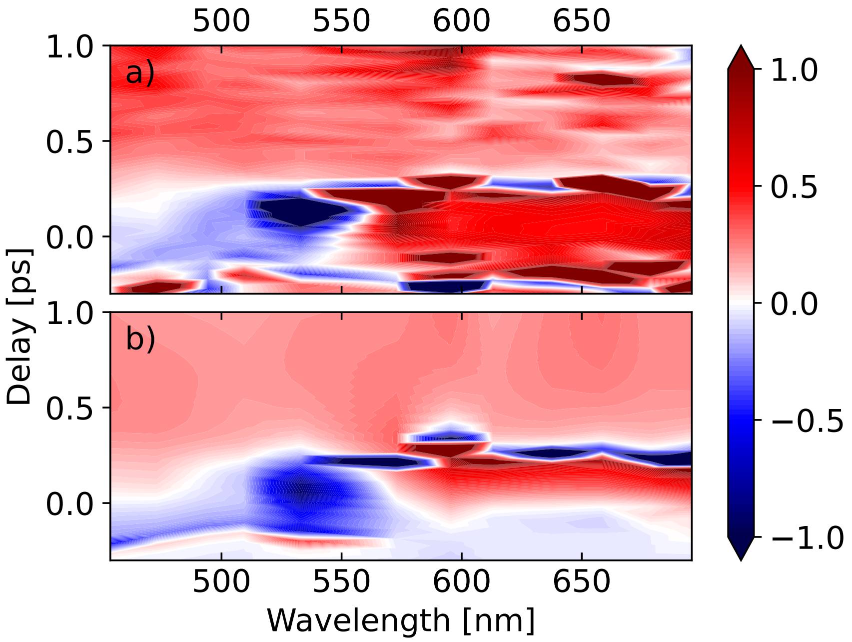

Figure 7.6: ONP rotational anisotropy. a) Experimental signal b) Model anisotropy from global analysis of polarized signals. For more details see text.

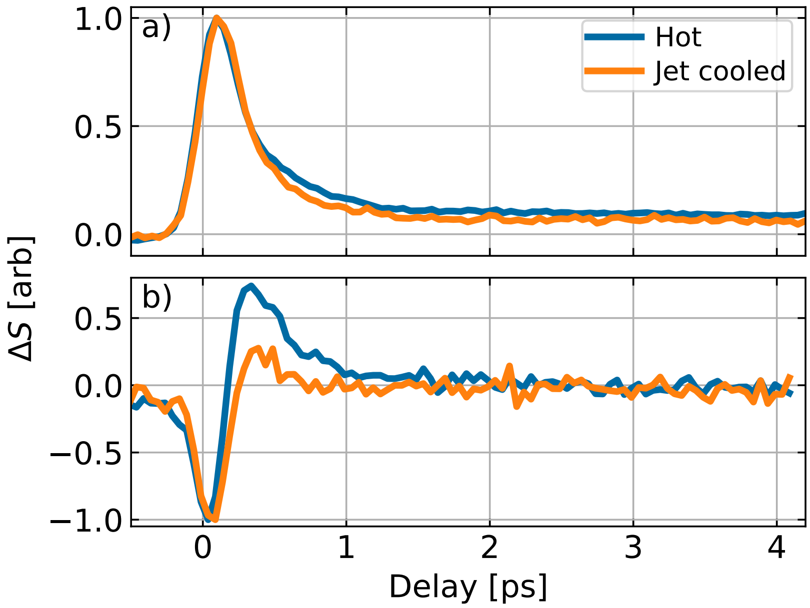

Figure 7.7: Dependence of signal on rotational temperature for hot (≈ 365K) and jet-cooled (≈ 80K). Scans recorded at probe wavelength of, a), 472 nm and, b), 626 nm

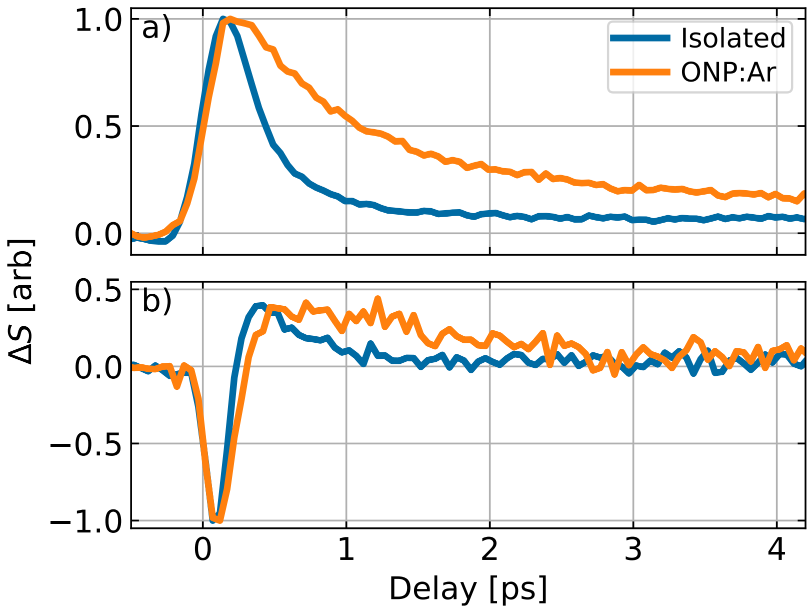

Figure 7.8: Comparison of isolated ONP signal with dynamics in the clustered ONP:Ar system. Isolated signals recorded in 0.3 Bar stagnation pressure of He. ONP:Ar signal recorded with 2.6 Bar Ar stagnation pressure. Scans recorded at probe wavelengths of, a), 455 nm and, b), 581 nm.

The results are shown, compared to the isolated jet cooled signal, in Fig. 7.7 at 2 probe wavelengths of, a), 472 nm and, b), 626 nm. The data shown is normalized to the maximum of the absolute value of the signal. The nozzle for the source is heated to ≈ 365K for the "Hot" sample. Assuming similar cooling to the previous study in Chapter 6, the jet cooled sample has a rotational temperature of ≈ 80K.

Overall, changing the internal energy seems to have a small effect on the dynamics. At 472 nm in Fig. 7.7a), where there is no SE, there is very little effect to the signal. There is a small difference in the intermediate time constant, corresponding to the A_3 DAS feature in Fig. 7.3b), that is observable around 1 ps.

At 626 nm in Fig. 7.7b) where ESA and SE overlap, the effect of temperature is more pronounced. The hot data shows a much larger proportion of ESA compared to the SE which is indicative of an energy-dependent decay channel in the excited state which favors the longer-lived ESA feature at increased temperatures, similar to the effect discussed in Chapter 6. This corresponds to either an increase of DAS component A_3 and/or a decrease in A_1 from the global fit in Fig. 7.3b). Even though the ratio of ESA and SE are changed, the associated time constants are unaffected, consistent with the results at 472 nm.

As discussed in Chapter 6, by using Ar carrier gas instead of He we previously observed Ar cluster formation leading to hindrance of internal conversion channels which require large internal motion. We perform the same comparison measurements here, shown in Fig. 7.8 for probe wavelengths of, a), 455 nm and, b), 581 nm for the dynamics in the clustered ONP:Ar sample vs the isolated, jet cooled molecule. The Ar carrier gas stagnation pressure is 2.6 Bar. In the case of ONP, we cannot use the decay of the rotational anisotropy for further confirmation of cluster formation as discussed in Chapter 6 for salicylideneaniline. This is because, as discussed previously, the dynamics of ONP are completed before the loss of anisotropy is expected to occur.

Similar to the effect of temperature, the major change to ONP:Ar signal is on the intermediate time constant associated with A_3. At both example wavelengths in Fig. 7.8, the prompt signal is unchanged. The predominant effect is observed as an increase in the intermediate ESA time constant, τ_3, which increases substantially, from 400 fs to ≈ 2 ps without any discernible changes to the relative amplitude. The hindrance related to this affect will be discussed in section 7.4.

7.3.3 Calculated transition dipole moments

The SE transitions and expected rotational anisotropy calculated from several geometries from the works of Xu et al. [9, 13] are summarized in Table 7.2. The first column is the ONP geometry of interest, adopting the naming convention from the original work and Fig. 7.2. The second column indicates which isomer of the geometry, either *ortho*- or *aci*- nitrophenol. The third column and fourth columns are the nature and center wavelength of the transition. All transitions are included that fall near or within the probe range of the current experiment and have a nonzero excitation magnitude. The energy window is wider than the actual probe range due to the accuracy of the calculated transitions. For context, the same level of theory overestimates the pump absorption energy by ≈ 1 eV – 280 nm vs 355 nm for theory and experiment, respectively. Relative TDM angles, $\Delta\theta$ are calculated from the dot product of the relevant excited state TDM with the pump TDM and the initial anisotropy is the calculated via Eqn. (7.8 and is listed in the fourth column. These geometries were selected from dynamics trajectories as relevant points along the internal conversion and intersytem crossing pathways. For the limited geometries in Table 7.2, the only SE signals with $r_0 \approx 0.4$ are geometries prior to ESIPT. All *aci*-NP SE signal occur from TDMs perpendicular to the pump transition.

7.3.4 Calculated fragment absorption

As discussed previously, several fragments have been measured or inferred to form after the photolysis of ONP. A summary of the aromatic parent structures remaining after photolysis is shown in Fig. 7.9. The geometries shown are taken from Vereecken et al. [11], and the black text underneath is the naming convention from that work. Additionally, the blue text under several

Geometry	Isomer	Transition	λ_{peak} [nm]	r_0
S_0S_1-CI	*aci-*	$S_0 \leftarrow S_1$	1268	-0.17
S_1-NP	*ortho-*	$S_0 \leftarrow S_1$	509	0.06
S_1-TS	*ortho-*	$S_0 \leftarrow S_1$	327	0.39
S_1-iso1	*aci-*	$S_0 \leftarrow S_1$	678	-0.20
S_1T_2-IC1	*ortho-*	$S_0 \leftarrow S_1$	314	0.40
S_1T_1-IC	*aci-*	$S_0 \leftarrow S_1$	687	-0.19
T_2 iso1	*aci-*	$T_1 \leftarrow T_2$	1336	-0.20

Table 7.2: Calculated transition center wavelengths and initial anisotropy, r_0, for potential stimulated emission signals in geometries relevant to the relaxation of ONP. Column 2 indicates the isomer of nitrophenol, either *ortho-* or *aci-* as shown in Fig. 7.1. Geometries are from [9, 13] using their naming conventions.

of the structures label similar structures found by Guo et al. [14] using their naming conventions.

A summary of the simulated transition center wavelengths found in the structures outlined in Fig. 7.9 is shown in Tables 7.3 and 7.4 for the geometries from Vereecken et al. and Guo et al., respectively. In both tables, the leftmost column indicates the fragment produced during photolysis, followed by the larger parent whose absorption is being investigated as well as the spin multiplicity of the ground state that the calculation was performed in. The rightmost column lists any transition center wavelengths with nonzero oscillator strength near the probe range of the current spectrometer. All the structures investigated have transitions which may be present in the current investigation.

Due to the relatively poor and under-investigated ability of open shell TDDFT to predict transition strengths accurately, the predicted oscillator strengths are not listed [286]. Additionally, since the branching ratios and potential yields of each fragment is unknown, the theoretical absorption cannot be calculated for direct comparison to experiment.

7.4 Discussion

Many nitroaromatic molecules exhibit short-lived stimulated emission, but the origin of the signal is disputed. Several investigations attribute this signal to the singlet lifetime before ISC to the triplet manifold [272, 273, 287, 288] while the rest argue it is a sign of rapid internal conversion in the singlet manifold [10, 289]. ONP is no exception to this trend, as evidenced by the shortest, negative component, A_1, in Fig. 7.3b) and also observed in solution by Ernst et al. [10].

Here, we argue that this feature is a signature of rapid ISC based on the correspondence between the experimental and theoretical rotational anisotropies,

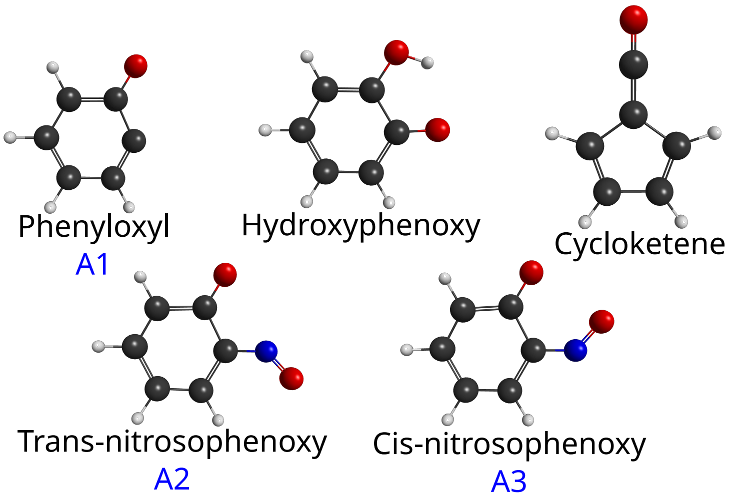

Figure 7.9: Parent fragment structures from Vereecken et al. [11] and using their notation in black text, with absorption summarized in Table 7.3. Additionally, similar structures from Guo et al. are labeled in blue with absorption summarized in Table 7.4.

Fragment	Absorbing parent	Spin state	Transition energy [eV]
HONO	Cycloketene	S	4.641
HONO	Phenyloxyl	T	2.773
			3.596
			3.625
OH	Nitrosophenoxy_cis	D	3.151
			3.201
OH	Nitrosophenoxy_trans	D	3.167
NO	Hydroxyphenoxy	D	2.333
			3.994
			4.323

Table 7.3: Summary of transitions found near the experimental probe range for parent aromatic fragments producing HONO, OH, or NO. Geometries are from [11] and are shown in Fig. 7.9.

Fragment	Absorbing parent	Spin state	Transition energy [eV]
HONO	A1	T	2.745 3.583 3.652 3.918
OH	A2	D	3.108
OH	A3	D	3.101 3.199

Table 7.4: Summary of transitions found near the experimental probe range for parent aromatic fragments producing HONO, OH. Geometries are from [14] and are shown in Fig. 7.9, labeled in blue.

r_0. Our global analysis of the experimental data including orientational effects, shown in Fig. 7.6 and summarized in Table 7.1 show that the A_1 component has $r_0 \approx 0.4$. The theoretical r_0 calculations summarized in Table 7.2, show that r_0 values near 0.4 occur only from geometries prior to ESIPT and become 0.2 post proton transfer. As discussed in the introduction, the S_0/S_1 CI is a post-ESIPT geometry with a 90° twist around the C-N bond [9, 10]. The SE signal from internal conversion via this CI would have to change r_0 values with time, which we do not observe. Additionally, similar features have been observed in solution-phase nitrophenolates, including 4-nitrophenol which lacks the internal hydrogen bond making ESIPT impossible [290]. Therefore, we assign the A_1 component to the singlet lifetime prior to ISC, contrary to the explanation put forth by Ernst et al. [10]. A_2 is most likely ESA from the same state as A_1 as it has a similar time constant and t^{shift}.

The long-lived signal in ONP has been recorded in the gas-phase and in a variety of solvents [10, 258, 290–292]. We observe this feature as well, as the weak ESA feature A_4. This signal has been previously assigned to a long-lived triplet state, which is a potential explanation in the present case. Alternatively, since ONP is known to fragment on ultrafast time scales as discussed in the introduction, this long-lived signal may be due to a photoloysis product. As discussed in section 7.3.3, there are several potential transitions in the parent aromatic fragments, summarized by tables 7.3 and 7.4 that are near our probe range. At the current level of theory, we cannot cleanly determine which fragment or fragments are contributing to our signal. Additionally, there is no reported phosphorescence in ONP which supports the long-lived signal not being a trapped triplet population.

Due to the number of competing relaxation channels in ONP, assignment of the intermediate A_3 component is difficult. The associated time constant of 420 fs indicates that it is most likely a signature of internal conversion, but it is hard to determine if it is occurring in the singlets, triplets, or both. From the global analysis A_3 required a delay of $\approx$ 200 fs to properly model the experimental data and the TDM changed from the previous ESA component.

This means that prior to the A_3 dynamics, an orientational or electronic change occurred, most likely due to ISC to the triplet manifold. We therefore assign A_3 to the relaxation channel proposed by Xu et al. [9] that involves ISC to the triplets followed by ISC back to the ground state without ESIPT. This is shown in as the bottom left pathway in Fig. 7.2. Xu et al., found this pathway to have a time constant of ≈ 300 fs, in agreement with the experiment.

Additionally, the trends observed with changing temperature and clustering effects further confirm the A_1 and A_3 component assignments. The ISC point from S_1 to T_2 (S_1T_2-IC1 in [13])is very near the Franck-Condon point, meaning that minimal rearrangement is required. There are negligible changes to the A_1/A_2 components assigned to this ISC pathway when the temperature or cluster environment is varied in Figs. 7.7 and 7.8, which agrees with this model. The ISC point between T_1 and S_0 (S_0T_1-ICX in [9]) has an out-of-plane rotation of the nitro side chain. Significant internal conversion would be required to reach this ISC point, and the temperature and cluster effects to the A_3 component assigned to this pathway are consistent with this. At higher temperatures, more internal energy allows for a greater population reaching the crossing point, as seen in Fig. 7.7b). Additionally, in Ar clusters where hindrance to internal rotation is expected (as in Chapter 6), a significant slowdown is expected which is observable in Fig. 7.8.

7.5 Conclusions and Future Directions

We use gas-phase TA combined with global analysis and quantum chemistry methods to understand the complex competition between ESIPT, ISC, and fragmentation in *ortho*-nitrophenol. In general, our signals resemble the TA recorded in solution [10] but our interpretation differs. We find good agreement with the dynamics theoretically proposed by Xu et al. [9, 13] and also see potential signs of fragmentation from structures reported both by Guo et al. [14] and Vereecken et al. [11].

To summarize, our results conclude that after excitation to S_1 ONP crosses to the triplet T_2 in the first 90 fs, detectable as short-lived SE. A portion of molecules become trapped in the T_1 state where fragmentation may occur, which is the origin of the long-lived ESA feature. Additionally, a fraction of excited molecules cross back to S_0, and returning to the starting point with a time constant of 420 fs. Temperature- and cluster-dependent scans agree with these assignments.

Several avenues, both experimentally and theoetically, can be explored to further disentangle the complex dynamics in ONP. Calculating a theoretical TAS from dynamics simulations, as was done in Chapter 6, could could help improve spectral assignments. Dynamics simulations at the ab-initio multiple-spawning level including intersystem crossing have recently been implemented [293, 294] but adding these couplings to the current method is difficult and post-processing to calculate spectra has not been done. Additionally, more accurate simulations of the aromatic fragments could provide more accurate determination of the long-lived signal. The orientational dependence observed in the current experiment is unexpected and relatively unique in the TAS community. Improving the global analysis of the rotational-dependent polarized signals could also help understand the complex dynamics in ONP. Using a better kinetic model coupling rotational and electronic time constants to untangle ISC mechanisms could improve assignment of dynamics, but, to our knowledge, this has never been done in literature.

Chapter 8

Conclusion

This dissertation introduced broadband cavity-enhanced transient absorption spectroscopy (CE-TAS) and its application to ultrafast dynamics in the gas phase. This new technique serves as halfway point between conventional solution-phase TAS and gas-phase time-resolved photoelectron spectroscopy (TRPES) as it shares the observable of the former and the sample environment of the latter. Often, TAS and TRPES disagree, and the reasoning is typically assigned to solvent effects. The unique capability of CE-TAS to record TAS in the gas phase enables direct comparisons between different experimental observables and to theoretical calculations. We hope this will lead to a greater understanding of the projections involved when making an excited-state measurement and open a dialogue on the fundamental limitations of different techniques. Also, working in a molecular beam enables new sample avenues unexplored in TAS previously, such as clusters.

Significant technological advancements were required for the development of CE-TAS, as described in this dissertation. The development of tunable frequency comb sources was discussed in Chapters 2 and 3 in the near infrared and visible spectral ranges, respectively, with low phase noise and ultrafast pulse durations at a 100 MHz repetition rate. Additionally, a tunable femtosecond enhancement cavity operating in the visible was described in Chapter 4. This enhancement cavity has a tuning range from 450 to 700 nm (235 THz) with an average finesse of ≈ 600. To our knowledge, this is the first demontration of tunable cavity-enhanced frequency combs. All of these novel developments have broad applications, both in further ultrafast studies to be discussed below and in more conventional linear spectroscopies. The near-infrared frequency comb discussed in Chapter 2 has already been used for several other studies from our group [177, 295], with more on the way.

The CE-TAS instrument was described in detail in Chapter 5. The spectrometer can record pump/probe data with a sensitivity of $\Delta OD < 2 \times 10^{-9}$ for reasonable (≈ 1 sec per delay) averaging times across the entire probe tuning range. Assuming similar conditions to the salicylideneaniline experiment described chapter 6: pump and probe absorption cross-section of $\approx 3 \times 10^{-17}$ cm^2, 150 μm pump beam waist, and 500 mW of pump power, this sensitivity corresponds to a column density of $\approx 1\times10^{11}$ cm^{-2} or, assuming a pump/probe interaction length of 1 mm, a sample density of $\approx 1\times10^{12}$ cm^{-3} [69]. For comparison to condensed-phase measurements, this sample density is equivalent to a concentration of $\approx$ 100 picomolar or 10^{-4} monolayer. At higher pump powers via cavity enhancement the measurable sample density can easily decrease by an order of magnitude, enabling measurements from molecules with lower vapor pressures.

In this dissertation I reported on ultrafast molecular dynamics of several molecules which undergo excited-state intramolecular proton transfer. In Chapter 6, I discussed the photochromism of salicylideneaniline, where we found that, after photoexcitation, the formation of the photochromic transient occurs in parallel to a fluorescent state which relaxes to the ground state in 1.8 ps. In Chapter 7 I analyzed the complex competition between internal conversion, intersystem crossing, and photolysis of *ortho*-nitrophenol. We found prompt intersystem crossing within 100 fs followed by rapid internal conversion in the triplet manifold via a twisted geometry conical intersection and also evidence of fragmentation on longer time scales. In both of these studies, assigning signals to dynamics was assisted by varying the molecule's internal temperature and cluster environment, an experimental "knob" unique to molecular beam studies. We change the internal temperature by using an effusive vs jet-cooled source which isolates dynamics that have a barrier or energy-dependent distribution in the excited state. By using Ar carrier gas in a jet-cooled molecular, we observed large clustering effects which hinder internal conversion in the molecule and allowed us to assign signatures based on the amount of structural changes required for a particular decay pathway. This hindrance effect is a useful tool for the comparison of dynamics in the gas phase vs. solid state, akin to ultrafast spectroscopy in rare-gas matrices, which is typically difficult to accomplish [254–256].

8.1 The observables problem

In the three molecules presented in this dissertation, our CE-TAS results agree more closely with previous transient absorption studies recorded in solution than with gas-phase TRPES. From these results, it seems like the experimental observable – optical absorption vs photoelectron – may be more important than the sample environment – solution vs. gas. This is an interesting and unexpected trend that points to the effects of measurement projections discussed in Chapter 1.

The reasoning behind this disagreement is not clear and requires further study, but there are some small effects inherent to TRPES that are not always addressed experimentally. The first is the effect of "energy windowing" as discussed in Chapter 1, where the probe pulse does not have sufficient energy to ionize the molecule from the entire excited state potential energy surface [19, 20, 23, 40]. A similar effect is also possible in TAS measurements but, due to the resonance requirement, blue- or red-shifting would be observed prior to the decay of signal to indicate the potential energy surface diverging. Additionally, in multiphoton TRPES studies, the existence of intermediate resonances in the neutral molecule can affect the photoionization yield and affect the overall decay of the signal. These resonances can also occur in the continuum, called shape resonances, which can affect the photoion yield and skew interpretations [296].

We hope that further studies, both from our group and others, will provide additional insight into this complex problem. There has been progress in TRPES measurements from solution-phase samples via the liquid microjet approach [297, 298] which is in a similar situation to CE-TAS as being a halfway point between conventional TAS and TRPES. Additionally, in both TAS and TRPES, some of the drawbacks discussed above may be captured and accounted for by modeling the observable directly in theoretical simulations, where progress has been made [24, 25, 299].

8.2 Outlook

As discussed, the initial measurements from CE-TAS are interesting both for the molecular dynamics being studied and from a more fundamental experimental observables perspective. To further explore these trends, measurements on more samples are required. Currently, the instrument is moving to a 266 nm pump beam via fourth harmonic generation rather than the 355 nm third harmonic pump results discussed here. There are several motivations for this change. First, more molecules absorb farther in the UV which expands the possible pool of samples to study. Additionally, 266 nm conveniently overlaps with the third harmonic of a conventional Ti:Saph laser, which enables more comparisons to other ultrafast studies. Specifically, most of the DNA nucleobases absorb in this region and are some of the most studied systems in ultrafast spectroscopy due to their involvement in DNA photoprotection [300, 301]. There are well-established differences between experiments using TAS [300] or 2D spectroscopy [302] vs TRPES [19, 301, 303] making these molecules ideal for investigation with CE-TAS.

Beyond CE-TAS, the technique and instrument development presented here is relevant for future cavity-enhanced ultrafast spectroscopy studies in different spectral regions. As discussed in Chapter 2, a major motivation for the laser development described in this dissertation is to do two-dimensional infrared spectroscopy (2DIR) on hydrogen-bonded systems. Both the initial CE-TAS demonstration and the current broadband spectrometer have sufficient sensitivity to perform nonlinear spectroscopy in molecular beams [1, 30]. Since transient absorption and 2DIR spectroscopies are both third-order nonlinear mixing signals [51, 304], similar sensitivity is expected in the two-dimensional case. The nonlinear signal readout is more complicated in 2DIR, but schemes for accomplishing this using f_0-shifted frequency combs and higher-order cavity modes have already been published by our group [71]. Additionally, the same 2DIR schemes have broad applications in trace gas detection and parsing complex mixtures in breath analysis, explosives and narcotics detection, and other demanding applications [305–308].

Appendix A

Pre-time zero signal and global analysis

As discussed in detail previously [1], the pump-probe signal measured in the cavity-enhanced spectrometer includes a subtracted "reference" signal which is recorded from a copy of the probe comb coupled into the probe cavity backwards and delayed by $\approx 5ns$. The reference signal is subtracted from the probe signal in an autobalanced detector, resulting in a recorded molecular signal, $\Delta S(\lambda, t)$ of the form

$$\Delta S(\lambda, t) = \beta(\lambda)[\Delta I(\lambda, t) - \Delta I(\lambda, t + 5\text{ ns})] \tag{A.1}$$

Where $\beta = \frac{\pi}{\mathcal{F}(\lambda)}\frac{1}{I_{probe}}$ is the inverse of the cavity enhancement factor divided by the static probe intensity (which matches the reference due to autobalancing). ΔI is the pump-induced change in absorption and τ is the pump/probe delay. The reference subtraction reduces common-mode noise which increases absorption sensitivity and also removes quasi-static signal offset due to long-lived molecular dynamics, or multi-excitation effects caused by the necessarily high repetition rate of the experiment (100 MHz). Cavity finesse, $\mathcal{F}$, is measured at every probe wavelength immediately following pump/probe scans to use in signal calculations.

Fig. A.1 shows how ΔI is recorded in CE-TAS for an example system featuring biexponential decay. The multicolored scans separated by 10 ns ($1/\text{f}_{\text{rep}}$) represent individual molecular responses from each subsequent pump excitation and the black line is the sum of these which would be recorded by the actual spectrometer. To construct $\Delta S(t)$ from $\Delta I(t)$, the reference signal, $\Delta I(t+5ns)$ is subtracted as shown for 2 example points by the vertical dashed lines in Fig. A.1. As seen in the figure, the point at -0.5 ns captures an inverted molecular signal from the previous excitations, resulting in a nonzero offset at negative delays. The resulting $\Delta S(t)$ is shown in Fig. A.2 as well as the original $\Delta I(t)$. It is clear that the short time dynamics are identical on both and only the long-lived signal displaces $\Delta S(t)$ vertically.

The TA spectra, both experimental and simulated, are fit to a sum of expo-

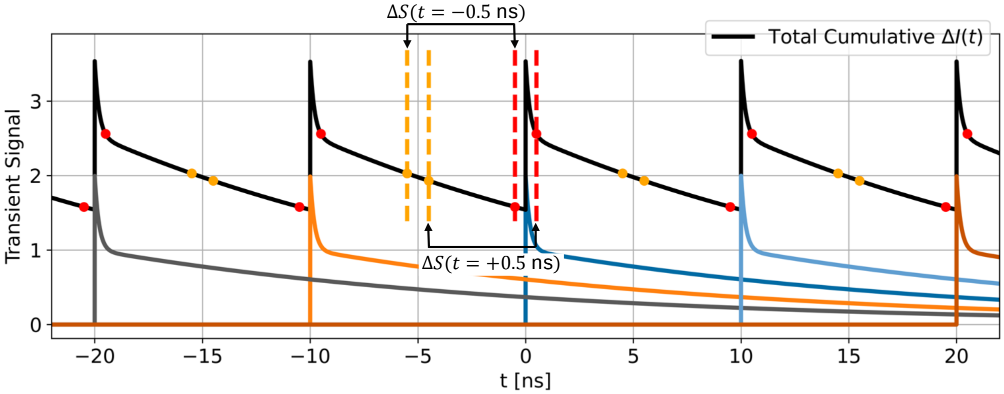

Figure A.1: Illustration of origin of negative delay signal. The sample is pumped at $f_{\mathrm{rep}} = 100$ MHz. Each excitation pulse launches a bi-exponential decay molecular response (colored lines) with $\tau_1 = 0.2$ ns and $\tau_2 = 20$ ns $= 2/f_{\mathrm{rep}}$. The CE-TAS signal $\Delta S(\tau)$ is constructed from the difference between the total cumulative steady state change in absorbance signal ΔI sampled at the probe pulses (red dots) and the reference pulses (orange dots) via equation (A.1). For molecules with signals with lifetimes on the order of $1/f_{\mathrm{rep}}$ or longer, this can lead to nonzero signals before time zero, as illustrated in Fig. A.2.

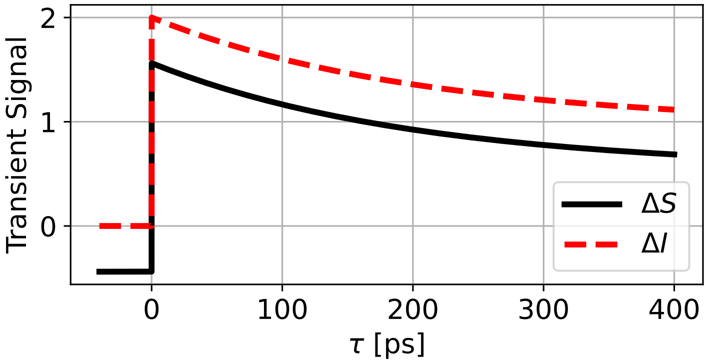

Figure A.2: CE-TAS signal ΔS corresponding the scenario of Fig. A.1. A sizable negative signal is seen before time zero.

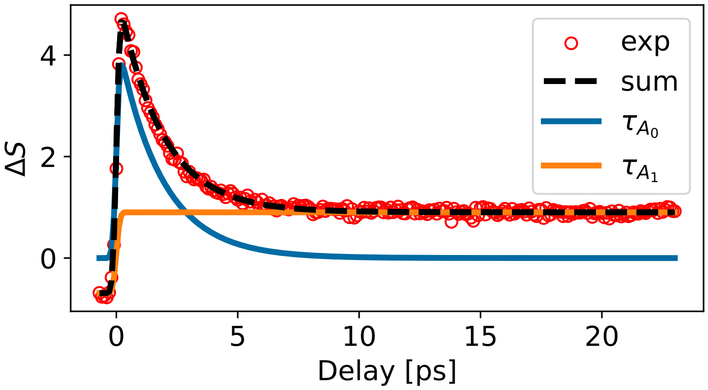

Figure A.3: Single scan fit at 455 nm with isolated time constant contributions using equation A.4.

nential decays convolved with the wavelength-dependent instrument response.

$$G(\lambda,t)=\mathrm{IRF}(\lambda,t)\otimes\sum_{\mathrm{n}}\mathrm{X_n}(\lambda)\exp(-t/\tau_{\mathrm{n}}) \tag{A.2}$$

Where $A_n(\lambda)$ is the decay associated spectra for each time constant τ_{n}. To model the full experimental $\Delta S(t)$, including the pre-time 0 "artifact" discussed above, we directly simulate the reference subtraction and sum over the next 20 probe-reference pulses by shifting the time axis of the fit by the time spacing between pulses ($1/\mathrm{f_{rep}}$):

$$\Delta S_{\mathrm{model}}(\lambda,t)=\sum_{m=0}^{N}G(\lambda,t+m/f_{\mathrm{rep}})-G(\lambda,t+m/f_{\mathrm{rep}}+5\ \mathrm{ns}) \tag{A.3}$$

N = 20 pulses was chosen as the upper limit of the sum based on the average transit time of the molecular beam across the diameter of the probe beam. The difference between the fit and experimental/simulated data is minimized using a Levenberg–Marquardt fit algorithm. For all experimental spectra, the instrument response is derived from a fit of the signal rising edge to an error function at each probe wavelength. This approximation was used since previous measurements of SA concluded that the proton transfer occurred below our instrument time resolution [7,] so a step-like molecular signal could be assumed. The fitting routine was run multiple (¿50) times starting from different points in parameter space and the global minimum was used as the final optimum fit.

By combining equations A.2 and A.3 and reversing the order of summations, the fit model can also be written as:

$$\Delta S_{\mathrm{model}}(\lambda,t)=\mathrm{IRF}(\lambda,t)\times\sum_{\mathrm{n}}\mathrm{X_n}(\lambda)\times\sum_{m=0}^{20}\left[\exp(-(t+m/\mathrm{f_{rep}})/\tau_{\mathrm{n}})-\exp(-(t+m/\mathrm{f_{rep}}+5\mathrm{ns})/\tau_{\mathrm{n}})\right] \tag{A.4}$$

where the different time components can be isolated. An example of this procedure is shown in Fig. A.3 for a single scan of isolated SA. The long-lived signal captures all of the pre-time 0 signal and the short time component is unaffected by the multi-pulse fitting.

Appendix B

Additional fits and computational methods for salicylideneaniline

B.1 Goodness of fit

To verify the applicability of the fit models used in the main text, fits using the same approach outlined above for different number of fit components are shown here.

B.2 Computational Methods

B.2.1 Post-processing of Non-adiabatic Molecular Dynamics Trajectories

The gas-phase TAS of SA was simulated by post-processing the trajectories of 2 ps excited-state non-adiabatic molecular dynamics (NAMD) simulations. The trajectories of *Ab-initio* Multiple Spawning (AIMS) [228,229,309] NAMD simulations were thankfully provided by Pijeau *et al.* and the details of the simulation are described in reference [196]. The AIMS data consisted of more than 2000 trajectory basis functions distributed between the S_1 and S_0 electronic states and contained a total of 854,760 geometric conformations with 715,618 conformations belonging to the S_1 electronic state. Both the S_1 and S_0 geometries were time-resolved by using 1000 a.u ($\sim$24.2 fs) time intervals for a total of 84 sampling windows. Within each window, 80 distinct conformations were selected by using the k-means clustering algorithm weighted by the electronic population of the trajectory basis functions representing the conformation. The weighted k-means clustering used the pairwise RMSD distance matrices which were calculated by using the MDTraj [310] library. Within each sampling window, the cluster centroid was translated and rotated by using the Kabsch algorithm [311] to minimize the RMSD between the centroid and op-

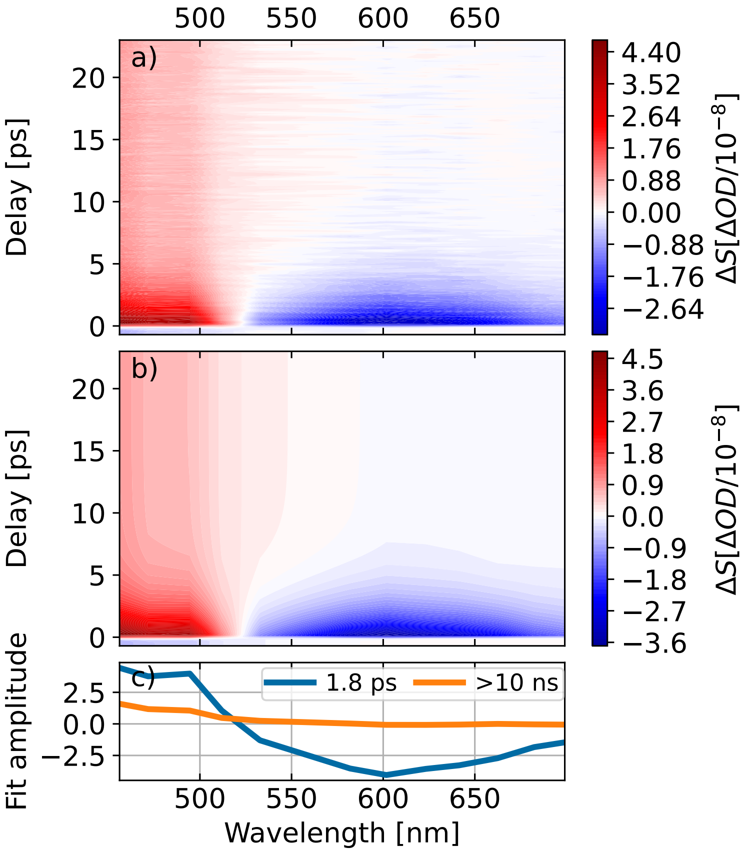

Figure B.1: 2 component parallel fit model on isolated SA. a) Experimental spectrum. b) Spectrum returned from fit. c) DAS from b).

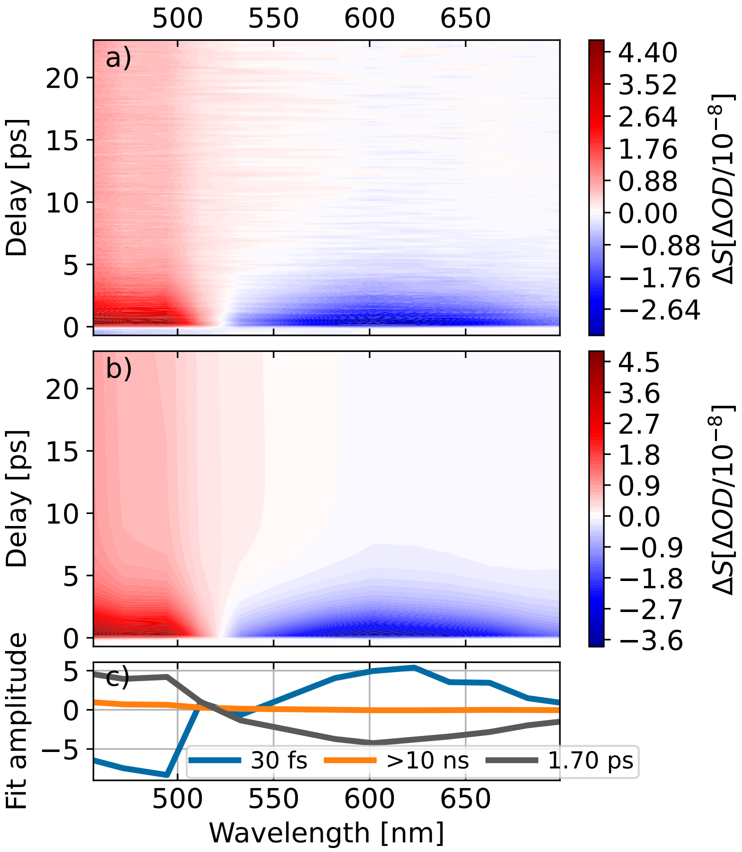

Figure B.2: 3 component parallel fit model on isolated SA. a) Experimental spectrum. b) Spectrum returned from fit. c) DAS from b).

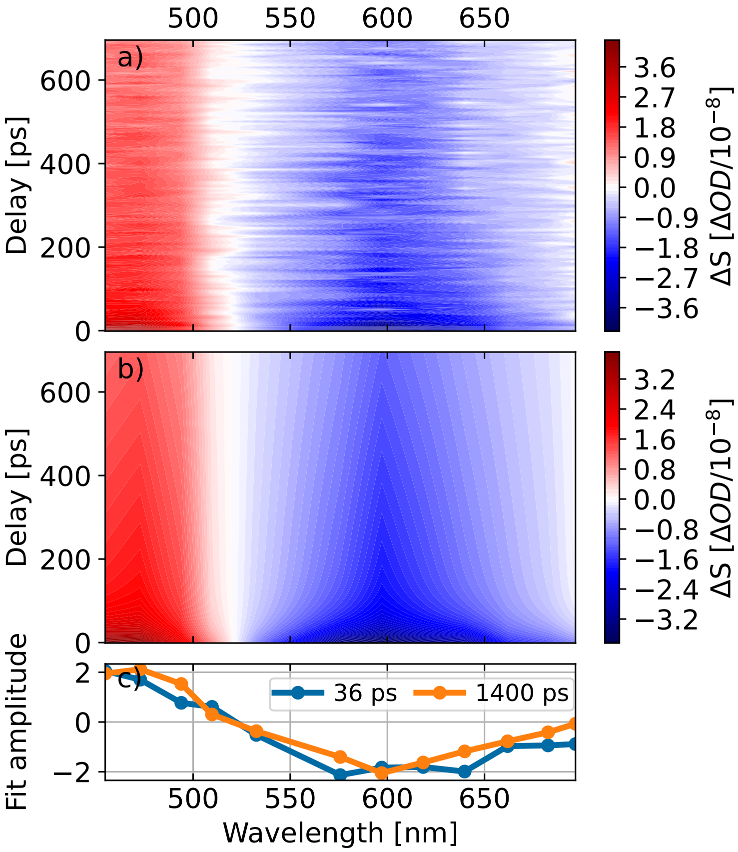

Figure B.3: 2 component parallel fit model on SA:Ar. a) Experimental spectrum. b) Spectrum returned from fit. c) DAS from b).

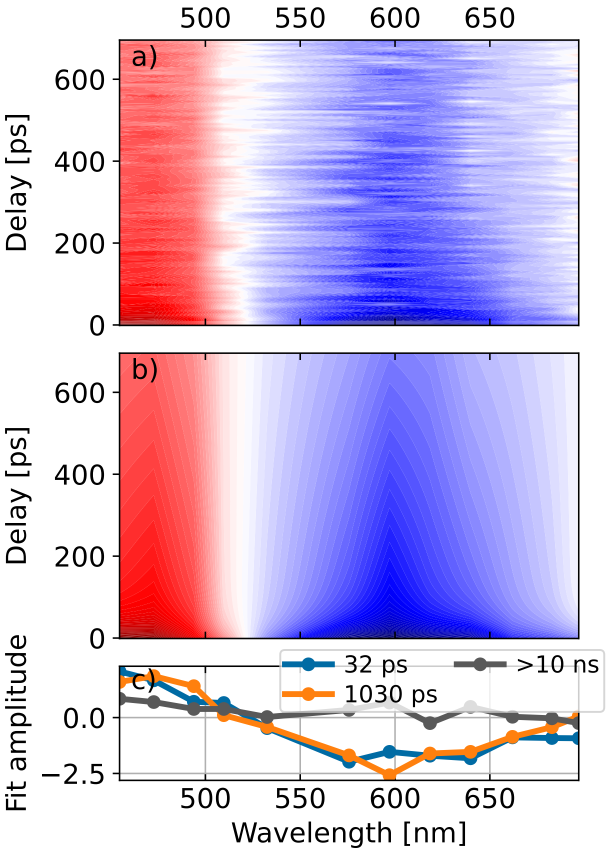

Figure B.4: 3 component parallel fit model on SA:Ar. a) Experimental spectrum. b) Spectrum returned from fit. c) DAS from b).

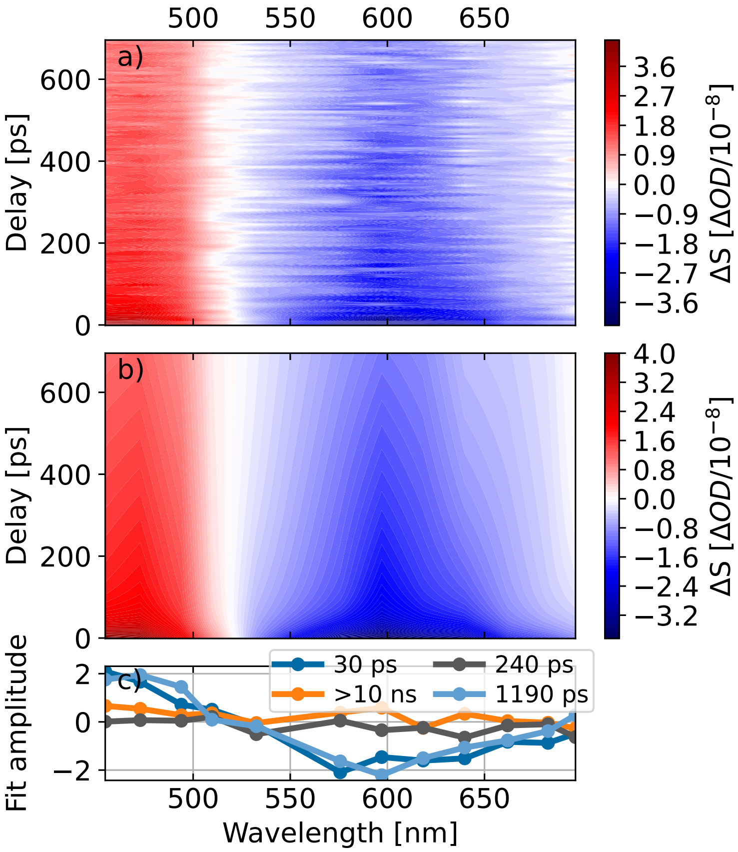

Figure B.5: 4 component parallel fit model on SA:Ar. a) Experimental spectrum. b) Spectrum returned from fit. c) DAS from b).

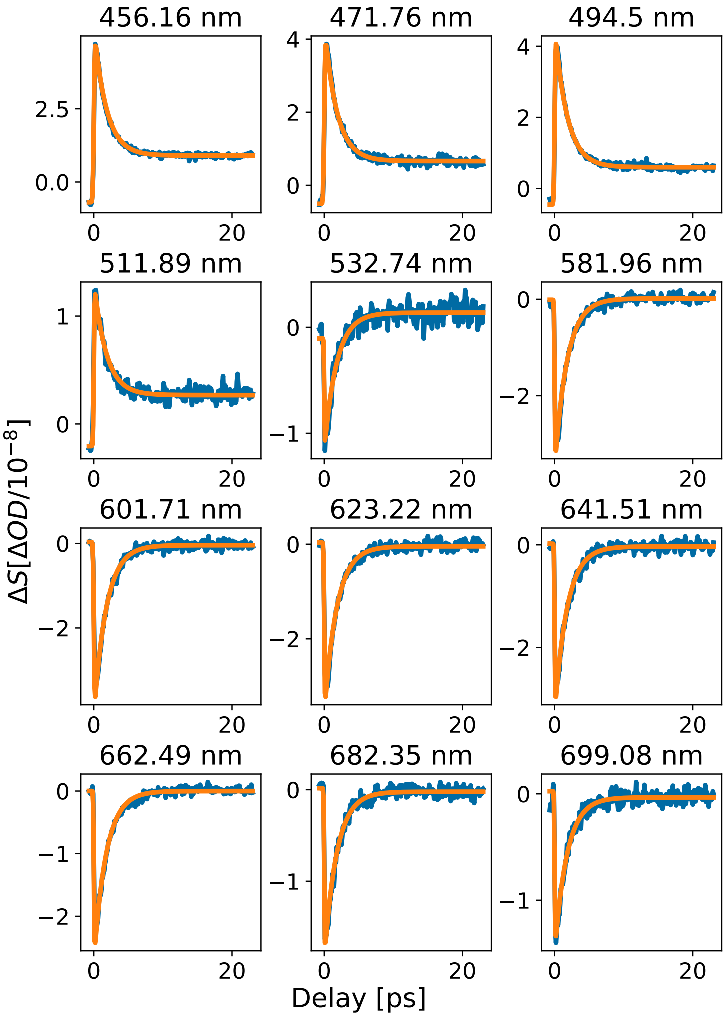

Figure B.6: Isolated SA spectral lineouts including corresponding 2 component fit traces.

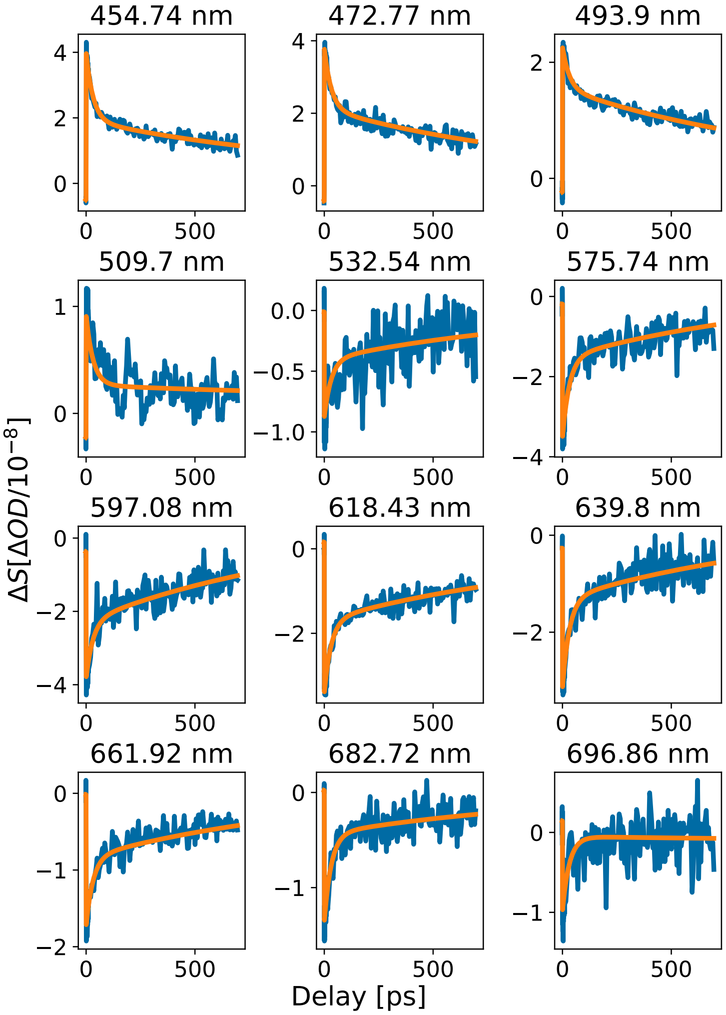

Figure B.7: SA:Ar spectral lineouts including corresponding 3 component fit traces.

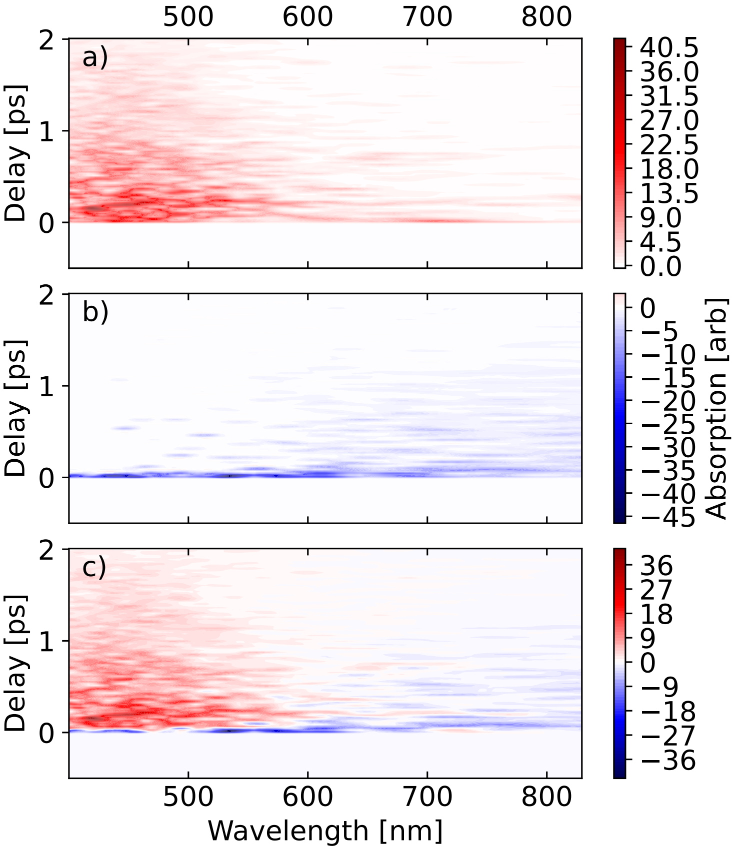

Figure B.8: Raw, unconvolved simulated spectrum. a) ESA b) SE c) total signal.

timized S_0 enol geometry oriented along the z-axis of its transition dipole. A total of 6720 representative time-resolved conformations on S_1 were selected for the TAS simulations. Because simulations were stopped upon quenching of the majority of the population to S_0, we did not include S_0 population in the TAS calculation.

B.2.2 Simulation of TAS

The simulation of TAS uses our GPU accelerated implementation of the Time-Dependent Complete Active Space Configuration Interaction (TD-CASCI) [227] method, implemented in the TeraChem suite of programs [247]. The details of the method can be found in Ref. [227]. Briefly, in TD-CASCI the time-dependent electronic wave function $\Psi(t)$, is expressed as a linear combination of Slater determinants, $\{\Phi_K\}$,

$$\Psi(t) = \sum_K C_K(t)\Phi_K \tag{B.1}$$

where $C_K(t)$ are the time-dependent CI expansion coefficients. The time-dependent wave function is propagated by numerically solving the time-dependent

Schrodinger equation,

$$i\frac{\partial \mathbf{C}(t)}{\partial t} = \mathbf{H}(t)\mathbf{C}(t) \tag{B.2}$$

Our GPU-accelerated implementation calculates the **HC** products *on-the-fly*, avoiding the computationally expensive procedures of building, storing, and/or diagonalizing the CI Hamiltonian. Propagation is carried out via a second-order symplectic split operator integrator.

To include the explicit field effects, the Hamiltonian at any time t is expressed in the electric dipole approximation,

$$\hat{H}(t) = \hat{H}_0 - \hat{\boldsymbol{\mu}} \cdot \mathbf{d}E(t) \tag{B.3}$$

where $\hat{H}_0$ is the field-free molecular Hamiltonian, and $\hat{\boldsymbol{\mu}}$ is the molecular dipole operator. The scalar function, $E(t)$, is the time-dependent external field strength, and d is the unit vector in the field polarization direction. The obtained time correlation function can be used to get the energy spectrum of the electronic wave function after excitation with a pulse,

$$R(t) = \mathbf{C}(\varepsilon)^{\dagger}\mathbf{C}(\varepsilon + t) \tag{B.4}$$

where ε corresponds to the time at the end of the pulse. The absorption spectrum of any electronic state can be obtained by the Fourier transform of the $R(t)$ after excitation with a δ-function pulse. To reduce the effects of the spectral leakage, the Hanning Windowing function was applied to raw $R(t)$ prior to the Fast Fourier transform of the obtained time correlation function of Eq. 4.

The spectrum is shifted such that the zero of energy is at the initial (S_1) state energy. Signal with positive energy corresponds to excite state absorption (ESA), while signal with negative energy corresponds to stimulated emission (SE). The signal corresponding to the negative energy axis after shifting represents the SE. The total spectrum, including both ESA and SE and defined only for $E \geq 0$, is computed according to:

$$R_{ESA-SE}(E) = R(E) - R(-E) \tag{B.5}$$

Prior to the above summation, shifts are applied to the TD-CASCI spectra to provide more accurate energetics. The ESA signal in the simulated TAS was blue-shifted by 0.944 eV which represents the difference in the $S_3 \leftarrow S_1$ vertical excitation energy of the S_0 enol ground state minimum at SA-4-FOMO(0.25)-CAS(8,8)CI and the more accurate SA-4-CAS(8,8)PT2 levels. The $S_3 \leftarrow S_1$ transition was used as a reference due to significantly higher values of the oscillator strength compared to the $S_2 \leftarrow S_1$ transition at the SA-4-CAS(8,8)PT2 level. The SE signal was red-shifted by 1.595 eV, setting the S_0/S_1 vertical excitation energy of the S_0 enol conformation computed at SA-4-FOMO(0.25)-CAS(8,8)CI level to the position of experimental absorption maximum [224]. The overlap of the SE and ESA and, therefore, the overall spectral shape and zero crossing is very dependent on the relative shifts applied to each signal but the overall time dynamics are independent of shifting as can be seen in Fig. B.8.

In order to construct the experimentally isotropic observable from a static aligned molecule, first the magnitude of the signal is constructed $R_{total}(E) = R_x(E) + R_y(E) + R_z(E)$. The parallel, perpendicular, and magic angle signals can then be calculated from the angular dependent nonlinear absorption equation from ref [276] simplified to each case:

$$R_{\parallel}(E) = \frac{1}{15}(R_x(E) + R_y(E) + 3R_z(E)) \tag{B.6}$$

$$R_{\perp}(E) = \frac{1}{15}(2R_x(E) + 2R_y(E) + R_z(E)) \tag{B.7}$$

$$R_{\mathrm{MA}}(E) = R_{total}(E)/9 \tag{B.8}$$

The ESA and SE are shown in Fig. B.8a) and b). The total, unconvolved TAS signal is shown in Fig. B.8c). The spectrum was constructed by using the electronic spectrum of the time-resolved geometries of SA at FOMO(0.25)-TD-CAS(8,8)CI/6-31g** [231] level using a δ-kick with a field strength of 10^{24} W/m^2 polarized separately along the x, y and z directions of the molecular axis for a duration of 0.062 a.u (0.0015 fs). The electronic dynamics were propagated for 15000 time steps with a step size of Δt = 0.124 a.u. (0.003 fs) which represents the $\sim$1860 a.u (45 fs) electronic dynamics.

B.2.3 Twisted Enol spectrum

The simulated TAS spectrum of twisted enol geometries is shown in Fig. B.9. As discussed in the main text, this spectrum only includes contribution from enol geometries with a CN twist angle $< 140°$, indicative of internal conversion from planar geometries (180°) towards CI2 ($\approx 90°$). Note that the maximum amplitude shown on Fig. B.9 is approximately one order of magnitude smaller than that shown on the full spectrum (main text Fig. 7a))

B.2.4 Photochrome absorption simulation

The simulated ground-state absorption of the two potential photochrome candidates – the trans-keto and rotated enol – are shown in Fig. B.10. Optimized geometries for both conformers are from [12]. Spectra were generated using TD-CASCI method with the same level of theory and energy shifts as the SE discussed above.

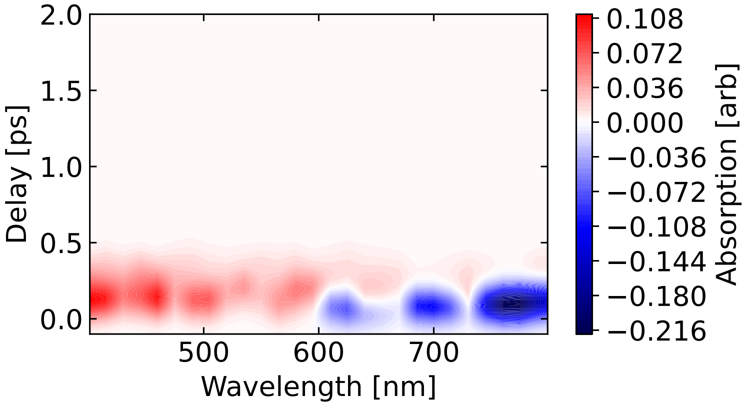

Figure B.9: Theoretical TAS from enol geometries with central CN twist angles of < 140°, indicative of the CN twist relaxation mechanism via CI2. Note that the maximum amplitude shown here is more than an order of magnitude smaller than the main spectral features on the full spectrum in the main text.

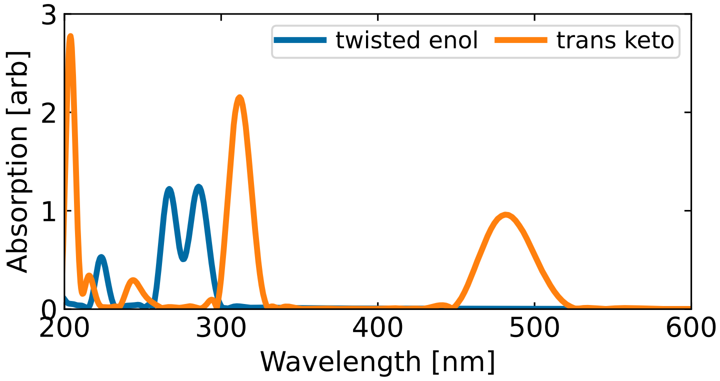

Figure B.10: Ground-state absorption from twisted enol and keto photochrome candidates using optimized geometries from [12].

Bibliography

[1] Myles C. Silfies, Grzegorz Kowzan, Neomi Lewis, and Thomas K. Allison. Broadband cavity-enhanced ultrafast spectroscopy. *Physical Chemistry Chemical Physics*, 23(16):9743–9752, April 2021.

[2] Myles C. Silfies, Grzegorz Kowzan, Yuning Chen, Neomi Lewis, Ryan Hou, Robin Baehre, Tobias Gross, and Thomas K. Allison. Widely tunable cavity-enhanced frequency combs. *Optics Letters*, 45(7):2123–2126, April 2020.

[3] Yuning Chen, Myles C. Silfies, Grzegorz Kowzan, Jose Miguel Bautista, and Thomas K. Allison. Tunable visible frequency combs from a Yb-fiber-laser-pumped optical parametric oscillator. *Applied Physics B*, 125(5):81, April 2019.

[4] Matthew Reichert, Honghua Hu, Manuel R. Ferdinandus, Marcus Seidel, Peng Zhao, Trenton R. Ensley, Davorin Peceli, Jennifer M. Reed, Dmitry A. Fishman, Scott Webster, David J. Hagan, and Eric W. Van Stryland. Temporal, spectral, and polarization dependence of the nonlinear optical response of carbon disulfide. *Optica*, 1(6):436–445, December 2014.

[5] Matthew Reichert, Honghua Hu, Manuel R. Ferdinandus, Marcus Seidel, Peng Zhao, Trenton R. Ensley, Davorin Peceli, Jennifer M. Reed, Dmitry A. Fishman, Scott Webster, David J. Hagan, and Eric W. Van Stryland. Temporal, spectral, and polarization dependence of the nonlinear optical response of carbon disulfide: Erratum. *Optica*, 3(6):657–658, June 2016.

[6] S. Lochbrunner, A. Szeghalmi, K. Stock, and M. Schmitt. Ultrafast proton transfer of 1-hydroxy-2-acetonaphthone: Reaction path from resonance Raman and transient absorption studies. *The Journal of Chemical Physics*, 122(24):244315, June 2005.

[7] Taro Sekikawa, Oliver Schalk, Guorong Wu, Andrey E. Boguslavskiy, and Albert Stolow. Initial Processes of Proton Transfer in Salicylideneaniline Studied by Time-Resolved Photoelectron Spectroscopy. *The Journal of Physical Chemistry A*, 117(14):2971–2979, April 2013.

[8] Marcin Ziółek, Jacek Kubicki, Andrzej Maciejewski, Ryszard Naskrecki, and Anna Grabowska. An ultrafast excited state intramolecular proton transfer (ESPIT) and photochromism of salicylideneaniline (SA) and its "double" analogue salicylaldehyde azine (SAA). A controversial case. *Physical Chemistry Chemical Physics*, 6(19):4682–4689, September 2004.

[9] Chao Xu, Le Yu, Chaoyuan Zhu, Jianguo Yu, and Zexing Cao. Intersystem crossing-branched excited-state intramolecular proton transfer for o-nitrophenol: An ab initio on-the-fly nonadiabatic molecular dynamic simulation. *Scientific Reports*, 6(1):26768, May 2016.

[10] Hanna A. Ernst, Thomas J. A. Wolf, Oliver Schalk, Núria González-García, Andrey E. Boguslavskiy, Albert Stolow, Matthias Olzmann, and Andreas-Neil Unterreiner. Ultrafast Dynamics of o-Nitrophenol: An Experimental and Theoretical Study. *The Journal of Physical Chemistry A*, 119(35):9225–9235, September 2015.

[11] L. Vereecken, H. K. Chakravarty, B. Bohn, and J. Lelieveld. Theoretical Study on the Formation of H- and O-Atoms, HONO, OH, NO, and NO2 from the Lowest Lying Singlet and Triplet States in Ortho-Nitrophenol Photolysis. *International Journal of Chemical Kinetics*, 48(12):785–795, 2016.

[12] Juan Manuel Ortiz-Sánchez, Ricard Gelabert, Miquel Moreno, and José M. Lluch. Electronic-structure and quantum dynamical study of the photochromism of the aromatic Schiff base salicylideneaniline. *The Journal of Chemical Physics*, 129(21):214308, December 2008.

[13] Chao Xu, Le Yu, Chaoyuan Zhu, and Jianguo Yu. Photoisomerization Reaction Mechanisms of o-Nitrophenol Revealed by Analyzing Intersystem Crossing Network at the MRCI Level. *The Journal of Physical Chemistry A*, 119(42):10441–10450, October 2015.

[14] Shaoxun Guo and Hui Li. Photolysis of nitrophenols in gas phase and aqueous environment: A potential daytime source for atmospheric nitrous acid (HONO). *Environmental Science: Atmospheres*, 3(1):143–155, January 2023.

[15] Margherita Maiuri, Marco Garavelli, and Giulio Cerullo. Ultrafast Spectroscopy: State of the Art and Open Challenges. *Journal of the American Chemical Society*, 142(1):3–15, January 2020.

[16] Albert Stolow, Arthur E. Bragg, and Daniel M. Neumark. Femtosecond time-resolved photoelectron spectroscopy. *Chemical Reviews*, 104(4):1719–1758, 2004.

[17] Guorong Wu, Paul Hockett, and Albert Stolow. Time-resolved photoelectron spectroscopy: From wavepackets to observables. *Physical Chemistry Chemical Physics*, 13(41):18447–18467, October 2011.

[18] Attila Szabo and Neil S. Ostlund. *Modern Quantum Chemistry: Introduction to Advanced Electronic Structure Theory.* Courier Corporation, July 1996.

[19] Hanneli R. Hudock, Benjamin G. Levine, Alexis L. Thompson, Helmut Satzger, D. Townsend, N. Gador, S. Ullrich, Albert Stolow, and Todd J. Martínez. Ab Initio Molecular Dynamics and Time-Resolved Photoelectron Spectroscopy of Electronically Excited Uracil and Thymine. *The Journal of Physical Chemistry A*, 111(34):8500–8508, August 2007.

[20] H. Tao, T. K. Allison, T. W. Wright, A. M. Stooke, C. Khurmi, J. van Tilborg, Y. Liu, R. W. Falcone, A. Belkacem, and T. J. Martinez. Ultrafast internal conversion in ethylene. I. The excited state lifetime. *The Journal of Chemical Physics*, 134(24):244306, June 2011.

[21] T. K. Allison, H. Tao, W. J. Glover, T. W. Wright, A. M. Stooke, C. Khurmi, J. van Tilborg, Y. Liu, R. W. Falcone, T. J. Martínez, and A. Belkacem. Ultrafast internal conversion in ethylene. II. Mechanisms and pathways for quenching and hydrogen elimination. *The Journal of Chemical Physics*, 136(12):124317, March 2012.

[22] M. S. Schuurman and A. Stolow. Dynamics at conical intersections. *Annual Review of Physical Chemistry*, 69:427–450, 2018.

[23] Yusong Liu, Spencer L. Horton, Jie Yang, J. Pedro F. Nunes, Xiaozhe Shen, Thomas J. A. Wolf, Ruaridh Forbes, Chuan Cheng, Bryan Moore, Martin Centurion, Kareem Hegazy, Renkai Li, Ming-Fu Lin, Albert Stolow, Paul Hockett, Tamás Rozgonyi, Philipp Marquetand, Xijie Wang, and Thomas Weinacht. Spectroscopic and structural probing of excited-state molecular dynamics with time-resolved photoelectron spectroscopy and ultrafast electron diffraction. *Physical Review X*, 10:021016, April 2020.

[24] Rocío Borrego-Varillas, Artur Nenov, Piotr Kabaciński, Irene Conti, Lucia Ganzer, Aurelio Oriana, Vishal Kumar Jaiswal, Ines Delfino, Oliver Weingart, Cristian Manzoni, Ivan Rivalta, Marco Garavelli, and Giulio Cerullo. Tracking excited state decay mechanisms of pyrimidine nucleosides in real time. *Nature Communications*, 12(1):7285, December 2021.

[25] Matthias Ruckenbauer, Sebastian Mai, Philipp Marquetand, and Leticia González. Revealing Deactivation Pathways Hidden in Time-Resolved Photoelectron Spectra. *Scientific Reports*, 6(1):35522, October 2016.

[26] J. V. Ortiz. Dyson-orbital concepts for description of electrons in molecules. *The Journal of Chemical Physics*, 153(7):070902, August 2020.

[27] C. Melania Oana and Anna I. Krylov. Dyson orbitals for ionization from the ground and electronically excited states within equation-of-motion coupled-cluster formalism: Theory, implementation, and examples. *The Journal of Chemical Physics*, 127(23):234106, December 2007.

[28] Irene Conti, Giulio Cerullo, Artur Nenov, and Marco Garavelli. Ultrafast Spectroscopy of Photoactive Molecular Systems from First Principles: Where We Stand Today and Where We Are Going. *Journal of the American Chemical Society*, 142(38):16117–16139, September 2020.

[29] Albert DeFusco, Noriyuki Minezawa, Lyudmila V. Slipchenko, Federico Zahariev, and Mark S. Gordon. Modeling Solvent Effects on Electronic Excited States. *The Journal of Physical Chemistry Letters*, 2(17):2184–2192, September 2011.

[30] Melanie A. R. Reber, Yuning Chen, and Thomas K. Allison. Cavity-enhanced ultrafast spectroscopy: Ultrafast meets ultrasensitive. *Optica*, 3(3):311–317, March 2016.

[31] David J. Tannor. *Introduction to Quantum Mechanics*. University Science Books, January 2007.

[32] Rudi Berera, Rienk van Grondelle, and John T. M. Kennis. Ultrafast transient absorption spectroscopy: Principles and application to photosynthetic systems. *Photosynthesis Research*, 101(2-3):105–118, September 2009.

[33] C. Ruckebusch, M. Sliwa, P. Pernot, A. de Juan, and R. Tauler. Comprehensive data analysis of femtosecond transient absorption spectra: A review. *Journal of Photochemistry and Photobiology C: Photochemistry Reviews*, 13(1):1–27, March 2012.

[34] Rocío Borrego-Varillas, Lucia Ganzer, Giulio Cerullo, and Cristian Manzoni. Ultraviolet Transient Absorption Spectrometer with Sub-20-fs Time Resolution. *Applied Sciences*, 8(6):989, June 2018.

[35] Ivo H. M. van Stokkum, Delmar S. Larsen, and Rienk van Grondelle. Global and target analysis of time-resolved spectra. *Biochimica et Biophysica Acta (BBA) - Bioenergetics*, 1657(2):82–104, July 2004.

[36] Joseph S. Beckwith, Christopher A. Rumble, and Eric Vauthey. Data analysis in transient electronic spectroscopy – an experimentalist's view. *International Reviews in Physical Chemistry*, 39(2):135–216, April 2020.

[37] Joseph M. Beechem, Marcel Ameloot, and Ludwig Brand. Global and Target Analysis of Complex Decay Phenomena. *Instrumentation Science & Technology*, 14(3-4):379–402, January 1985.

[38] Daniel M Neumark. Time-Resolved Photoelectron Spectroscopy of Molecules and Clusters. *Annual Review of Physical Chemistry*, 52(1):255–277, 2001.

[39] Michael S. Schuurman and Valérie Blanchet. Time-resolved photoelectron spectroscopy: The continuing evolution of a mature technique. *Physical Chemistry Chemical Physics*, 24(34):20012–20024, August 2022.

[40] Shunsuke Adachi, Tom Schatteburg, Alexander Humeniuk, Roland Mitrić, and Toshinori Suzuki. Probing ultrafast dynamics during and after passing through conical intersections. *Physical Chemistry Chemical Physics*, 21(26):13902–13905, July 2019.

[41] Spencer L. Horton, Yusong Liu, Pratip Chakraborty, Philipp Marquetand, Tamás Rozgonyi, Spiridoula Matsika, and Thomas Weinacht. Strong-field- versus weak-field-ionization pump-probe spectroscopy. *Physical Review A*, 98(5):053416, November 2018.

[42] J. J. Scherer, J. B. Paul, A. O'Keefe, and R. J. Saykally. Cavity Ringdown Laser Absorption Spectroscopy: History, Development, and Application to Pulsed Molecular Beams. *Chemical Reviews*, 97(1):25–52, February 1997.

[43] Stephen M. Ball and Roderic L. Jones. Broad-Band Cavity Ring-Down Spectroscopy. *Chemical Reviews*, 103(12):5239–5262, December 2003.

[44] Abhijit Maity, Sanchi Maithani, and Manik Pradhan. Cavity Ring-Down Spectroscopy: Recent Technological Advancements, Techniques, and Applications. *Analytical Chemistry*, 93(1):388–416, January 2021.

[45] Adam J. Fleisher, David A. Long, Zachary D. Reed, Joseph T. Hodges, and David F. Plusquellic. Coherent cavity-enhanced dual-comb spectroscopy. *Optics Express*, 24(10):10424–10434, May 2016.

[46] Florian Adler, Michael J. Thorpe, Kevin C. Cossel, and Jun Ye. Cavity-enhanced direct frequency comb spectroscopy: Technology and applications. *Annual Review of Analytical Chemistry*, 3(1):175–205, 2010.

[47] A. Foltynowicz, P. Masłowski, A. J. Fleisher, B. J. Bjork, and J. Ye. Cavity-enhanced optical frequency comb spectroscopy in the mid-infrared application to trace detection of hydrogen peroxide. *Applied Physics B*, 110(2):163–175, February 2013.

[48] Grzegorz Kowzan, Dominik Charczun, Agata Cygan, Ryszard S. Trawiński, Daniel Lisak, and Piotr Masłowski. Broadband Optical Cavity Mode Measurements at Hz-Level Precision With a Comb-Based VIPA Spectrometer. *Scientific Reports*, 9(1):1–10, June 2019.

[49] Warren Nagourney. *Quantum Electronics for Atomic Physics and Telecommunication*. OUP Oxford, May 2014.

[50] Gianluca Gagliardi and Hans-Peter Loock, editors. *Cavity-Enhanced Spectroscopy and Sensing*. Springer Series in Optical Sciences. Springer-Verlag, Berlin Heidelberg, 2014.

[51] Andrew Weiner. *Ultrafast Optics*. Wiley, 2009.

[52] Tara Fortier and Esther Baumann. 20 years of developments in optical frequency comb technology and applications. *Communications Physics*, 2(1):1–16, December 2019.

[53] Nathan R. Newbury. Searching for applications with a fine-tooth comb. *Nat Photon*, 5(4):186–188, April 2011.

[54] Marissa L. Weichman, P. Bryan Changala, Jun Ye, Zaijun Chen, Ming Yan, and Nathalie Picque. Broadband molecular spectroscopy with optical frequency combs. *Journal of Molecular Spectroscopy*, 355:66–78, 2019.

[55] Gianni Di Domenico, Stéphane Schilt, and Pierre Thomann. Simple approach to the relation between laser frequency noise and laser line shape. *Applied Optics*, 49(25):4801–4807, September 2010.

[56] Miao Zhu and John L. Hall. Stabilization of optical phase/frequency of a laser system: Application to a commercial dye laser with an external stabilizer. *Journal of the Optical Society of America B*, 10(5):802, May 1993.

[57] Jérôme Faist, Gustavo Villares, Giacomo Scalari, Markus Rösch, Christopher Bonzon, Andreas Hugi, and Mattias Beck. Quantum Cascade Laser Frequency Combs. *Nanophotonics*, 5(2):272–291, June 2016.

[58] Gustavo Villares, Andreas Hugi, Stéphane Blaser, and Jérôme Faist. Dual-comb spectroscopy based on quantum-cascade-laser frequency combs. *Nature Communications*, 5(1):5192, October 2014.

[59] T. J. Kippenberg, R. Holzwarth, and S. A. Diddams. Microresonator-Based Optical Frequency Combs. *Science*, 332(6029):555–559, April 2011.

[60] Scott B. Papp, Katja Beha, Pascal Del'Haye, Franklyn Quinlan, Hansuek Lee, Kerry J. Vahala, and Scott A. Diddams. Microresonator frequency comb optical clock. *Optica*, 1(1):10–14, July 2014.

[61] Andrew J. Metcalf, Connor D. Fredrick, Ryan C. Terrien, Scott B. Papp, and Scott A. Diddams. 30 GHz electro-optic frequency comb spanning 300 THz in the near infrared and visible. *Optics Letters*, 44(11):2673–2676, June 2019.

[62] David R. Carlson, Daniel D. Hickstein, Wei Zhang, Andrew J. Metcalf, Franklyn Quinlan, Scott A. Diddams, and Scott B. Papp. Ultrafast electro-optic light with subcycle control. *Science*, 361(6409):1358–1363, September 2018.

[63] Theodor W. Hänsch. Nobel Lecture: Passion for precision. *Reviews of Modern Physics*, 78(4):1297–1309, November 2006.

[64] John L. Hall. Nobel Lecture: Defining and measuring optical frequencies. *Reviews of Modern Physics*, 78(4):1279–1295, November 2006.

[65] Ian Coddington, Nathan Newbury, and William Swann. Dual-comb spectroscopy. *Optica*, 3(4):414–426, April 2016.

[66] R. Jason Jones and Jun Ye. Femtosecond pulse amplification by coherent addition in a passive optical cavity. *Optics Letters*, 27(20):1848–1850, 2002.

[67] R. Jason Jones and Jun Ye. High-repetition-rate coherent femtosecond pulse amplification withan external passive optical cavity. *Optics Letters*, 29(23):2812–2814, December 2004.

[68] S. Holzberger, N. Lilienfein, M. Trubetskov, H. Carstens, F. Lücking, V. Pervak, F. Krausz, and I. Pupeza. Enhancement cavities for zero-offset-frequency pulse trains. *Optics Letters*, 40(10):2165–2168, May 2015.

[69] Yuning Chen. *Cavity-Enhanced Ultrafast Spectroscopy*. PhD thesis, State University of New York at Stony Brook, United States – New York, 2018.

[70] M. Trubetskov, T. Amotchkina, N. Lilienfein, S. Holzberger, F. Krausz, I. Pupeza, and V. Pervak. Design, Production and Characterization of Mirrors for Ultra-Broadband, High-Finesse Enhancement Cavities. In *Optical Interference Coatings*, page ThA.2. Optica Publishing Group, June 2016.

[71] Thomas K. Allison. Cavity-enhanced ultrafast two-dimensional spectroscopy using higher order modes. *Journal of Physics B: Atomic, Molecular and Optical Physics*, 50(4):044004, 2017.

[72] J. B. Paul, R. A. Provencal, C. Chapo, A. Petterson, and R. J. Saykally. Infrared cavity ringdown spectroscopy of water clusters: O–D stretching bands. *The Journal of Chemical Physics*, 109(23):10201–10206, December 1998.

[73] J. B. Paul, C. P. Collier, R. J. Saykally, J. J. Scherer, and A. O'Keefe. Direct Measurement of Water Cluster Concentrations by Infrared Cavity Ringdown Laser Absorption Spectroscopy. *The Journal of Physical Chemistry A*, 101(29):5211–5214, July 1997.

[74] Martin E. Fermann and Ingmar Hartl. Ultrafast Fiber Laser Technology. *IEEE Journal of Selected Topics in Quantum Electronics*, 15(1):191–206, January 2009.

[75] Nathan R. Newbury and William C. Swann. Low-noise fiber-laser frequency combs (Invited). *JOSA B*, 24(8):1756–1770, August 2007.

[76] Govind P. Agrawal. *Nonlinear Fiber Optics*. Academic Press, August 2019.

[77] Robert W. Boyd. *Nonlinear Optics*. Elsevier, April 2020.

[78] Sterling Backus, Charles G. Durfee, Margaret M. Murnane, and Henry C. Kapteyn. High power ultrafast lasers. *Review of Scientific Instruments*, 69(3):1207–1223, March 1998.

[79] David J. Jones, Scott A. Diddams, Jinendra K. Ranka, Andrew Stentz, Robert S. Windeler, John L. Hall, and Steven T. Cundiff. Carrier-Envelope Phase Control of Femtosecond Mode-Locked Lasers and Direct Optical Frequency Synthesis. *Science*, 288(5466):635–639, April 2000.

[80] Axel Ruehl, Michael J. Martin, Kevin C. Cossel, Lisheng Chen, Hugh McKay, Brian Thomas, Craig Benko, Liang Dong, John M. Dudley, Martin E. Fermann, Ingmar Hartl, and Jun Ye. Ultra-Broadband Coherent Supercontinuum Frequency Comb. *Physical Review A*, 84(1), July 2011.

[81] J. L. Wagener, P. F. Wysocki, M. J. F. Digonnet, H. J. Shaw, and D. J. DiGiovanni. Effects of concentration and clusters in erbium-doped fiber lasers. *Optics Letters*, 18(23):2014–2016, December 1993.

[82] N. V. Kiritchenko, L. V. Kotov, M. A. Melkumov, M. E. Likhachev, M. M. Bubnov, M. V. Yashkov, A. Yu Laptev, and A. N. Guryanov. Effect of ytterbium co-doping on erbium clustering in silica-doped glass. *Laser Physics*, 25(2):025102, January 2015.

[83] K. L. Corwin, N. R. Newbury, J. M. Dudley, S. Coen, S. A. Diddams, B. R. Washburn, K. Weber, and R. S. Windeler. Fundamental amplitude noise limitations to supercontinuum spectra generated in a microstructured fiber. *Applied Physics B*, 77(2):269–277, September 2003.

[84] Tyler W. Neely, Todd A. Johnson, and Scott A. Diddams. High-power broadband laser source tunable from 3.0 Mm to 4.4 Mmbased on a femtosecond Yb:fiber oscillator. *Optics Letters*, 36(20):4020–4022, October 2011.

[85] Alexander M. Heidt, Alexander Hartung, Gurthwin W. Bosman, Patrizia Krok, Erich G. Rohwer, Heinrich Schwoerer, and Hartmut Bartelt. Coherent octave spanning near-infrared and visible supercontinuum generation in all-normal dispersion photonic crystal fibers. *Optics express*, 19(4):3775–3787, 2011.

[86] Daniele Brida, Günther Krauss, Alexander Sell, and Alfred Leitenstorfer. Ultrabroadband Er:fiber lasers: Ultrabroadband Er:fiber lasers. *Laser & Photonics Reviews*, 8(3):409–428, May 2014.

[87] Daniel L. Maser, Gabriel Ycas, William I. Depetri, Flavio C. Cruz, and Scott A. Diddams. Coherent frequency combs for spectroscopy across the 3–5 Mm region. *Applied Physics B*, 123(5):142, May 2017.

[88] Gabriel George Ycas. *Laser Frequency Combs for Precision Astronomical Spectroscopy*. PhD thesis, University of Colorado at Boulder, 2013.

[89] Daniel L. Maser. *Generation of Mid-Infrared Frequency Combs for Spectroscopic Applications*. PhD thesis, University of Colorado at Boulder, 2017.

[90] Johan Hult. A Fourth-Order Runge–Kutta in the Interaction Picture Method for Simulating Supercontinuum Generation in Optical Fibers. *Journal of Lightwave Technology*, 25(12):3770–3775, December 2007.

[91] Gabriel Ycas. pyNLO: Nonlinear optics modeling for Python, July 2023.

[92] A.E. Siegman. *Lasers*. University Science Books, 1986.

[93] R. H. Stolen and Chinlon Lin. Self-phase-modulation in silica optical fibers. *Physical Review A*, 17(4):1448–1453, April 1978.

[94] C. V. Raman. A new radiation. *Proceedings of the Indian Academy of Sciences - Section A*, 37(3):333–341, March 1928.

[95] James T. Murray, Richard C. Powell, and Nasser Peyghambarian. Properties of stimulated Raman scattering in crystals. *Journal of Luminescence*, 66–67:89–93, December 1995.

[96] H. M. Pask. The design and operation of solid-state Raman lasers. *Progress in Quantum Electronics*, 27(1):3–56, January 2003.

[97] Ozdal Boyraz and Bahram Jalali. Demonstration of a silicon Raman laser. *Optics Express*, 12(21):5269–5273, October 2004.

[98] Shawn P. Mulvaney and Christine D. Keating. Raman Spectroscopy. *Analytical Chemistry*, 72(12):145–158, June 2000.

[99] Ewen Smith and Geoffrey Dent. *Modern Raman Spectroscopy: A Practical Approach.* John Wiley & Sons, April 2019.

[100] JP Gordon. Theory of the soliton self-frequency shift. *Optics letters*, 11(10), October 1986.

[101] S. V. Chernikov and P. V. Mamyshev. Femtosecond soliton propagation in fibers with slowly decreasing dispersion. *JOSA B*, 8(8):1633–1641, August 1991.

[102] M. Erkintalo, Y. Q. Xu, S. G. Murdoch, J. M. Dudley, and G. Genty. Cascaded Phase Matching and Nonlinear Symmetry Breaking in Fiber Frequency Combs. *Physical Review Letters*, 109(22), November 2012.

[103] T. R. Schibli, I. Hartl, D. C. Yost, M. J. Martin, A. Marcinkevičius, M. E. Fermann, and J. Ye. Optical frequency comb with submillihertz linewidth and more than 10 W average power. *Nature Photonics*, 2(6):355–359, June 2008.

[104] Axel Ruehl, Andrius Marcinkevicius, Martin E. Fermann, and Ingmar Hartl. 80 W, 120 fs Yb-fiber frequency comb. *Optics Letters*, 35(18):3015–3017, September 2010.

[105] Wolfgang Dr Hänsel, Ronald Dr Holzwarth, Ralf Doubek, and Michael Dr Mei. Laser with non-linear optical loop mirror, September 2013.

[106] Wolfgang Hänsel, Heinar Hoogland, Michele Giunta, Sebastian Schmid, Tilo Steinmetz, Ralf Doubek, Peter Mayer, Sven Dobner, Carsten Cleff, Marc Fischer, and Ronald Holzwarth. All polarization-maintaining fiber laser architecture for robust femtosecond pulse generation. *Applied Physics B*, 123(1):41, January 2017.

[107] W. Hänsel, M. Giunta, M. Lezius, M. Fischer, and R. Holzwarth. Electro-optic modulator for rapid control of the carrier-envelope offset frequency. In *2017 Conference on Lasers and Electro-Optics (CLEO)*, pages 1–2, May 2017.

[108] Aline S. Mayer, Wilfrid Grosinger, Jakob Fellinger, Georg Winkler, Lukas W. Perner, Stefan Droste, Sarper H. Salman, Chen Li, Christoph M. Heyl, Ingmar Hartl, and Oliver H. Heckl. Flexible all-PM NALM Yb:fiber laser design for frequency comb applications: Operation regimes and their noise properties. *Optics Express*, 28(13):18946–18968, June 2020.

[109] Esther Baumann, Fabrizio R. Giorgetta, Jeffrey W. Nicholson, William C. Swann, Ian Coddington, and Nathan R. Newbury. High-performance, vibration-immune, fiber-laser frequency comb. *Optics Letters*, 34(5):638–640, March 2009.

[110] J. W. Nicholson, A. D. Yablon, P. S. Westbrook, K. S. Feder, and M. F. Yan. High power, single mode, all-fiber source of femtosecond pulses at 1550 nm and its use in supercontinuum generation. *Optics Express*, 12(13):3025–3034, June 2004.

[111] H. Mashiko, A. Suda, and K. Midorikawa. All-reflective interferometric autocorrelator for the measurement of ultra-short optical pulses. *Applied Physics B*, 76(5):525–530, May 2003.

[112] H. Mashiko, A. Suda, and K. Midorikawa. Second-order autocorrelation functions for all-reflective interferometric autocorrelator. *Applied Physics B*, 87(2):221–226, April 2007.

[113] Xinlong Li, Melanie A. R. Reber, Christopher Corder, Yuning Chen, Peng Zhao, and Thomas K. Allison. High-power ultrafast Yb:fiber laser frequency combs using commercially available components and basic fiber tools. *Review of Scientific Instruments*, 87(9):093114, September 2016.

[114] R. Paschotta, J. Nilsson, A.C. Tropper, and D.C. Hanna. Ytterbium-doped fiber amplifiers. *IEEE Journal of Quantum Electronics*, 33(7):1049–1056, July 1997.

[115] J. J. Koponen, M. J. Söderlund, H. J. Hoffman, and S. K. T. Tammela. Measuring photodarkening from single-mode ytterbium doped silica fibers. *Optics Express*, 14(24):11539–11544, November 2006.

[116] R. Paschotta, J. Nilsson, P. R. Barber, J. E. Caplen, A. C. Tropper, and D. C. Hanna. Lifetime quenching in Yb-doped fibres. *Optics Communications*, 136(5):375–378, April 1997.

[117] L. Kuznetsova, F.W. Wise, S. Kane, and J. Squier. Chirped-pulse amplification near the gain-narrowing limit of Yb-doped fiber using a reflection grism compressor. *Applied Physics B*, 88(4):515–518, September 2007.

[118] Alexander Sell, Günther Krauss, Rüdiger Scheu, Rupert Huber, and Alfred Leitenstorfer. 8-fs pulses from a compact Er: Fiber system: Quantitative modeling and experimental implementation. *Optics express*, 17(2):1070–1077, 2009.

[119] Florian Tauser, Florian Adler, and Alfred Leitenstorfer. Widely tunable sub-30-fs pulses from a compact erbium-doped fiber source. *Optics Letters*, 29(5):516–518, March 2004.

[120] Neomi Lewis. *Towards Cavity-Enhanced 2DIR Spectroscopy.* PhD thesis, Stony Brook University, June 2021.

[121] Henry Timmers, Abijith Kowligy, Alex Lind, Flavio C. Cruz, Nima Nader, Myles Silfies, Gabriel Ycas, Thomas K. Allison, Peter G. Schunemann, Scott B. Papp, and Scott A. Diddams. Molecular fingerprinting with bright, broadband infrared frequency combs. *Optica*, 5(6):727–732, June 2018.

[122] Alexander J. Lind, Abijith Kowligy, Henry Timmers, Flavio C. Cruz, Nima Nader, Myles C. Silfies, Thomas K. Allison, and Scott A. Diddams. Mid-Infrared Frequency Comb Generation and Spectroscopy with Few-Cycle Pulses and ${\ensuremath{\chi}}^{(2)}$ Nonlinear Optics. *Physical Review Letters*, 124(13):133904, April 2020.

[123] Arman Cingöz, Dylan C. Yost, Thomas K. Allison, Axel Ruehl, Martin E. Fermann, Ingmar Hartl, and Jun Ye. Direct frequency comb spectroscopy in the extreme ultraviolet. *Nature*, 482(7383):68–71, February 2012.

[124] F. Quinlan, G. Ycas, S. Osterman, and S. A. Diddams. A 12.5 GHz-spaced optical frequency comb spanning ¿400 nm for near-infrared astronomical spectrograph calibration. *Review of Scientific Instruments*, 81(6):063105, 2010.

[125] Yang Yang, David Burghoff, Darren J. Hayton, Jian-Rong Gao, John L. Reno, and Qing Hu. Terahertz multiheterodyne spectroscopy using laser frequency combs. *Optica*, 3(5):499–502, May 2016.

[126] Albert Schliesser, Nathalie Picque, and Theodor W. Hansch. Mid-infrared frequency combs. *Nat Photon*, 6(7):440–449, July 2012.

[127] Marcus Seidel, Xiao Xiao, Syed A. Hussain, Gunnar Arisholm, Alexander Hartung, Kevin T. Zawilski, Peter G. Schunemann, Florian Habel, Michael Trubetskov, Vladimir Pervak, Oleg Pronin, and Ferenc Krausz. Multi-watt, multi-octave, mid-infrared femtosecond source. *Science Advances*, 4(4):eaaq1526, April 2018.

[128] Nick Leindecker, Alireza Marandi, Robert L. Byer, Konstantin L. Vodopyanov, Jie Jiang, Ingmar Hartl, Martin Fermann, and Peter G. Schunemann. Octave-spanning ultrafast OPO with 2.6-6.1µm instantaneous bandwidth pumped by femtosecond Tm-fiber laser. *Optics Express*, 20(7):7046–7053, March 2012.

[129] Kevin F. Lee, Jie Jiang, C. Mohr, J. Bethge, M. E. Fermann, Nick Leindecker, Konstantin L. Vodopyanov, Peter G. Schunemann, and I. Hartl.

Carrier envelope offset frequency of a doubly resonant, nondegenerate, mid-infrared GaAs optical parametric oscillator. *Optics Letters*, 38(8):1191–1193, April 2013.

[130] Axel Ruehl, Alessio Gambetta, Ingmar Hartl, Martin E. Fermann, Kjeld SE Eikema, and Marco Marangoni. Widely-tunable mid-infrared frequency comb source based on difference frequency generation. *Optics letters*, 37(12):2232–2234, 2012.

[131] Grzegorz Soboń, Tadeusz Martynkien, Paweł Mergo, Lucile Rutkowski, and Aleksandra Foltynowicz. High-power frequency comb source tunable from 2.7 to 4.2 μm based on difference frequency generation pumped by an Yb-doped fiber laser. *Optics Letters*, 42(9):1748–1751, May 2017.

[132] Tobias Steinle, Florian Mörz, Andy Steinmann, and Harald Giessen. Ultra-stable high average power femtosecond laser system tunable from 1.33 to 20 μm. *Optics Letters*, 41(21):4863–4866, November 2016.

[133] Tobias Steinle, Andy Steinmann, Robin Hegenbarth, and Harald Giessen. Watt-level optical parametric amplifier at 42 MHz tunable from 1.35 to 4.5 μm coherently seeded with solitons. *Optics Express*, 22(8):9567–9573, April 2014.

[134] Mario Barbatti, Adélia JA Aquino, Hans Lischka, Christian Schriever, Stefan Lochbrunner, and Eberhard Riedle. Ultrafast internal conversion pathway and mechanism in 2-(2′-hydroxyphenyl) benzothiazole: A case study for excited-state intramolecular proton transfer systems. *Physical Chemistry Chemical Physics*, 11(9):1406–1415, 2009.

[135] Nawee Kungwan, Felix Plasser, Adélia J. A. Aquino, Mario Barbatti, Peter Wolschann, and Hans Lischka. The effect of hydrogen bonding on the excited-state proton transfer in 2-(2′-hydroxyphenyl)benzothiazole: A TDDFT molecular dynamics study. *Physical Chemistry Chemical Physics*, 14(25):9016, 2012.

[136] Michael F. Vansco, Hongwei Li, and Marsha I. Lester. Prompt release of O 1D products upon UV excitation of CH2OO Criegee intermediates. *The Journal of Chemical Physics*, 147(1):013907, 2017.

[137] K. Moutzouris, F. Adler, F. Sotier, D. Träutlein, and A. Leitenstorfer. Multimilliwatt ultrashort pulses continuously tunable in the visible from a compact fiber source. *Optics letters*, 31(8):1148–1150, 2006.

[138] Haohua Tu and Stephen A Boppart. Ultraviolet-visible non-supercontinuum ultrafast source enabled by switching single silicon strand-like photonic crystal fibers. *Optics Express*, 17:17983–17988, September 2009.

[139] Wenlong Tian, Zhaohua Wang, Xianghao Meng, Ninghua Zhang, Jiangfeng Zhu, and Zhiyi Wei. High-power, widely tunable, green-pumped femtosecond BiB3O6 optical parametric oscillator. *Optics Letters*, 41(21):4851–4854, November 2016.

[140] C. Cleff, J. Epping, P. Gross, and C. Fallnich. Femtosecond OPO based on LBO pumped by a frequency-doubled Yb-fiber laser-amplifier system for CARS spectroscopy. *Applied Physics B*, 103(4):795–800, June 2011.

[141] Nicola Coluccelli, Daniele Viola, Vikas Kumar, Antonio Perri, Marco Marangoni, Giulio Cerullo, and Dario Polli. Tunable 30 fs light pulses at 1 W power level from a Yb-pumped optical parametric oscillator. *Optics Letters*, 42(21):4545–4548, November 2017.

[142] Chenglin Gu, Minglie Hu, Limeng Zhang, Jintao Fan, Youjian Song, Chingyue Wang, and Derryck T. Reid. High average power, widely tunable femtosecond laser source from red to mid-infrared based on an Yb-fiber-laser-pumped optical parametric oscillator. *Optics Letters*, 38(11):1820–1822, June 2013.

[143] Chenglin Gu, Minglie Hu, Jintao Fan, Youjian Song, Bowen Liu, Lu Chai, Chingyue Wang, and Derryck T. Reid. High power tunable femtosecond ultraviolet laser source based on an Yb-fiber-laser pumped optical parametric oscillator. *Optics Express*, 23(5):6181–6186, March 2015.

[144] Jintao Fan, Chenglin Gu, Chingyue Wang, and Minglie Hu. Extended femtosecond laser wavelength range to 330 nm in a high power LBO based optical parametric oscillator. *Optics Express*, 24(12):13250–13257, June 2016.

[145] Richard A. McCracken, Ilaria Gianani, Adam S. Wyatt, and Derryck T. Reid. Multi-color carrier-envelope-phase stabilization for high-repetition-rate multi-pulse coherent synthesis. *Optics Letters*, 40(7):1208–1211, April 2015.

[146] M. Ghotbi, A. Esteban-Martin, and M. Ebrahim-Zadeh. BiB3O6 femtosecond optical parametric oscillator. *Optics Letters*, 31(21):3128–3130, November 2006.

[147] J. H. Sun, B. J. S. Gale, and D. T. Reid. Composite frequency comb spanning 0.4-2.4μm from a phase-controlled femtosecond Ti:sapphire laser and synchronously pumped optical parametric oscillator. *Optics Letters*, 32(11):1414–1416, June 2007.

[148] R. Jason Jones. Precision stabilization of femtosecond lasers to high-finesse optical cavities. *Physical Review A*, 69(5), 2004.

[149] Yohei Kobayashi, Kenji Torizuka, Alireza Marandi, Robert L. Byer, Richard A. McCracken, Zhaowei Zhang, and Derryck T. Reid. Femtosecond optical parametric oscillator frequency combs. *Journal of Optics*, 17(9):094010, 2015.

[150] Yohei Kobayashi and Kenji Torizuka. Measurement of the optical phase relation among subharmonic pulses in a femtosecond optical parametric oscillator. *Optics Letters*, 25(11):856–858, June 2000.

[151] H.R. Telle, B. Lipphardt, and J. Stenger. Kerr-lens, mode-locked lasers as transfer oscillators for optical frequency measurements. *Applied Physics B*, 74(1):1–6, January 2002.

[152] Bachana Lomsadze and Steven T. Cundiff. Frequency combs enable rapid and high-resolution multidimensional coherent spectroscopy. *Science*, 357(6358):1389–1391, September 2017.

[153] Jenna Bergevin, Tsung-Han Wu, Jeremy Yeak, Brian E. Brumfield, Sivanandan S. Harilal, Mark C. Phillips, and R. Jason Jones. Dual-comb spectroscopy of laser-induced plasmas. *Nature Communications*, 9(1):1273, 2018.

[154] Matz Liebel, Costanza Toninelli, and Niek F. van Hulst. Room-temperature ultrafast nonlinear spectroscopy of a single molecule. *Nature Photonics*, 12(1):45–49, 2018.

[155] Dario Polli, Vikas Kumar, Carlo M. Valensise, Marco Marangoni, and Giulio Cerullo. Broadband coherent raman scattering microscopy. *Laser & Photonics Reviews*, 12(9):1800020, 2018.

[156] Chuangtian Chen, Yicheng Wu, Aidong Jiang, Bochang Wu, Guiming You, Rukang Li, and Shujie Lin. New nonlinear-optical crystal: LiB_3O_5. *Journal of the Optical Society of America B*, 6:616–621, April 1989.

[157] SNLO. *'SNLO nonlinear optics code available from A. V. Smith, AS-Photonics, Albuquerque, NM.*

[158] Travis C. Briles, Dylan C. Yost, Arman Cingöz, Jun Ye, and Thomas R. Schibli. Simple piezoelectric-actuated mirror with 180 kHz servo bandwidth. *Optics Express*, 18(10):9739–9746, May 2010.

[159] Marcel Wunram, Patrick Storz, Daniele Brida, and Alfred Leitenstorfer. Ultrastable fiber amplifier delivering 145-fs pulses with 6-μJ energy at 10-MHz repetition rate. *Optics Letters*, 40(5):823–826, March 2015.

[160] Y. R. Shen. *The Principles of Nonlinear Optics.* Wiley, 1984.

[161] R. W. P. Drever, J. L. Hall, F. V. Kowalski, J. Hough, G. M. Ford, A. J. Munley, and H. Ward. Laser phase and frequency stabilization using an optical resonator. *Applied Physics B*, 31(2):97–105, June 1983.

[162] Joshua C. Bienfang, Russell F. Teehan, and Craig A. Denman. Phase noise transfer in resonant optical cavities. *Review of Scientific Instruments*, 72(8):3208–3214, July 2001.

[163] Chenchen Wan, Peng Li, Axel Ruehl, and Ingmar Hartl. Coherent frequency division with a degenerate synchronously pumped optical parametric oscillator. *Optics Letters*, 43(5):1059–1062, March 2018.

[164] Takuro Ideguchi, Simon Holzner, Birgitta Bernhardt, Guy Guelachvili, Nathalie Picque, and Theodor W. Hansch. Coherent Raman spectroimaging with laser frequency combs. *Nature*, 502(7471):355–358, October 2013.

[165] Nazanin Hoghooghi, Robert J. Wright, Amanda S. Makowiecki, William C. Swann, Eleanor M. Waxman, Ian Coddington, and Gregory B. Rieker. Broadband coherent cavity-enhanced dual-comb spectroscopy. *Optica*, 6(1):28–33, January 2019.

[166] C. Benko, A. Ruehl, M. J. Martin, K. S. E. Eikema, M. E. Fermann, I. Hartl, and J. Ye. Full phase stabilization of a Yb:fiber femtosecond frequency comb via high-bandwidth transducers. *Optics Letters*, 37(12):2196–2198, June 2012.

[167] M. Ebrahimzadeh, P.J. Phillips, and S. Das. Low-threshold midinfrared optical parametric oscillation in periodically poled LiNbO3 synchronously pumped by a Ti:sapphire laser. *Applied Physics B*, 72(7):793–801, May 2001.

[168] Titus Gherman and Daniele Romanini. Modelocked Cavity–Enhanced absorption spectroscopy. *Optics Express*, 10(19):1033–1042, September 2002.

[169] Arthur K Mills, T J Hammond, Matthew H C Lam, and David J Jones. XUV frequency combs via femtosecond enhancement cavities. *Journal of Physics B: Atomic, Molecular and Optical Physics*, 45(14):142001, 2012.

[170] Christopher Corder, Peng Zhao, Jin Bakalis, Xinlong Li, Matthew D. Kershis, Amanda R. Muraca, Michael G. White, and Thomas K. Allison. Ultrafast extreme ultraviolet photoemission without space charge. *Structural Dynamics*, 5(5):054301, September 2018.

[171] A. K. Mills, S. Zhdanovich, M. X. Na, F. Boschini, E. Razzoli, M. Michiardi, A. Sheyerman, M. Schneider, T. J. Hammond, V. Süss,

C. Felser, A. Damascelli, and D. J. Jones. Cavity-enhanced high harmonic generation for extreme ultraviolet time- and angle-resolved photoemission spectroscopy. *Review of Scientific Instruments*, 90(8):083001, August 2019.

[172] T. Saule, S. Heinrich, J. Schötz, N. Lilienfein, M. Högner, O. deVries, M. Plötner, J. Weitenberg, D. Esser, J. Schulte, P. Russbueldt, J. Limpert, M. F. Kling, U. Kleineberg, and I. Pupeza. High-flux ultrafast extreme-ultraviolet photoemission spectroscopy at 18.4 MHz pulse repetition rate. *Nature Communications*, 10(1):458, 2019.

[173] Craig Benko, Linqiang Hua, Thomas K. Allison, Franççois Labaye, and Jun Ye. Cavity-enhanced field-free molecular alignment at a high repetition rate. *Physical Review Letters*, 114:153001, April 2015.

[174] Roland Krischek, Witlef Wieczorek, Akira Ozawa, Nikolai Kiesel, Patrick Michelberger, Thomas Udem, and Harald Weinfurter. Ultraviolet enhancement cavity for ultrafast nonlinear optics and high-rate multiphoton entanglement experiments. *Nat Photon*, 4(3):170–173, March 2010.

[175] P. Bryan Changala, Marissa L. Weichman, Kevin F. Lee, Martin E. Fermann, and Jun Ye. Rovibrational quantum state resolution of the C60 fullerene. *Science*, 363(6422):49–54, January 2019.

[176] Chadi Abd Alrahman, Amir Khodabakhsh, Florian M. Schmidt, Zhechao Qu, and Aleksandra Foltynowicz. Cavity-enhanced optical frequency comb spectroscopy of high-temperature H_2O in a flame. *Optics Express*, 22(11):13889–13895, June 2014.

[177] Anthony Catanese, Jay Rutledge, Myles C. Silfies, Xinlong Li, Henry Timmers, Abijith S. Kowligy, Alex Lind, Scott A. Diddams, and Thomas K. Allison. Mid-infrared frequency comb with 6.7 W average power based on difference frequency generation. *Optics Letters*, 45(5):1248–1251, March 2020.

[178] Franz X. Kaertner, Li-Jin Chen, and Guoqing Chang. Broadband dispersion-free optical filter cavities based on dielectric mirrors with complementary dispersion, March 2015.

[179] J. M. Herbelin, J. A. McKay, M. A. Kwok, R. H. Ueunten, D. S. Urevig, D. J. Spencer, and D. J. Benard. Sensitive measurement of photon lifetime and true reflectances in an optical cavity by a phase-shift method. *Applied Optics*, 19(1):144–147, January 1980.

[180] Richard Engeln, Gert von Helden, Giel Berden, and Gerard Meijer. Phase shift cavity ring down absorption spectroscopy. *Chemical Physics Letters*, 262(1):105–109, November 1996.

[181] Christopher Corder, Peng Zhao, Jin Bakalis, Xinlong Li, Matthew D. Kershis, Amanda R. Muraca, Michael G. White, and Thomas K. Allison. Development of a tunable high repetition rate XUV source for time-resolved photoemission studies of ultrafast dynamics at surfaces. *Proc.SPIE*, 10519:10519 – 10519 – 7, 2018.

[182] N. Lilienfein, C. Hofer, M. Högner, T. Saule, M. Trubetskov, V. Pervak, E. Fill, C. Riek, A. Leitenstorfer, J. Limpert, F. Krausz, and I. Pupeza. Temporal solitons in free-space femtosecond enhancement cavities. *Nature Photonics*, 13(3):214–218, 2019.

[183] D.R. Miller. Free jet sources. In G. Scoles, editor, *Atomic and Molecular Beam Methods*. Oxford University Press, 1988.

[184] Włodzimierz Jarzeba, Victor V. Matylitsky, Andreas Weichert, and Christoph Riehn. Rotational coherence spectroscopy of benzene by femtosecond degenerate four-wave mixing. *Physical Chemistry Chemical Physics*, 4:451–454, 2002.

[185] Ioachim Pupeza, Xun Gu, Ernst Fill, Tino Eidam, Jens Limpert, Andreas Tünnermann, Ferenc Krausz, and Thomas Udem. Highly sensitive dispersion measurement of a high-power passive optical resonator using spatial-spectral interferometry. *Optics Express*, 18(25):26184–26195, December 2010.

[186] Philip C. D. Hobbs. Ultrasensitive laser measurements without tears. *Applied Optics*, 36(4):903–920, February 1997.

[187] Peter M. Felker and Ahmed H. Zewail. Purely rotational coherence effect and time-resolved sub-Doppler spectroscopy of large molecules. I. Theoretical. *The Journal of Chemical Physics*, 86(5):2460–2482, March 1987.

[188] S. Lochbrunner, T. Schultz, M. Schmitt, J. P. Shaffer, M. Z. Zgierski, and Albert Stolow. Dynamics of excited-state proton transfer systems via time-resolved photoelectron spectroscopy. *The Journal of Chemical Physics*, 114(6):2519–2522, February 2001.

[189] Javier Catalan and Juan Carlos del Valle. Toward the photostability mechanism of intramolecular hydrogen bond systems. The photophysics of 1'-hydroxy-2'-acetonaphthone. *Journal of the American Chemical Society*, 115(10):4321–4325, May 1993.

[190] Abderrazzak Douhal, Françoise Lahmani, and Ahmed H. Zewail. Proton-transfer reaction dynamics. *Chemical Physics*, 207(2):477–498, July 1996.

[191] DeGui Kong, Qing Chang, YaChen Gao, Hong'An Ye, LiXin Zhang, Guang Shi, XueRu Zhang, YuXiao Wang, Kun Yang, and YingLin Song. Nonlinear absorption of CS2 at the wavelength of 400nm with femtosecond pulses. *Physica B: Condensed Matter*, 407(8):1279–1281, April 2012.

[192] D. W. Allan. Statistics of atomic frequency standards. *Proceedings of the IEEE*, 54(2):221–230, 1966.

[193] C. Schriever, S. Lochbrunner, E. Riedle, and D. J. Nesbitt. Ultrasensitive ultraviolet-visible 20fs absorption spectroscopy of low vapor pressure molecules in the gas phase. *Review of Scientific Instruments*, 79(1):013107, January 2008.

[194] Christian Schriever. Kohärenz auf reaktiven Potentialflächen: Beobachtung und Analyse molekularer Dynamik. page 197.

[195] Arshad Mehmood. First-principles Simulations of Ultrafast Transient Absorption Spectrum. *inprogress*, 2023.

[196] Shiela Pijeau, Donneille Foster, and Edward G. Hohenstein. Effect of Nonplanarity on Excited-State Proton Transfer and Internal Conversion in Salicylideneaniline. *The Journal of Physical Chemistry A*, 122(25):5555–5562, June 2018.

[197] P. M. Felker, J. S. Baskin, and A. H. Zewail. Rephasing of collisionless molecular rotational coherence in large molecules. *The Journal of Physical Chemistry*, 90(5):724–728, February 1986.

[198] Nadja Heine and Knut R. Asmis. Cryogenic ion trap vibrational spectroscopy of hydrogen-bonded clusters relevant to atmospheric chemistry. *International Reviews in Physical Chemistry*, 34(1):1–34, 2015.

[199] Claire Vallance and Cathy M. Rushworth. Cavity ringdown spectroscopy for the analysis of small liquid volumes. In *Cavity-Enhanced Spectroscopy and Sensing*. Springer-Verlag, 2014.

[200] Myles C. Silfies, Arshad Mehmood, Grzegorz Kowzan, Edward G. Hohenstein, Benjamin G. Levine, and Thomas K. Allison. Ultrafast internal conversion and photochromism in gas-phase salicylideneaniline. https://arxiv.org/abs/2306.05645v1, June 2023.

[201] Kingo Uchida. Photochromism. Molecules and Systems. Edited by Heinz Dürr and Henri Bouas-Laurent. *Angewandte Chemie International Edition*, 43(26):3362–3362, 2004.

[202] Hem C. Joshi and Liudmil Antonov. Excited-State Intramolecular Proton Transfer: A Short Introductory Review. *Molecules (Basel, Switzerland)*, 26(5):1475, March 2021.

[203] Panwang Zhou and Keli Han. Unraveling the Detailed Mechanism of Excited-State Proton Transfer. *Accounts of Chemical Research*, 51(7):1681–1690, July 2018.

[204] Aravin Prince Periyasamy, Martina Vikova, and Michal Vik. A review of photochromism in textiles and its measurement. *Textile Progress*, 49(2):53–136, April 2017.

[205] Seon-Jeong Lim, Jangwon Seo, and Soo Young Park. Photochromic Switching of Excited-State Intramolecular Proton-Transfer (ESIPT) Fluorescence: A Unique Route to High-Contrast Memory Switching and Nondestructive Readout. *Journal of the American Chemical Society*, 128(45):14542–14547, November 2006.

[206] M. Irie. Photochromism: Memories and SwitchesIntroduction. *Chemical Reviews*, 100(5):1683–1684, May 2000.

[207] Ling Chen, Jia-Wen Ye, Hai-Ping Wang, Mei Pan, Shao-Yun Yin, Zhang-Wen Wei, Lu-Yin Zhang, Kai Wu, Ya-Nan Fan, and Cheng-Yong Su. Ultrafast water sensing and thermal imaging by a metal-organic framework with switchable luminescence. *Nature Communications*, 8(1):15985, June 2017.

[208] H. Mishra, V. Misra, M. S. Mehata, T. C. Pant, and H. B. Tripathi. Fluorescence Studies of Salicylic Acid Doped Poly(vinyl alcohol) Film as a Water/Humidity Sensor. *The Journal of Physical Chemistry A*, 108(12):2346–2352, March 2004.

[209] Meng Qin, Yu Huang, Fengyu Li, and Yanlin Song. Photochromic sensors: A versatile approach for recognition and discrimination. *Journal of Materials Chemistry C*, 3(36):9265–9275, September 2015.

[210] Robert I. Cukier and Daniel G. Nocera. Proton-Coupled Electron Transfer. *Annual Review of Physical Chemistry*, 49(1):337–369, 1998.

[211] Sharon Hammes-Schiffer and Alexei A. Stuchebrukhov. Theory of Coupled Electron and Proton Transfer Reactions. *Chemical Reviews*, 110(12):6939–6960, December 2010.

[212] D. Higelin and H. Sixl. Spectroscopic studies of the photochromism of N-salicylideneaniline mixed crystals and glasses. *Chemical Physics*, 77(3):391–400, June 1983.

[213] Michael Ottolenghi and Donald S. McClure. Photochromism. I. The Spectroscopy and Energy Levels of Salicylideneaniline. *The Journal of Chemical Physics*, 46(12):4613–4620, 1967.

[214] T. Rosenfeld, M. Ottolenghi, and A.Y. Meyer. Photochromic Anils. Structure of Photoisomers and Thermal Relaxation Processes. *Mol. Photochem*, 5(1):39–60, 1973.

[215] Krzysztof Kownacki, Andrzej Mordzinski, Robert Wilbrandt, and Anna Grabowska. Laser-induced absorption and fluorescence studies of photochromic Schiff bases. *Chemical Physics Letters*, 227(3):270–276, September 1994.

[216] Marek Z. Zgierski and Anna Grabowska. Photochromism of salicylideneaniline (SA). How the photochromic transient is created: A theoretical approach. *The Journal of Chemical Physics*, 112(14):6329–6337, April 2000.

[217] Lasse Spörkel, Ganglong Cui, and Walter Thiel. Photodynamics of Schiff Base Salicylideneaniline: Trajectory Surface-Hopping Simulations. *The Journal of Physical Chemistry A*, 117(22):4574–4583, June 2013.

[218] R. Destro, A. Gavezzotti, and M. Simonetta. Salicylideneaniline. *Acta Crystallographica Section B: Structural Crystallography and Crystal Chemistry*, 34(9):2867–2869, September 1978.

[219] Tetsuro Yuzawa, Hiroaki Takahashi, and Hiro-o Hamaguchi. Submicrosecond time-resolved infrared study on the structure of the photoinduced transient species of salicylideneaniline in acetonitrile. *Chemical Physics Letters*, 202(3):221–226, January 1993.

[220] Mihaela Avadanei, Nihal Kuş, Vasile Cozan, and Rui Fausto. Structure and Photochemistry of N-Salicylidene-p-carboxyaniline Isolated in Solid Argon. *The Journal of Physical Chemistry A*, 119(34):9121–9132, August 2015.

[221] Ryoichi Nakagaki, Takayoshi Kobayashi, Junko Nakamura, and Saburo Nagakura. Spectroscopic and Kinetic Studies of the Photochromism of N-Salicylideneanilines and Related Compounds. *Bulletin of the Chemical Society of Japan*, 50(8):1909–1912, August 1977.

[222] Michel Sliwa, Nicolas Mouton, Cyril Ruckebusch, Lionel Poisson, Abdenacer Idrissi, Stéphane Aloïse, Ludovic Potier, Julien Dubois, Olivier Poizat, and Guy Buntinx. Investigation of ultrafast photoinduced processes for salicylidene aniline in solution and gas phase: Toward a general photo-dynamical scheme. *Photochemical & Photobiological Sciences*, 9(5):661–669, May 2010.

[223] Sivaprasad Mitra and Naoto Tamai. Femtosecond spectroscopic study on photochromic salicylideneaniline. *Chemical Physics Letters*, 282(5):391–397, January 1998.

[224] Sivaprasad Mitra and Naoto Tamai. Dynamics of photochromism in salicylideneaniline: A femtosecond spectroscopic study. *Physical Chemistry Chemical Physics*, 5(20):4647–4652, October 2003.

[225] P. F. Barbara, P. M. Rentzepis, and L. E. Brus. Photochemical kinetics of salicylidenaniline. *Journal of the American Chemical Society*, 102(8):2786–2791, April 1980.

[226] William Rodríguez-Córdoba, Jimena S. Zugazagoitia, Elisa Collado-Fregoso, and Jorge Peon. Excited State Intramolecular Proton Transfer in Schiff Bases. Decay of the Locally Excited Enol State Observed by Femtosecond Resolved Fluorescence. *The Journal of Physical Chemistry A*, 111(28):6241–6247, July 2007.

[227] Wei-Tao Peng, B. Scott Fales, and Benjamin G. Levine. Simulating Electron Dynamics of Complex Molecules with Time-Dependent Complete Active Space Configuration Interaction. *Journal of Chemical Theory and Computation*, 14(8):4129–4138, August 2018.

[228] M. Ben-Nun, Jason Quenneville, and Todd J. Martínez. Ab Initio Multiple Spawning: Photochemistry from First Principles Quantum Molecular Dynamics. *The Journal of Physical Chemistry A*, 104(22):5161–5175, June 2000.

[229] Basile F. E. Curchod and Todd J. Martínez. Ab Initio Nonadiabatic Quantum Molecular Dynamics. *Chemical Reviews*, 118(7):3305–3336, April 2018.

[230] Benjamin G. Levine, Andrew S. Durden, Michael P. Esch, Fangchun Liang, and Yinan Shu. CAS without SCF—Why to use CASCI and where to get the orbitals. *The Journal of Chemical Physics*, 154(9):090902, March 2021.

[231] Petr Slavíček and Todd J. Martínez. Ab initio floating occupation molecular orbital-complete active space configuration interaction: An efficient approximation to CASSCF. *The Journal of Chemical Physics*, 132(23):234102, June 2010.

[232] Edward G. Hohenstein. Analytic formulation of derivative coupling vectors for complete active space configuration interaction wavefunctions with floating occupation molecular orbitals. *The Journal of Chemical Physics*, 145(17):174110, November 2016.

[233] Edward G. Hohenstein, Marine E. F. Bouduban, Chenchen Song, Nathan Luehr, Ivan S. Ufimtsev, and Todd J. Martínez. Analytic first derivatives of floating occupation molecular orbital-complete active space configuration interaction on graphical processing units. *The Journal of Chemical Physics*, 143(1):014111, July 2015.

[234] Daniel Hollas, Lukáš Šištík, Edward G. Hohenstein, Todd J. Martínez, and Petr Slavíček. Nonadiabatic Ab Initio Molecular Dynamics with the Floating Occupation Molecular Orbital-Complete Active Space Configuration Interaction Method. *Journal of Chemical Theory and Computation*, 14(1):339–350, January 2018.

[235] Shiela Pijeau and Edward G. Hohenstein. Improved Complete Active Space Configuration Interaction Energies with a Simple Correction from Density Functional Theory. *Journal of Chemical Theory and Computation*, 13(3):1130–1146, March 2017.

[236] Mary A. Rohrdanz, Katie M. Martins, and John M. Herbert. A long-range-corrected density functional that performs well for both ground-state properties and time-dependent density functional theory excitation energies, including charge-transfer excited states. *The Journal of Chemical Physics*, 130(5):054112, February 2009.

[237] Pratip Chakraborty, Yusong Liu, Samuel McClung, Thomas Weinacht, and Spiridoula Matsika. Time Resolved Photoelectron Spectroscopy as a Test of Electronic Structure and Nonadiabatic Dynamics. *The Journal of Physical Chemistry Letters*, 12(21):5099–5104, June 2021.

[238] Michał Andrzej Kochman, Bo Durbeej, and Adam Kubas. Simulation and Analysis of the Transient Absorption Spectrum of 4-(N,N-Dimethylamino)benzonitrile (DMABN) in Acetonitrile. *The Journal of Physical Chemistry A*, 125(39):8635–8648, October 2021.

[239] Davide Avagliano, Matteo Bonfanti, Artur Nenov, and Marco Garavelli. Automatized protocol and interface to simulate QM/MM time-resolved transient absorption at TD-DFT level with COBRAMM. *Journal of Computational Chemistry*, 43(24):1641–1655, 2022.

[240] Andrew S. Durden and Benjamin G. Levine. Floquet Time-Dependent Configuration Interaction for Modeling Ultrafast Electron Dynamics. *Journal of Chemical Theory and Computation*, 18(2):795–806, February 2022.

[241] Xiaosong Li, Niranjan Govind, Christine Isborn, A. Eugene DePrince, and Kenneth Lopata. Real-Time Time-Dependent Electronic Structure Theory. *Chemical Reviews*, 120(18):9951–9993, September 2020.

[242] Umberto De Giovannini, Gustavo Brunetto, Alberto Castro, Jessica Walkenhorst, and Angel Rubio. Simulating Pump–Probe Photoelectron and Absorption Spectroscopy on the Attosecond Timescale with Time-Dependent Density Functional Theory. *ChemPhysChem*, 14(7):1363–1376, 2013.

[243] Adam Bruner, Daniel LaMaster, and Kenneth Lopata. Accelerated Broadband Spectra Using Transition Dipole Decomposition and Padé Approximants. *Journal of Chemical Theory and Computation*, 12(8):3741–3750, August 2016.

[244] Daniel R. Nascimento and A. Eugene III DePrince. Linear Absorption Spectra from Explicitly Time-Dependent Equation-of-Motion Coupled-Cluster Theory. *Journal of Chemical Theory and Computation*, 12(12):5834–5840, December 2016.

[245] Joshua J. Goings, Patrick J. Lestrange, and Xiaosong Li. Real-time time-dependent electronic structure theory. *WIREs Computational Molecular Science*, 8(1), January 2018.

[246] Ivan S. Ufimtsev and Todd J. Martinez. Quantum Chemistry on Graphical Processing Units. 3. Analytical Energy Gradients, Geometry Optimization, and First Principles Molecular Dynamics. *Journal of Chemical Theory and Computation*, 5(10):2619–2628, October 2009.

[247] Stefan Seritan, Christoph Bannwarth, Bryan S. Fales, Edward G. Hohenstein, Christine M. Isborn, Sara I. L. Kokkila-Schumacher, Xin Li, Fang Liu, Nathan Luehr, James W. Snyder Jr., Chenchen Song, Alexey V. Titov, Ivan S. Ufimtsev, Lee-Ping Wang, and Todd J. Martínez. TeraChem: A graphical processing unit-accelerated electronic structure package for large-scale ab initio molecular dynamics. *WIREs Computational Molecular Science*, 11(2):e1494, 2021.

[248] B. Scott Fales and Benjamin G. Levine. Nanoscale Multireference Quantum Chemistry: Full Configuration Interaction on Graphical Processing Units. *Journal of Chemical Theory and Computation*, 11(10):4708–4716, October 2015.

[249] Jianzhang Zhao, Shaomin Ji, Yinghui Chen, Huimin Guo, and Pei Yang. Excited state intramolecular proton transfer (ESIPT): From principal photophysics to the development of new chromophores and applications in fluorescent molecular probes and luminescent materials. *Phys. Chem. Chem. Phys.*, 14(25):8803–8817, 2012.

[250] Paweł Wnuk, Gotard Burdziński, Michel Sliwa, Michał Kijak, Anna Grabowska, Jerzy Sepioł, and Jacek Kubicki. From ultrafast events to equilibrium – uncovering the unusual dynamics of ESIPT reaction: The case of dually fluorescent diethyl-2,5-(dibenzoxazolyl)-hydroquinone. *Physical Chemistry Chemical Physics*, 16(6):2542–2552, 2014.

[251] Sebok Lee, Jaebeom Lee, and Yoonsoo Pang. Excited state intramolecular proton transfer of 1,2-dihydroxyanthraquinone by femtosecond transient absorption spectroscopy. *Current Applied Physics*, 15(11):1492–1499, November 2015.

[252] Udo Buck and Reinhard Krohne. Cluster size determination from diffractive He atom scattering. *The Journal of Chemical Physics*, 105(13):5408–5415, October 1996.

[253] M. Barbatti, G. Granucci, M. Persico, and H. Lischka. Semiempirical molecular dynamics investigation of the excited state lifetime of ethylene. *Chemical Physics Letters*, 401(1):276–281, January 2005.

[254] E. Engel, K. Schmidt, D. Beljonne, J.-L. Brédas, J. Assa, H. Fröb, K. Leo, and M. Hoffmann. Transient absorption spectroscopy and quantum-chemical studies of matrix-isolated perylene derivatives. *Physical Review B*, 73(24):245216, June 2006.

[255] M. Gühr, M. Bargheer, P. Dietrich, and N. Schwentner. Predissociation and Vibrational Relaxation in the B State of I2 in a Kr Matrix. *The Journal of Physical Chemistry A*, 106(50):12002–12011, December 2002.

[256] Raphaël Thon, Wutharath Chin, Jean-Pierre Galaup, Aimeric Ouvrard, Bernard Bourguignon, and Claudine Crépin. Vibrational Perturbations of W(CO)6 Trapped in a Molecular Lattice Probed by Linear and Nonlinear Spectroscopy. *The Journal of Physical Chemistry A*, 117(34):8145–8156, August 2013.

[257] Iustinian Bejan, Yasin Abd El Aal, Ian Barnes, Thorsten Benter, Birger Bohn, Peter Wiesen, and Jörg Kleffmann. The photolysis of ortho-nitrophenols: A new gas phase source of HONO. *Physical Chemistry Chemical Physics*, 8(17):2028–2035, April 2006.

[258] Yuki Nitta, Oliver Schalk, Hironori Igarashi, Satoi Wada, Takuro Tsutsumi, Kenichiro Saita, Tetsuya Taketsugu, and Taro Sekikawa. Real-Time Probing of an Atmospheric Photochemical Reaction by Ultrashort Extreme Ultraviolet Pulses: Nitrous Acid Release from o-Nitrophenol. *The Journal of Physical Chemistry Letters*, 12(1):674–679, January 2021.

[259] Manuvesh Sangwan and Lei Zhu. Absorption Cross Sections of 2-Nitrophenol in the 295–400 nm Region and Photolysis of 2-Nitrophenol at 308 and 351 nm. *The Journal of Physical Chemistry A*, 120(50):9958–9967, December 2016.

[260] Shi-Bo Cheng, Can-Hua Zhou, Hong-Ming Yin, Ju-Long Sun, and Ke-Li Han. OH produced from o-nitrophenol photolysis: A combined experimental and theoretical investigation. *The Journal of Chemical Physics*, 130(23):234311, June 2009.

[261] Admin Alif, Jean-François Pilichowski, and Pierre Boule. Photochemistry and environment XIII: Phototransformation of 2-nitrophenol in aqueous solution. *Journal of Photochemistry and Photobiology A: Chemistry*, 59(2):209–219, July 1991.

[262] Claudia Mohr, Felipe D. Lopez-Hilfiker, Peter Zotter, André S. H. Prévôt, Lu Xu, Nga L. Ng, Scott C. Herndon, Leah R. Williams, Jonathan P. Franklin, Mark S. Zahniser, Douglas R. Worsnop, W. Berk Knighton, Allison C. Aiken, Kyle J. Gorkowski, Manvendra K. Dubey, James D. Allan, and Joel A. Thornton. Contribution of Nitrated Phenols to Wood Burning Brown Carbon Light Absorption in Detling, United Kingdom during Winter Time. *Environmental Science & Technology*, 47(12):6316–6324, June 2013.

[263] Peng Lin, Nir Bluvshtein, Yinon Rudich, Sergey A. Nizkorodov, Julia Laskin, and Alexander Laskin. Molecular Chemistry of Atmospheric Brown Carbon Inferred from a Nationwide Biomass Burning Event. *Environmental Science & Technology*, 51(20):11561–11570, October 2017.

[264] Kou-San Ju and Rebecca E. Parales. Nitroaromatic Compounds, from Synthesis to Biodegradation. *Microbiology and Molecular Biology Reviews : MMBR*, 74(2):250, June 2010.

[265] Iustinian Gabriel Bejan, Romeo-Iulian Olariu, and Peter Wiesen. Secondary Organic Aerosol Formation from Nitrophenols Photolysis under Atmospheric Conditions. *Atmosphere*, 11(12):1346, December 2020.

[266] N. C. Michenfelder, H. A. Ernst, C. Schweigert, M. Olzmann, and A.-N. Unterreiner. Ultrafast stimulated emission of nitrophenolates in organic and aqueous solutions. *Physical Chemistry Chemical Physics*, 20(16):10713–10720, April 2018.

[267] C. L. Thomsen, J. Thøgersen, and S. R. Keiding. Ultrafast Charge-Transfer Dynamics: Studies of p-Nitroaniline in Water and Dioxane. *The Journal of Physical Chemistry A*, 102(7):1062–1067, February 1998.

[268] Konstantin B. Borisenko, Charles W. Bock, and Istvan Hargittai. Intramolecular Hydrogen Bonding and Molecular Geometry of 2-Nitrophenol from a Joint Gas-Phase Electron Diffraction and ab Initio Molecular Orbital Investigation. *The Journal of Physical Chemistry*, 98(5):1442–1448, February 1994.

[269] Maki Nagaya, Satoshi Kudoh, and Munetaka Nakata. Infrared spectrum and structure of the aci-nitro form of 2-nitrophenol in a low-temperature argon matrix. *Chemical Physics Letters*, 427(1):67–71, August 2006.

[270] Samuel McClung, Dakshitha Abeygunewardane, Spiridoula Matsika, and Thomas Weinacht. Excited-state dynamics of o-nitrophenol studied with UV pump–VUV probe time-resolved photoelectron and photoion spectroscopy. *The Journal of Chemical Physics*, 158(14):144303, April 2023.

[271] Namitha Brijit Bejoy, Prahlad Roy Chowdhury, and G. Naresh Patwari. Modulating the Roaming Dynamics for the NO Release in ortho-Nitrobenzenes. *The Journal of Physical Chemistry Letters*, 14(11):2816–2822, March 2023.

[272] M. A. El-Sayed. Spin—Orbit Coupling and the Radiationless Processes in Nitrogen Heterocyclics. *The Journal of Chemical Physics*, 38(12):2834–2838, June 1963.

[273] M. A. El-Sayed. The Radiationless Processes Involving Change of Multiplicity in the Diazenes. *The Journal of Chemical Physics*, 36(2):573–574, January 1962.

[274] G. Bhaskar Dutt, Marcel Ameloot, Delia Bernik, R. Martín Negri, and Frans C. De Schryver. Global Analysis of Unmatched Polarized Fluorescence Decay Curves of Systems Exhibiting a Residual Anisotropy at Long Times. *The Journal of Physical Chemistry*, 100(23):9751–9761, January 1996.

[275] Marc Crutzen, Marcel Ameloot, Noel Boens, R. Martin Negri, and Frans C. De Schryver. Global analysis of unmatched polarized fluorescence decay curves. *The Journal of Physical Chemistry*, 97(31):8133–8145, August 1993.

[276] Robin M. Hochstrasser. Two-dimensional IR-spectroscopy: Polarization anisotropy effects. *Chemical Physics*, 266(2):273–284, May 2001.

[277] Peter M. Felker. Rotational coherence spectroscopy: Studies of the geometries of large gas-phase species by picosecond time-domain methods. *The Journal of Physical Chemistry*, 96(20):7844–7857, October 1992.

[278] R. M. Hochstrasser, M. A. Pereira, P. E. Share, M. J. Sarisky, Y. R. Kim, S. T. Repinec, R. J. Sension, J. R. G. Thorne, M. Iannone, R. Diller, P. A. Anfinrud, C. Han, T. Lian, and B. Locke. Anisotropy studies of ultrafast dipole reorientations. *Proceedings of the Indian Academy of Sciences - Chemical Sciences*, 103(3):351–362, March 1991.

[279] Hans-Joachim Werner, Peter J. Knowles, Frederick R. Manby, Joshua A. Black, Klaus Doll, Andreas Heßelmann, Daniel Kats, Andreas Köhn, Tatiana Korona, David A. Kreplin, Qianli Ma, Thomas F. Miller, III, Alexander Mitrushchenkov, Kirk A. Peterson, Iakov Polyak, Guntram Rauhut, and Marat Sibaev. The Molpro quantum chemistry package. *The Journal of Chemical Physics*, 152(14):144107, April 2020.

[280] David M. Jonas, Matthew J. Lang, Yutaka Nagasawa, Taiha Joo, and Graham R. Fleming. Pump-Probe Polarization Anisotropy Study of

Femtosecond Energy Transfer within the Photosynthetic Reaction Center of *Rhodobacter sphaeroides* R26. *The Journal of Physical Chemistry*, 100(30):12660–12673, January 1996.

[281] Oliver Schalk and Andreas N. Unterreiner. The influence of rotational diffusion on transient anisotropy in ultrafast experiments. *Physical Chemistry Chemical Physics*, 12(3):655–666, December 2009.

[282] Y.-S. Lin, P. A. Pieniazek, Mino Yang, and J. L. Skinner. On the calculation of rotational anisotropy decay, as measured by ultrafast polarization-resolved vibrational pump-probe experiments. *The Journal of Chemical Physics*, 132(17):174505, May 2010.

[283] H. Keller-Rudek, G. K. Moortgat, R. Sander, and R. Sörensen. The MPI-Mainz UV/VIS Spectral Atlas of Gaseous Molecules of Atmospheric Interest. *Earth System Science Data*, 5(2):365–373, December 2013.

[284] J. K. Thomas, J. Rabani, M. S. Matheson, E. J. Hart, and S. Gordon. Absorption Spectrum of the Hydroxyl Radical1. *The Journal of Physical Chemistry*, 70(7):2409–2410, July 1966.

[285] Giuseppe M. J. Barca, Colleen Bertoni, Laura Carrington, Dipayan Datta, Nuwan De Silva, J. Emiliano Deustua, Dmitri G. Fedorov, Jeffrey R. Gour, Anastasia O. Gunina, Emilie Guidez, Taylor Harville, Stephan Irle, Joe Ivanic, Karol Kowalski, Sarom S. Leang, Hui Li, Wei Li, Jesse J. Lutz, Ilias Magoulas, Joani Mato, Vladimir Mironov, Hiroya Nakata, Buu Q. Pham, Piotr Piecuch, David Poole, Spencer R. Pruitt, Alistair P. Rendell, Luke B. Roskop, Klaus Ruedenberg, Tosaporn Sattasathuchana, Michael W. Schmidt, Jun Shen, Lyudmila Slipchenko, Masha Sosonkina, Vaibhav Sundriyal, Ananta Tiwari, Jorge L. Galvez Vallejo, Bryce Westheimer, Marta Włoch, Peng Xu, Federico Zahariev, and Mark S. Gordon. Recent developments in the general atomic and molecular electronic structure system. *The Journal of Chemical Physics*, 152(15):154102, April 2020.

[286] Zhendong Li and Wenjian Liu. Critical Assessment of TD-DFT for Excited States of Open-Shell Systems: I. Doublet–Doublet Transitions. *Journal of Chemical Theory and Computation*, 12(1):238–260, January 2016.

[287] William Rodríguez-Córdoba, Luis Gutiérrez-Arzaluz, Fernando Cortés-Guzmán, and Jorge Peon. Excited state dynamics and photochemistry of nitroaromatic compounds. *Chemical Communications*, 57(92):12218–12235, 2021.

[288] Rodrigo Morales-Cueto, Mariana Esquivelzeta-Rabell, Jimena Saucedo-Zugazagoitia, and Jorge Peon. Singlet Excited-State Dynamics of Ni-

tropolycyclic Aromatic Hydrocarbons: Direct Measurements by Femtosecond Fluorescence Up-Conversion. *The Journal of Physical Chemistry A*, 111(4):552–557, February 2007.

[289] B. Heinz, T. Schmierer, S. Laimgruber, and P. Gilch. Excited state processes of nitrobenzaldehydes probed by ultrafast fluorescence and absorption spectroscopy. *Journal of Photochemistry and Photobiology A: Chemistry*, 199(2):274–281, September 2008.

[290] Sullivan Bailey-Darland, Taylor D. Krueger, and Chong Fang. Ultrafast Spectroscopies of Nitrophenols and Nitrophenolates in Solution: From Electronic Dynamics and Vibrational Structures to Photochemical and Environmental Implications. *Molecules*, 28(2):601, January 2023.

[291] Alessandra Ciavardini, Marcello Coreno, Carlo Callegari, Carlo Spezzani, Giovanni De Ninno, Barbara Ressel, Cesare Grazioli, Monica de Simone, Antti Kivimäki, Paolo Miotti, Fabio Frassetto, Luca Poletto, Carla Puglia, Simonetta Fornarini, Marco Pezzella, Enrico Bodo, and Susanna Piccirillo. Ultra-Fast-VUV Photoemission Study of UV Excited 2-Nitrophenol. *The Journal of Physical Chemistry A*, 123(7):1295–1302, February 2019.

[292] M. Takezaki, N. Hirota, and M. Terazima. Nonradiative Relaxation Processes and Electronically Excited States of Nitrobenzene Studied by Picosecond Time-Resolved Transient Grating Method. https://pubs.acs.org/doi/pdf/10.1021/jp963095t, May 1997.

[293] Dmitry A. Fedorov, Spencer R. Pruitt, Kristopher Keipert, Mark S. Gordon, and Sergey A. Varganov. Ab Initio Multiple Spawning Method for Intersystem Crossing Dynamics: Spin-Forbidden Transitions between 3B1 and 1A1 States of GeH2. *The Journal of Physical Chemistry A*, 120(18):2911–2919, May 2016.

[294] Basile F. E. Curchod, Clemens Rauer, Philipp Marquetand, Leticia González, and Todd J. Martínez. Communication: GAIMS–Generalized Ab Initio Multiple Spawning for both internal conversion and intersystem crossing processes. *The Journal of Chemical Physics*, 144(10):101102, March 2016.

[295] Jay Rutledge, Anthony Catanese, Daniel D. Hickstein, Scott A. Diddams, Thomas K. Allison, and Abijith S. Kowligy. Broadband ultraviolet-visible frequency combs from cascaded high-harmonic generation in quasi-phase-matched waveguides. *JOSA B*, 38(8):2252–2260, August 2021.

[296] Susan M. Bellm and Katharine L. Reid. Reevaluation of the Use of Photoelectron Angular Distributions as a Probe of Dynamical Processes:

Strong Dependence of Such Distributions from ${S}_{1}$ Paradifluorobenzene on Photoelectron Kinetic Energy. *Physical Review Letters*, 91(26):263002, December 2003.

[297] Toshinori Suzuki. Ultrafast photoelectron spectroscopy of aqueous solutions. *The Journal of Chemical Physics*, 151(9):090901, 2019.

[298] Yo-ichi Yamamoto, Yoshi-Ichi Suzuki, and Toshinori Suzuki. Charge Transfer Reactions from I– to Polar Protic Solvents Studied Using Ultrafast Extreme Ultraviolet Photoelectron Spectroscopy. *The Journal of Physical Chemistry Letters*, 14(4):1052–1058, February 2023.

[299] Francesco Segatta, Mattia Russo, Daniel R. Nascimento, Davide Presti, Francesco Rigodanza, Artur Nenov, Andrea Bonvicini, Alberto Arcioni, Shaul Mukamel, Margherita Maiuri, Luca Muccioli, Niranjan Govind, Giulio Cerullo, and Marco Garavelli. In Silico Ultrafast Nonlinear Spectroscopy Meets Experiments: The Case of Perylene Bisimide Dye. *Journal of Chemical Theory and Computation*, 17(11):7134–7145, November 2021.

[300] Chris T. Middleton, Kimberly de La Harpe, Charlene Su, Yu Kay Law, Carlos E. Crespo-Hernández, and Bern Kohler. DNA Excited-State Dynamics: From Single Bases to the Double Helix. *Annual Review of Physical Chemistry*, 60(1):217–239, May 2009.

[301] Hiroyuki Saigusa. Excited-state dynamics of isolated nucleic acid bases and their clusters. *Journal of Photochemistry and Photobiology C: Photochemistry Reviews*, 7(4):197–210, December 2006.

[302] Chien-hung Tseng, Péter Sándor, Marija Kotur, Thomas C. Weinacht, and Spiridoula Matsika. Two-Dimensional Fourier Transform Spectroscopy of Adenine and Uracil Using Shaped Ultrafast Laser Pulses in the Deep UV. *The Journal of Physical Chemistry A*, 116(11):2654–2661, March 2012.

[303] Susanne Ullrich, Thomas Schultz, Marek Z. Zgierski, and Albert Stolow. Electronic relaxation dynamics in DNA and RNA bases studied by time-resolved photoelectron spectroscopy. *Physical Chemistry Chemical Physics*, 6(10):2796, 2004.

[304] Peter Hamm and Martin Zanni. *Concepts and Methods of 2D Infrared Spectroscopy.* Cambridge University Press, February 2011.

[305] Grzegorz Kowzan and Thomas K. Allison. Theory of rotationally resolved two-dimensional infrared spectroscopy including polarization dependence and rotational coherence dynamics. *Physical Review A*, 106(4):042819, October 2022.

[306] Grzegorz Kowzan and Thomas K. Allison. Controlling Rotationally Resolved Two-Dimensional Infrared Spectra with Polarization. *The Journal of Physical Chemistry Letters*, 13(50):11650–11654, December 2022.

[307] Qizhong Liang, Ya-Chu Chan, Jutta Toscano, Kristen K. Bjorkman, Leslie A. Leinwand, Roy Parker, Eva S. Nozik, David J. Nesbitt, and Jun Ye. Breath analysis by ultra-sensitive broadband laser spectroscopy detects SARS-CoV-2 infection. *Journal of Breath Research*, 17(3):036001, April 2023.

[308] Qizhong Liang, Ya-Chu Chan, P. Bryan Changala, David J. Nesbitt, Jun Ye, and Jutta Toscano. Ultrasensitive multispecies spectroscopic breath analysis for real-time health monitoring and diagnostics. *Proceedings of the National Academy of Sciences*, 118(40):e2105063118, October 2021.

[309] M Ben-Nun and Todd J Martínez. Photodynamics of ethylene: Ab initio studies of conical intersections. *Chemical Physics*, 259(2):237–248, September 2000.

[310] Robert T. McGibbon, Kyle A. Beauchamp, Matthew P. Harrigan, Christoph Klein, Jason M. Swails, Carlos X. Hernández, Christian R. Schwantes, Lee-Ping Wang, Thomas J. Lane, and Vijay S. Pande. MDTraj: A Modern Open Library for the Analysis of Molecular Dynamics Trajectories. *Biophysical Journal*, 109(8):1528–1532, October 2015.

[311] W. Kabsch. A solution for the best rotation to relate two sets of vectors. *Acta Crystallographica Section A: Crystal Physics, Diffraction, Theoretical and General Crystallography*, 32(5):922–923, September 1976.